Affordable Extended Hyperbolic Moment Closures for Rarefied Gas-Flow Predictions

by

Ethan Rice

A thesis submitted to the University of Ottawa
in partial fulfillment of the requirements for
the Ph.D. degree in Mechanical Engineering

Department of Mechanical Engineering
University of Ottawa

Abstract

For the past 75 years, moment closures have been a promising method of gas-flow prediction for rarefied gases, as they offer significant mathematical and computational advantages over other applicable methods in regimes outside of local thermodynamic equilibrium. However, many of these advantages come from their ability to be formulated as hyperbolic systems of balance laws. Only recently have there been generalizable hyperbolic closures which can be expressed in closed form, and many of these closures have been restricted to simplified one-dimensional gases. While mathematically elegant, this limits the practical use of these new hierarchies to academic problems. Extending their desirable mathematical properties to real multidimensional gases has proven difficult, and a new method to handle this extension is the goal of this thesis.

First, existing hierarchies of moment closures are presented, as well as their mathematical properties. Next, the technique by which higher-order moment models can be constructed is presented, with two new 20-moment closures being developed as a result. Linear stability of these models is presented, along with their performance in canonical discontinuous gas-flow problems for the continuum, transition, and free-molecular flow regimes. The traditional formulation of boundary conditions in kinetic theory is difficult to replicate in this framework. Instead, a new formulation of the Knudsen-layer boundary condition is presented, with results for both the 10-moment and 20-moment equations in canonical boundary-value problems. Finally, results for more realistic gas-flow problems in rarefied settings are shown. Strong shocks, and flows with regions of large translational non-equilibrium, are also explored. Further possible extensions for the models, such as for diatomic gases and plasmas, conclude the thesis.

Acknowledgements

There are many people this thesis would not have come together without. First and foremost, I would like to thank my supervisor James G. McDonald. What started as a request in my final year of undergraduate studies to help me complete my course credits as fast as possible, ironically turned in to the six years of work that went in to this thesis. Every day I get to wake up and push myself by facing new challenges in mathematics, physics, and computer science, thanks to his support. I would also like to thank my committee members, Edgar Matida and Matei Radulescu, for their support of my work through the proposal and revision stages of this thesis, as well as the efforts of Brian Maxwell and Henning Struchtrup in their involvement with my final oral examination.

My fellow students in the lab have also been huge contributors to my graduate education and work. In particular, Éloïse Plante-Sabourin and Stefano Boccelli have been enormous aides, and helped me by producing all the reference solutions throughout this thesis. William Morin and Benoit Allard's shared love of the development of new non-equilibrium models has given me tons of insight in to my work. Osman El-Gohtmi has spent countless hours helping me in the programming and implementation of my models into BLawB. Everyone else in the lab, Brendan Sommers, Kevin Cheevers, Farzane Zangene, have been incredible colleagues to share the space with.

I would also be remiss to not thank the University of Ottawa Gee-Gees Varsity Swim program for their constant support of my endeavours. Despite retiring as a swimmer at the end of my undergraduate studies, head coaches Dave Heinbuch and Vincenzo Sljuka have continued to keep me involved as an assistant coach. Giving me a space to excel outside of research (as well as their financial support throughout my graduate studies) is

something I will be eternally grateful for. My former teammates, and the athletes I have had the pleasure to coach, continue to push to be the best version of myself possible.

Perhaps most importantly, I would like to thank my amazing family. My parents, Kirk and Janice, as well as my brother, Oliver, have been huge supporters of every adventure I throw myself in to. They have always been there to provide love and encouragement. My wife, Katie, has been with me every step of the way during the course of this work. She has helped me as an editor, provided me with every cup of coffee consumed during the writing process, and listened to every presentation with no background in the subject matter. Her love and support means the world to me.

Computational resources for performing all the calculations reported herein were provided by the Digital Research Alliance of Canada. Funding for this research was graciously provided by my supervisor James McDonald through the Natural Sciences and Engineering Research Council of Canada Discovery Grant.

- Ethan Rice, April 2026

Contents

List of Figures

"Nicht der Besitz der Wahrheit, sondern das erfolgreiche Ringen um sie macht das Glück des Forschers aus; denn alles Verweilen ermüdet und erschlafft auf die Dauer. Ein starkes, gesundes Leben gedeiht nur durch Arbeit und Fortschritt"

Max Planck — *Wege zur physikalischen Erkenntnis: Reden und Vorträge*

Chapter 1

Introduction

Fluid mechanics is one of the oldest of the applied sciences, and for centuries it has been studied by mathematicians, scientists, and engineers, remaining to this day as an active area of research. Traditional fluid mechanics often deals with fluids under the continuum assumption, where the fluid is well approximated as a continuous medium. While this is a good assumption for many applications, the reality is that all matter is made of discrete particles. While models developed under the continuum assumption, like the Navier-Stokes equations, can accurately predict fluid behaviour for a wide variety of situations, there are regimes where the effects of the particles which make up a fluid become relevant, and the assumption of a continuous medium is invalid.

The kinetic theory of gases offers a way to connect the discrete to the continuous, showing how the cumulative effects of molecular motion for a gas in local thermodynamic equilibrium can give rise to the equations derived under the continuum assumption. But simultaneously, kinetic theory also describes the breakdown of the continuum assumption. In the absence of sufficiently frequent interparticle collisions, a gas can leave local thermodynamic equilibrium. Many practical applications, such as spacecraft re-entry, high atmosphere flight, nano-scale flows, or plasma flows, have regions of non-equilibrium which become relevant for accurate modelling. Without consideration of these effects, traditional models can predict physically inaccurate flow behaviour.

One quantity which can give a sense of whether or not the molecular effects of the

gas need to be considered is the Knudsen number,

$$\mathrm{Kn} = \frac{\lambda}{L}\,, \tag{1.1}$$

where λ is the mean free path, or a measure of the space between gas particles, and L is a representative length of the flow being studied. For small Knudsen numbers, a fluid can be reliably modelled as a continuum, and traditional methods of fluid mechanics such as the Euler or Navier-Stokes equations are perfectly valid. For very large Knudsen numbers, particle methods like direct simulation Monte Carlo (DSMC) [2] can simply track representative particles of the gas. Directly integrating the kinetic equations, like the method proposed by Mieussens [3], can also be used to resolve non-equilibrium effects. However, for regimes where the mean free path and representative length are roughly the same order, or

$$10^{-2} < \mathrm{Kn} < 10^{1}\,, \tag{1.2}$$

the continuum assumption is invalid, while the tracking of particles or direct integration are too computationally expensive. It is in this so-called transition regime where moment methods have the most to offer.

Moment methods are a probabilistic model, tracking the statistics of gas particles instead of the particles themselves. These statistics can then be shown to correspond to the typical macroscopic properties that engineers care about. These models also result in a mathematically convenient balance-law formulation, which can be solved through a wide-range of efficient numerical methods [4–8]. Reliable moment methods would allow for significant reduction in computation time, while still providing accurate predictions for regimes with moderate non-equilibrium.

There are still many problems limiting the widespread adoption of moment methods. While many hierarchies of moment closures exist, such as the original Grad hierarchy [9], the maximum-entropy hierarchy [10–12], and many more [13–15], they often rely on proposing a distribution function for the gas particles. This can then lead to inconvenient mathematical formulation of the resulting partial differential equations (PDEs). The

Grad hierarchy only has a small region near equilibrium in which the PDEs remain hyperbolic. Outside this region, this hierarchy predicts complex-valued wave speeds, and initial value problems become ill-posed. Regularizations of the Grad model permit high-order derivatives, and lose the desirable hyperbolic balance-law formulation [16]. The maximum-entropy hierarchy can cover almost the entire realizable space and have hyperbolicity, but has a distribution function which cannot be integrated in closed form for higher-order closures [17]. Instead, computationally inefficient numerical integration needs to be relied upon, which comes at a significant cost for practical applications.

Recent advances have offered new, much more mathematically convenient models, relying not on the prescription of a specific distribution and instead on the desirable properties of the PDEs that will be constructed. The Quadrature-based Method of Moments (QMOM) of Fox and Laurent [18–21], and the Method of Orthogonal Polynomials of Morin and McDonald [22], have given rise to hierarchies of moment methods which are robustly hyperbolic for all realizable states of the gas. However, these methods come with drawbacks as well, notably that until now they have been restricted to academic, one-dimensional gases. Extending the closures to a realistic, multidimensional gas setting, and retaining the mathematical advantages they were designed to have, has proven challenging. Other models like the GENERIC-13 closure [23, 24], which uses the structure of Grad's 13-moment closure, are not easily extendable to arbitrary higher orders of moments.

1.1 Thesis Structure

The goal of this Ph.D. thesis is to build upon the new hierarchy of one-dimensional closures and find a technique in order to extend these closures into a formulation which can be used for practical multidimensional gas-flow predictions. For simplicity, only monatomic gases are considered, but with the full three-dimensional velocity space. Beginning in Chapter 2, the kinetic theory of gases is covered in detail. This includes a review of the kinetic equations, how the Euler equations arise from a gas in local thermo-

dynamic equilibrium, and some existing closure hierarchies, such as Grad and maximum entropy. Then, as the basis for the new models developed in this work, the new hierarchy of one-dimensional closures is reviewed. Chapter 3 then covers the development of the new extended hierarchy of moment closures, defining some of the mathematical properties that are desirable to replicate in the new models. Two 20-moment models that were developed as a result of this work are then presented. Their linear stability is demonstrated through a dispersion analysis of each model. Canonical flow problems for a monatomic gas solved with each of the models of the new hierarchy are shown in Chapter 4, including Sod shock-tube Riemann problems and discontinuous bubble problems for the continuum, transition, and free-molecular regimes. This chapter also includes a discussion of the numerical methods used for the solution of the models.

As a consequence of the new techniques being used to derive moment closures, the formulation of solid-wall boundary conditions becomes difficult to obtain. Chapter 5 includes a review of the traditional method by which solid-wall and gas-particle interactions are modelled, and then presents a new way to obtain boundary fluxes which are valid for multidimensional, hyperbolic models. The new formulation is compared against the traditional formulation with the 10-moment equations, and then applied to the 20-moment equations. Canonical boundary value problems, such as Couette flow and heat transfer through a fluid, are shown across the three regimes of interest, and compared to known solutions of these simplified cases. Realistic cases which incorporate both the new model and boundary conditions are presented in Chapter 6, investigating practical settings in which these new models are most applicable. This includes high-speed, rarefied flows past simple objects, and strong shock-structure prediction. Possible further extensions of the models to polyatomic gases and plasmas are discussed before this work is concluded in Chapter 7.

In addition to the main content of the thesis, a number of related works are included in the appendices. These materials address aspects of the broader problems encountered during the course of the Ph.D. work that fall outside the immediate scope of the thesis, but contribute to the overall completeness and rigour of the work. Appendix A shows

a 35-moment closure, which is the next higher-order member of the hierarchy discussed in Chapter 3, to demonstrate construction of further higher-order moment closures using the techniques developed in this work. Appendix B shows the derivation of the exact free-molecular solution of the discontinuous bubble problem shown in Section 4.3, to give confidence in the reference solutions provided throughout. These additional details are included as they may be of interest to the reader, but are not required for the understanding of the ideas discussed in the main body of the work.

1.2 Major Contributions of the Thesis

This work presents three primary contributions to the development of models for non-equilibrium gas flow predictions. They are:

- A technique by which to construct robustly hyperbolic moment closures for any number of moments, as well as the development and analysis of multiple models within this framework.
- The formulation of a novel solid-wall boundary-conditions treatment capable of replicating the Knudsen-layer approximation for moment closures that are not derived from a known distribution function.
- Applications of the newly developed higher-order moment models in multidimensional, non-equilibrium flow prediction.

Together, these contributions provide a mathematically consistent and computationally practical framework for non-equilibrium flow simulation. This extends the applicability of moment closures to practical multidimensional gas flows in both the continuum and transition regimes.

Chapter 2

Kinetic-Theory Background

In the kinetic theory of gases, the statistical behaviour of gas-particle interactions is what gives rise to the macroscopic effects of a flow. Typically, a velocity distribution function, $\mathcal{F}(x_i, v_i, t)$, is prescribed, describing the probability of finding a particle at position, x_i, with a velocity, v_i, at a time, t. Multiplying by the particle mass, m, and relevant velocity weights, then integrating this distribution over the entire velocity space gives rise to the moments which describe the macroscopic state of the gas. Some familiar moments are

$$\begin{aligned} U_0 &= \iiint_\infty m\mathcal{F}(x_i, v_i, t)\,\mathrm{d}v_i = \langle m\mathcal{F}\rangle = \rho\,, \\ U_i &= \iiint_\infty mv_i\mathcal{F}(x_i, v_i, t)\,\mathrm{d}v_i = \langle mv_i\mathcal{F}\rangle = \rho u_i\,, \\ U_{ij} &= \iiint_\infty mv_iv_j\mathcal{F}(x_i, v_i, t)\,\mathrm{d}v_i = \langle mv_iv_j\mathcal{F}\rangle = \rho u_iu_j + P_{ij}\,, \end{aligned} \tag{2.1}$$

which give the mass, momentum, and energy densities of the gas. For brevity, the notation, $\langle\cdots\rangle$, represents the integration over all velocity space. One can also define the random velocity of the fluid, $c_i = v_i - u_i$, shifting the distribution in to the frame of reference of the bulk velocity of the gas. By definition, all moments of any term with a single random velocity are zero, or

$$\langle mc_i\mathcal{F}\rangle = 0\,, \tag{2.2}$$

and gives the higher-order moments in a more convenient and brief form. Some relevant higher-order moments in this work are defined as

$$\begin{aligned} P_{ij} &= \langle m c_i c_j \mathcal{F} \rangle \ , \\ Q_{ijk} &= \langle m c_i c_j c_k \mathcal{F} \rangle \ , \\ R_{ijkl} &= \langle m c_i c_j c_k c_l \mathcal{F} \rangle \ , \\ S_{ijklm} &= \langle m c_i c_j c_k c_l c_m \mathcal{F} \rangle \ , \end{aligned} \tag{2.3}$$

with P_{ij} being related to the variances and covariances of the distribution function, Q_{ijk} being related to the skewness of the distribution function, R_{ijkl} being related to the kurtosis of the distribution function, and S_{ijklm} being related to the hyperskewness of the distribution function. The full, convected form of these moments can be computed as

$$\begin{aligned} U_{ijk} &= \langle m v_i v_j v_k \mathcal{F} \rangle \\ &= \langle m \left(u_i + c_i\right) \left(u_j + c_j\right) \left(u_k + c_k\right) \mathcal{F} \rangle \\ &= \langle m \left(u_i u_j u_k + c_i u_j u_k + c_j u_i u_k + c_k u_i u_j + c_i c_j u_k + c_i c_k u_j + c_j c_k u_i + c_i c_j c_k\right) \mathcal{F} \rangle \\ &= \rho u_i u_j u_k + P_{ij} u_k + P_{ik} u_j + P_{jk} u_i + Q_{ijk} \, , \end{aligned} \tag{2.4}$$

$$\begin{aligned} U_{ijkl} =& \rho u_i u_j u_k u_l + P_{ij} u_k u_l + P_{ik} u_j u_l + P_{jk} u_i u_l + P_{il} u_j u_k + P_{jl} u_i u_k + P_{kl} u_i u_j \\ &+ Q_{ijk} u_l + Q_{ijl} u_k + Q_{ikl} u_j + Q_{ikl} u_j + Q_{jkl} u_i + R_{ijkl} \, , \end{aligned} \tag{2.5}$$

and so on, becoming increasingly expansive for higher-order moments. These contributions of the lower-order moments do not need to be considered when taking moments with c_i weights, but they will be needed to ensure translational invariance in velocity space. For brevity, this work often only lists the relevant random components of the relevant moments for each higher-order method, but the full convected forms are considered when necessary, such as during the computation of the solutions to the resulting PDEs.

While these statistical properties may be in a more general form than is typically seen in traditional fluid mechanics, they can often be easily related to more commonly

understood properties of a gas. For instance, the generalized anisotropic pressure tensor,

$$P_{ij} = \begin{bmatrix} P_{xx} & P_{xy} & P_{xz} \\ P_{xy} & P_{yy} & P_{yz} \\ P_{xz} & P_{yz} & P_{zz} \end{bmatrix}, \tag{2.6}$$

contains the variances and covariances of the distribution function, but can also be related to the thermodynamic pressure, p, through the relationship, $p = \frac{1}{3}(P_{xx} + P_{yy} + P_{zz})$, and the deviatoric stresses, τ_{ij}, with the relationship $P_{ij} = p\delta_{ij} - \tau_{ij}$, for a monatomic gas. The generalized third-order heat-flux tensor, Q_{ijk}, can be related to the traditional heat flux vector through its half trace, or $q_i = \frac{1}{2}Q_{ijj}$. Higher-order moments, such as R_{ijkl} and S_{ijklm}, are less familiar in a physical sense, however, this does not mean they do not play an important role in the physics of the gas. Outside thermodynamic equilibrium, consideration of these higher-order moments is increasingly important for physically accurate predictions.

How the distribution function changes, and how this can result in partial differential equations (PDEs) is shown in Section 2.1. The Euler equations, and how they relate to local thermodynamic equilibrium is shown in Section 2.2. The original moment closure of Grad, as well as the maximum entropy hierarchy, are presented in Sections 2.3 and 2.4 respectively. Finally, the one-dimensional closures which this work uses as inspiration to build the new hierarchy of multidimensional closures are shown in Section 2.5.

2.1 The Boltzmann Equation

The time evolution of the distribution function is described by the Boltzmann equation,

$$\frac{\partial \mathcal{F}}{\partial t} + v_i \frac{\partial \mathcal{F}}{\partial x_i} + \frac{\partial (a_i \mathcal{F})}{\partial v_i} = \frac{\delta \mathcal{F}}{\delta t}, \tag{2.7}$$

where a_i represents the particle acceleration and the term $\frac{\delta \mathcal{F}}{\delta t}$ describes particle collision interactions. This equation can be simplified in the absence of any external acceleration fields, taking $a_i = 0$, which isolates the convective part of the equation that this work is

most focused on modelling.

Directly solving the high-dimensional Boltzmann equation is usually impractical. Instead, a velocity weight vector can be defined as $\boldsymbol{w} = [w_1, w_2, \ldots, w_n]^{\mathrm{T}}$, which can then multiply the Boltzmann equation along with particle mass, m, to give

$$m\boldsymbol{w}\frac{\partial}{\partial t}\mathcal{F} + m\boldsymbol{w}\frac{\partial}{\partial x_i}v_i\mathcal{F} = m\boldsymbol{w}\frac{\delta\mathcal{F}}{\delta t}\,, \tag{2.8}$$

and moments can be taken. As both the particle mass and velocity weight variables are independent of the temporal and spatial dimensions, t and x_i, and the velocity integral is taken over velocity space alone, the differential operators can commute. This gives

$$\frac{\partial}{\partial t}\left\langle m\boldsymbol{w}\mathcal{F}\right\rangle + \frac{\partial}{\partial x_i}\left\langle m\boldsymbol{w}v_i\mathcal{F}\right\rangle = \left\langle m\boldsymbol{w}\frac{\delta\mathcal{F}}{\delta t}\right\rangle\,, \tag{2.9}$$

known as Maxwell's equation of change. It can be written more succinctly,

$$\frac{\partial\boldsymbol{U}}{\partial t} + \frac{\partial\boldsymbol{F}_i}{\partial x_i} = \boldsymbol{S}\,, \tag{2.10}$$

with a solution vector of the known moments, $\boldsymbol{U}$, their corresponding fluxes, $\boldsymbol{F}_i$, and a source vector, $\boldsymbol{S}$. As can be seen in Equation (2.9), the flux term will always be one order higher than the corresponding moment in the solution vector. For the lower-order moments in the solution vector, this means that any flux is simply the next higher-order moment that is being tracked. However, for the highest-order moment in the solution vector, the so-called closing flux is not known. The goal of moment closures therefore becomes the choice of the closing fluxes in Maxwell's equation of change in such a way to close the system and generate a set of PDEs which best describe the way the statistics of the distribution function changes. One of the most desirable properties is that it results in a hyperbolic system of PDEs, discussed in Section 2.1.1. In general, the source term is also unclosed, however this work considers well known approximations to the collision operator to focus on the construction of closing fluxes, discussed in Section 2.1.2.

2.1.1 Hyperbolic Moment Closures

While a variety of forms of closing fluxes for a given set of moments exist, there are some restrictions on what could be considered useful for practical application. The most important property that this work is concerned with is robust hyperbolicity. By assuming that the closing fluxes are some function of the known moments, Maxwell's equation of change can be reexpressed as

$$\frac{\partial \boldsymbol{U}}{\partial t} + \frac{\mathrm{d}\boldsymbol{F}_{\mathrm{i}}}{\mathrm{d}\boldsymbol{U}} \frac{\partial \boldsymbol{U}}{\partial x_i} = \boldsymbol{S}\,, \tag{2.11}$$

where $\frac{\mathrm{d}\boldsymbol{F}_{\mathrm{i}}}{\mathrm{d}\boldsymbol{U}}$ is the flux Jacobian. A system of first-order partial differential equations like this is then said to be hyperbolic if its flux Jacobian possesses real Eigenvalues and a complete set of linearly independent Eigenvectors in every spatial direction. Hyperbolicity ensures finite propagation speed, the existence of characteristic wave families, and confidence for the well-posedness of the Cauchy problem. For moment closures, preserving hyperbolicity over physically admissible states is desirable to ensuring robustness and numerical tractability.

2.1.2 Collision Modelling

Aside from the closing flux, the other inconvenient part of the Boltzmann equation that must be treated is the collision operator, as modelling inter-particle collision effects is a high-dimensional problem. Under the assumptions that only binary collisions between molecules occur, with independent particle velocities, and that a single collision does not appreciably change the distribution of particle velocities of the gas, the collision integral has the form

$$\frac{\delta \mathcal{F}}{\delta t} = \left\langle \int_0^{2\pi} \int_0^{\pi} \left(\mathcal{F}' \mathcal{F}^{1\prime} - \mathcal{F}\mathcal{F} \right) \left| v_i - v_i^1 \right| \sigma \sin\theta \mathrm{d}\theta \mathrm{d}\phi \right\rangle_{v_i'}\,, \tag{2.12}$$

where $\mathcal{F}$ and $\mathcal{F}^1$ are the distribution functions of two colliding particles evaluated before the collision has occurred with velocities v_i and v_i^1 respectively. Their distributions after the collision has occurred are denoted with $\mathcal{F}'$ and $\mathcal{F}^{1\prime}$ for the post-collision velocities v_i'

and $v_i^{1\prime}$. The angles θ and ϕ are the deflection and solid angles of the particles undergoing collisions, and σ is the differential cross-section [15, 25]. For any moment taken with velocity weights w of the collision operator that is then integrated over the space v_i,

$$\left\langle w\frac{\delta\mathcal{F}}{\delta t}\right\rangle_{v_i} = \left\langle\left\langle\int_0^{2\pi}\int_0^{\pi} w\left(\mathcal{F}'\mathcal{F}^{1\prime}-\mathcal{F}\mathcal{F}\right)\left|v_i-v_i^1\right|\sigma\sin\theta\mathrm{d}\theta\mathrm{d}\phi\right\rangle_{v_i'}\right\rangle_{v_i}, \tag{2.13}$$

leaves a difficult to handle eight-dimensional integral (with each $\langle\cdots\rangle$ representing a triple integral over the velocity spaces of v_i and v_i', along with the two integrals of the deflection angles θ and ϕ), which is often prohibitively complicated to compute.

The present work primarily focuses on the left-hand side of the Boltzmann equation, and construction of hyperbolic closing fluxes. For simplicity, the right-hand side that models collisions can instead be handled with an approximate treatment, so long as the important properties of the collision operator are respected. One of its properties is that collisions are a mechanism by which the distribution function of the gas will return to local thermodynamic equilibrium. In this state, the gas has a Maxwell-Boltzmann distribution,

$$\mathcal{M} = \frac{\rho}{m}\left(\frac{\rho}{2\pi p}\right)^{\frac{3}{2}}\exp\left(\frac{\rho}{2p}(v_i-u_i)(v_i-u_i)\right), \tag{2.14}$$

which is a function of the density, ρ, the bulk velocity, u_i, and the thermodynamic pressure, p.

For many cases, the simple relaxation-time BGK model [26] can be used, which attenuates any non-equilibrium distribution, $\mathcal{F}$, to the Maxwell-Boltzmann distribution, $\mathcal{M}$, over the timescale, τ. This approximates the collision integral as

$$\frac{\delta\mathcal{F}}{\delta t}\approx-\frac{\mathcal{F}-\mathcal{M}}{\tau}, \tag{2.15}$$

while still respecting the overall effect of the collision operator. If τ is large, it corresponds to free molecular regime, where particle collisions are infrequent and the effect of this source term is near-zero. If τ is small, then any non-equilibrium effect is quickly attenuated back to the Maxwellian, recovering the continuum regime and thermodynamic

equilibrium. Equation (2.13) with this approximation now becomes

$$\left\langle w\frac{\delta\mathcal{F}}{\delta t}\right\rangle_{v_i} \approx -\frac{1}{\tau}\left(\langle mw\mathcal{F}\rangle - \langle mw\mathcal{M}\rangle\right) , \tag{2.16}$$

making moments with this approximation much simpler to compute.

The choice of the timescale is handled in two different ways throughout this work. For the cases presented in Chapter 4, a constant value for the timescale is chosen to keep the PDEs in the regime of interest. Later, in Chapter 6, a more physically accurate collision model is used. The collision timescale can be related to the viscosity of the gas,

$$\tau = \frac{\mu}{p} , \tag{2.17}$$

which can be modelled as a power law,

$$\mu = \mu_{ref}\left(\frac{T}{T_{ref}}\right)^{\omega} , \tag{2.18}$$

based on the local thermodynamic temperature, T, as well as reference viscosity for the gas, μ_{ref}, at the temperature, T_{ref}, that scales with the power, ω [2]. As this work is concerned with a monatomic gas, Argon gas is used, with the values [27]

$$\begin{aligned} \mu_{ref} &= 2.1149 \times 10^{-5}\ \text{Pa s} , \\ T_{ref} &= 273\ \text{K} , \\ \omega &= 0.81 . \end{aligned}$$

Thus, modelling the temperature dependence of Argon's viscosity.

2.2 The Euler Equations

If the distribution function of a gas is known as a function of the moments in the solution vector, then it can be directly integrated to find the form of the closing flux. The simplest possible distribution which models real three-dimensional gases is the Maxwell-

Boltzmann distribution, defined in Equation (2.14), corresponding to the gas being in its local thermodynamic equilibrium state. By choosing $\mathcal{F} = \mathcal{M}$, and taking three velocity weights $\boldsymbol{w} = [1, v_i, \frac{1}{2}v_i v_i]^T$ corresponding to the mass, momentum and energy moments of the gas, the PDEs can be directly integrated from the distribution. The resulting form of Maxwell's equation of change then leads to

$$\frac{\partial}{\partial t}(\rho) + \frac{\partial}{\partial x_i}(\rho u_i) = 0\,, \tag{2.19}$$

$$\frac{\partial}{\partial t}(\rho u_i) + \frac{\partial}{\partial x_j}(\rho u_i u_j + p\delta_{ij}) = 0\,, \tag{2.20}$$

$$\frac{\partial}{\partial t}\left(\frac{1}{2}\rho u_i u_i + \frac{3}{2}p\right) + \frac{\partial}{\partial x_j}\left(\frac{1}{2}\rho u_i u_i u_j + \frac{5}{2}p u_j\right) = 0\,, \tag{2.21}$$

where δ_{ij} is the Kronecker delta function,

$$\delta_{ij} = \begin{cases} 1 & \text{if } i = j, \\ 0 & \text{if } i \neq j. \end{cases} \tag{2.22}$$

Equation (2.19) is the traditional continuity equation, Equation (2.20) is the traditional momentum conservation equation, and Equation (2.21) is the traditional energy conservation equation for a monatomic gas. While these equations do accurately predict adiabatic, inviscid gases, they cannot model any deviation from thermodynamic equilibrium. For more complicated settings, further modelling of the gas behaviour is required.

2.3 Grad's Closure

The original hierarchy of moment closures which can model physics in non-equilibrium states, was the method of Grad in 1949 [9]. This closure uses a Hermite polynomial expansion around the Maxwellian

$$\mathcal{F} = (\alpha_0 H_0 + \alpha_i H_i + \alpha_{ij} H_{ij} + \dots)\,\mathcal{M}\,, \tag{2.23}$$

as the assumed distribution of the gas. The Hermite polynomials $H_{i_0,i_1,i_2,\ldots,i_N}$ are the set of orthogonal polynomials when the Maxwellian is taken as the weight, and are defined as

$$H_{i_0,i_1,\ldots,i_N} = \frac{1}{\mathcal{M}} \frac{\partial^N}{\partial c_{i_0} \partial c_{i_1} \ldots \partial c_{i_N}} \mathcal{M} \,, \tag{2.24}$$

where N is the order of Hermite polynomial derived and c_{i_1} to c_{i_N} are the corresponding random velocities in each direction. The orthogonality of the polynomials means that

$$\iiint_{\infty} H_{i_0,i_1,\ldots,i_N} H_{j_0,j_1,\ldots,j_M} \mathcal{M} \, \mathrm{dc_x} \, \mathrm{dc_y} \, \mathrm{dc_z} = 0 \quad \text{when} \quad i_0, i_1, \ldots, i_N \neq j_0, j_1, \ldots, j_M \,, \tag{2.25}$$

resulting in only the polynomials of a lower-order than the velocity weight being relevant when computing a moment. This also means that each closure coefficient, $\alpha_{i_1,i_2,\ldots,i_N}$, is independent of any higher-order moments, and lower-order polynomials do not have any of the higher-order coefficients.

As an example of a closure in Grad's hierarchy, the 20-moment closure is considered. This closure has 20 variables: a scalar density of the gas ρ, a three-dimensional vector for the velocity of the gas u_i, a generalized symmetric pressure tensor P_{ij} with six entries, and a generalized symmetric heat-flux tensor Q_{ijk} with ten entries. The distribution function is then of the form

$$\mathcal{F} = \left(\alpha_0 H_0 + \alpha_i H_i + \alpha_{ij} H_{ij} + \alpha_{ijk} H_{ijk}\right) \mathcal{M} \,, \tag{2.26}$$

with the associated Hermite polynomials being given by

$$\begin{aligned}
H_0 &= 1 \,, \\
H_i &= -\frac{\rho}{p} c_i \,, \\
H_{ij} &= -\frac{\rho^2}{p^2} c_i c_j - \frac{\rho}{p} \delta_{ij} \,, \\
H_{ijk} &= -\frac{\rho^3}{p^3} c_i c_j c_k + \frac{\rho^2}{p^2} \left(c_i \delta_{jk} + c_j \delta_{ik} + c_k \delta_{ij}\right) \,,
\end{aligned} \tag{2.27}$$

up to third order. In order to be consistent with the 20 known moments of $\boldsymbol{U}$, the closure coefficients are

$$\begin{aligned}
&\alpha_0 = 1\,,\\
&\alpha_i = 0\,,\\
&\alpha_{ij} = (\delta_{im}\delta_{jn} + \delta_{in}\delta_{jm})^{-1}\left(\frac{P_{mn} - p\delta_{mn}}{\rho}\right)\,,\\
&\alpha_{ijk} = -(\delta_{im}\delta_{jn}\delta_{ko} + \delta_{im}\delta_{jo}\delta_{kn} + \delta_{in}\delta_{jm}\delta_{ko} + \delta_{in}\delta_{jo}\delta_{km} + \delta_{io}\delta_{jn}\delta_{km} + \delta_{io}\delta_{jm}\delta_{kn})^{-1}\left(\frac{Q_{mno}}{\rho}\right)\,,
\end{aligned} \tag{2.28}$$

fully defining the distribution function. The closing flux can then be integrated from the distribution function, and has the form

$$R_{ijkl} = \frac{p}{\rho}\left[\delta_{ij}P_{kl} + \delta_{ik}P_{jl} + \delta_{il}P_{jk} + \delta_{kl}P_{ij} + \delta_{jl}P_{ik} + \delta_{jk}P_{il} - (\,\delta_{ij}\delta_{kl} + \delta_{ik}\delta_{jl} + \delta_{il}\delta_{jk}\,)p\right]\,. \tag{2.29}$$

Thus, closing the system. The resulting PDEs for the Grad hierarchy are

$$\frac{\partial}{\partial t}(\rho) + \frac{\partial}{\partial x_i}(\rho u_i) = 0 \tag{2.30}$$

$$\frac{\partial}{\partial t}(\rho u_i) + \frac{\partial}{\partial x_j}(\rho u_i u_j + P_{ij}) = 0 \tag{2.31}$$

$$\frac{\partial}{\partial t}(\rho u_i u_j + P_{ij}) + \frac{\partial}{\partial x_k}(\rho u_i u_j u_k + P_{ij}u_k + P_{ik}u_j + P_{jk}u_i + Q_{ijk}) = \boldsymbol{S}_{ij}(\boldsymbol{U}) \tag{2.32}$$

$$\begin{aligned}
&\frac{\partial}{\partial t}(\rho u_i u_j u_k + P_{ij}u_k + P_{ik}u_j + P_{jk}u_i + Q_{ijk}) + \frac{\partial}{\partial x_l}(\rho u_i u_j u_k u_l + P_{ij}u_k u_l + P_{ik}u_j u_l\\
&+ P_{jk}u_i u_l + P_{il}u_j u_k + P_{jl}u_i u_k + P_{kl}u_i u_j + Q_{ijk}u_l + Q_{ijl}u_k + Q_{ikl}u_j + Q_{jkl}u_i + R_{ijkl})\\
&= \boldsymbol{S}_{ijk}(\boldsymbol{U})
\end{aligned} \tag{2.33}$$

being the resulting mass, momentum, energy and heat-flux conservation laws. The right-hand side terms, $\boldsymbol{S}_{ij}(\boldsymbol{U})$ and $\boldsymbol{S}_{ijk}(\boldsymbol{U})$, can easily be computed from Equation 2.16, with $w = v_i v_j$, and $w = v_i v_j v_k$, respectively.

While Grad's closure can model heat flux, it can only produce results in a small region of hyperbolicity near equilibrium[28]. Far from equilibrium, but for states which are perfectly physically realizable for a gas, Grad's closure does not remain hyperbolic.

This leaves initial-value problems ill-posed, limiting practical applications for which this hierarchy can be used. There are regularization techniques [16, 29], however these permit higher-order derivatives and lose the strictly hyperbolic, balance-law formulation. Recent work has been done to develop a robustly hyperbolic formulation of the Grad hierarchy, however this is limited to the 13-moment model alone [23, 24]. This work will instead find a framework that is both extendable to any desired higher-order closure, and retain the hyperbolic balance-law formulation, with all the advantages that come with it.

2.4 Maximum-Entropy Closures

One of the most desirable forms of distribution function comes from the maximum-entropy hierarchy. This was originally proposed by Dreyer [10], Müller and Ruggeri [11], as well as Levermore [12]. These distributions are the result of finding the distribution function which has the maximum entropy while the known moments are respected. The mathematically formal definition of the entropy maximization problem is

$$\max_{\mathcal{F}} \langle -(\mathcal{F} \ln \mathcal{F} - \mathcal{F}) \rangle \ , \tag{2.34}$$

such that the moments can be computed with the relevant velocity weights, or more formally

$$\boldsymbol{U} = \langle \boldsymbol{w} \mathcal{F} \rangle \ . \tag{2.35}$$

The solution of this optimization problem of the distribution function can be accomplished with a vector of Lagrange multipliers, $\boldsymbol{\alpha}$, redefining the maximization problem as

$$\mathcal{L} = \max_{\mathcal{F}} \langle -(\mathcal{F} \ln \mathcal{F} - \mathcal{F}) \rangle - \boldsymbol{\alpha}^T \left(\boldsymbol{U} - \langle \boldsymbol{w} \mathcal{F} \rangle \right) , \tag{2.36}$$

where the distribution with the maximum entropy is the critical point of $\mathcal{L}$. This can be computed by taking the derivative $\frac{\partial \mathcal{L}}{\partial \mathcal{F}}$ and solving for its 0, which gives

$$\frac{\partial \mathcal{L}}{\partial \mathcal{F}} = \left\langle \ln \mathcal{F} - \boldsymbol{\alpha}^T \boldsymbol{w} \right\rangle = 0 \, , \tag{2.37}$$

as the solution to the optimization. The result is that the maximum-entropy solution is

$$\mathcal{F} = \exp(\boldsymbol{\alpha}^T \boldsymbol{w}) \,, \tag{2.38}$$

which corresponds to the choice of an exponential to a polynomial power as a distribution function. This includes the already discussed choice of the Maxwellian distribution as the lowest-order member of the hierarchy, and through the choice of the free parameters in $\boldsymbol{\alpha}^T$ and velocity weights, in theory can extend to an indefinite higher-order number of moments.

While very mathematically elegant, the maximum-entropy hierarchies are not without their problems. Integration of exponentials to polynomial powers higher than second-order is impossible in closed form, requiring computationally expensive numerical integration in order to find the corresponding velocity distribution. These exponentials can also only be constructed for odd-ordered moment sets, as the required exponentials for even-ordered moment sets do not have finite integrals across all of velocity space. There is also a set of realizable moments for which the entropy maximization problem has no solution [30], further complicating finding the distribution from a given set of moments. Nevertheless, structures that arise from the maximum-entropy hierarchy are incredibly desirable, and this work aims to leverage some of them in the construction of the new robust higher-order closures.

2.4.1 Proof of Hyperbolicity for the Maximum-Entropy Hierarchy

One of the properties of maximum-entropy closures is that, as was originally shown by Levermore [12], they are guaranteed to be globally hyperbolic. By defining density and flux potentials,

$$h\left(\boldsymbol{\alpha}\right) = \left\langle \exp\left(\boldsymbol{\alpha}^T \boldsymbol{w}\right) \right\rangle \,, \quad \text{and} \quad f_i\left(\boldsymbol{\alpha}\right) = \left\langle v_i \exp\left(\boldsymbol{\alpha}^T \boldsymbol{w}\right) \right\rangle \,, \tag{2.39}$$

then the moments and their fluxes can be written as

$$\frac{\mathrm{d}h}{\mathrm{d}\boldsymbol{\alpha}} = \left\langle \boldsymbol{w} \exp\left(\boldsymbol{\alpha}^T \boldsymbol{w}\right) \right\rangle , \quad \text{and} \quad \frac{\mathrm{d}f_i}{\mathrm{d}\boldsymbol{\alpha}} = \left\langle \boldsymbol{w} v_i \exp\left(\boldsymbol{\alpha}^T \boldsymbol{w}\right) \right\rangle . \tag{2.40}$$

Maxwell's equation of change from (2.10) is therefore

$$\frac{\partial}{\partial t}\left(\frac{\mathrm{d}h}{\mathrm{d}\boldsymbol{\alpha}}\right) + \frac{\partial}{\partial x_i}\left(\frac{\mathrm{d}f_i}{\mathrm{d}\boldsymbol{\alpha}}\right) = \boldsymbol{S} , \tag{2.41}$$

which can be rewritten as

$$\left(\frac{\mathrm{d}^2 h}{\mathrm{d}\boldsymbol{\alpha}\mathrm{d}\boldsymbol{\alpha}}\right)\frac{\partial \boldsymbol{\alpha}}{\partial t} + \left(\frac{\mathrm{d}^2 f_i}{\mathrm{d}\boldsymbol{\alpha}\mathrm{d}\boldsymbol{\alpha}}\right)\frac{\partial \boldsymbol{\alpha}}{\partial x_i} = \boldsymbol{S} , \tag{2.42}$$

after taking the second derivatives of the density and flux potentials. This gives the time evolution of the closure coefficients for the maximum-entropy distribution. Hyperbolicity is assured so long as $\frac{\mathrm{d}^2 h}{\mathrm{d}\boldsymbol{\alpha}\mathrm{d}\boldsymbol{\alpha}}$ is symmetric positive definite, and $\frac{\mathrm{d}^2 f_i}{\mathrm{d}\boldsymbol{\alpha}\mathrm{d}\boldsymbol{\alpha}}$ is symmetric. From the definition of the density potential,

$$\frac{\mathrm{d}^2 h}{\mathrm{d}\boldsymbol{\alpha}\mathrm{d}\boldsymbol{\alpha}} = \left\langle \boldsymbol{w}\boldsymbol{w}^T \exp\left(\boldsymbol{\alpha}^T \boldsymbol{w}\right) \right\rangle , \tag{2.43}$$

which, for any weighting vector, v, becomes

$$v^T \frac{\mathrm{d}^2 h}{\mathrm{d}\boldsymbol{\alpha}\mathrm{d}\boldsymbol{\alpha}} v = \frac{\mathrm{d}^2 h}{\mathrm{d}\boldsymbol{\alpha}\mathrm{d}\boldsymbol{\alpha}} = \left\langle v^T \boldsymbol{w}\boldsymbol{w}^T v \exp\left(\boldsymbol{\alpha}^T \boldsymbol{w}\right) \right\rangle \geq 0 , \tag{2.44}$$

and is both symmetric and positive definite. The flux potential is of the form,

$$\frac{\mathrm{d}^2 f_i}{\mathrm{d}\boldsymbol{\alpha}\mathrm{d}\boldsymbol{\alpha}} = \left\langle v_i \boldsymbol{w}\boldsymbol{w}^T \exp\left(\boldsymbol{\alpha}^T \boldsymbol{w}\right) \right\rangle , \tag{2.45}$$

and is symmetric. Transport equations of this kind are in the form of a Godunov symmetric hyperbolic system [31], and can be shown to be equivalent to the Friedrichs-Lax form for hyperbolic systems [12, 32].

2.4.2 The Gaussian 10-Moment Closure

The last member of the maximum-entropy hierarchy which is integrable in closed form results in the 10-moment equations. This assumes that the gas has a Gaussian distribution,

$$\mathcal{G} = -\frac{\rho}{m\det\left(P_{ij}\right)^{1/2}}\left(\frac{\rho}{2\pi}\right)^{3/2}\exp\left(-\frac{\rho}{2}P_{ij}^{-1}v_iv_j\right)\,, \tag{2.46}$$

with a fully generalized pressure tensor, P_{ij}, and allows for the modelling of shear stresses and temperature anisotropies in the fluid. Much like the Maxwellian, the Gaussian can be directly integrated with the weight vector, $\boldsymbol{w} = [1, v_i, v_iv_j]^T$, to give rise to the PDEs

$$\frac{\partial}{\partial t}\left(\rho\right) + \frac{\partial}{\partial x_i}\left(\rho u_i\right) = 0\,, \tag{2.47}$$

$$\frac{\partial}{\partial t}\left(\rho u_i\right) + \frac{\partial}{\partial x_j}\left(\rho u_iu_j + P_{ij}\right) = 0\,, \tag{2.48}$$

$$\frac{\partial}{\partial t}\left(\rho u_iu_j + P_{ij}\right) + \frac{\partial}{\partial x_k}\left(\rho u_iu_ju_k + P_{ij}u_k + P_{ik}u_j + P_{jk}u_i\right) = \boldsymbol{S}_{ij}\left(\boldsymbol{U}\right)\,, \tag{2.49}$$

as the conservation laws for the mass, momentum, and energy densities of the fluid. This hierarchy is analyzed further in Section 3.2, and used as inspiration for the new technique to construct higher-order closures.

2.4.3 Higher-Order Approximations to the Maximum-Entropy Hierarchy

There are some approximations of the maximum-entropy hierarchy, but they too have their drawbacks. The solution to higher-order closing fluxes of the entropy maximization problem can be approximated in closed form [17, 33], but this technique loses robust hyperbolicity when extended to multidimensional gases. The distribution function itself can be approximated to be integrable, such as with the ϕ-divergence closures [14]. This technique assumes that the distribution function is a power series expansion of the Maxwellian,

$$\mathcal{F} = \mathcal{M}\left(1 + \frac{\boldsymbol{\alpha}^T\boldsymbol{w}}{N}\right)^N\,, \tag{2.50}$$

approximating higher-order distribution functions of the kind shown in Equation (2.38). These can then be truncated to any desired order, N. However, for even-ordered values of N, this hierarchy does not have unique solutions to the closure coefficients for given moment states. For the odd-orders of N, there are regions of negative density in velocity space which require additional treatment. Approximations to the hierarchy which are well-behaved remain elusive.

2.5 New One-Dimensional Techniques

More recent advances in moment closures have lead to a much more convenient formulation, which relies less on an integrable distribution function and instead on the desired mathematical properties of the resulting PDEs, flux Jacobians, and their characteristic polynomials. These families include the Quadrature-based Method of Moments (QMOM) closures of Fox and Laurent [18–21] as well as the Method of Orthogonal Polynomials of Morin and McDonald [22]. Thus far, these closures have only been developed in a single dimension of both physical and velocity spaces. This reduces all the solution variables from vectors and tensors to scalars, and greatly simplifies the problem of retaining hyperbolicity. This work develops extensions to these new techniques, in order to extend their desirable mathematical properties to regimes that are practical for typical engineering problems.

2.5.1 Quadrature Based Moment Closures

The original hierarchy which generated interest in direct manipulation of the flux Jacobian has largely been the QMOM hierarchy, developed by Fox et al. [18–21, 34]. While later works would generalize the structure of the resulting PDEs, the original method did propose a distribution function. Quadrature methods propose a weighted sum,

$$\mathcal{F} = \sum_{i=0}^{n} w_i \delta_i (v - \lambda_i) \,, \tag{2.51}$$

as the distribution function for a one-dimensional gas, where $\delta_i(v - \lambda_i)$ is a Dirac delta function centered at λ_i, and w_i is a corresponding weight. This formulation can be shown to have many of the properties of the maximum-entropy hierarchy [35], and results in many simplifications to the resulting PDE structures.

One of these simplifications is to the structures resulting from the flux Jacobian, which is

$$\frac{\mathrm{d}\boldsymbol{F}}{\mathrm{d}\boldsymbol{U}} = \begin{bmatrix} 0 & 1 & 0 & \cdots & 0 \\ 0 & 0 & 1 & \cdots & 0 \\ \vdots & \vdots & \vdots & \ddots & \vdots \\ 0 & 0 & 0 & \cdots & 1 \\ \frac{\partial F_n}{\partial U_0} & \frac{\partial F_n}{\partial U_1} & \frac{\partial F_n}{\partial U_2} & \cdots & \frac{\partial F_n}{\partial U_n} \end{bmatrix}, \tag{2.52}$$

having the form of a companion matrix for one-dimensional gases. These matrices are convenient, as the characteristic polynomial becomes

$$\det\left(\lambda I - \frac{\mathrm{d}\boldsymbol{F}}{\mathrm{d}\boldsymbol{U}}\right) = \lambda^n - \frac{\partial F_n}{\partial U_n}\lambda^{n-1} - \cdots - \frac{\partial F_n}{\partial U_1}\lambda - \frac{\partial F_n}{\partial U_0} = 0\,, \tag{2.53}$$

with the final row of the matrix becoming the coefficients of the characteristic polynomial. The Eigendecomposition of the flux Jacobian in this framework is also convenient,

$$\frac{\mathrm{d}\boldsymbol{F}}{\mathrm{d}\boldsymbol{U}} = \boldsymbol{R}\boldsymbol{\Lambda}\boldsymbol{R}^{-1}\,, \tag{2.54}$$

where $\boldsymbol{R}$ is the matrix of Eigenvectors, and $\boldsymbol{\Lambda}$, is a diagonal matrix of the associated Eigenvalues. In this setting, the right Eigenvectors take the form of a Vandermonde matrix,

$$\boldsymbol{R} = \begin{bmatrix} 1 & 1 & 1 & 1 \\ \lambda_0 & \lambda_1 & \cdots & \lambda_{n-1} \\ \lambda_0^2 & \lambda_1^2 & \cdots & \lambda_{n-1}^2 \\ \vdots & \vdots & \ddots & \vdots \\ \lambda_0^{n-1} & \lambda_1^{n-1} & \cdots & \lambda_{n-1}^{n-1} \end{bmatrix}, \tag{2.55}$$

for an n-th order closure. By constructing the moments through prescription of the

Eigenvalues, any given state has an associated diagonal matrix of weights,

$$\boldsymbol{U} = \boldsymbol{R}\boldsymbol{W} \,, \tag{2.56}$$

which is diagonal for quadrature-based moment closures [19, 22]. In combination with Equation (2.55), any moment is therefore a weighted sum,

$$U_m = \sum_{i=0}^{n-1} w_i \lambda_i^m \,, \tag{2.57}$$

and the flux vector is the same, as when using the Eigendecomposition of the flux Jacobian, it can be seen as

$$\boldsymbol{F} = \boldsymbol{R}\boldsymbol{\Lambda}\boldsymbol{R}^{-1}\boldsymbol{U} = \boldsymbol{R}\boldsymbol{\Lambda}\boldsymbol{W} \,, \tag{2.58}$$

or the same weighted sums as the solution vector, except one power of λ_i higher.

Unfortunately, HyQMOM's development has been limited to one-dimensional gases, and much like the maximum-entropy hierarchy, was only able to be constructed for odd-ordered moment sets. Real, three-dimensional gases, lead to much more complex equations and flux Jacobians, and the study of extending the desirable mathematical structures of the one-dimensional solutions into a realistic setting is of great interest.

2.5.2 Orthogonal Polynomial Based Closures

Inspired by the success of the QMOM hierarchy, Morin and McDonald developed orthogonal polynomial based closures [22]. In this work, they show how one could directly modify the flux Jacobian, and retain balance-law form. This analysis formalized how the coefficients of a companion matrix must be prescribed in order to result in a valid flux Jacobian. They begin by noting that well-defined moment closure systems are homogeneous, or that for any scaling, α, the moments and their fluxes must have the relationship,

$$\alpha\boldsymbol{U} = \langle \alpha m w \mathcal{F} \rangle \,, \quad \text{and} \quad \alpha\boldsymbol{F}(\boldsymbol{U}) = \langle \alpha m v_i w \mathcal{F} \rangle \,, \tag{2.59}$$

scaling both the moments and the fluxes by the same amount. This leads to Euler's theorem for a homogeneous function of degree m,

$$\alpha^m \boldsymbol{F}(\boldsymbol{U}) = \boldsymbol{F}(\alpha \boldsymbol{U}) \,, \tag{2.60}$$

and differentiating with respect to the scalar parameter α,

$$m\alpha^{m-1} \boldsymbol{F}(\boldsymbol{U}) = \frac{\mathrm{d}\boldsymbol{F}}{\mathrm{d}\boldsymbol{U}}(\alpha \boldsymbol{U}) \cdot \frac{\mathrm{d}}{\mathrm{d}\alpha}(\alpha \boldsymbol{U}) \tag{2.61}$$

which for first-order homogeneity, becomes

$$\boldsymbol{F} = \frac{\mathrm{d}\boldsymbol{F}}{\mathrm{d}\boldsymbol{U}} \boldsymbol{U} \,. \tag{2.62}$$

If the flux Jacobian is then of the form shown in Equation (2.52), the final row can be taken as a vector,

$$\boldsymbol{A} = \begin{bmatrix} \frac{\partial F_n}{\partial U_0} & \frac{\partial F_n}{\partial U_1} & \frac{\partial F_n}{\partial U_2} & \cdots & \frac{\partial F_n}{\partial U_n} \end{bmatrix} , \tag{2.63}$$

and results in the closing flux,

$$F_n = U_{n+1} = \boldsymbol{A} \cdot \boldsymbol{U} \,, \tag{2.64}$$

which is solely a function of the coefficients along the bottom row of the flux Jacobian and the known moments. Since the rest of the flux Jacobian is constant values of 0 or 1, the flux Jacobian can be decomposed as

$$\frac{\mathrm{d}\boldsymbol{F}}{\mathrm{d}\boldsymbol{U}} = \left(\frac{\partial \boldsymbol{F}}{\partial \boldsymbol{U}}\right)_{\boldsymbol{A}} + \left(\frac{\partial \boldsymbol{F}}{\partial \boldsymbol{A}}\right)_{\boldsymbol{U}} \left(\frac{\partial \boldsymbol{A}}{\partial \boldsymbol{U}}\right) \,, \tag{2.65}$$

where $\left(\frac{\partial \boldsymbol{F}}{\partial \boldsymbol{A}}\right)_{\boldsymbol{U}}$ and $\left(\frac{\partial \boldsymbol{F}}{\partial \boldsymbol{U}}\right)_{\boldsymbol{A}}$ are the partial derivatives holding the known moments constant, and the form of the final row constant, respectively. The matrix $\frac{\mathrm{d}\boldsymbol{A}}{\mathrm{d}\boldsymbol{U}}$ can also be written as

$$\frac{\mathrm{d}\boldsymbol{A}}{\mathrm{d}\boldsymbol{U}} = \frac{\mathrm{d}^2 \mathrm{U}_{\mathrm{n+1}}}{\mathrm{d}\boldsymbol{U}\mathrm{d}\boldsymbol{U}} \,, \tag{2.66}$$

or the Hessian of the closing flux with respect to the known moments.

When building the closing flux, in order to produce a hyperbolic system of equations, its derivatives with respect to the known moments must have the form

$$\frac{\mathrm{dU_{n+1}}}{\mathrm{d}\boldsymbol{U}} = \boldsymbol{A} + \boldsymbol{U}^T \left(\frac{\mathrm{d^2U_{n+1}}}{\mathrm{d}\boldsymbol{U}\mathrm{d}\boldsymbol{U}} \right) , \tag{2.67}$$

but the vector $\boldsymbol{A}$ was defined as the final row of the flux Jacobian, and should be exactly equivalent to $\frac{\mathrm{dU_{n+1}}}{\mathrm{d}\boldsymbol{U}}$ for any choices of the entries in $\boldsymbol{A}$. Therefore, if the transpose of the moments are in the left null space of the matrix $\frac{\mathrm{d}\boldsymbol{A}}{\mathrm{d}\boldsymbol{U}}$, such that

$$\boldsymbol{U}^T \left(\frac{\mathrm{d^2U_{n+1}}}{\mathrm{d}\boldsymbol{U}\mathrm{d}\boldsymbol{U}} \right) = 0 , \tag{2.68}$$

then the prescribed matrix is the flux Jacobian of the system. With these rules, Morin and McDonald were able to not only show how HyQMOM retains its hyperbolicity through ensuring the characteristic polynomial of the flux Jacobian is guaranteed to have real-valued roots, but also create closures for even-ordered sets of moments.

For example, the four moment equations of Morin and McDonald in one-dimension of physical space and in the absence of particle collisions are given as

$$\frac{\partial}{\partial t}\left(\rho\right) + \frac{\partial}{\partial x}\left(\rho u\right) = 0 , \tag{2.69}$$

$$\frac{\partial}{\partial t}\left(\rho u\right) + \frac{\partial}{\partial x}\left(\rho u^2 + p\right) = 0 , \tag{2.70}$$

$$\frac{\partial}{\partial t}\left(\rho u^2 + p\right) + \frac{\partial}{\partial x}\left(\rho u^3 + 3pu + q\right) = 0 , \tag{2.71}$$

$$\frac{\partial}{\partial t}\left(\rho u^3 + 3pu + q\right) + \frac{\partial}{\partial x}\left(\rho u^4 + 6pu + 4qu + r\right) = 0 , \tag{2.72}$$

for the scalar variables ρ, u, p and q. The first three equations are the typical mass, momentum and energy conservation laws that are expected from moment closures, with the additional consideration of heat flux in the conservation of energy equation. The random component of the closing flux r has the form

$$r = 2\frac{q^2}{p} + 3\frac{p^2}{\rho} , \tag{2.73}$$

and results in a 4-moment model that is guaranteed to have robust hyperbolicity for any value of ρ, u, p, and q. This closure and the hierarchies associated with it offer a flexible framework for generating robustly hyperbolic moment closures. However, they come with one large caveat, these structures only exist in this one-dimensional setting. In this simplified model, all of the vectors and tensors that arise from integration of a multidimensional distribution function, as shown in Equations 2.4 and 2.5, reduce to scalar values. Real, multidimensional gases have more complicated statistics and flux Jacobians, where there are multiple closing fluxes, and additional rotational properties that must be respected. This currently leaves practical applications of these styles of closures limited. Extending these closures into realistic multidimensional physics is the first major contribution of this thesis, shown in Chapter 3.

Chapter 3

Block-Diagonal Extended Moment Closures

The primary goal of the Ph.D. work is the creation of a new technique to extend the mathematically elegant one-dimensional closures outlined in Section 2.5.2 into realistic three-dimensional settings. As with the method of orthogonal polynomials, instead of prescribing a distribution function, the characteristic polynomials are constructed directly to have desirable Eigenvalues, and then imposed to be the characteristic polynomial of the flux Jacobian. Taking inspiration from the 10-moment equations outlined in Section 2.4.2, some of the resulting structure of the equations are leveraged to develop a new technique for building robustly hyperbolic systems.

The goals of the new technique, and the desirable properties it should have, are described in Section 3.1. Some analysis of the 10-moment equations is performed in Section 3.2 that is used as the starting point for the development of new models. Then, the technique by which the new hierarchy of closures is built from is shown in Section 3.3, with two 20-moment closures being developed in Sections 3.3.1 and 3.3.2. A 35-moment closure built following the same technique is demonstrated in Appendix A. The stability of the 20-moment models is shown in Section 3.4, and a final discussion on some of the resulting mathematical deficiencies is presented in Section 3.5.

3.1 Goals of the New Technique

In order to have a new method to construct higher-order closures for multidimensional gases, properties of both the generalizable hyperbolic closures mentioned in Section 2.5.2 and Section 3.2 need to be replicated. The properties desired for a new method are that

1. The flux Jacobian has real roots and the method is robustly hyperbolic for all physically realizable states,

2. The moments have the correct convected form for translational invariance,

3. The system of equations should be rotationally invariant.

The first and most important property is to ensure that the closure is robustly hyperbolic. As outlined in Section 2.1.1, if the flux Jacobian has real Eigenvalues and linearly independent Eigenvectors, the system is hyperbolic. This is achieved using the orthogonal polynomial based closures to construct a desirable characteristic polynomial that is guaranteed to have real roots for all realizable states.

The second and third properties pertain to Galilean invariance, or that the frame of reference does not affect the solution to the PDEs. The second property pertains to the information from the lower-order moments, and that it is properly convected into the higher-order moments. For example, the third-order moment is the tensor U_{ijk}, found by integration over the velocities v_i, v_j, and v_k, as shown in Equation (2.4) and is given as

$$\langle m v_i v_j v_k \mathcal{F} \rangle = \rho u_i u_j u_k + P_{ij} u_k + P_{ik} u_j + P_{jk} u_i + Q_{ijk} \tag{3.1}$$

being a combination of all the permutations of the lower-order moments in the indicated directions. This becomes increasingly complex for every additional index of the tensor, as demonstrated in Equation (2.5). In order to fulfill the second property, it is sufficient to ensure that every closing flux moment $U_{ijk\ldots l}$ has all the correct terms to convect the lower-order moment information correctly.

The third property has been found to be the most challenging to obtain, as ensuring that the one-dimensional scalar closing flux is extended to a correctly formed tensor in

multiple dimensions has proven difficult. Currently, the third property is not entirely fulfilled in the present work. Instead, this work considers an easier goal. By constructing the Jacobians for all directions in three-dimensional space, and ensuring that the closing fluxes that appear in multiple Jacobians are proposed so that they are in agreement with each other, rotational asymmetries can be found to be reduced. This does not force the closing fluxes to be in the form of a proper tensor, but it can at least be shown that the fluxes of a moment are invariant under an exchange of axis. Discussions of the issues to construct a rotationally invariant closure are included in Section 3.5, and the numerical experiments in Chapter 4 demonstrate that the issue is negligible for the target regimes of moment methods.

It is also highly desirable that a new method is easily extendable, not just being a 13-moment closure (being the first contracted closure which includes a heat-flux vector) or a 20-moment closure (which is the next set of uncontracted moments after 10), but to any complete set of higher-order, uncontracted moments as well (e.g. 35, 56, and so on). This would give a new way to build moment methods that include higher-order statistics for a wider breadth of regimes and problems.

3.2 Structure of the 10-Moment Equations

As mentioned in Section 2.4.2, the 10-moment equations are an interesting candidate of equations to extend for higher-order moment closures. While they can already account for moderate non-equilibrium effects like shear stresses and temperature anisotropies, the equations are adiabatic, lacking a treatment for heat flux. This work leverages some of the properties of these equations in order to generate models which can allow for higher-order non-equilibrium effects.

To begin the analysis of the 10-moment equations, the traditional order of Equations (2.47), (2.48), and (2.49) is changed. Instead of presenting them by mass conservation, then momentum conservation, and finally energy conservation, the solution and

flux vectors are reordered to be

$$\boldsymbol{U} = \begin{bmatrix} \rho \\ \rho u_x \\ \rho u_x^2 + P_{xx} \\ \rho u_y \\ \rho u_x u_y + P_{xy} \\ \rho u_z \\ \rho u_x u_z + P_{xz} \\ \rho u_y^2 + P_{yy} \\ \rho u_y u_z + P_{yz} \\ \rho u_z^2 + P_{zz} \end{bmatrix}, \text{ and } \boldsymbol{F}_x = \begin{bmatrix} \rho u_x \\ \rho u_x^2 + P_{xx} \\ \rho u_x^3 + 3P_{xx}u_x \\ \rho u_x u_y + P_{xy} \\ \rho u_x^2 u_y + 2P_{xy}u_x + P_{xx}u_y \\ \rho u_x u_z + P_{xz} \\ \rho u_x^2 u_z + 2P_{xz}u_x + P_{xx}u_z \\ \rho u_x u_y^2 + 2P_{xy}u_y + P_{yy}u_x \\ \rho u_x u_y u_z + P_{yz}u_x + P_{xz}u_y + P_{xy}u_z \\ \rho u_x u_x^2 + 2P_{xz}u_z + P_{zz}u_x \end{bmatrix}, \tag{3.2}$$

where they are arranged by increasing powers of velocity weights, v_x. This ordering reveals some interesting structures in the x-direction flux Jacobian

$$\frac{\mathrm{d}\boldsymbol{F}_\mathrm{x}}{\mathrm{d}\boldsymbol{U}} = \begin{bmatrix} 0 & 1 & 0 & 0 & 0 & 0 & 0 & 0 & 0 & 0 \\ 0 & 0 & 1 & 0 & 0 & 0 & 0 & 0 & 0 & 0 \\ u_x^3 - 3\frac{P_{xx}u_x}{\rho} & -3u_x^2 + 3\frac{P_{xx}}{\rho} & 3u_x & 0 & 0 & 0 & 0 & 0 & 0 & 0 \\ 0 & 0 & 0 & 0 & 1 & 0 & 0 & 0 & 0 & 0 \\ u_x^2 u_y - \frac{P_{xx}u_y}{\rho} - \frac{2P_{xy}u_x}{\rho} & -2u_x u_y + \frac{2P_{xy}}{\rho} & u_y & -u_x^2 + \frac{P_{xx}}{\rho} & 2u_x & 0 & 0 & 0 & 0 & 0 \\ 0 & 0 & 0 & 0 & 0 & 0 & 1 & 0 & 0 & 0 \\ u_x^2 u_z - \frac{P_{xx}u_z}{\rho} - \frac{2P_{xz}u_x}{\rho} & -2u_x u_z + \frac{2P_{xz}}{\rho} & u_z & 0 & 0 & -u_x^2 + \frac{P_{xx}}{\rho} & 2u_x & 0 & 0 & 0 \\ u_x u_y^2 - \frac{P_{yy}u_x}{\rho} - \frac{2P_{xy}u_y}{\rho} & -u_y^2 + \frac{P_{yy}}{\rho} & 0 & -2u_x u_y + \frac{2P_{xy}}{\rho} & 2u_y & 0 & 0 & u_x & 0 & 0 \\ u_x u_y u_z - \frac{P_{yz}u_x}{\rho} - \frac{P_{xz}u_y}{\rho} - \frac{P_{xy}u_z}{\rho} & -u_y u_z + \frac{P_{yz}}{\rho} & 0 & -u_x u_z + \frac{P_{xz}}{\rho} & u_z & -u_x u_y + \frac{P_{xy}}{\rho} & u_y & 0 & u_x & 0 \\ u_x u_z^2 - \frac{P_{zz}u_x}{\rho} - \frac{2P_{xz}u_z}{\rho} & -u_z^2 + \frac{P_{zz}}{\rho} & 0 & 0 & 0 & -2u_x u_z + \frac{2P_{xz}}{\rho} & 2u_z & 0 & 0 & u_x \end{bmatrix}. \tag{3.3}$$

While not as simple as the Jacobian shown in Equation (2.52), there are some exploitable features. A first notable property is that the upper right portion of the matrix is sparse, and the matrix is lower block diagonal. Computing the characteristic polynomial of the matrix gives

$$\det\left(\lambda I - \frac{\mathrm{d}\boldsymbol{F}_\mathrm{x}}{\mathrm{d}\boldsymbol{U}}\right) = \mathrm{He}_3\left(\sqrt{\frac{\rho}{\mathrm{P_{xx}}}}\left(\lambda - \mathrm{u_x}\right)\right) \cdot \mathrm{He}_2^2\left(\sqrt{\frac{\rho}{\mathrm{P_{xx}}}}\left(\lambda - \mathrm{u_x}\right)\right) \cdot \mathrm{He}_1^3\left(\sqrt{\frac{\rho}{\mathrm{P_{xx}}}}\left(\lambda - \mathrm{u_x}\right)\right) = 0\,, \tag{3.4}$$

where $\mathrm{He_n(x)}$ is the n^{th} probabilist Hermite polynomial. The roots of this equation, and therefore the Eigenvalues of the flux Jacobian, are

$$\boldsymbol{\lambda} = \begin{bmatrix} u_x - \sqrt{3\frac{P_{xx}}{\rho}} \\ u_x \\ u_x + \sqrt{3\frac{P_{xx}}{\rho}} \\ u_x - \sqrt{\frac{P_{xx}}{\rho}} \\ u_x + \sqrt{\frac{P_{xx}}{\rho}} \\ u_x - \sqrt{\frac{P_{xx}}{\rho}} \\ u_x + \sqrt{\frac{P_{xx}}{\rho}} \\ u_x \\ u_x \\ u_x \end{bmatrix}, \tag{3.5}$$

with the first three waves corresponding to the third-order Hermite polynomial, the next four the two second-order Hermite polynomials, and the last three the first-order Hermite polynomials. The characteristic polynomial breaking up like this comes from the block lower-triangular form of the matrix. The relevant blocks are highlighted in Figure 3.1, where diagonal blocks, which contribute to the Eigenvalues of the overall system, are shown in black and labelled with their corresponding size. Zeroes are shown in white, and non-zero lower-triangle elements that do not contribute to the Eigenvalues are shown in grey.

Looking at each block individually reveals that they break down into smaller com-

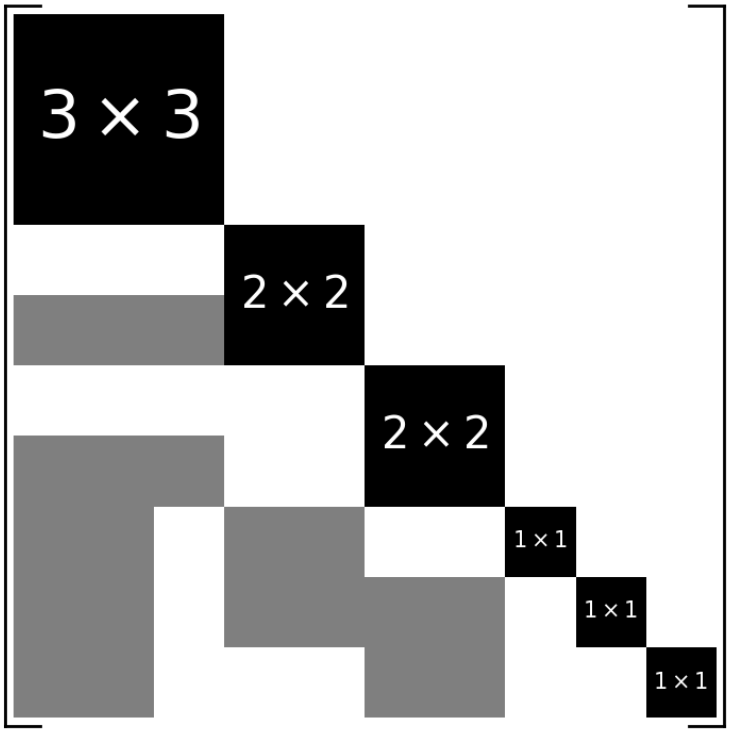

Figure 3.1: 10-moment closure flux Jacobian block diagonal structure.

panion matrices

$$\widehat{\frac{\partial \boldsymbol{F}_x}{\partial \boldsymbol{U}}}_{3\times 3} = \begin{bmatrix} 0 & 1 & 0 \\ 0 & 0 & 1 \\ u_x^3 - 3\frac{P_{xx}u_x}{\rho} & -3u_x^2 + 3\frac{P_{xx}}{\rho} & 3u_x \end{bmatrix}, \tag{3.6}$$

$$\widehat{\frac{\partial \boldsymbol{F}_x}{\partial \boldsymbol{U}}}_{2\times 2} = \begin{bmatrix} 0 & 1 \\ -u_x^2 + \frac{P_{xx}}{\rho} & 2u_x \end{bmatrix}, \tag{3.7}$$

$$\widehat{\frac{\partial \boldsymbol{F}_x}{\partial \boldsymbol{U}}}_{1\times 1} = \begin{bmatrix} u_x \end{bmatrix}, \tag{3.8}$$

and can be constructed with only those moments that have x-direction indices (e.g. only U_0, U_x, and U_{xx} are required to build the subsystems relevant to the Eigenvalues of the x-direction Jacobian shown). The new method proposed in this work generalizes this structure, giving a technique to construct closures of higher-orders.

3.3 New Robustly Hyperbolic 20-Moment Closures

Instead of focusing on an integrable distribution function for multidimensional gases, this work instead proposes focusing on constructing hyperbolic flux Jacobians directly. By taking inspiration from the lower block diagonal structure that exists in the 10-moment equations, then building hyperbolic subsystems along the diagonal for each group of moments, and finally using the lower triangular entries to ensure translational invariance, robust hyperbolic multidimensional systems can easily be constructed. This results in a 20-moment closure, shown in Section 3.3.1, which extends the 4^{th} order member of the one-dimensional orthogonal-polynomial hierarchy to a multidimensional gas, and respects the first two properties of Section 3.1. A second 20-moment closure is then presented in Section 3.3.2, which additionally tries to respect property three of Section 3.1 by forcing the closures that are constructed in each Jacobian to have the same form. The continuation of the hierarchy, extending 5^{th} order moment methods to a 35-moment closure is shown in Appendix A. The new technique for the construction of these novel closures is demonstrated here.

The first step of the new technique is rearranging the moments in the solution vector such that the top entries as those with indices entirely in one of the primary directions. For the x-direction, this would be the moments

$$\begin{aligned}
U_0 &= \rho\,, \\
U_x &= \rho u_x\,, \\
U_{xx} &= \rho u_x^2 + P_{xx}\,, \\
U_{xxx} &= \rho u_x^3 + 3P_{xx}u_x + Q_{xxx}\,, \\
U_{xxxx} &= \rho u_x^4 + 6P_{xx}u_x^2 + 4Q_{xxx}u_x + R_{xxxx}\,,
\end{aligned} \tag{3.9}$$

where U_{xxxx} is the closing flux for the first block of the 20-moment, with the random moment R_{xxxx} being the only unknown moment. The moments of this system are exclusively those with only x indices, and no moments where y or z indices appear. The only way to introduce these variables would be choosing a form for R_{xxxx} that introduces

them. By avoiding this, the first equations of the system can be decoupled from any other subsequent moments and subsystems.

Next, starting with a first-order moment with an index in a transverse direction, again order the higher moments in increasing powers of x. For the moments with one y index, these are

$$\begin{aligned}
U_y &= \rho u_y \,, \\
U_{xy} &= \rho u_x u_y + P_{xy} \,, \\
U_{xxy} &= \rho u_x u_y + 2P_{xy} u_x + P_{xx} u_y + Q_{xxx} \,, \\
U_{xxxy} &= \rho u_x^3 u_y + 3P_{xy} u_x^2 + 3P_{xx} u_x u_y + 3Q_{xxy} u_x + Q_{xxx} u_y + R_{xxxy} \,,
\end{aligned} \tag{3.10}$$

and are similar for those with one z index. Noticing that these moments are either those that appeared in the previous subsystem, or those which are introduced as part of this system. These again only have the closing flux U_{xxxy}, and only one new choice, the form of R_{xxxy}.

This pattern continues, rearranging for U_{yy} to U_{xxyy}, U_{zz} to U_{xxzz}, and U_{yz} to U_{xxyz}, results in a partial decoupling, such that only moments from the previous subsystems, or new moments which were introduced for that subsystem can be used to construct the closures without breaking the block diagonal pattern.

With this partial decoupling, the closing fluxes can be constructed one at a time. Starting with a closure for the moments in Equation (3.9),

$$\widehat{\boldsymbol{F}} = \widehat{\frac{\mathrm{d}\boldsymbol{F}}{\mathrm{d}\boldsymbol{U}}}_{4\times 4} \widehat{\boldsymbol{U}} = \begin{bmatrix} 0 & 1 & 0 & 0 \\ 0 & 0 & 1 & 0 \\ 0 & 0 & 0 & 1 \\ \frac{\partial U_{xxxx}}{\partial U_0} & \frac{\partial U_{xxxx}}{\partial U_x} & \frac{\partial U_{xxxx}}{\partial U_{xx}} & \frac{\partial U_{xxxx}}{\partial U_{xxx}} \end{bmatrix} \begin{bmatrix} U_0 \\ U_x \\ U_{xx} \\ U_{xxx} \end{bmatrix} , \tag{3.11}$$

where $\widehat{\boldsymbol{U}}$ is the subsystem moments, $\widehat{\boldsymbol{F}}$ is the subsystem fluxes, and $\widehat{\frac{\mathrm{d}\boldsymbol{F}}{\mathrm{d}\boldsymbol{U}}}_{4\times 4}$ is the 4×4 block which is inserted along the diagonal of the Jacobian. The next subsystem is the

subsystem shown in Equation (3.10), and can then be closed with

$$\widehat{\boldsymbol{F}} = \widehat{\frac{\mathrm{d}\boldsymbol{F}}{\mathrm{d}\boldsymbol{U}}}_{3\times 3}\widehat{\boldsymbol{U}} = \begin{bmatrix} 0 & 1 & 0 \\ 0 & 0 & 1 \\ \frac{\partial U_{xxxy}}{\partial U_y} & \frac{\partial U_{xxxy}}{\partial U_{xy}} & \frac{\partial U_{xxxy}}{\partial U_{xxy}} \end{bmatrix} \begin{bmatrix} U_y \\ U_{xy} \\ U_{xxy} \end{bmatrix}, \tag{3.12}$$

and so on, continuing for the 2×2 and 1×1 subsystems. The resulting structure, when only considering Property 1, is shown in Figure 3.2. Because of this decoupling, the characteristic polynomial also breaks up in to a product of smaller, easier to manage polynomials, like that of the 10-moment model shown in Equation (3.4). For any closure constructed in this way, the characteristic polynomial is

$$\det\left(\lambda I - \frac{\mathrm{d}\boldsymbol{F}_{\mathrm{x}}}{\mathrm{d}\boldsymbol{U}}\right) = \prod_{i=1}^{n} \det\left(\lambda I_{i\times i} - \widehat{\frac{\mathrm{d}\boldsymbol{F}_{\mathrm{x}}}{\mathrm{d}\boldsymbol{U}}}_{i\times i}\right)^{n-i+1} = 0\,, \tag{3.13}$$

where n is the largest $n \times n$ subsystem used in the construction of the matrix, and $\widehat{\frac{\mathrm{d}\boldsymbol{F}_{\mathrm{x}}}{\mathrm{d}\boldsymbol{U}}}_{i\times i}$ are the i^{th} subsystems. This reduces the problem of ensuring real Eigenvalues from being that of a 20^{th}-order polynomial, in to more manageable 4^{th}-and-lower-order polynomials.

While this ensures a matrix that has real Eigenvalues, it must also be shown that the resulting matrix is the flux Jacobian of the full system. Figure 3.2 shows that this is not the case, as the closing flux for the subsystems are constructed using the moments U_0, U_x, and U_{xx}, but this matrix implies $\frac{\partial U_{xxxy}}{\partial U_0} = \frac{\partial U_{xxxy}}{\partial U_x} = \frac{\partial U_{xxxy}}{\partial U_{xx}} = 0$. This causes the fluxes of the moments to break the structure required to fulfill property 2, therefore violating translational invariance.

To ensure the matrix is the Jacobian of the system and be translationally invariant, the multidimensional equivalent of the condition in Equation (2.68) must be ensured. This condition must be checked for all rows pertaining to a closing flux, but if it is respected, then the matrix that has been built from this technique is the flux Jacobian of the resulting equations. More formally

$$\boldsymbol{U}^T\left(\frac{\mathrm{d}^2\mathrm{F}_{\mathrm{ij...k}}}{\mathrm{d}\boldsymbol{U}\mathrm{d}\boldsymbol{U}}\right) = 0\,, \tag{3.14}$$

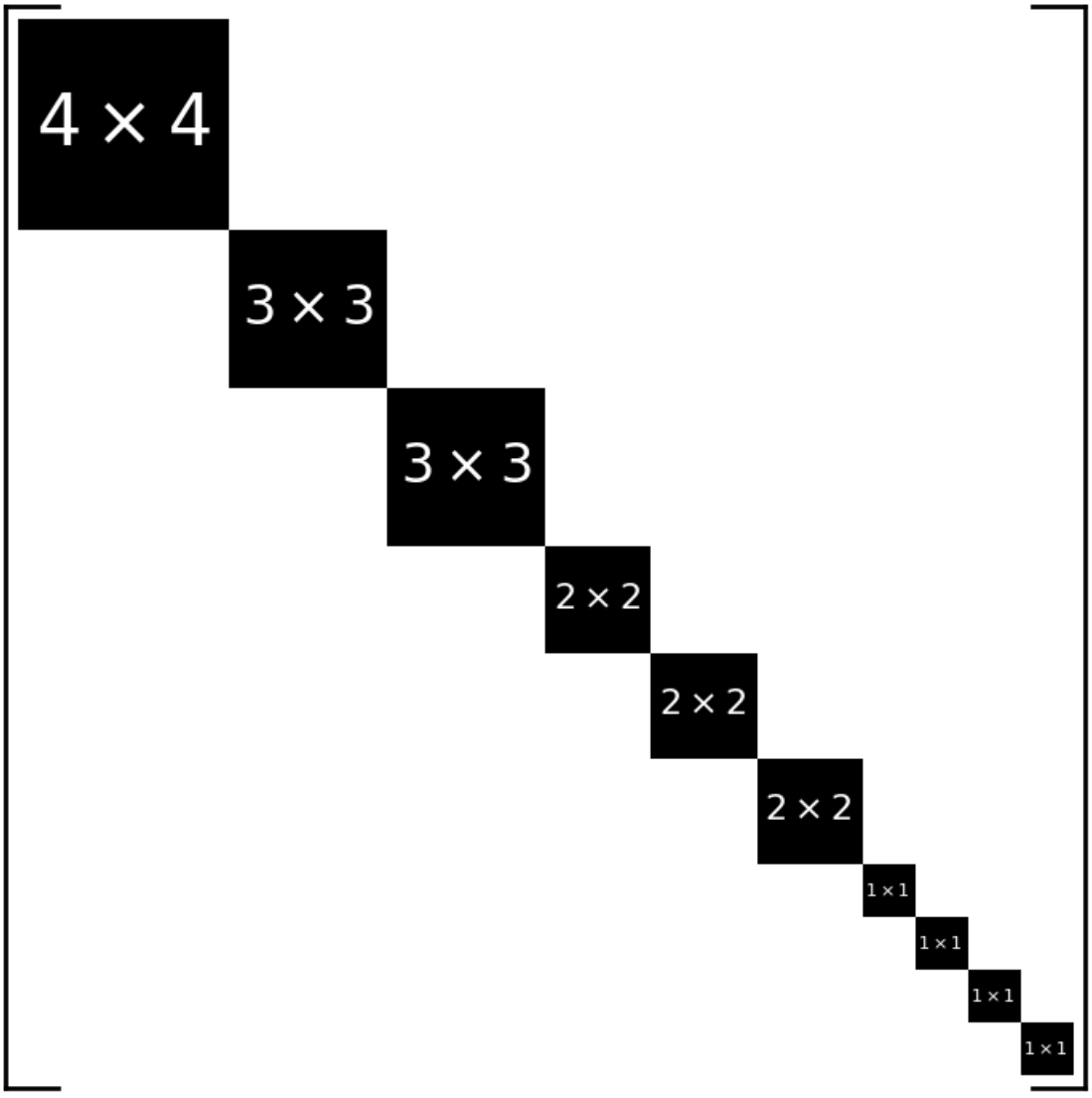

Figure 3.2: 20-moment hyperbolic block diagonal matrix structure

must hold for every closing flux $F_{ij\ldots k}$.

For the two 20-moment closures presented in this work, the 4-moment closure of Morin and McDonald [22] is used as the 4×4 subsystem. The random component of the 4th order closing flux is known to be

$$R_{xxxx} = 2\frac{Q_{xxx}^2}{P_{xx}} + 3\frac{P_{xx}^2}{\rho}\,, \tag{3.15}$$

and results in the subsystem with the Jacobian

$$\widehat{\frac{\mathrm{d}\boldsymbol{F}_{\mathrm{x}}}{\mathrm{d}\boldsymbol{U}}}_{4\times4} = \begin{bmatrix} 0 & 1 & 0 & 0 \\ 0 & 0 & 1 & 0 \\ 0 & 0 & 0 & 1 \\ \frac{\partial U_{xxxx}}{\partial U_0} & \frac{\partial U_{xxxx}}{\partial U_x} & \frac{\partial U_{xxxx}}{\partial U_{xx}} & \frac{\partial U_{xxxx}}{\partial U_{xxx}} \end{bmatrix}, \tag{3.16}$$

in the top left corner of the full flux Jacobian, where the closing flux derivatives are

$$\begin{aligned}
\frac{\partial U_{xxxx}}{\partial U_0} &= -u_x^4 - 4\frac{Q_{xxx}u_x^3}{P_{xx}} + 6\frac{P_{xx}u_x^2}{\rho} - 2\frac{Q_{xxx}^2u_x^2}{P_{xx}^2} + 8\frac{Q_{xxx}u_x}{\rho} - 3\frac{P_{xx}^2}{\rho^2}\,, \\
\frac{\partial U_{xxxx}}{\partial U_x} &= 4u_x^3 + 12\frac{Q_{xxx}u_x^2}{P_{xx}} - 12\frac{P_{xx}u_x}{\rho} + 4\frac{Q_{xxx}^2u_x}{P_{xx}^2} - 8\frac{Q_{xxx}}{\rho}\,, \\
\frac{\partial U_{xxxx}}{\partial U_{xx}} &= -6u_x^2 - 12\frac{Q_{xxx}u_x}{P_{xx}} + 6\frac{P_{xx}}{\rho} - 2\frac{Q_{xxx}^2}{P_{xx}^2}\,, \\
\frac{\partial U_{xxxx}}{\partial U_{xxx}} &= 4u_x + 4\frac{Q_{xxx}}{P_{xx}}.
\end{aligned}$$

The rest of the Jacobians are treated in two different ways. In Section 3.3.1, the remaining systems simply use the subsystems of the 10-moment equations shown in Equations (3.6), (3.7), and (3.8). Translational invariance is then imposed through further treatment of the Jacobian. Section 3.3.2 imposes additional symmetries to try and fulfill Property 3 as closely as possible. By constructing Jacobians for all three of the x, y, and z directions, which result in the same closing fluxes, an improved closure is found.

3.3.1 A Translationally Invariant 20-Moment Closure

For a first possible 20-moment closure, the 4×4 block is the one shown in Equation (3.16), the 3×3 blocks are the ones shown in Equations (3.6), the 2×2 blocks are the ones shown in Equations (3.7), and the 1×1 blocks are the ones shown in Equations (3.8). The random moments for the closing fluxes constructed this way are

$$
\begin{aligned}
&R_{xxxx} = 2\frac{Q_{xxx}^2}{P_{xx}} + 3\frac{P_{xx}^2}{\rho}\,, \\
&R_{xxxy} = 3\frac{P_{xx}P_{xy}}{\rho}\,, \qquad R_{xxxz} = 3\frac{P_{xx}P_{xz}}{\rho}\,, \\
&R_{xxyy} = \frac{P_{xx}P_{yy}}{\rho}\,, \qquad R_{xxyz} = \frac{P_{xx}P_{yz}}{\rho}\,, \qquad R_{xxzz} = \frac{P_{xx}P_{zz}}{\rho}\,, \\
&R_{xyyy} = 0 \qquad\quad R_{xyyz} = 0 \qquad\quad R_{xyzz} = 0 \qquad\quad R_{xzzz} = 0\,,
\end{aligned}
\tag{3.17}
$$

which are guaranteed to give a robustly hyperbolic closure for all realizable states of the gas.

However, Properties 2 and 3 are not automatically fulfilled. As this technique restricts closing fluxes to decouple from the other subsystems, some random moments, which should be used to build the convected moment, cannot be reached if it does not appear in the subsystem Jacobian or the set of moments being considered to build the closing flux. As an example, the U_{xxyy} can be built using the 2×2 subsystem of the 10-moment equations,

$$
\begin{bmatrix} U_{xyy} \\ U_{xxyy} \end{bmatrix} = \begin{bmatrix} 0 & 1 \\ -u_x^2 + \frac{P_{xx}}{\rho} & 2u_x \end{bmatrix} \begin{bmatrix} U_{yy} \\ U_{xyy} \end{bmatrix}\,, \tag{3.18}
$$

and the resulting form of U_{xxyy} is

$$
U_{xxyy} = \rho u_x^2 u_y^2 + 4P_{xy}u_x u_y + P_{yy}u_x^2 + 2Q_{xyy}u_x + R_{xxyy}\,, \tag{3.19}
$$

however this differs from the convected moment expansion,

$$
\langle m v_x v_x v_y v_y \mathcal{F} \rangle = \rho u_x^2 u_y^2 + 4P_{xy}u_x u_y + P_{yy}u_x^2 + P_{xx}u_y^2 + 2Q_{xyy}u_x + 2Q_{xxy}u_y + R_{xxyy}\,, \tag{3.20}
$$

and is missing the $P_{xx}u_y^2$ and $2Q_{xxy}u_y$ terms. Conveniently, the missing terms are always those of previously treated subsystems, and can easily be re-introduced through the lower triangle of the flux Jacobian without spoiling the hyperbolicity. This is then sufficient to fulfill Property 2. A similar technique can be used to construct $\frac{\mathrm{d}\boldsymbol{F}_\mathrm{y}}{\mathrm{d}\boldsymbol{U}}$ and $\frac{\mathrm{d}\boldsymbol{F}_\mathrm{z}}{\mathrm{d}\boldsymbol{U}}$.

The Jacobian which fulfills Properties 1 and 2 has the structure shown in Figure 3.3, and results in a system of 20 equations in balance law form, which have a characteristic polynomial in the form of Equation (3.13) that is guaranteed to have real roots. Therefore, the system is guaranteed to be hyperbolic for any realizable state of the gas.

3.3.2 An Improved 20-Moment Closure

It is evident in Section 3.3.1 that without considering Property 3, some directional preference has been introduced. This can easily be seen by comparing the resulting construction of the same closing flux for R_{xyyy} in each of the x and y-directions. For the x-direction Jacobian $\frac{\mathrm{d}\boldsymbol{F}_\mathrm{x}}{\mathrm{d}\boldsymbol{U}}$, as shown in Section 3.3.1,

$$R_{xyyy} = 0\,, \tag{3.21}$$

as a result of the 1×1 subsystem. But following the same process in the y-direction Jacobian,

$$R_{xyyy} = 3\frac{P_{xy}P_{yy}}{\rho} \tag{3.22}$$

as it a result of the 3×3 subsystem in $\frac{\mathrm{d}\boldsymbol{F}_\mathrm{y}}{\mathrm{d}\boldsymbol{U}}$. This inequivalence implies that fluxes behave differently depending on the direction being considered.

If the closing flux presented in Equation (3.15) is examined further, there are two dimensional groups which add together to build the random component of the closing moment. These are the heat flux term $2Q_{xxx}^2/P_{xx}$, and the pressure term $3P_{xx}/\rho$. If the full closing flux tensor is assumed to have the same groups, then the full closing flux

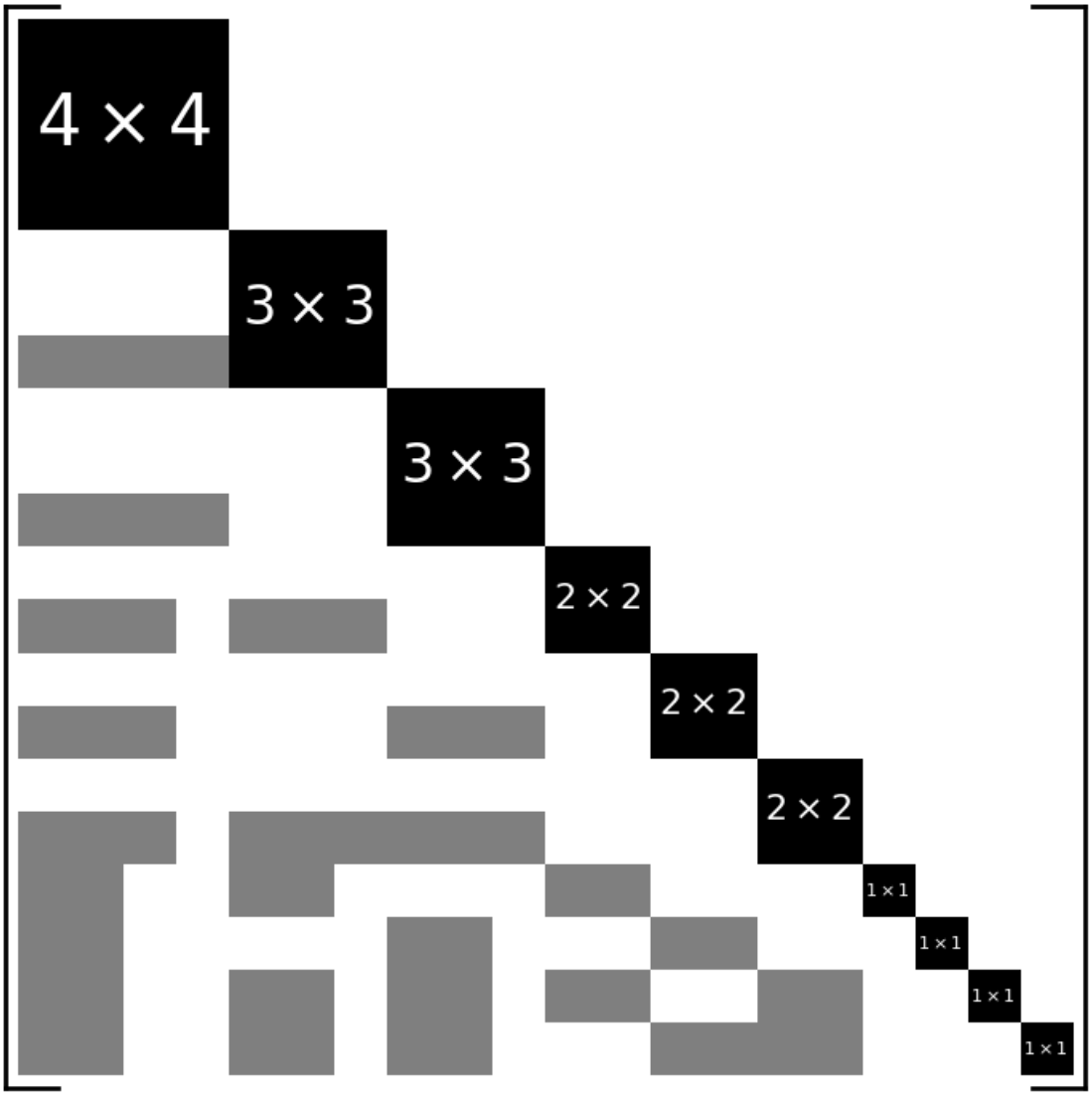

Figure 3.3: Translationally invariant 20-moment closure flux Jacobian structure

tensor can be assumed to have the form

$$R_{ijkl} = \widetilde{R_{ijkl}} + \overline{R_{ijkl}}\,, \tag{3.23}$$

such that $\widetilde{R_{ijkl}}$ contains terms involving heat fluxes, and $\overline{R_{ijkl}}$ contains only the pressures and density. For the flux presented in Equation (3.15), this means

$$\widetilde{R_{xxxx}} = 2\frac{Q_{xxx}^2}{P_{xx}}\,, \quad \text{and} \quad \overline{R_{xxxx}} = 3\frac{P_{xx}^2}{\rho}\,, \tag{3.24}$$

which should remain in this form regardless of the system chosen to generate the set of closures that satisfy Property 3.

One possible form of $\overline{R_{ijkl}}$ is easily obtainable simply by analyzing the 10 moment closure further. In the absence of heat fluxes, the moments of R_{ijkl} simply become

$$\overline{R_{ijkl}} = \frac{P_{ij}P_{kl} + P_{ik}P_{jl} + P_{il}P_{jk}}{\rho}\,, \tag{3.25}$$

which either exactly corresponds to terms in the first 20 moment closure presented, such as the $3P_{xx}^2/\rho$ term of R_{xxxx}, or partially, such as with R_{xxyy}. For this flux, the $P_{xx}P_{yy}/\rho$ term appears, but now there is an additional $2P_{xy}^2/\rho$. Notably the addition of these terms never break the block diagonalization, meaning the Eigenvalues are still easily obtained and can be guaranteed to be real valued.

The terms containing the heat flux are much more complicated. Just from inspection of the $2Q_{xxx}^2/P_{xx}$ term, somehow eight indices need to be reconciled with a fourth order tensor. However, by treating each entry separately, some symmetries can be imposed.

Terms which include two-pairs of repeated indices, such as R_{xxyy}, are easy to treat. By introducing the heat fluxes which appear in each of the 2×2 subsystems, and scaling them with the pressure tensor entry from those subsystems, the heat flux term

$$\widetilde{R_{xxyy}} = \frac{Q_{xxy}^2}{P_{xx}} + \frac{Q_{xyy}^2}{P_{yy}}\,, \tag{3.26}$$

can be used. It is not desirable to introduce Q_{xxx} or Q_{yyy}, as this would break the block

diagonalization in the opposing Jacobian (for instance, adding Q_{yyy} would add entries to the right of the 2×2 block in $\frac{\mathrm{d}\boldsymbol{F}_\mathrm{x}}{\mathrm{d}\boldsymbol{U}}$. This results in the 2×2 system

$$\widehat{\frac{\mathrm{d}\boldsymbol{F}_\mathrm{x}}{\mathrm{d}\boldsymbol{U}}}_{2\times2} = \begin{bmatrix} 0 & 1 \\ -u_x^2 - 2\frac{Q_{xyy}u_x}{P_{yy}} - 2\frac{Q_{xyy}^2}{P_{yy}^2} + \frac{P_{xx}}{\rho} & 2u_x + 2\frac{Q_{xyy}}{P_{yy}} \end{bmatrix}, \tag{3.27}$$

for $\frac{\mathrm{d}\boldsymbol{F}_\mathrm{x}}{\mathrm{d}\boldsymbol{U}}$, and a similar form (but with x and y indices swapped) for $\frac{\mathrm{d}\boldsymbol{F}_\mathrm{y}}{\mathrm{d}\boldsymbol{U}}$.

For all terms that have three repeated indices, such as R_{xxxy} or R_{xyyy},

$$\widetilde{R_{xxxy}} = 2\frac{Q_{xxx}Q_{xxy}}{P_{xx}}, \tag{3.28}$$

was found to be a convenient extension, including that subsystems heat flux, as well as the previous subsystem which it can be coupled to without breaking diagonalization. The new 3×3 subsystem block in $\frac{\mathrm{d}\boldsymbol{F}_\mathrm{x}}{\mathrm{d}\boldsymbol{U}}$ is

$$\widehat{\frac{\mathrm{d}\boldsymbol{F}_\mathrm{x}}{\mathrm{d}\boldsymbol{U}}}_{3\times3} = \begin{bmatrix} 0 & 1 & 0 \\ 0 & 0 & 1 \\ u_x^3 + 2\frac{Q_{xxx}u_x^2}{P_{xx}} - 3\frac{P_{xx}u_x}{\rho} - \frac{Q_{xxx}}{\rho} & -3u_x^2 - 4\frac{Q_{xxx}u_x}{P_{xx}} + 3\frac{P_{xx}}{\rho} & 3u_x + 2\frac{Q_{xxx}}{P_{xx}} \end{bmatrix}, \tag{3.29}$$

and the 1×1 subsystem block in $\frac{\mathrm{d}\boldsymbol{F}_\mathrm{y}}{\mathrm{d}\boldsymbol{U}}$ is

$$\widehat{\frac{\mathrm{d}\boldsymbol{F}_\mathrm{y}}{\mathrm{d}\boldsymbol{U}}}_{1\times1} = \begin{bmatrix} u_y + 2\frac{Q_{xxy}}{P_{xx}} \end{bmatrix}, \tag{3.30}$$

both can be shown to have real-valued Eigenvalues for all realizable states.

The three remaining terms, R_{xxyz}, R_{xyyz}, and R_{xyzz}, can similarly be coupled to previous subsystems to achieve a working heat flux term, and forced to be symmetric between all three Jacobians. Again, breaking the closing fluxes up into the possible heat fluxes that can be used without breaking diagonalization results in

$$\widetilde{R_{xxyz}} = \frac{Q_{xxy}Q_{xxz}}{P_{xx}} + \frac{Q_{xxx}Q_{xyz}}{P_{xx}}, \tag{3.31}$$

with similar entries for the other two. These have 2×2 subsystem

$$\widehat{\frac{\mathrm{d}\boldsymbol{F}_{\mathrm{x}}}{\mathrm{d}\boldsymbol{U}}}_{2\times 2} = \begin{bmatrix} 0 & 1 \\ -u_x^2 - \frac{Q_{xxx}u_x}{P_{xx}} + \frac{P_{xx}}{\rho} & 2u_x + \frac{Q_{xxx}}{P_{xx}} \end{bmatrix}, \tag{3.32}$$

and 1×1 subsystems

$$\widehat{\frac{\mathrm{d}\boldsymbol{F}_{\mathrm{y}}}{\mathrm{d}\boldsymbol{U}}}_{1\times 1} = \begin{bmatrix} u_y + \frac{Q_{xxy}}{P_{xx}} \end{bmatrix}, \quad \text{and} \quad \widehat{\frac{\mathrm{d}\boldsymbol{F}_{\mathrm{z}}}{\mathrm{d}\boldsymbol{U}}}_{1\times 1} = \begin{bmatrix} u_z + \frac{Q_{xxz}}{P_{xx}} \end{bmatrix}, \tag{3.33}$$

in the other two Jacobians.

The final result is the following set of closing moments

$$R_{xxxx} = 2\frac{Q_{xxx}^2}{P_{xx}} + 3\frac{P_{xx}^2}{\rho},$$

$$R_{yyyy} = 2\frac{Q_{yyy}^2}{P_{yy}} + 3\frac{P_{yy}^2}{\rho},$$

$$R_{zzzz} = 2\frac{Q_{zzz}^2}{P_{zz}} + 3\frac{P_{zz}^2}{\rho},$$

$$R_{xxxy} = 2\frac{Q_{xxx}Q_{xxy}}{P_{xx}} + 3\frac{P_{xx}P_{xy}}{\rho},$$

$$R_{xxxz} = 2\frac{Q_{xxx}Q_{xxz}}{P_{xx}} + 3\frac{P_{xx}P_{xz}}{\rho},$$

$$R_{xyyy} = 2\frac{Q_{xyy}Q_{yyy}}{P_{yy}} + 3\frac{P_{xy}P_{yy}}{\rho},$$

$$R_{xzzz} = 2\frac{Q_{zzz}Q_{xzz}}{P_{zz}} + 3\frac{P_{xz}P_{zz}}{\rho},$$

$$R_{yyyz} = 2\frac{Q_{yyy}Q_{yyz}}{P_{yy}} + 3\frac{P_{yy}P_{yz}}{\rho},$$

$$R_{yzzz} = 2\frac{Q_{zzz}Q_{yzz}}{P_{zz}} + 3\frac{P_{yz}P_{zz}}{\rho},$$

$$R_{xxyy} = \frac{Q_{xxy}^2}{P_{xx}} + \frac{Q_{xyy}^2}{P_{yy}} + \frac{P_{xx}P_{yy}}{\rho} + 2\frac{P_{xy}^2}{\rho},$$

$$R_{xxzz} = \frac{Q_{xxz}^2}{P_{xx}} + \frac{Q_{xzz}^2}{P_{zz}} + \frac{P_{xx}P_{zz}}{\rho} + 2\frac{P_{xz}^2}{\rho},$$

$$R_{yyzz} = \frac{Q_{yyz}^2}{P_{yy}} + \frac{Q_{yzz}^2}{P_{zz}} + \frac{P_{yy}P_{zz}}{\rho} + 2\frac{P_{yz}^2}{\rho}\,,$$

$$R_{xxyz} = \frac{Q_{xxy}Q_{xxz}}{P_{xx}} + \frac{Q_{xxx}Q_{xyz}}{P_{xx}} + \frac{P_{xx}P_{yz}}{\rho} + 2\frac{P_{xy}P_{xz}}{\rho}\,,$$

$$R_{xyyz} = \frac{Q_{xyy}Q_{yyz}}{P_{yy}} + \frac{Q_{yyy}Q_{xyz}}{P_{yy}} + \frac{P_{xz}P_{yy}}{\rho} + 2\frac{P_{xy}P_{yz}}{\rho}\,,$$

$$R_{xyzz} = \frac{Q_{yzz}Q_{xzz}}{P_{zz}} + \frac{Q_{zzz}Q_{xyz}}{P_{zz}} + \frac{P_{xy}P_{zz}}{\rho} + 2\frac{P_{xz}P_{yz}}{\rho}\,,$$

which no longer result in different closures for each Jacobian, and become identical to the 10-moment closure in the absence of heat flux. The final Jacobian structure is also still in the easily analyzable block diagonal form, shown in Figure 3.4. The closing fluxes can also be shown to satisfy Equation (2.68) for every state.

3.4 Linear Stability of the New Models

One of the important features of hyperbolic-relaxation models is that they exhibit dispersive wave behaviour, where information travels at different finite speeds depending on wavelength. When looking at perturbations around equilibrium, the apparent propagation speed depends on the wave number of the disturbance, k. This dispersion relationship determines not only the speeds at which information can travel for the two models that have been developed, but also determines their linear stability [36–38]. For small perturbations from local thermodynamic equilibrium, the waves should diminish in strength to remain linearly stable.

Equations of the form shown in Equation (2.11) can be evaluated in two states; the first at the solution vector state in local thermodynamic equilibrium, $\boldsymbol{U}_e$, which takes the form

$$\frac{\partial \boldsymbol{U}_e}{\partial t} + \frac{\mathrm{d}\boldsymbol{F}_\mathrm{i}}{\mathrm{d}\boldsymbol{U}}\frac{\partial \boldsymbol{U}_e}{\partial x_i} = 0\,, \tag{3.34}$$

and the second state, $\boldsymbol{U}_p$, for some a small perturbation from equilibrium, which takes the form

$$\frac{\partial \boldsymbol{U}_p}{\partial t} + \frac{\mathrm{d}\boldsymbol{F}_\mathrm{i}}{\mathrm{d}\boldsymbol{U}}\frac{\partial \boldsymbol{U}_p}{\partial x_i} = \frac{\mathrm{d}\boldsymbol{S}}{\mathrm{d}\boldsymbol{U}}\boldsymbol{U}_p\,, \tag{3.35}$$

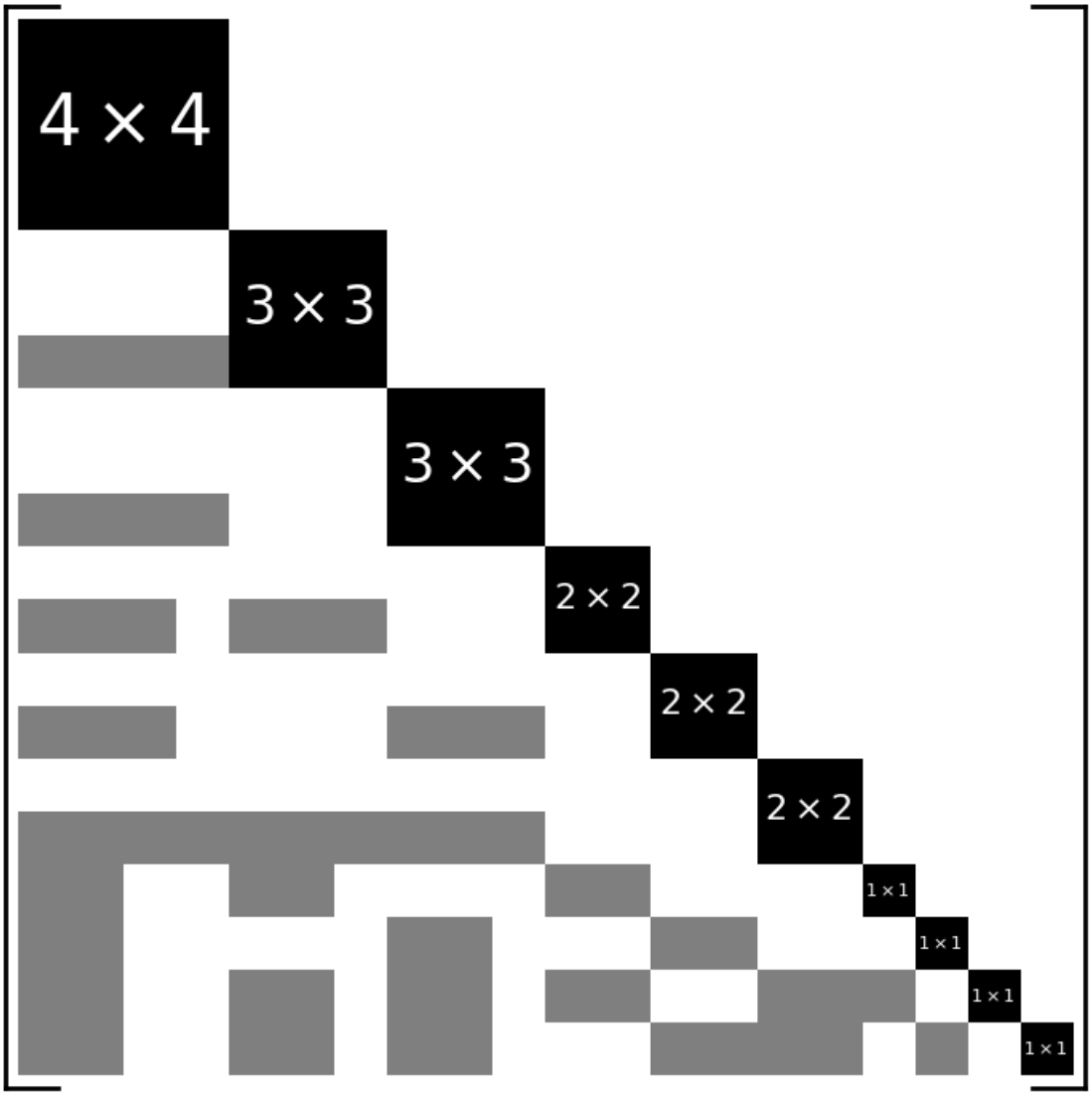

Figure 3.4: Improved 20-moment closure flux Jacobian structure

where $\frac{\partial \boldsymbol{S}}{\partial \boldsymbol{U}}$ is the Jacobian of the source term. Equation (3.35) can be rewritten in the form of a linear operator

$$\left(\boldsymbol{I}\frac{\partial}{\partial t} + \frac{\mathrm{d}\boldsymbol{F}_{\mathrm{i}}}{\mathrm{d}\boldsymbol{U}}\frac{\partial}{\partial x_i} - \frac{\mathrm{d}\boldsymbol{S}}{\mathrm{d}\boldsymbol{U}}\right)\boldsymbol{U}_d = 0\,, \tag{3.36}$$

on the solution ansatz $\boldsymbol{U}_d$. The effect of the wave number, k, and how it acts on this operator, can be studied. For an initial-value problem, with an initial conditions of the form

$$\boldsymbol{U}_d\,(x,0) = \boldsymbol{U}_0 \exp\left(-ikx\right), \tag{3.37}$$

and a solution ansatz of the form

$$\boldsymbol{U}_d\,(x,t) = \boldsymbol{V}_d\,(t) \exp\left(-ikx\right), \tag{3.38}$$

which can be substituted into Equation (3.36). This yields the system of ordinary differential equations

$$\frac{d\boldsymbol{V}_d}{dt} = \left(ik\frac{\mathrm{d}\boldsymbol{F}_{\mathrm{i}}}{\mathrm{d}\boldsymbol{U}} + \frac{\mathrm{d}\boldsymbol{S}}{\mathrm{d}\boldsymbol{U}}\right)\boldsymbol{V}_d\,, \tag{3.39}$$

that has the solution

$$\boldsymbol{V}_d(t) = \boldsymbol{U}_0 \exp\left[it\left(k\frac{\mathrm{d}\boldsymbol{F}_{\mathrm{i}}}{\mathrm{d}\boldsymbol{U}} - i\frac{\mathrm{d}\boldsymbol{S}}{\mathrm{d}\boldsymbol{U}}\right)\right]. \tag{3.40}$$

The Eigenvalues of the matrix formed in the solution can be found by solving

$$\det\left(k\frac{\mathrm{d}\boldsymbol{F}_{\mathrm{i}}}{\mathrm{d}\boldsymbol{U}} - i\frac{\mathrm{d}\boldsymbol{S}}{\mathrm{d}\boldsymbol{U}} - \omega\boldsymbol{I}\right) = 0\,, \tag{3.41}$$

which are complex. Each Eigenvalue then has the form

$$\omega = \omega_R + i\omega_I\,, \tag{3.42}$$

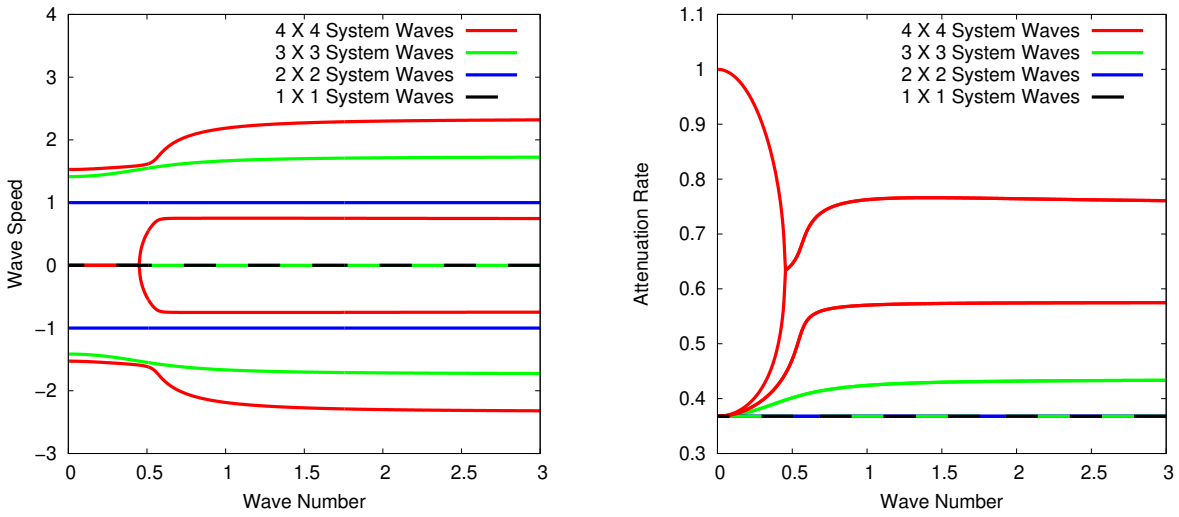

(a) (b)

Figure 3.5: Dispersion analysis for the translationally invariant 20-moment closure

and the appropriate wave speed of the disturbed solution can be found as

$$\lambda = \omega_R(k)/k\,, \tag{3.43}$$

with the attenuation rate being

$$\exp\left[-\omega_I(k)\right]. \tag{3.44}$$

Plotting the wave speeds of the perturbed solution for a range of wave numbers shows the dispersive wave behaviour between equilibrium and non-equilibrium states. Plotting the attenuation rate demonstrates the stability of the model, so long as they stay on the range $[0, 1]$. For this analysis, a non-dimensional equilibrium is used, such that the density $\rho = 1$, the mean velocities $u_x = u_y = u_z = 0$, and the thermodynamic pressure $p = 1$.

The dispersion analysis for the two 20-moment models are shown in Figure 3.5 for the translationally invariant model from Section 3.3.1, and Figure 3.6 for the improved model from Section 3.3.2. The wave speeds and attenuation rates have been grouped according to the corresponding subsystem that they originate from, based on Equation (3.13).

At high wave numbers, the free-molecular wave speeds of each model can be seen on the right-hand side of the wave speed plots. These can be organized by the Eigenvalues

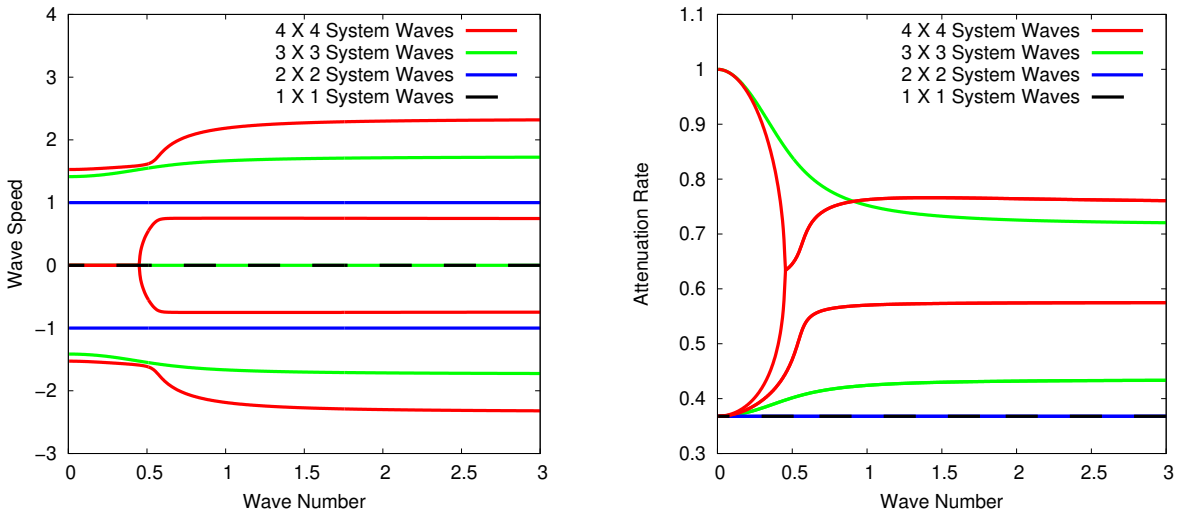

(a) (b)

Figure 3.6: Dispersion analysis for the improved 20-moment closure

that were prescribed with the diagonal subsystem Jacobians. On the left-hand side of each plot for low wave numbers, the source term dominates and the standard Maxwellian distribution wave speeds can be seen. The attenuation rate for both models stays roughly on the range $[0.367, 1]$, indicating they are both linearly stable over a wide range of wave numbers. The result is that both models show the desirable wave dispersion when leaving equilibrium, and that the models remain linearly stable for equilibrium and non-equilibrium states.

3.5 Discussion of Rotational Invariance

Despite forcing the flux Jacobians $\frac{\mathrm{d}\boldsymbol{F}_\mathrm{x}}{\mathrm{d}\boldsymbol{U}}$, $\frac{\mathrm{d}\boldsymbol{F}_\mathrm{y}}{\mathrm{d}\boldsymbol{U}}$, and $\frac{\mathrm{d}\boldsymbol{F}_\mathrm{z}}{\mathrm{d}\boldsymbol{U}}$ to predict the same closure for their highest-order moments, rotational invariance is not completely achieved. For full rotational invariance, the closing moments should take the form of a proper fourth-order tensor, R_{ijkl}. At present, the closure in Section 3.3.2 cannot be written in this way.

There are some proposed tensors which do have the desirable rotational properties these models would hope to achieve. If the heat flux contribution to the closing flux as described in Equation (3.23) is assumed to be of the form

$$R_{ijkl} = Q_{ijm}\left(P^{-1}\right)_{mn} Q_{nkl} + 2Q_{ikm}\left(P^{-1}\right)_{mn} Q_{njl}\,, \tag{3.45}$$

then the closure is both rotationally and translationally invariant. In fact, the closures found in Section 3.3.2 are terms which appear in this expression, divided instead by the trace elements of the pressure tensor, P, instead of its full inverse. By introduction of the inverse of the full pressure tensor, the block diagonalization described in Section 3.3 is no longer maintained as pressure tensor entries from lower subsystems are introduced in the upper triangle of the flux Jacobian. This couples the terms in the characteristic polynomial together, and loses the form shown in Equation 3.13. This allows for much more freedom in the characteristic polynomial to have complex roots, and the model loses robust global hyperbolicity.

Another property which would be desirable of a moment closure is the construction of a Hankel matrix of the moments in the system [12, 35]. Quadrature methods, of which the new models are built from, can represent the solution vector and flux vectors as

$$\boldsymbol{U} = \boldsymbol{R}\mathcal{W}, \quad \text{and} \quad \boldsymbol{U} = \boldsymbol{R}\boldsymbol{\Lambda}\mathcal{W}\,, \tag{3.46}$$

where $\boldsymbol{R}$ is the matrix of Eigenvectors of the flux Jacobian, $\boldsymbol{\Lambda}$ is the diagonal matrix of the Eigenvalues, and $\mathcal{W}$ is a vector of appropriate weights. By taking a diagonal matrix of the weights $\boldsymbol{\mathcal{W}} = \text{diag}\,(\mathcal{W})$, the matrices

$$\boldsymbol{H} = \boldsymbol{R}\boldsymbol{\mathcal{W}}\boldsymbol{R}^T, \quad \text{and} \quad \boldsymbol{J} = \boldsymbol{R}\boldsymbol{\Lambda}\boldsymbol{\mathcal{W}}\boldsymbol{R}^T\,, \tag{3.47}$$

can be defined, such that

$$\frac{\mathrm{d}\boldsymbol{F}}{\mathrm{d}\boldsymbol{U}} = \boldsymbol{J}\boldsymbol{H}^{-1}\,, \tag{3.48}$$

is true as it recovers the original Eigendecomposition of the flux Jacobian. The matrix $\boldsymbol{H}$ then contains all the moments from order 0 to $2n$, and $\boldsymbol{J}$ contains all the moments from order 1 to $2n+1$. For the one-dimensional closures, the series of moments from orders 0 to $2n+1$ must have the correct structure, but for multidimensional closures this structure must be maintained for all the entries of the higher-order, multidimensional moments as well. For the 20-moment closures discussed in this work, this means not only does the

fourth-order closing flux need to be constructed in a way that agrees in every direction, but all moments up to the eighth-order as well.

In the absence of an integrable distribution function, and for methods which exclusively construct a flux Jacobian, it can be noted that

$$\boldsymbol{F}_i = \frac{\mathrm{d}\boldsymbol{F}_\mathrm{i}}{\mathrm{d}\boldsymbol{U}}\boldsymbol{U}\,, \tag{3.49}$$

increases the order of the moments by one, as per the flux Jacobians definition. Therefore, to construct higher order moments,

$$\begin{aligned} \boldsymbol{A} &= \frac{\mathrm{d}\boldsymbol{F}_\mathrm{x}}{\mathrm{d}\boldsymbol{U}}\frac{\mathrm{d}\boldsymbol{F}_\mathrm{x}}{\mathrm{d}\boldsymbol{U}}\boldsymbol{U}\,, & \boldsymbol{B} &= \frac{\mathrm{d}\boldsymbol{F}_\mathrm{x}}{\mathrm{d}\boldsymbol{U}}\frac{\mathrm{d}\boldsymbol{F}_\mathrm{y}}{\mathrm{d}\boldsymbol{U}}\boldsymbol{U}\,, \\ \boldsymbol{C} &= \frac{\mathrm{d}\boldsymbol{F}_\mathrm{y}}{\mathrm{d}\boldsymbol{U}}\frac{\mathrm{d}\boldsymbol{F}_\mathrm{x}}{\mathrm{d}\boldsymbol{U}}\boldsymbol{U}\,, & \boldsymbol{D} &= \frac{\mathrm{d}\boldsymbol{F}_\mathrm{y}}{\mathrm{d}\boldsymbol{U}}\frac{\mathrm{d}\boldsymbol{F}_\mathrm{y}}{\mathrm{d}\boldsymbol{U}}\boldsymbol{U}\,, \end{aligned} \tag{3.50}$$

should define vectors $\boldsymbol{A}$, $\boldsymbol{B}$, $\boldsymbol{C}$, and $\boldsymbol{D}$, that contain the second-through-sixth order moments of the 20-moment closures. By symmetry, the entries in $\boldsymbol{B}$ and $\boldsymbol{C}$ should contain identical moments, as only the order of the application of the flux Jacobians differs in their construction, but results in the same moments. This allows for the definition of the commutation property,

$$\boldsymbol{0} = \left(\frac{\mathrm{d}\boldsymbol{F}_\mathrm{x}}{\mathrm{d}\boldsymbol{U}}\frac{\mathrm{d}\boldsymbol{F}_\mathrm{y}}{\mathrm{d}\boldsymbol{U}} - \frac{\mathrm{d}\boldsymbol{F}_\mathrm{y}}{\mathrm{d}\boldsymbol{U}}\frac{\mathrm{d}\boldsymbol{F}_\mathrm{x}}{\mathrm{d}\boldsymbol{U}}\right)\boldsymbol{U}\,, \tag{3.51}$$

forcing the correct construction of the higher-order moments in a way that will properly extend to generate the matrix $\boldsymbol{H}$.

The models developed in this work do not fulfill the property described in Equation (3.51). However, the model presented in Section 3.3.2 does have more entries which are 0 when compared to the model presented in Section 3.3.1. This indicates that the improved model does more closely approximate the construction of the full matrix $\boldsymbol{H}$, even if some errors are introduced. The closing flux presented in Equation (3.45) does indeed fulfill Equation (3.51), but as mentioned does not retain robust hyperbolicity. At present, there has not been a block diagonal, or indeed any robustly hyperbolic closure, which can fulfill this property.

While this is a major deficiency for the theory surrounding models of this style, they are still a big improvement for moment closures by achieving the first two properties. Further, with sufficient collisions these defects do not present themselves, as the rotational deficiencies can be attenuated by the collision operator bringing the models back in to thermodynamic equilibrium. As the models have been built to agree with the Euler equations in equilibrium, and the value of the commutator for both models in equilibrium is $\mathbf{0}$, there is still promise for these models in regimes with moderate non-equilibrium. Chapter 4 demonstrates this through numerical experiments across the regimes of interest for the models.

Chapter 4

Canonical Flow Problems

In order to evaluate the performance of the new models, some simple discontinuous flow problems are solved. As mentioned in Section 2.1.2, these problems are for monatomic Argon gas, with $\gamma = 5/3$, and assuming constant collision timescales. A discussion of the numerical methods is included in Section 4.1. Section 4.2 demonstrates the models predictions for one-dimensional Riemann problems, while Section 4.3 shows the predictions for two-dimensional, discontinuous bubbles. While these problems are in one or two dimensions of physical space, they simulate a physically realistic three-dimensional gas.

For both sets of problems presented in this chapter, the three regimes of interest for moment methods, that is the continuum, transition, and free-molecular regimes, are investigated. In order to remain in the desired regime, a collision timescale, τ, must be chosen. For this investigation, they are chosen to be a constant value, which while not physically accurate does allow for easy comparison to the reference solutions. For these simple cases, fixed Dirichlet boundary conditions are used, however final times chosen are such that the waves do not propagate to the boundary of the domain, and therefore do not affect the results.

Both the 20-moment models from Sections 3.3.1 and 3.3.2 are used for the solution of these problems. Section 4.2 also includes the results for a 35-moment closure, developed in Appendix A, of the same style as the translational 20-moment closure from Section 3.3.1. Reference solutions were produced through direct discretization of the kinetic equations

and the collision operator [3], and are denoted as BGK solutions. Solutions of the Euler equations are also provided as a reference for what continuum assumption based methods would predict in these cases.

4.1 Numerical Methods

All the solutions presented throughout this work are computed through the implementation of the relevant models inside a numerical framework for the solution of balance laws [39]. This framework is a discontinuous-Galerkin (DG) scheme, and has both first and third-order accuracy capabilities. It has been designed to be highly parallelizable for use on high performance computing clusters. The scheme uses block-based mesh refinement, where blocks of smaller meshes are distributed across multiple CPUs. Due to the nature of the PDEs, the only information that needs to be transferred across the boundaries are the fluxes at the end of every timestep. This gives a very flexible framework for efficient computation of solutions.

The first-order scheme is the standard DG method [40], with piecewise constant basis functions, explicit Euler time-marching for evaluation of the fluxes, and implicit Euler time-marching for the evaluation of the source terms. Fluxes on the interfaces between cells computed with the method proposed by Harten, Lax and van Leer (HLL) [6]. This scheme is only used for preliminary testing, with a CFL number of 0.5 to ensure stability, and unless otherwise mentioned the results presented throughout this work use the more accurate third-order scheme.

The third-order scheme was originally proposed by Suzuki and van Leer [7], with additional analysis and the implementation used in this work provided by Kaufmann and McDonald [39]. It was specially designed for the solution of hyperbolic-relaxation laws with stiff source terms, with the same formulation as Equation 2.10. The test functions for this scheme are linear, but nevertheless achieve third-order accuracy in space and time (typically requiring quadratic test functions to achieve) with the carefully chosen Hancock predictor step for the evaluation of the fluxes. Radau IIA time-marching is used

for evaluation of the source terms, which is again a third-order accurate method [41]. Fluxes are once again computed on the interfaces using the HLL method, and slope-limiting is handled with the differentiable method proposed by Venkatakrishnan [42]. The CFL number was chosen to be 0.33, as this ensured stability without introducing too much numerical dissipation. The use of this scheme results in very low numerical dissipation for all of the 20-moment results.

4.2 Riemann Problems in One Spatial Dimension

The first set of problems are Sod shock-tube style Riemann problems. The left and right states are set to a stationary gas in equilibrium, with the density and pressure ratios between the left and the right sides

$$\frac{\rho_L}{\rho_R} = 3.335\,, \quad \text{and} \quad \frac{p_L}{p_R} = 4.0\,, \tag{4.1}$$

for all three problems. The Riemann problem is then solved at a resolution of 10 000 cells, with a domain $-L < x < L$. The final times were then chosen such that each solution showed the wave-patterns of the solution in each regime, but had not yet reached the boundaries of the domain. The continuum results are at a Knudsen number of around $\mathrm{Kn} = 4.3 \times 10^{-5}$, while the transition results are at a Knudsen number of around $\mathrm{Kn} = 4.3 \times 10^{-1}$. The free molecular results assume that the effect of the collisions is $\boldsymbol{S}_{ij}(\boldsymbol{U}) = \boldsymbol{S}_{ijk}(\boldsymbol{U}) = 0$, corresponding to an infinite collision relaxation time and therefore an infinite Knudsen number.

Reference solutions produced through direct discretization of the kinetic equation are only first-order accurate, but at an increased resolution of 20 480 cells in physical space to compensate. Due to the axisymmetry of the problem, and to help with the computational cost, the transverse velocities v_y and v_z can instead be represented as $v_r = \sqrt{v_y^2 + v_z^2}$, and integrated on a half domain $0 \leq v_r \leq v_f$ to the desired fastest velocity v_f. This can then be used to reconstruct the solution for the full three-dimensional gas. The velocity space domain was then made to be $-11\sqrt{p_R/\rho_R} \leq v_x \leq 11\sqrt{p_R/\rho_R}$ with 1000 discrete

velocities and $0 \leq v_r \leq 11\sqrt{p_R/\rho_R}$ with 500 discrete velocities.

Reference solutions of the Euler equations were produced with the third-order scheme at the same 10 000 resolution as the 20-moment solutions. This gives a sense of timescale of each problem with a more familiar model, by demonstrating how far the continuum waves propagate for each case.

Figures 4.1a to 4.1f show the density, velocity, temperature, and heat-flux profile solutions for the continuum flow regime with a collision operator timescale of $\tau = 2.0 \times 10^{-9} L\sqrt{\rho_R/p_R}$ and a solution time of $t_{\text{final}} = 1.3 \times 10^{-4} L\sqrt{\rho_R/p_R}$. Figures 4.2a to 4.2f, show the density, velocity, temperature, and heat flux profile solutions for the transition flow regime with a collision operator timescale of $\tau = 2.0 \times 10^{-5} L\sqrt{\rho_R/p_R}$ and a solution time of $t_{\text{final}} = 1.0 \times 10^{-4} L\sqrt{\rho_R/p_R}$. Figures 4.3a to 4.3f, show the density, velocity, temperature, and heat flux profile solutions for the free-molecular flow regime with a collision operator timescale of $\tau = 2.0 \times 10^{5} L\sqrt{\rho_R/p_R}$ and a solution time of $t_{\text{final}} = 7.5 \times 10^{-5} L\sqrt{\rho_R/p_R}$.

All of the new models have good agreement in the continuum regime, reflecting the gas quickly being attenuated back to equilibrium by the dominating source term. The only non-equilibrium effects that can be seen in the continuum regime are inside the shock, contact, and rarefaction waves, where the heat fluxes shown in Figures 4.1e and 4.1f are slightly non-zero, showing that the new models allow small perturbations from equilibrium in this regime. Otherwise, outside those waves, the solutions are identical to the Euler solution.

For the transition regime, the models all have excellent agreement with each other, and closely approximate the BGK solution. Minor discrepancies between the moment models and the BGK solution are expected, with the moment models having areas of sharper gradients and small heat flux overpredictions, but these defects remain relatively small. They are also reduced in the 35-moment solution when compared to the 20-moment solution, which is especially noticeable in Figures 4.2e and 4.2f, indicating higher-order predictions can indeed lead to more physically accurate modelling in this regime.

For the free-molecular regime, the model begins to deviate from the BGK solution

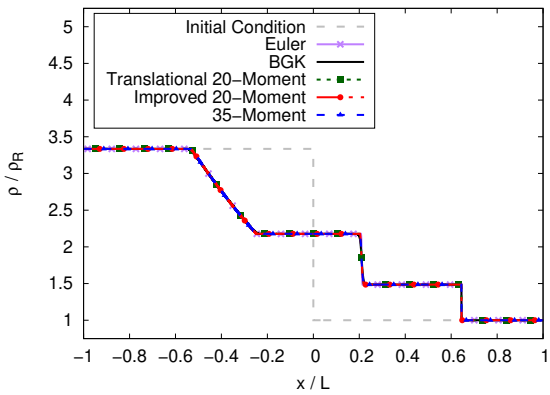

(a) Density profile

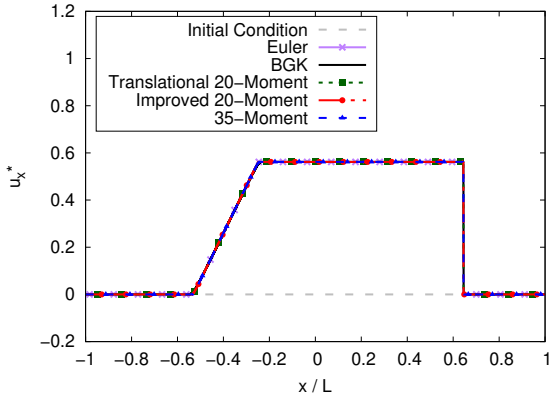

(b) Axial velocity profile

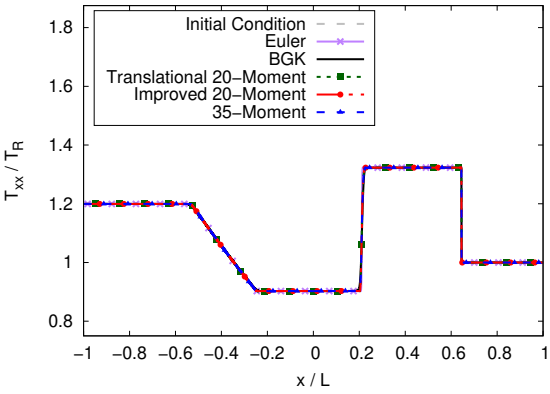

(c) Axial temperature profile

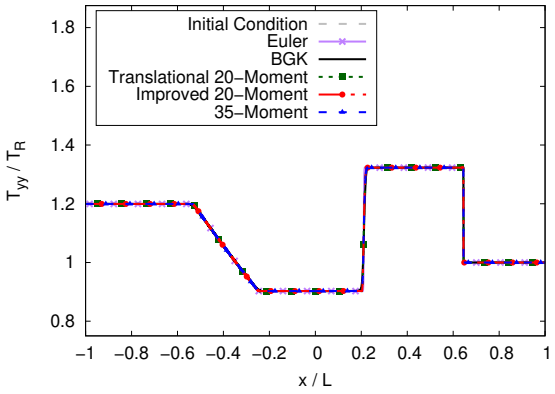

(d) Transverse temperature profile

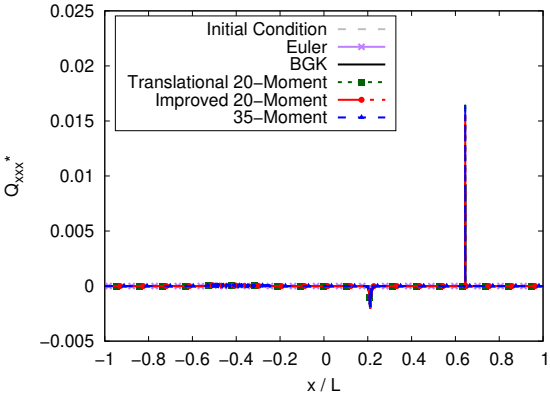

(e) Axial heat flux profile

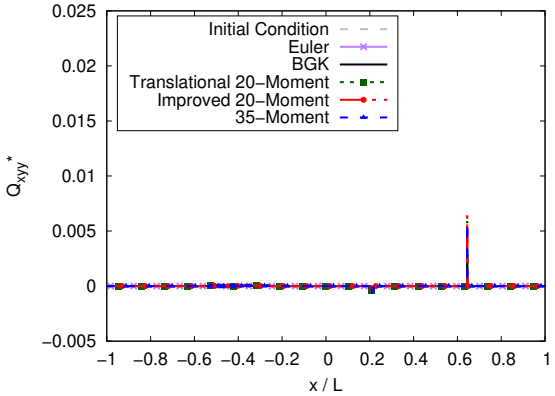

(f) Transverse heat flux profile

Figure 4.1: Continuum regime Riemann problem solutions for the new models, compared against BGK solutions

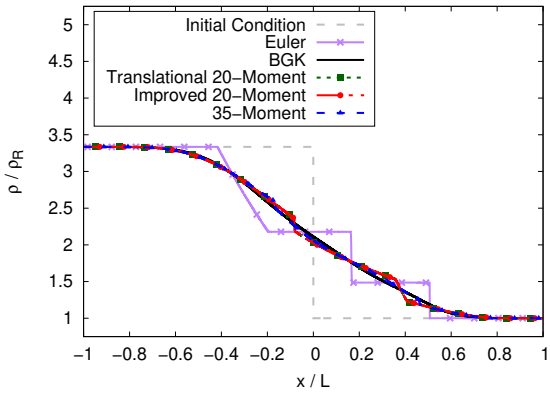

(a) Density profile

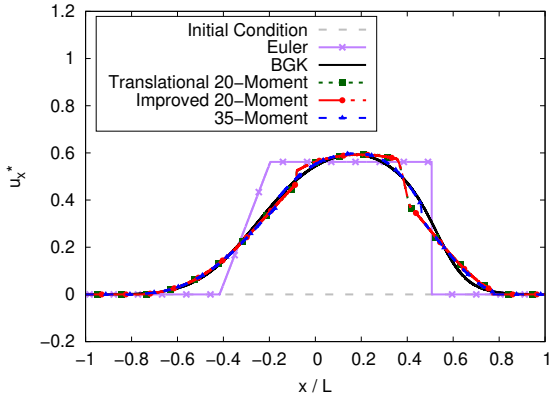

(b) Axial velocity profile

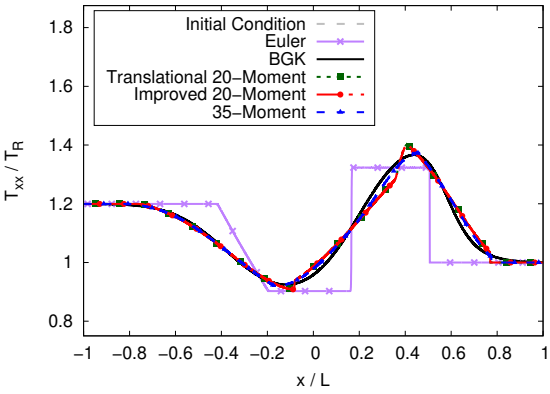

(c) Axial temperature profile

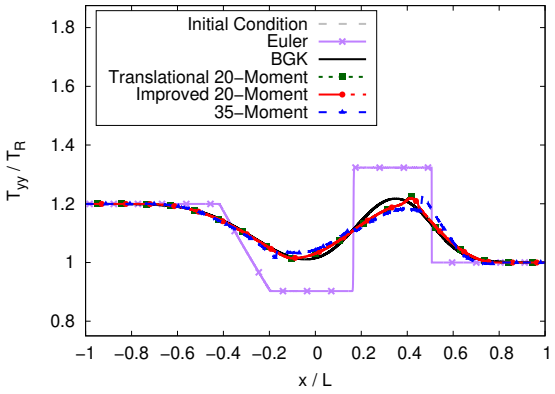

(d) Transverse temperature profile

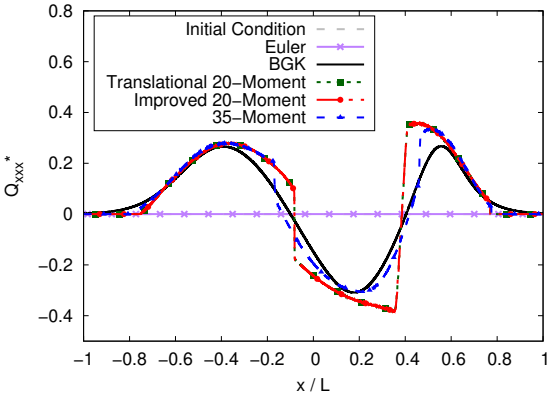

(e) Axial heat flux profile

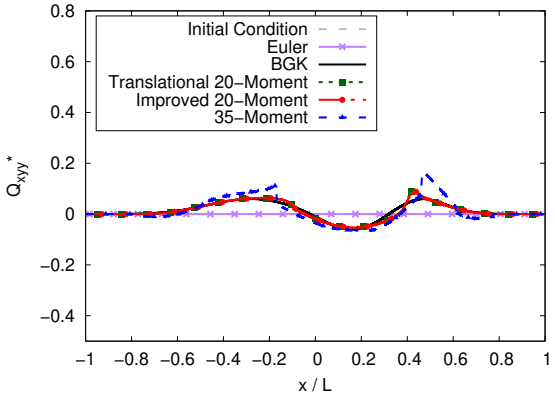

(f) Transverse heat flux profile

Figure 4.2: Transition regime Riemann problem solutions for the new models, compared against BGK solutions

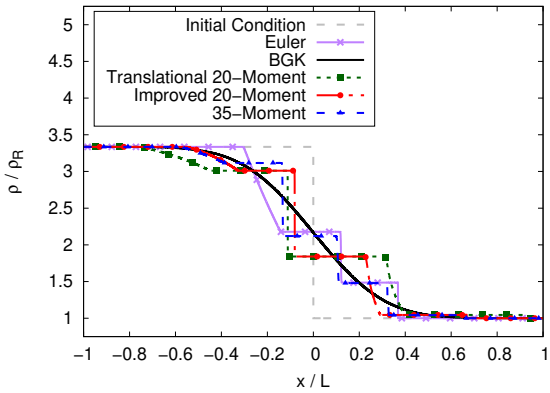

(a) Density profile

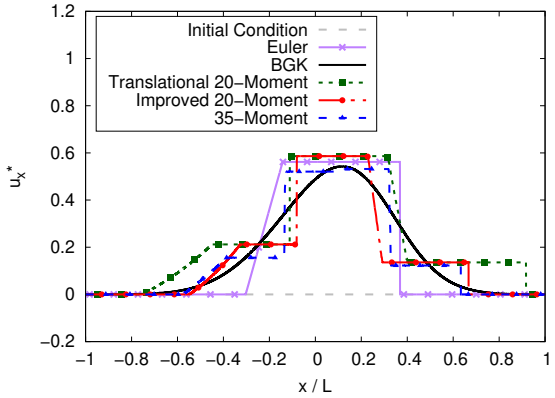

(b) Axial velocity profile

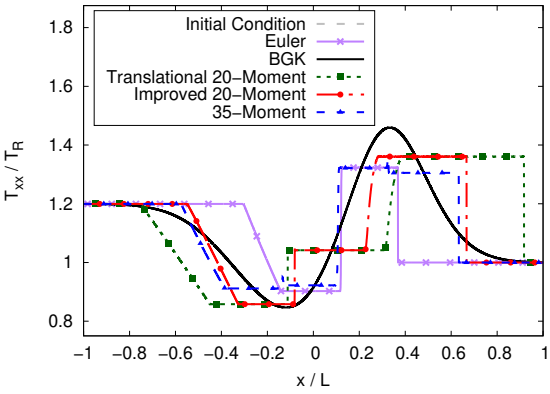

(c) Axial temperature profile

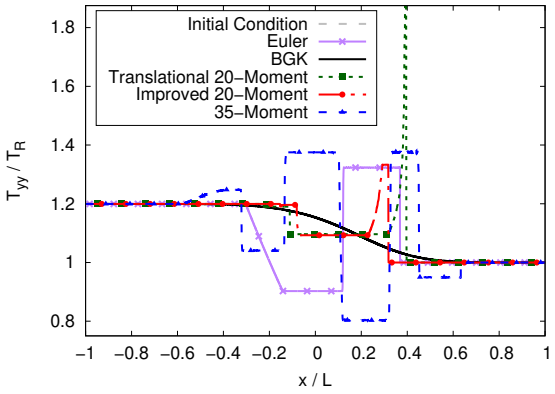

(d) Transverse temperature profile

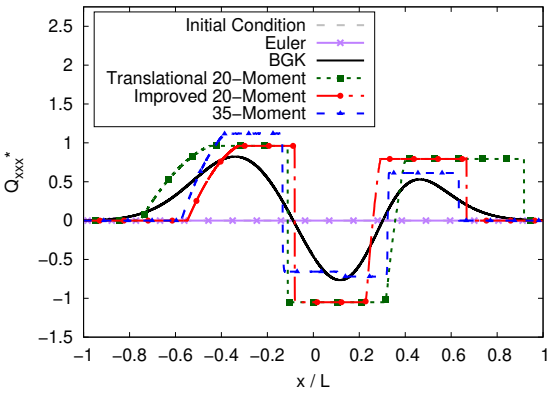

(e) Axial heat flux profile

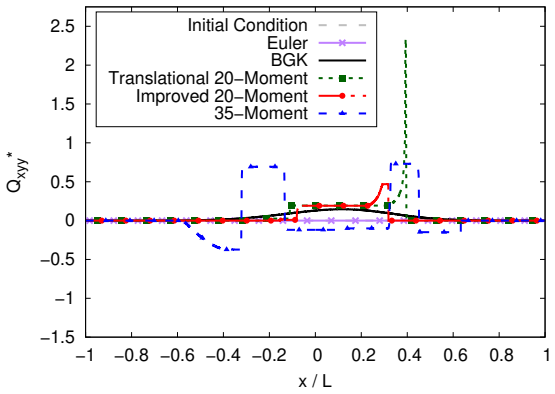

(f) Transverse heat flux profile

Figure 4.3: free-molecular regime Riemann problem solutions for the new models, compared against BGK solutions

according to the wave dispersion shown in Figures 3.5, 3.6 and A.2. In this case, the four waves that can be seen correspond to the 4×4 subsystem which were initially prescribed for the 20-moment model, and the five waves of the 35-moment model come from the 5×5 subsystem. These waves also correspond to the free-molecular, high-wave-number dispersion patterns on the far right-hand side of Figures 3.5, 3.6 and A.2.

Both the transition and free-molecular regimes show temperature anisotropy, or the decoupling of temperature based on the directions in which the particles are being excited. This can be seen in Figures 4.2c, 4.2d, 4.3c and 4.3d, as well as heat flux anisotropy in Figures 4.2e, 4.2f, 4.3e and 4.3f. This effect does not exist in the equilibrium regime, but is highly relevant for non-equilibrium flows, where it is known to appear. The importance of this effect is even more evident in Chapter 6, where practical non-equilibrium flows are investigated.

A final point of interest in Figures 4.3d and 4.3f is the formation of what appears to be a delta shock on the right most wave of the first 20-moment closure. This is smoothed out in the improved 20-moment closure, but its cause or physical relevance are unknown at this time.

4.3 Discontinuous Bubble Problems in Two Spatial Dimensions

While the Riemann problems discussed in Section 4.2 give a sense of the wave-structure of the models for a three-dimensional gas, they are restricted to one-dimensional physical space. How the models vary rotationally is also highly relevant. To evaluate the new models in this regard, a discontinuous bubble problem in the same style as a Riemann problem was studied. Once again, two states of the gas were considered, with

$$\frac{\rho_1}{\rho_2} = \frac{p_1}{p_2} = 2.0\,, \tag{4.2}$$

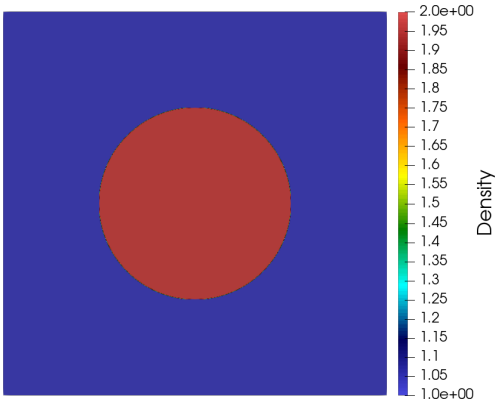

Figure 4.4: Discontinuous bubble initial condition.

where ρ_1 and p_1 are the density and pressure inside the bubble, and ρ_2 and p_2 are the state outside the bubble. The full domain was made to be $-L < x < L$ and $-L < y < L$ on a Cartesian mesh, with a bubble radius of $r = 0.5L$ centred on the origin. The initial condition is shown in Figure 4.4, and again the final time of the solutions was chosen to be $t_{\text{final}} = 0.5 \times 10^{-3} L\sqrt{\rho_1/p_1}$, so that the waves did not reach the boundary of the domain. The continuum results are at a Knudsen number of around $\text{Kn} = 2.3 \times 10^{-5}$, while the transition results are at a Knudsen number of around $\text{Kn} = 2.3 \times 10^{-2}$. As with the previous section, the free-molecular results have no collisions, corresponding to an infinite Knudsen number.

Results for the two 20-moment closure are shown for the continuum, transition, and free-molecular regimes, all at a 2048×2048 spatial resolution. Extracted line plots of each solution are also provided at 15° intervals from 0° to 90° to better demonstrate the angular properties of each model. Plots for the continuum regime density and radial heat flux solutions with a collision relaxation time of $\tau = 3.5 \times 10^{-10} L\sqrt{\rho_1/p_1}$ are shown from Figures 4.6 to 4.11. Plots for the transition regime density and radial heat flux solutions with a collision relaxation time of $\tau = 1.7 \times 10^{-5} L\sqrt{\rho_1/p_1}$ are shown from Figures 4.13 to 4.18. Finally, plots for the free-molecular regime density and radial heat flux solutions with a collision relaxation time of $\tau = 3.5 \times 10^{4} L\sqrt{\rho_1/p_1}$ are shown from Figures 4.20 to 4.25.

Reference solutions are shown in Figures 4.5, 4.12, and 4.19, with their density contours and the highest relevant moment of comparison for the reference model (e.g. temper-

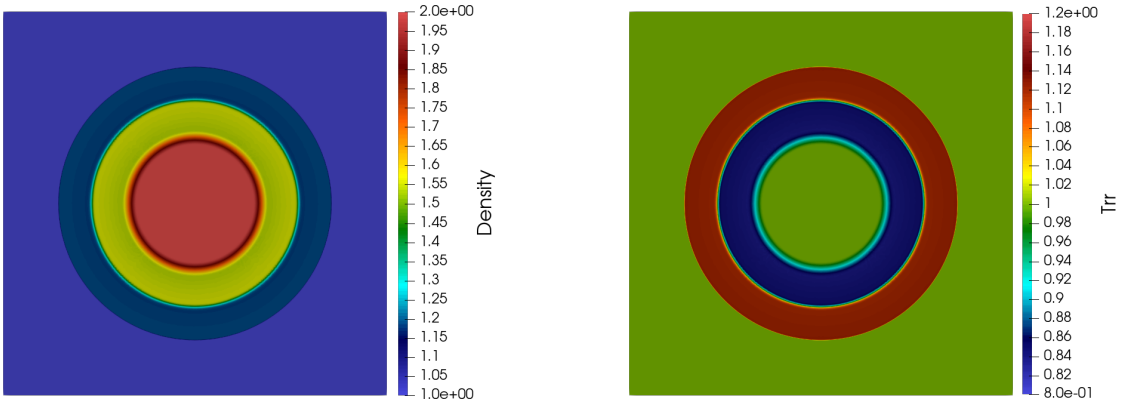

(a) Density contour plot (b) Temperature contour plot

Figure 4.5: Reference solution in the continuum regime, solved using Euler

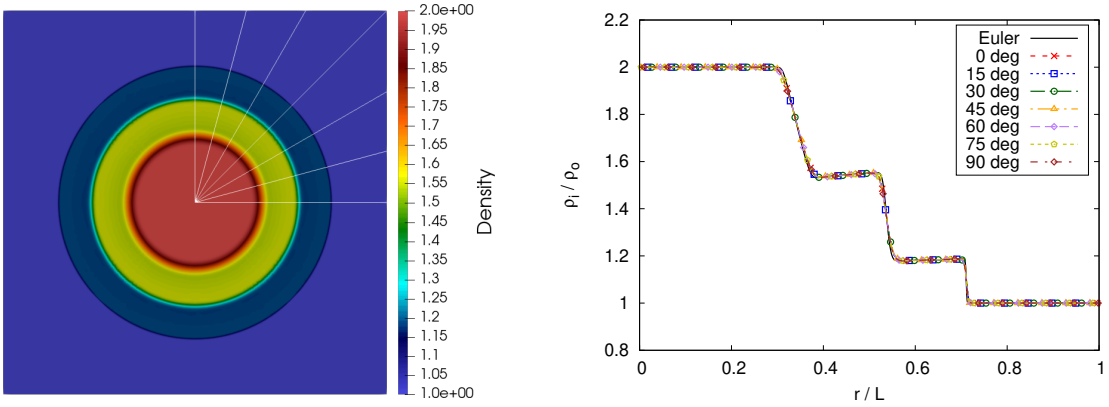

(a) Density contour plot (b) Density profiles in 15° intervals

Figure 4.6: Translationally invariant only 20-moment closure density profile solution in the continuum regime

ature for the Euler continuum regime prediction, and heat flux for the BGK transition and free-molecular regime predictions). The Euler solution is computed at the same 2048×2048 spatial resolution as the 20-moment solutions. The BGK solutions, due to the increased computational cost, have lower resolutions. The reference solutions for both the free-molecular and transition regime cases are at a 1024×1024 spatial resolution, and a $100 \times 100 \times 64$ velocity resolution, with the range $-7\sqrt{p_1/\rho_1} < v_i < 7\sqrt{p_1/\rho_1}$ for each direction. Due to the computational cost, any additional resolution would have insufficient memory available for the computation. However, there does exist an exact solution to the free-molecular problem, developed and shown in Appendix B. The exact free-molecular solution is recovered very well by the BGK solver, as is the continuum regime, so it can be assumed the transition-regime result is trustworthy as well.

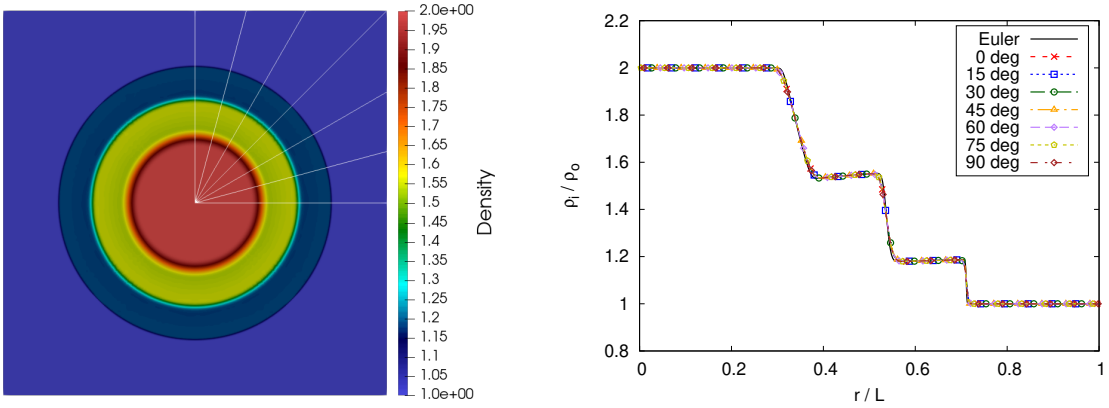

(a) Density contour plot

(b) Density profiles in 15° intervals

Figure 4.7: Improved 20-moment closure density profile solution in the continuum regime

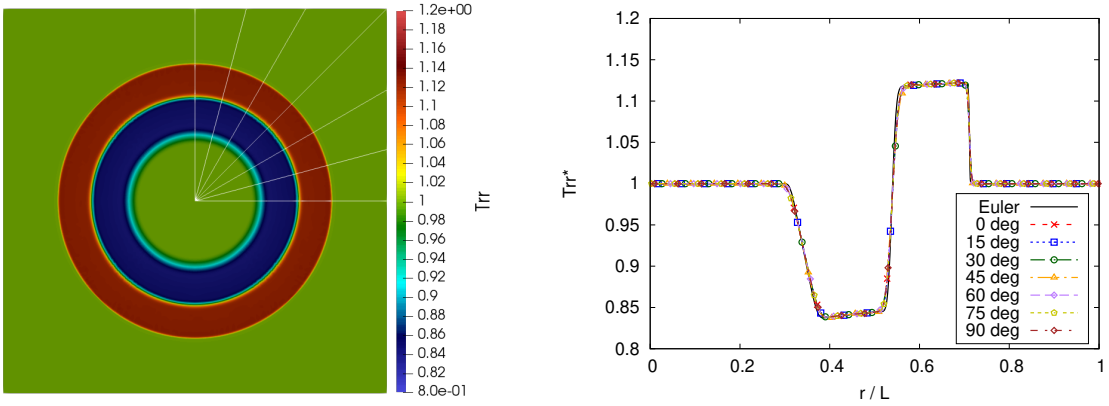

(a) Radial temperature contour plot

(b) Temperature profiles in 15° intervals

Figure 4.8: Translationally invariant only 20-moment closure temperature profile solution in the continuum regime

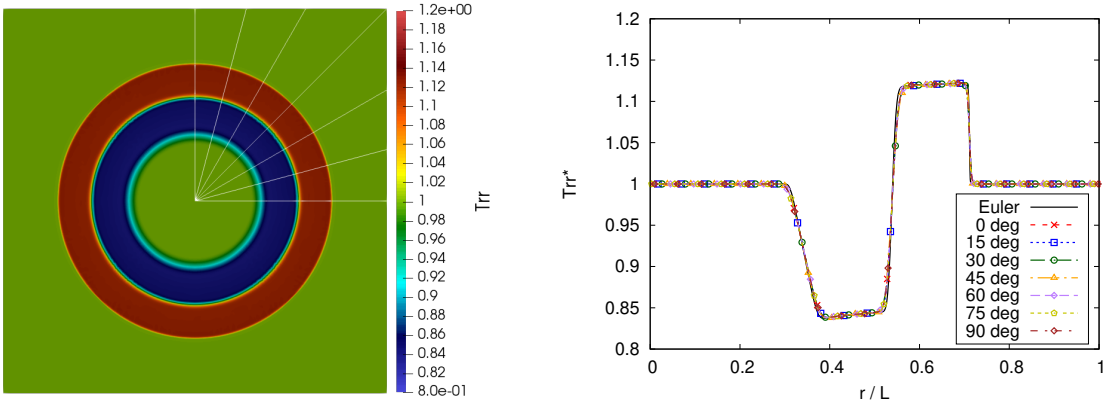

(a) Radial heat flux contour plot

(b) Temperature profiles in 15° intervals

Figure 4.9: Improved 20-moment closure temperature profile solution in the continuum regime

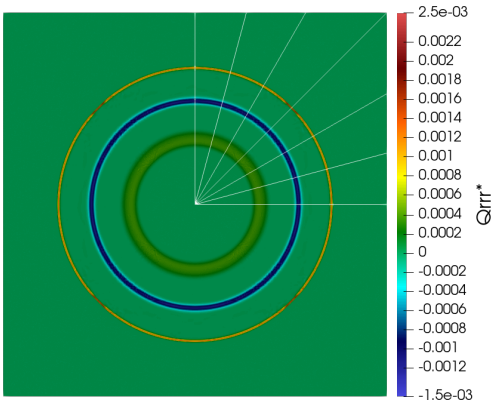

(a) Radial heat flux contour plot

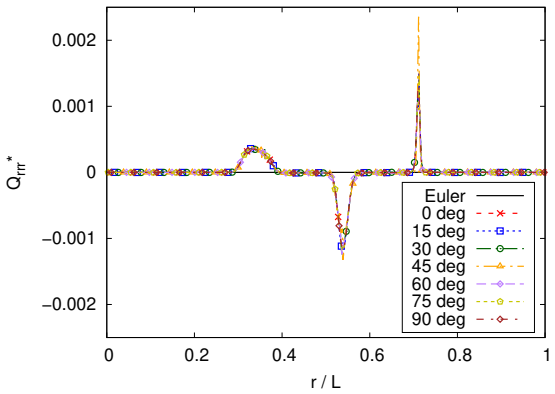

(b) Heat flux profiles in 15° intervals

Figure 4.10: Translationally invariant only 20-moment closure heat flux profile solution in the continuum regime

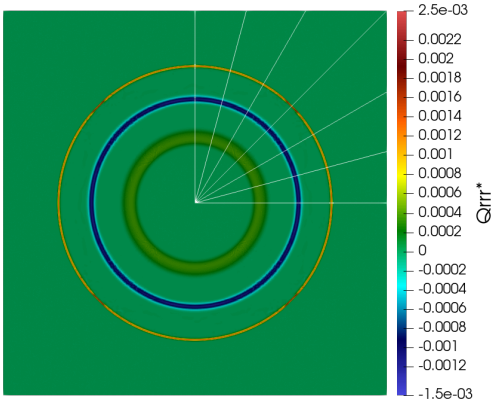

(a) Radial heat flux contour plot

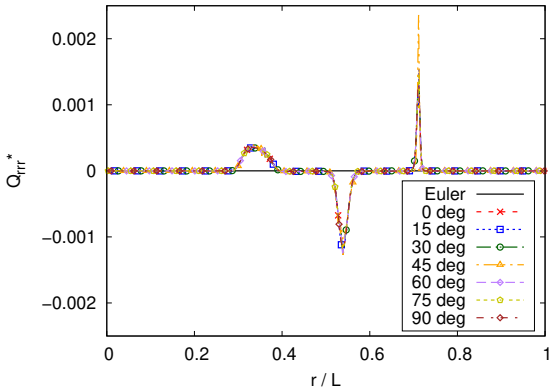

(b) Heat flux profiles in 15° intervals

Figure 4.11: Improved 20-moment closure heat flux profile solution in the continuum regime

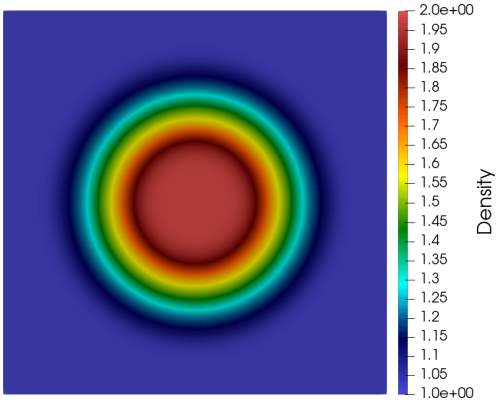

(a) Density contour plot

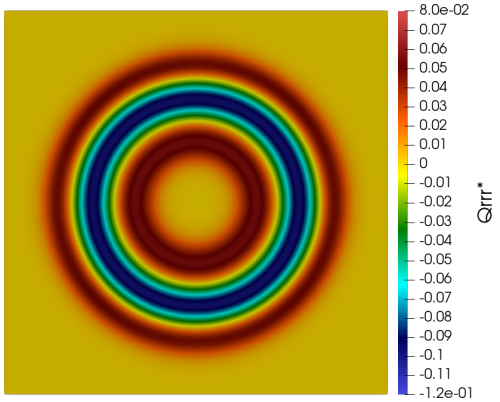

(b) Heat flux contour plot

Figure 4.12: Reference solution in the transition regime, solved using directly discretized kinetic equations

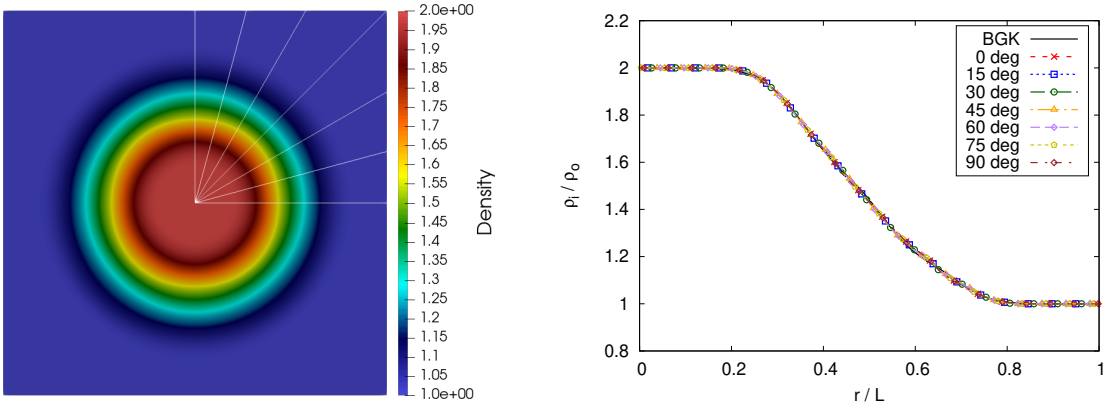

(a) Density contour plot (b) Density profiles in 15° intervals

Figure 4.13: Translationally invariant only 20-moment closure density profile solution in the transition regime

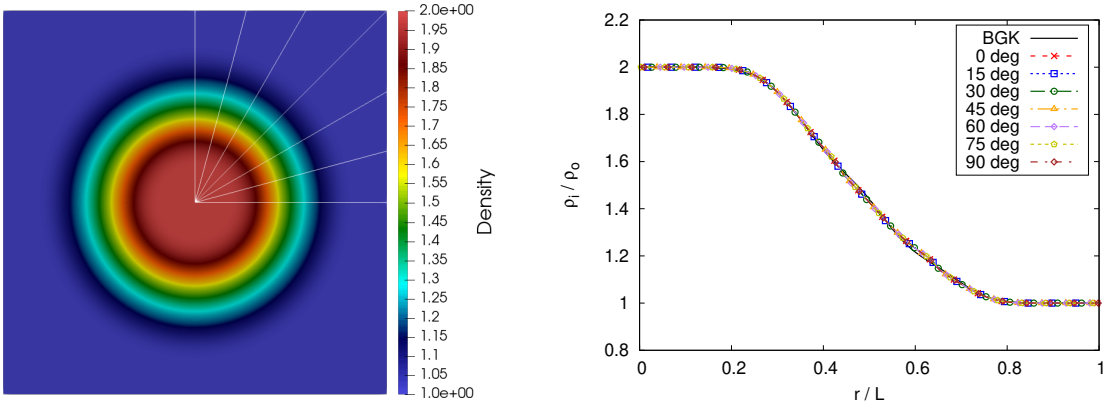

(a) Density contour plot (b) Density profiles in 15° intervals

Figure 4.14: Improved 20-moment closure density profile solution in the transition regime

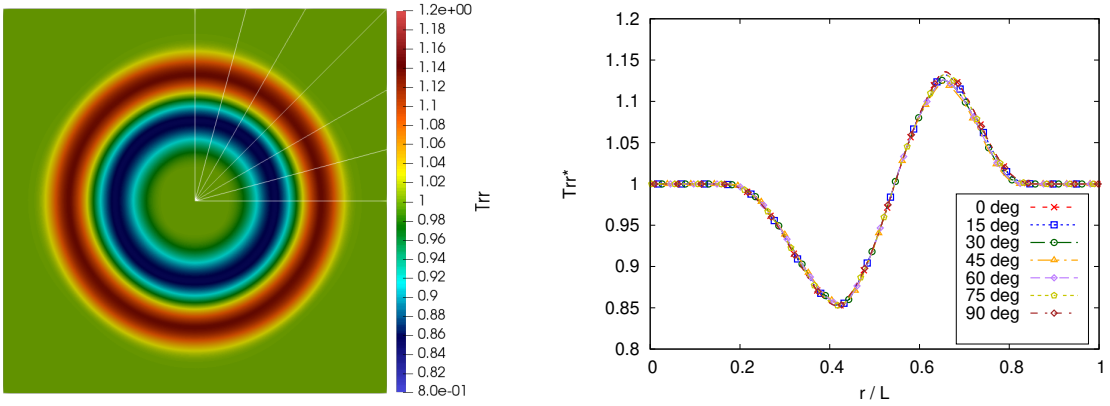

(a) Radial temperature contour plot (b) Temperature profiles in 15° intervals

Figure 4.15: Translationally invariant only 20-moment closure temperature profile solution in the transition regime

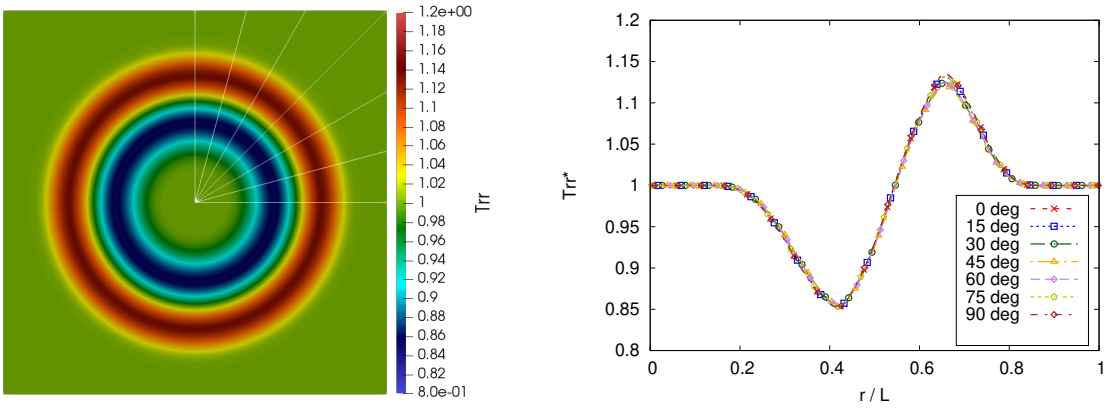

(a) Radial heat flux contour plot (b) Temperature profiles in 15° intervals

Figure 4.16: Improved 20-moment closure temperature profile solution in the transition regime

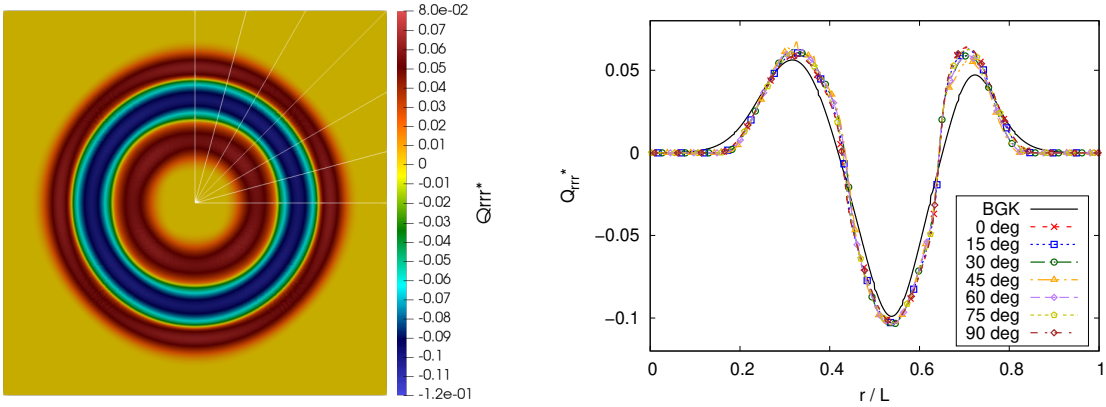

(a) Radial heat flux contour plot (b) Heat flux profiles in 15° intervals

Figure 4.17: Translationally invariant only 20-moment closure heat flux profile solution in the transition regime

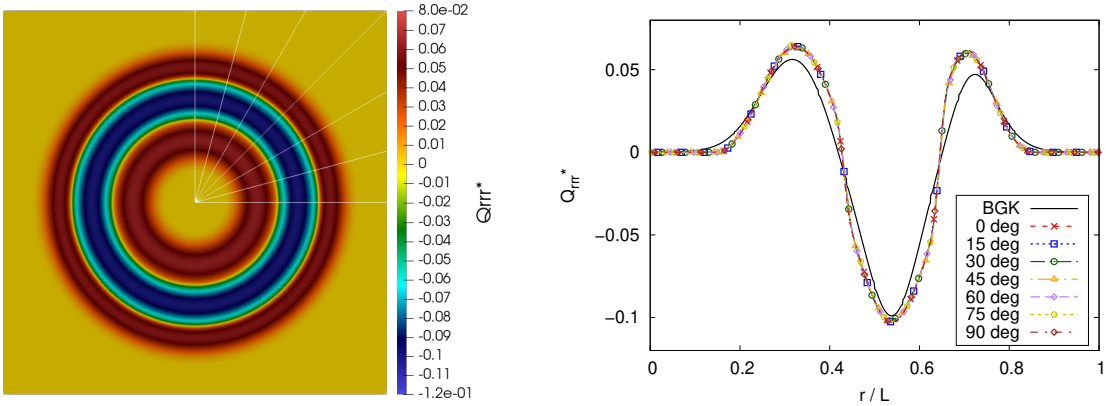

(a) Radial heat flux contour plot (b) Heat flux profiles in 15° intervals

Figure 4.18: Improved 20-moment closure heat flux profile solution in the transition regime

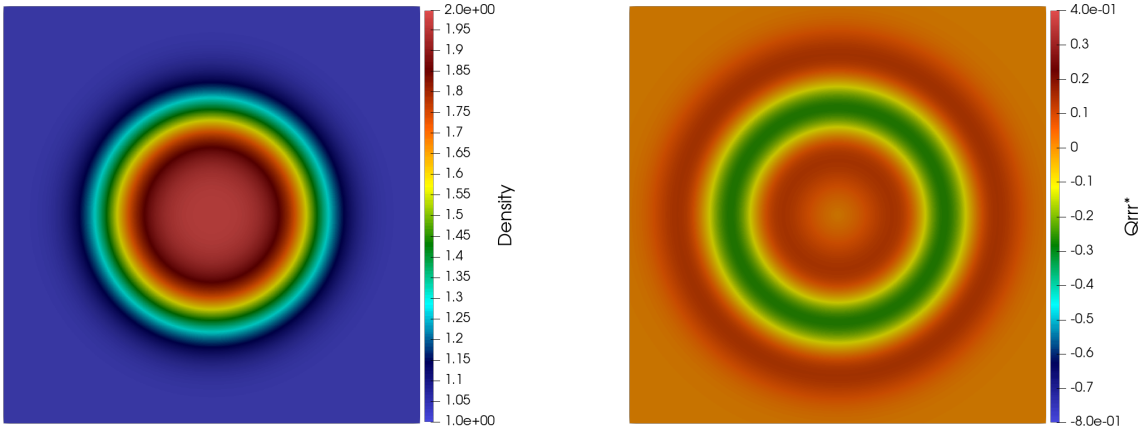

(a) Density contour plot (b) Radial heat flux contour plot

Figure 4.19: Reference solution for density in the free-molecular regime, solved using directly discretized kinetic equations

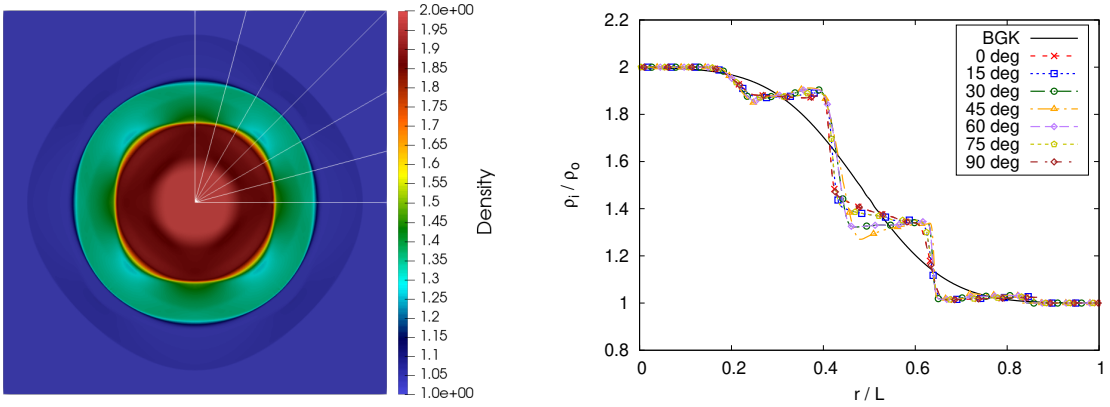

(a) Density contour plot (b) Density profiles in 15° intervals

Figure 4.20: Translationally invariant only 20-moment closure heat flux profile solution in the free-molecular regime

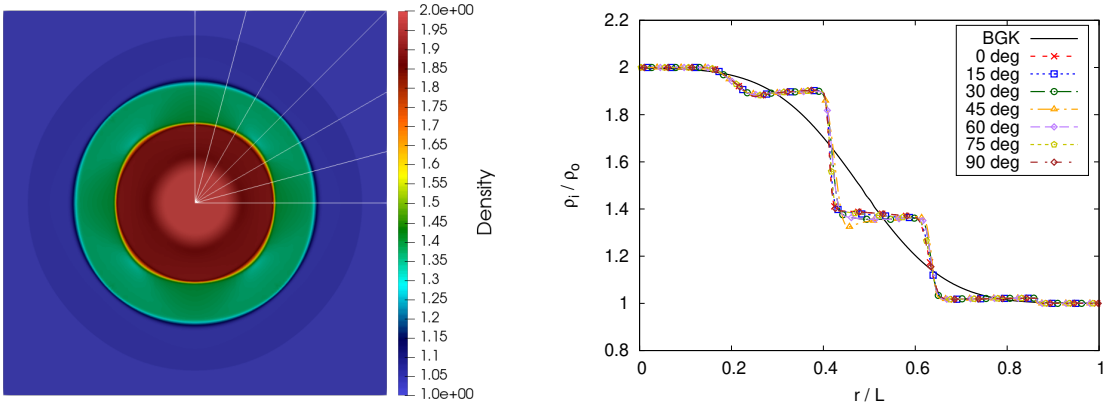

(a) Density contour plot (b) Density profiles in 15° intervals

Figure 4.21: Improved 20-moment closure heat flux profile solution in the free-molecular regime

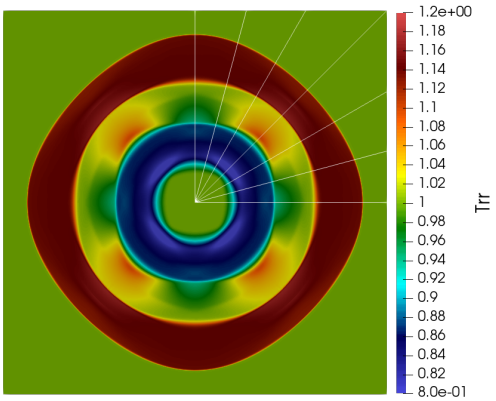

(a) Radial temperature contour plot

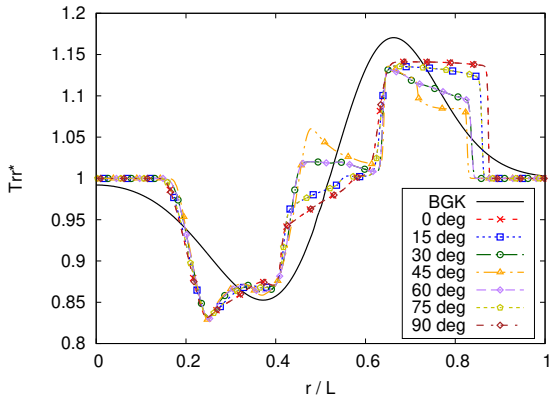

(b) Temperature profiles in 15° intervals

Figure 4.22: Translationally invariant only 20-moment closure temperature profile solution in the free-molecular regime

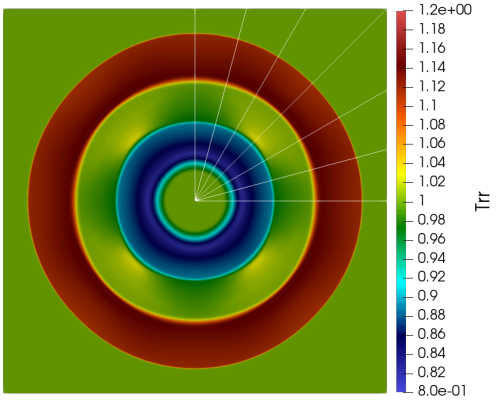

(a) Radial heat flux contour plot

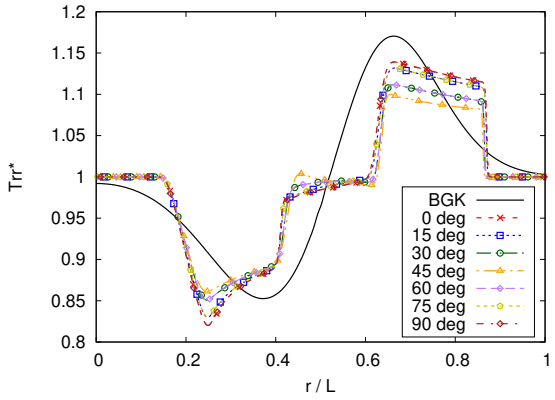

(b) Temperature profiles in 15° intervals

Figure 4.23: Improved 20-moment closure temperature profile solution in the free-molecular regime

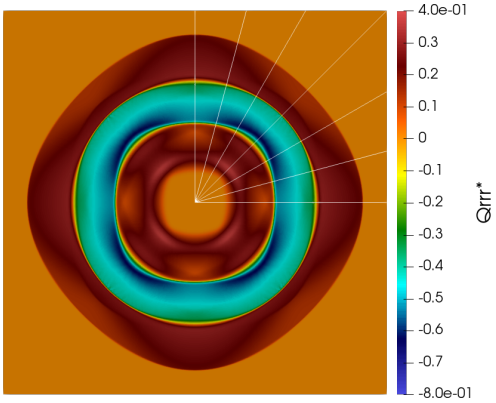

(a) Radial heat flux contour plot

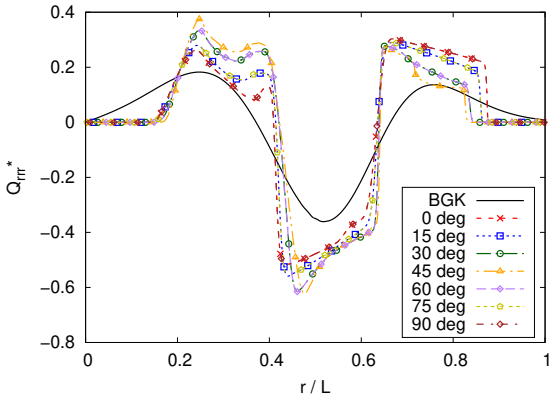

(b) Heat flux profiles in 15° intervals

Figure 4.24: Translationally invariant only 20-moment closure heat flux profile solution in the free-molecular regime

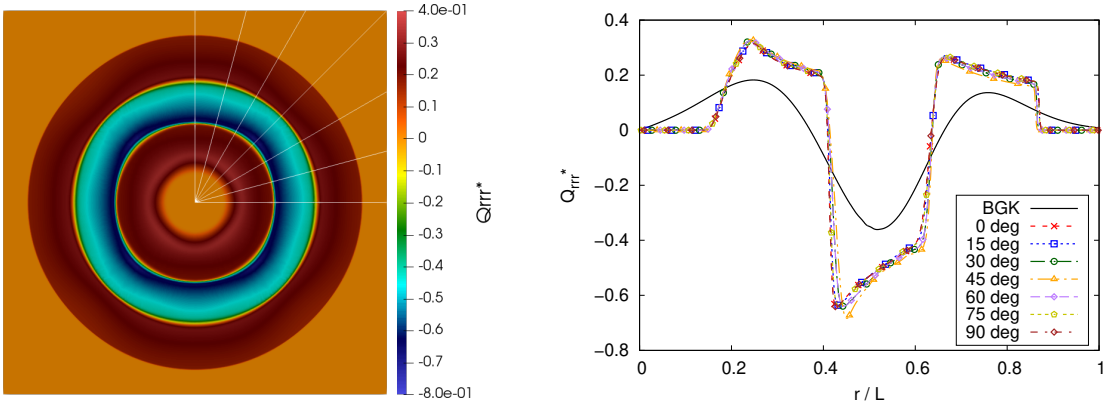

(a) Radial heat flux contour plot

(b) Heat flux profiles in 15° intervals

Figure 4.25: Improved 20-moment closure heat flux profile solution in the free-molecular regime

The results, particularly in the continuum and transition regimes, show very good agreement with their reference solutions. Figures 4.6 to 4.11 show that both models have near perfect agreement with their Euler solution counterparts in their density and temperature predictions. The only visible non-equilibrium in these results are the small perturbations in heat flux, shown in Figures 4.10 and 4.11. Figures 4.8 and 4.9 show that, much like the continuum results in Section 4.2, these are the regions in which the gas is heating or cooling across the resulting expansion fan, contact, and shock surfaces of the Riemann problem. This gives good confidence that the model will accurately capture near-equilibrium physics accurately.

More importantly, the transition regime is also captured accurately as Figures 4.13 to 4.18 still show good agreement with the BGK predictions. The changes from the state of the gas outside to the inside of the bubble in the transition regime are no longer the discrete elementary waves seen in the continuum regime. Instead, they are continuously differentiable regions. Figures 4.15 and 4.16 show the temperature of the gas inside the bubble decreases to a cooler state than it has initially, before heating up past the initial temperature, and finally returning to the outside temperature. The heat flux profiles, shown in Figures 4.17 and 4.18 reflect these changes. The two regions of cooling are about half the strength of the region of warming, and only small differences at the inflection points are noticeable between the BGK and 20-moment solutions. For practical multidimensional flow calculations in the transition regime, these are perfectly acceptable

differences given the reduction in computational cost.

The free-molecular regime highlights the rotational differences between the two models. While not the regime in which moment methods are expected to be useful, as particle-based methods are computationally affordable here, they highlight the wave propagation of the PDEs as discussed in Section 4.2. While collisions allow for energy modes to be transferred between the different directions, this regime allows for pure decoupling of the subsystems. Comparing Figures 4.20 to 4.25, it is obvious that the method is not perfectly rotationally invariant in this regime, with both variants of the 20-moment closure having asymmetric solutions when comparing their 0° and 90° direction solutions to the 45° one. However, the improved 20-moment closure is substantially more coherent than the translational only closure. It only has notable differences along the 45° line for the density and heat flux profiles as can be seen in Figures 4.21 and 4.25, when compared to the translationally invariant only closure shown in Figures 4.20 and 4.24. Temperature suffers a bit more, with the improved solution in Figure 4.23 having variation across the outermost wave, but is still more spatially coherent than the solution in Figure 4.22. While the improved closure is not perfectly rotationally invariant, it definitely has better properties than the translationally invariant only model.

Further, the issue of rotational dependence in the free-molecular regime is not completely devastating. As seen in Figures 4.6 to 4.18, almost any amount of collisions makes the solutions much more symmetric, as energy can be quickly dissipated between the different directions. Further, other non-equilibrium moment models, like the currently available methods for the QMOM hierarchy, are not fully rotationally invariant [21, 34]. With the continuum and transition regimes being the primary target of moment methods, and the new method being the first robustly hyperbolic method for multidimensional flows, the impact of the free-molecular limit not being perfectly rotationally invariant is minor.

Chapter 5

Solid-Wall Boundary Conditions

In standard kinetic theory, solid walls are often modelled with the Knudsen-layer approximation [15, 43]. Figure 5.1 shows the typical model of the Knudsen layer, and the two possibilities for particle interactions with the wall. Particles are assumed to either immediately be specularly reflected, bouncing off the wall after a single collision, or diffusely reflected after having multiple collisions with the wall and coming in to equilibrium with it. Incoming particles are therefore modelled as having the statistics of the gas, and outgoing particles are either specularly reflected with those statistics, or diffusely reflected with the statistics of the wall. The particle paths are shown where v_i is the incoming particle path, v_o is the outgoing specularly reflected particle path, and the dashed lines all represent v_d, which are the outgoing diffusely reflected particle paths.

This work considers two treatments of the Knudsen Layer. The first is the traditional direct integration of the boundary fluxes, demonstrated in Section 5.1. Then, due to the inability of the new models to follow this formulation, a new way of modelling the Knudsen layer is proposed in Section 5.2. Comparison between the two methods is presented in Section 5.3, followed by some canonical boundary value flow problems for both the 10-moment and 20-moment models using the new formulation are shown in Section 5.4. Finally, a discussion of how this treatment can be extended to include additional heat-transfer effects in to the wall concludes the chapter in Section 5.5.

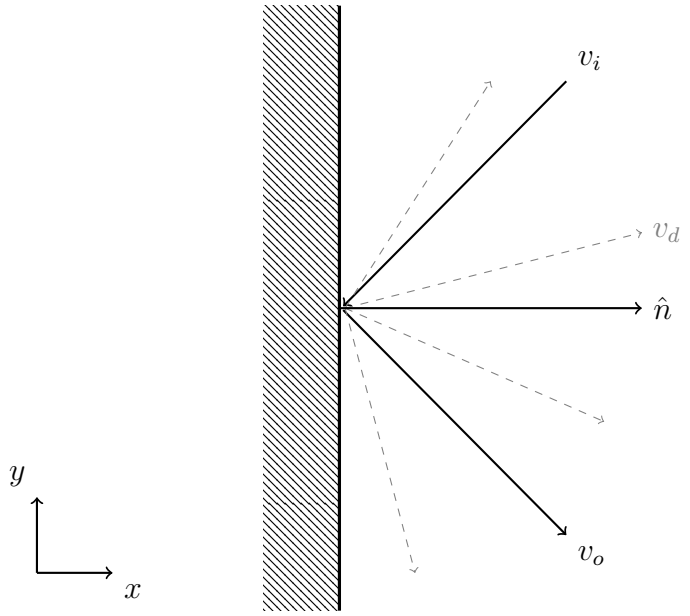

Figure 5.1: Illustration of solid wall and gas particle interactions

5.1 Traditional Treatment of the Knudsen Layer

In order to begin the treatment of the Knudsen layer, one has to define how much of the gas is being specularly or diffusely reflected. This is determined with an accommodation coefficient, χ, with $\chi = 0$ representing complete specular reflection, and $\chi = 1$ representing complete diffuse reflection. The distribution functions within the Knudsen layer for a wall normal to the x-direction is then given by

$$\overline{\mathcal{F}}(x_i, v_i, t) = \begin{cases} \mathcal{F}(x_i, v_i, t) & \text{if } v_x < 0 \\ \chi \mathcal{M}_w(x_i, v_i, t) + (1-\chi)\mathcal{F}(x_i, -v_x, v_y, v_z, t) & \text{if } v_x \geq 0 \end{cases}, \tag{5.1}$$

with the distribution of the incoming gas particles represented by $\mathcal{F}(x_i, v_i, t)$, and the Maxwellian, $\mathcal{M}_w(x_i, v_i, t)$, representing the particles emitted by the wall at the velocity, u_{w_i}, (with $u_{w_x} = 0$ assuming the frame of reference is that of the direction normal to the wall) and temperature density, Θ_w. The temperature density is related to the typical thermodynamic temperature in Kelvin, T_w, through the relationship $\Theta_w = R_s T_w$, where R_s is the specific gas constant. The emitted distribution can then be written as

$$\mathcal{M}_w(x_i, v_i, t) = \frac{\rho_w}{m}\left(\frac{1}{2\pi\Theta_w}\right)^{\frac{3}{2}} \exp\left(-\frac{1}{2\Theta_w}(v_i - u_{w_i})(v_i - u_{w_i})\right), \tag{5.2}$$

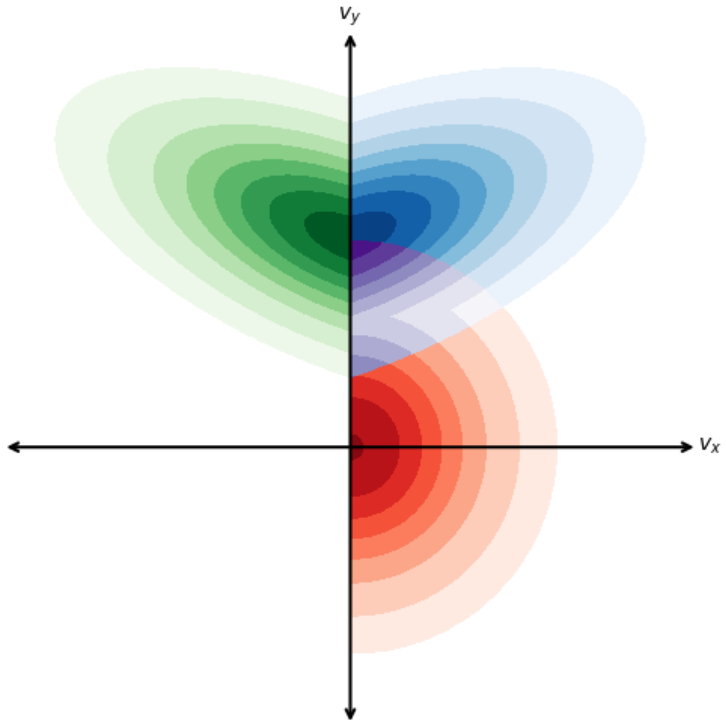

Figure 5.2: Example of the assumed distribution of the Knudsen layer for the 10-moment model

where the phase density, ρ_w, at the wall is unknown. It can be determined by the no-penetration condition, or that the flux of all incoming particles must be balanced by all outgoing particles. This leads to

$$0 = \int_{-\infty}^{\infty}\int_{-\infty}^{\infty}\int_{-\infty}^{0} mv_x\mathcal{F}(x_i, v_i, t)\partial v_x\partial v_y\partial v_z + \int_{-\infty}^{\infty}\int_{-\infty}^{\infty}\int_{0}^{\infty} mv_x\mathcal{M}_w(x_i, v_i, t)\partial v_x\partial v_y\partial v_z \,, \tag{5.3}$$

needing to be solved in order to fully define the Knudsen Layer. Traditionally, with a known distribution $\mathcal{F}$, the distribution in Equation (5.1) can then be integrated with the necessary velocity weights in order to produce boundary conditions.

As an illustrative example, the Knudsen layer for the 10-moment equations can be obtained by integration of Equation (5.1) by assuming $\mathcal{F}(x_i, v_i, t) = \mathcal{G}(x_i, v_i, t)$ in the form shown in Equation (2.46). A representation of the resulting distribution function is shown in Figure 5.2, where the incoming distribution of gas particles is shown in green, the specularly reflected distribution of gas particles are shown in blue, and the distribution of particles which have come in to equilibrium with the wall is shown in red. As both

the Maxwellian and Gaussian distributions are integrable in closed form, so too are their half-space integrals. For example, solving Equation (5.3) for the density of the particles which have been fully accommodated by the wall yields

$$\rho_w = \rho u_x \sqrt{\frac{\pi}{2\Theta_w}} \left[\operatorname{erf}\left(\sqrt{\frac{\rho}{2P_{xx}}} u_x \right) + 1 \right] + \sqrt{\frac{\rho P_{xx}}{\Theta_w}} \exp\left(-\frac{\rho u_x^2}{2P_{xx}} \right) , \tag{5.4}$$

for an arbitrary Gaussian and a stationary wall at temperature Θ_w. The expressions for the higher-order moments of $\overline{\mathcal{F}}(x_i, v_i, t)$ are increasingly expansive, but they can just as easily be computed by integration of Equation 5.1 with the relevant velocity weights.

5.2 Approximation of Knudsen Layer Fluxes

It is obvious why the standard procedure described in Section 5.1 is inappropriate for the models developed in Chapter 3. By bypassing an integrable distribution function in favour of directly constructing the flux Jacobian, there is no appropriate representation of the traditional half-space integration. Instead, a new more general procedure for the construction of the boundary fluxes is required in order to represent the Knudsen Layer.

One natural way to evaluate split fluxes like the ones in the Knudsen Layer is inspired by the Steger-Warming flux function [44, 45]. This general flux function uses the Eigen-decomposition of the flux Jacobian, which is suitable for the kinds of models developed in this work as they are guaranteed to have real-valued Eigenvalues. Steger and Warming propose that in order to evaluate the flux across a boundary,

$$\boldsymbol{F} \approx \frac{\mathrm{d}\boldsymbol{F}_{\mathrm{L}}}{\mathrm{d}\boldsymbol{U}}^{+} \boldsymbol{U}_L + \frac{\mathrm{d}\boldsymbol{F}_{\mathrm{R}}}{\mathrm{d}\boldsymbol{U}}^{-} \boldsymbol{U}_R \,, \tag{5.5}$$

where $\frac{\mathrm{d}\boldsymbol{F}_{\mathrm{L}}}{\mathrm{d}\boldsymbol{U}}^{+}$ is the Jacobian of the positive valued waves evaluated with the state of the gas on the left side of the boundary, $\boldsymbol{U}_L$, and $\frac{\mathrm{d}\boldsymbol{F}_{\mathrm{R}}}{\mathrm{d}\boldsymbol{U}}^{-}$ is the Jacobian of the negative valued waves evaluated with the state of the gas on the right side of the boundary, $\boldsymbol{U}_R$. After constructing each flux Jacobian from the two states, the matrix of Eigenvalues, $\boldsymbol{\Lambda}$, is

modified by

$$\boldsymbol{\Lambda}_{ij}^{+} = \max\left(0, \boldsymbol{\Lambda}_{ij}\right) , \quad \text{and} \quad \boldsymbol{\Lambda}_{ij}^{-} = \min\left(0, \boldsymbol{\Lambda}_{ij}\right) , \tag{5.6}$$

and the Jacobians are then constructed by

$$\frac{\mathrm{d}\boldsymbol{F}^{+}}{\mathrm{d}\boldsymbol{U}} = \boldsymbol{R}\boldsymbol{\Lambda}^{+}\boldsymbol{R}^{-1} , \quad \text{and} \quad \frac{\mathrm{d}\boldsymbol{F}^{-}}{\mathrm{d}\boldsymbol{U}} = \boldsymbol{R}\boldsymbol{\Lambda}^{-}\boldsymbol{R}^{-1} . \tag{5.7}$$

The result is that the only information being emitted from left to right is the positive valued waves of the left state, and vice versa for the right state. As the models developed in this work are heavily inspired by the QMOM hierarchy discussed in Section 2.5.1, this flux splitting procedure is effectively equivalent to truncating quadrature nodes which are on the inappropriate side for the effects of the gas or the wall.

This flux function it well studied in rarefied gas dynamics [45–48], due to being positivity preserving and naturally representing signal propagation across cell boundaries inside CFD schemes. However, it does not seem to have been used to represent the Knudsen layer in the literature. This work proposes an extension to this flux function which represents the same situation as described in Section 5.1, without having to evaluate any integrals.

The flux as a result of the Knudsen layer distribution is proposed to approximately be

$$\boldsymbol{F} \approx \frac{\mathrm{d}\boldsymbol{F}_{\mathrm{g}}{}^{-}}{\mathrm{d}\boldsymbol{U}}\boldsymbol{U}_g + \chi\frac{\mathrm{d}\boldsymbol{F}_{\mathrm{w}}{}^{+}}{\mathrm{d}\boldsymbol{U}}\boldsymbol{U}_w + (1-\chi)\frac{\mathrm{d}\boldsymbol{F}_{\mathrm{s}}{}^{+}}{\mathrm{d}\boldsymbol{U}}\boldsymbol{U}_s , \tag{5.8}$$

where $\boldsymbol{U}_g$ is the state of the incoming gas, $\boldsymbol{U}_s$ is the state of the specularly reflected gas, and $\boldsymbol{U}_w$ is the state of the gas in equilibrium with the wall. All of the Jacobians are evaluated at their corresponding state. For the models discussed in this work, the Jacobians are guaranteed to have real valued roots, and thus the procedure in Equation (5.6) can be followed for the appropriate sign of the emitted signals. In order to enforce the no-penetration condition, the fluxes for the incoming gas and a fully accommodated wall are computed such that

$$\boldsymbol{F}_g = \frac{\mathrm{d}\boldsymbol{F}_{\mathrm{g}}{}^{-}}{\mathrm{d}\boldsymbol{U}}\boldsymbol{U}_g , \quad \text{and} \quad \widehat{\boldsymbol{F}_w} = \frac{\mathrm{d}\boldsymbol{F}_{\mathrm{w}}{}^{+}}{\mathrm{d}\boldsymbol{U}}\widehat{\boldsymbol{U}_w} , \tag{5.9}$$

where the wall state, $\widehat{\boldsymbol{U}_w}$, is initially assumed to have $\widehat{\rho_w} = 1$, as well as the temperature and velocity of the wall. This gives the flux $\widehat{\boldsymbol{F}_w}$ that only needs to be scaled by a final ρ_w to ensure no-penetration. The scaling can be found by ensuring that the sum of the first entries of each flux are zero, giving

$$\rho_w = -\frac{\boldsymbol{F}_g[0]}{\widehat{\boldsymbol{F}_w}[0]}\,, \tag{5.10}$$

which ensures that the resulting mass flux is guaranteed to be 0. The final flux from the gas in equilibrium with wall is then

$$\boldsymbol{F}_w = \rho_w \frac{\mathrm{d}\boldsymbol{F}_{\mathrm{w}}{}^{+}}{\mathrm{d}\boldsymbol{U}} \widehat{\boldsymbol{U}_w}\,. \tag{5.11}$$

This results in a decent approximation of the effect of the Knudsen layer on the gas for any hyperbolic moment closure, without having to rely on integrable distribution functions.

5.3 Comparison of Boundary Flux Construction

In order to compare whether the procedure outlined in Section 5.2 is an accurate reflection of the fluxes imposed by the Knudsen layer, simple construction of the resulting moments using the new technique are done. First, an arbitrary Gaussian distribution for the incoming gas and Maxwellian distribution for the wall, both of which can be directly integrated as described in Section 5.1, are compared against the Steger-Warming approximation for both the 10-moment and 20-moment models. These are done over a range of bulk velocities normal to the wall, demonstrating how the approximation performs as different Eigenvalues are added or truncated to the construction of the Knudsen layer fluxes. Then, to investigate the effect of varying the wall temperature, the 20-moment model is compared against an integrable free molecular distribution function which results in heat transfer.

5.3.1 Gaussian Moment Investigation

The first study of the effectiveness of this style of moment construction chose to compare an arbitrary Gaussian. This allows for direct numerical integration of the exact fluxes normal to the wall, as well as construction via the Steger-Warming Knudsen-layer approximation for both the 10-moment and 20-moment models. The non-dimensional state of the gas that is used for demonstrative purposes is

$$\begin{aligned} &\rho = 1\,, && u_y = 1/2\,, && u_z = 0\,, \\ &P_{xx} = 2\,, && P_{xy} = -1/2\,, && P_{xz} = 0\,, \\ &P_{yy} = 1\,, && P_{yz} = 0\,, && P_{zz} = 5/4\,, \end{aligned} \tag{5.12}$$

and the wall being assumed to be stationary Maxwellian with $u_w = 0$, and $\Theta_w = 3/2$. It should be noted that this is a two-dimensional state for a three-dimensional gas, essentially with the x and y directions representing the normal and transverse directions to the wall, respectively. Due to this choice, any moments with odd powers of v_z can be omitted. The Knudsen-layer fluxes are plotted against a varying velocity normal to the wall, on the range $-5\sqrt{p/\rho} \leq u_x \leq 5\sqrt{p/\rho}$. This ensures that for both the 10-moment and 20-moment models, all Eigenvalues will either be activated or truncated across the entire range of velocities being studied. Three accommodation coefficients are used, with $\chi = 1$ representing full accommodation, $\chi = 0$ representing full specular reflection, and $\chi = 4/5$ representing a more realistic mixture of the two extremes. The fully accommodated fluxes are shown in Figure 5.3, the fully specular fluxes are shown in Figure 5.4, and the mixed fluxes are shown in Figure 5.5.

The specular case in Figure 5.4 is relatively simple, as only two fluxes, $\left\langle mv_x^2\overline{\mathcal{F}}\right\rangle$ and $\left\langle mv_x^2 v_y\overline{\mathcal{F}}\right\rangle$ have non-zero values, but both are accurately captured by both the 10-moment and 20-moment flux approximations. For the fully accommodated and mixed cases in Figures 5.3 and 5.5, all the fluxes shown have non-zero values across the range of velocities, and are very well approximated by the Steger-Warming Knudsen-layer treatment. In fact, as can be seen in the $\left\langle mv_x v_y^2\overline{\mathcal{F}}\right\rangle$ plots in these cases, the 20-moment's approximated fluxes

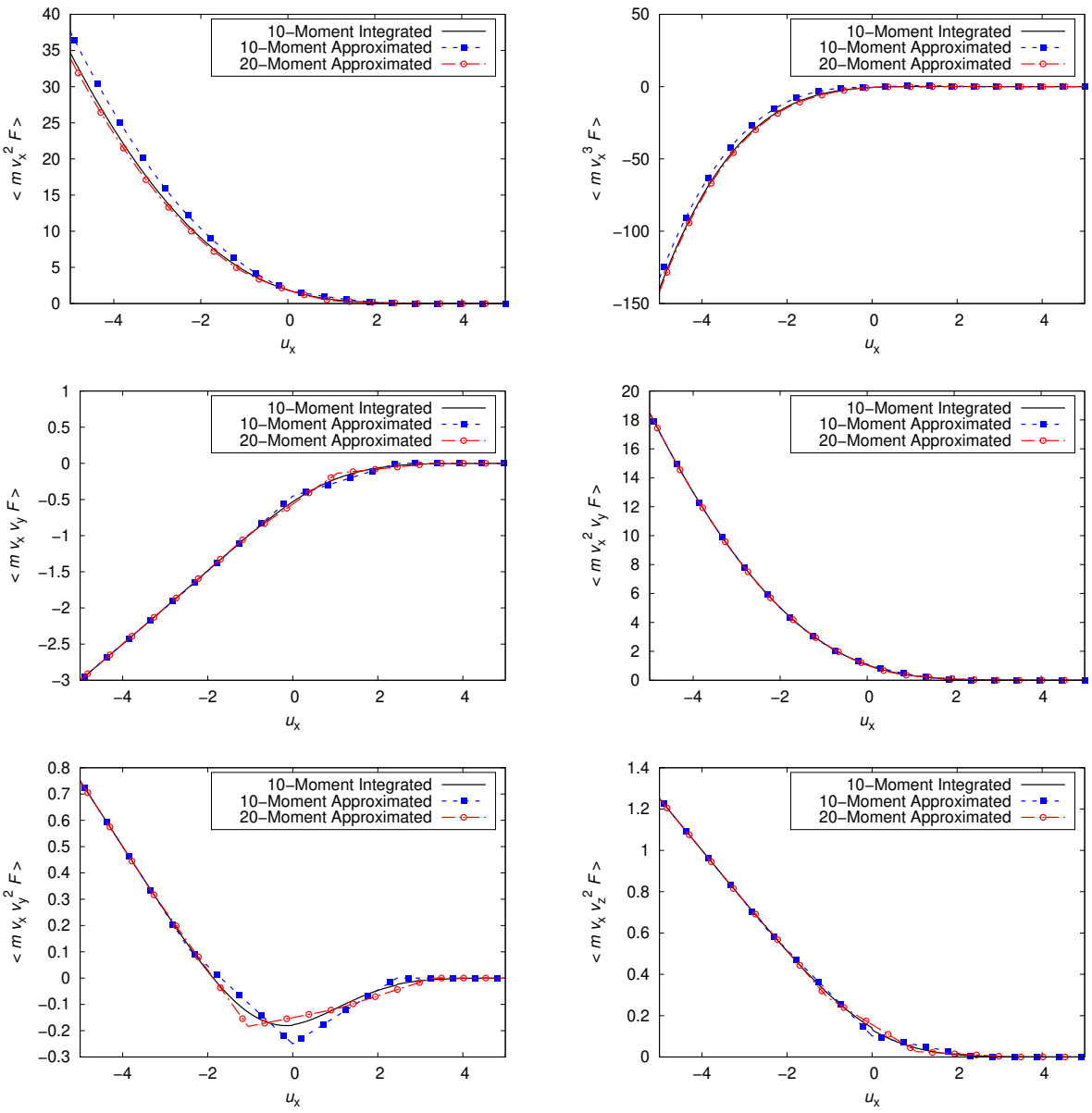

Figure 5.3: Knudsen-layer fluxes for the fully accommodated flux integrals of the 10-moment and 20-moment equations

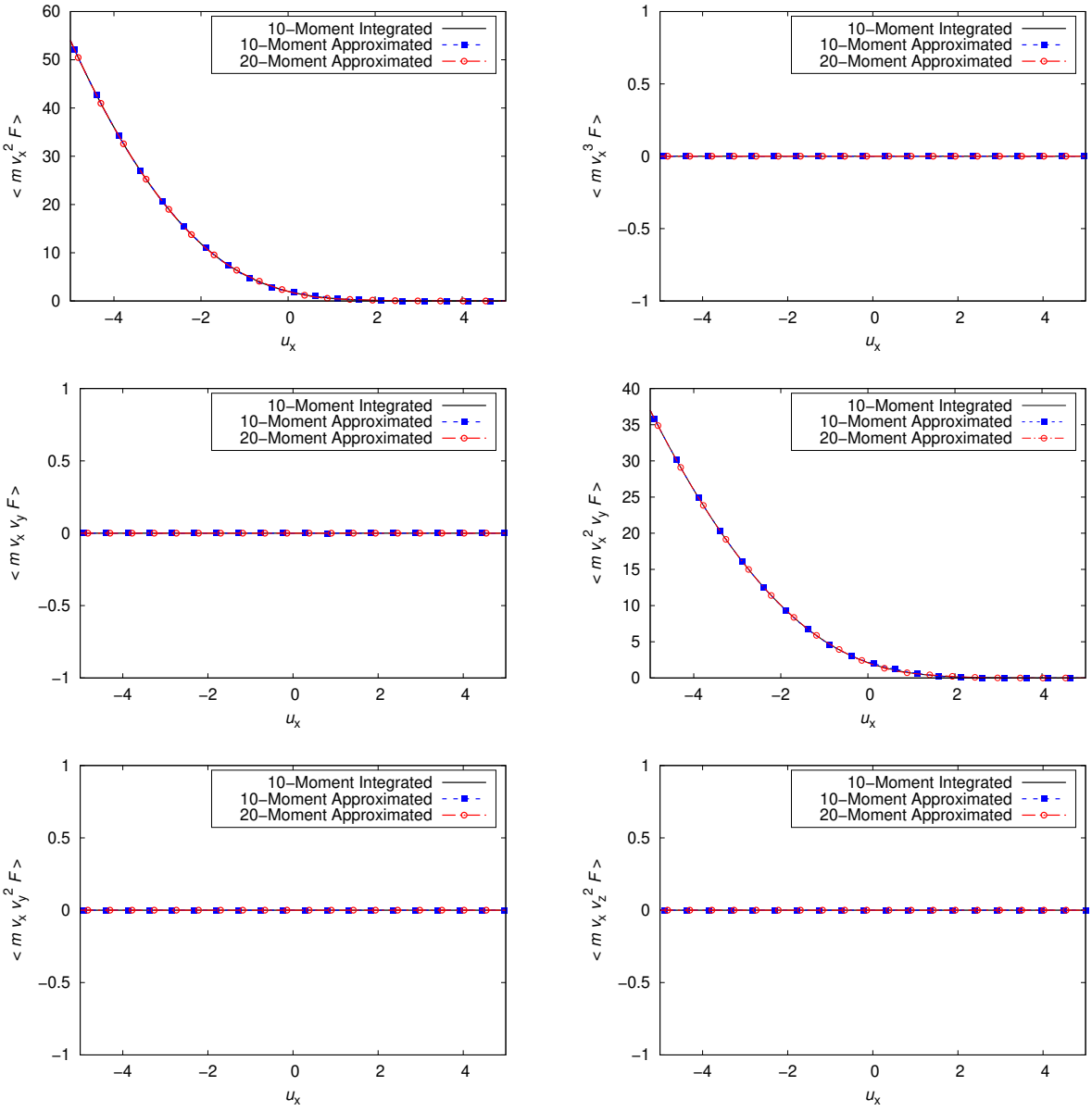

Figure 5.4: Knudsen-layer fluxes for the fully specular flux integrals of the 10-moment and 20-moment equations

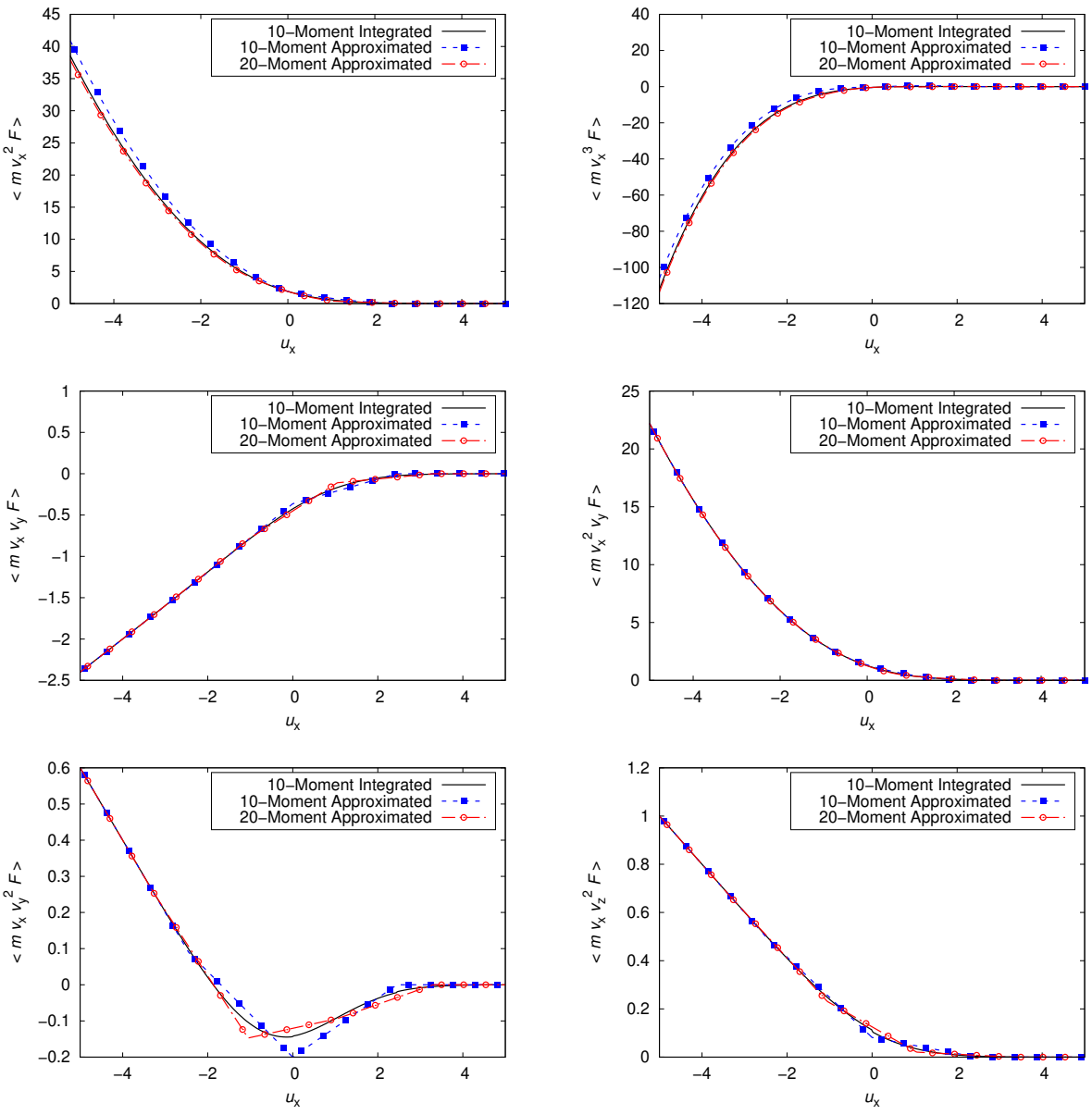

Figure 5.5: Knudsen-layer fluxes for the mixed accommodation flux integrals of the 10-moment and 20-moment equations

are even closer than those of the 10-moment approximation for the lower order moments.

The 20-moment models developed in this work also require closing fluxes for the higher-order moments R_{ijkl} in the wall direction. These are shown for the same state described in Equation (5.12) in Figure 5.6 for the accommodated, specular, and mixed cases. As the 20-moment model lacks a distribution function, these simply demonstrate the variation across the three choices of accommodation coefficient.

These fluxes demonstrate a trend which continues from the results shown in Figures 5.3 to 5.5, as the powers of v_x increase for the moment being approximated, the solution become increasingly smooth. Any cusps present are only in the approximations of moments with one v_x weight, and the higher-order approximations are more accurate when compared against the integration of the 10-moment equations. As discussed in Section 2.5.1, the closures in this framework are very similar to quadrature rules. However, the right Eigenvectors of the flux Jacobian, $\boldsymbol{R}$, are no longer in the form of a Vandermonde matrix. Instead, it is a matrix which has the same block-diagonalization as the flux Jacobian, but with smaller Vandermonde matrices along the diagonal. The result is that, instead of the order of the moment determining the power of the Eigenvalue in the sum, it is the order of how many v_x weights there are for that moment.

With the truncation technique described in Section 5.2, this means that, as different Eigenvalues are truncated, so too are any of the partial sums shown in Equation (2.57). Therefore, the shape of the fluxes of a single power of v_x in Figures 5.3, 5.4, 5.5, and 5.6, are the result of these partial sums being linear. As additional Eigenvalues are introduced or truncated, the slope changes and a cusp is introduced. Higher-order moments are increasingly differentiable, resulting in smoother results. This gives good confidence that, for the higher-order moment methods considered in this work, the closing fluxes of the models is well approximated inside the Knudsen layer using this technique.

5.3.2 Wall Temperature Investigation

To investigate the effect of varying wall temperatures, the 10-moment model can no longer be used as a reference, as it is adiabatic and lack the higher-order moments which are

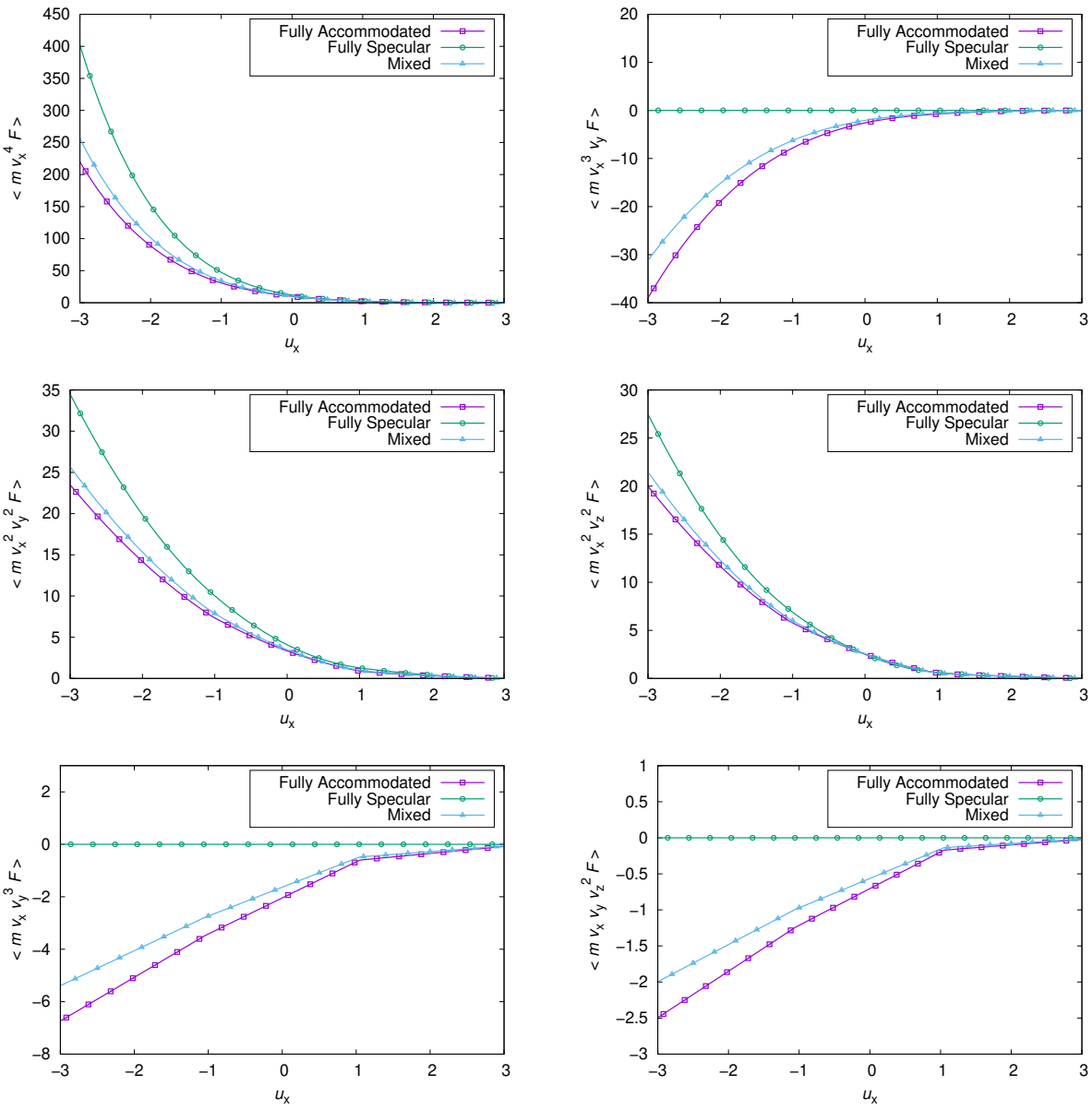

Figure 5.6: Knudsen-layer fluxes for the closing fluxes of the 20-moment model with the new boundary conditions

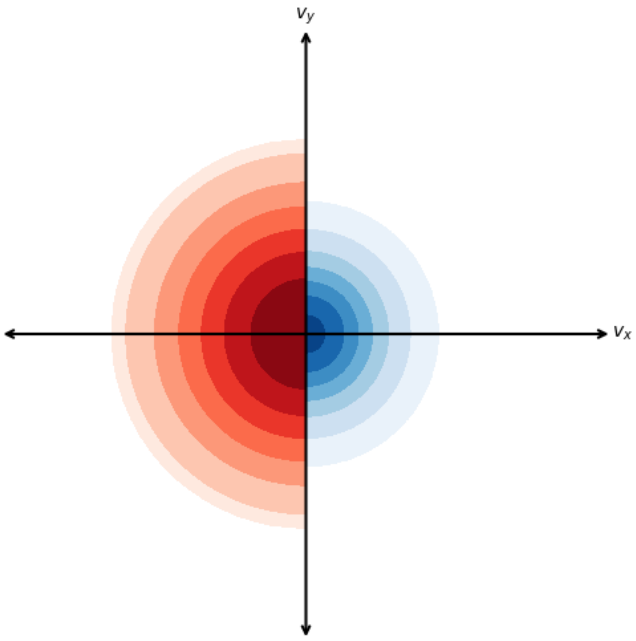

Figure 5.7: Free-molecular distribution resulting in heat transfer

needed to model heat transfer. Instead, a known free-molecular distribution function is used instead, shown in Figure 5.7. This distribution function represents a temperature slip from the wall to the state of the gas next to it. Due to the lack of collisions between particles in free-molecular flow, the particles at either temperature can only pass through each other. With a full accommodation coefficient $\chi = 1$, they come in to equilibrium with that boundary, and are remitted in the opposing direction. Particles with positive velocities are in equilibrium with the left boundary at temperature T_L and are shown in blue, while particles with negative velocities have come in to equilibrium with the right boundary at temperature T_R and are shown in red. By varying the right boundary temperature over the range $1/4T_L \leq T_R \leq 4T_L$, the effect of varying wall temperature is captured. This is shown in Figure 5.8.

It is obvious from Figure 5.8 that the new method performs quite well for predicting heat fluxes with moderate temperature ratios, but, as the temperature ratio increase above 2 or below 1/2, the method overpredicts the normal-to-the-wall heat flux Q_{xxx}, and underpredicts the transverse heat fluxes Q_{xyy} and Q_{xzz}. The closing flux R_{xxxx} fares better, but there is still some underprediction in the transverse R_{xxyy} and R_{xxzz} fluxes. However, as mentioned in Chapter 2, the anisotropic heat fluxes can be related to the

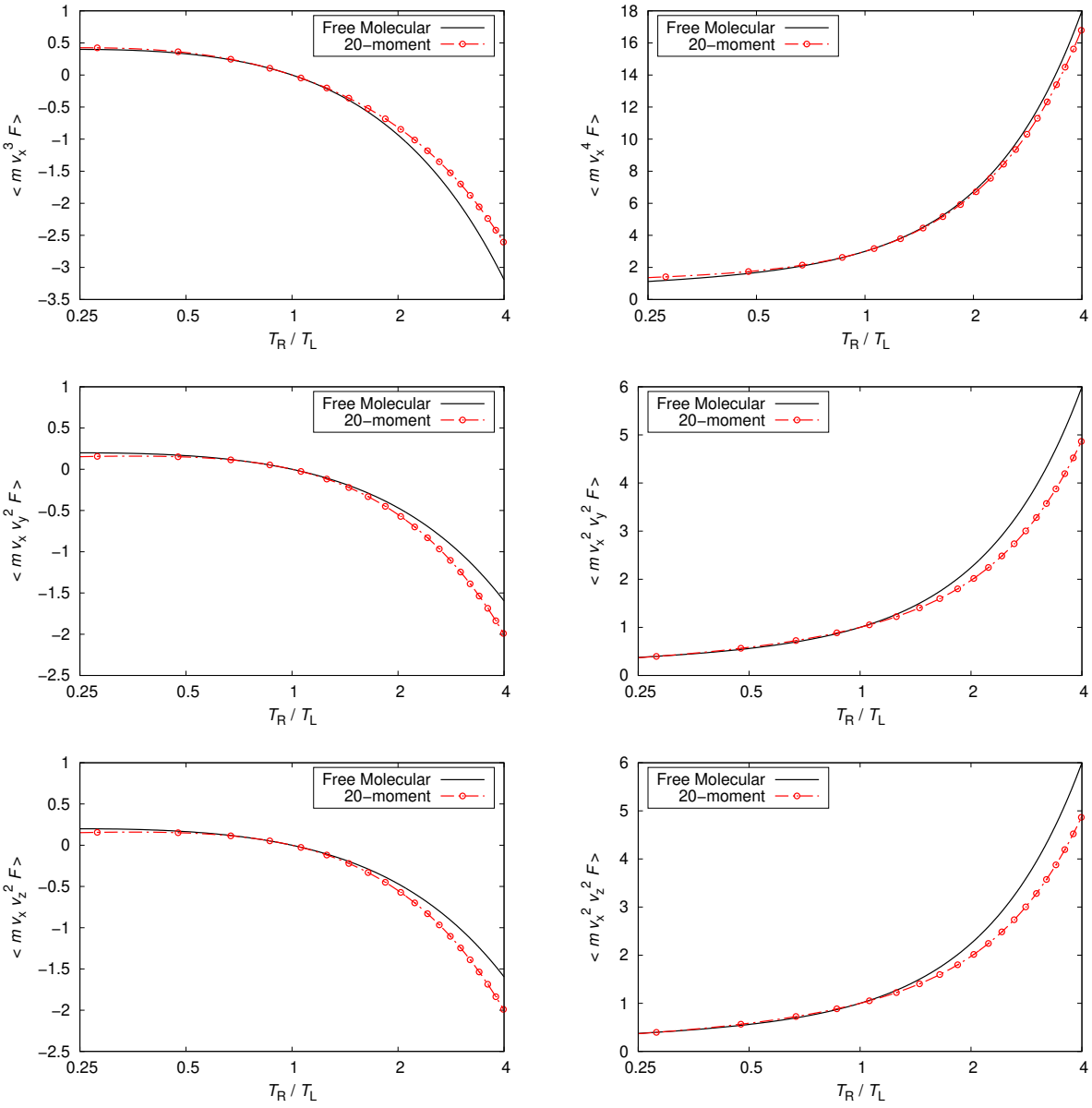

Figure 5.8: Solutions for the heat and closing fluxes for varying temperature ratios

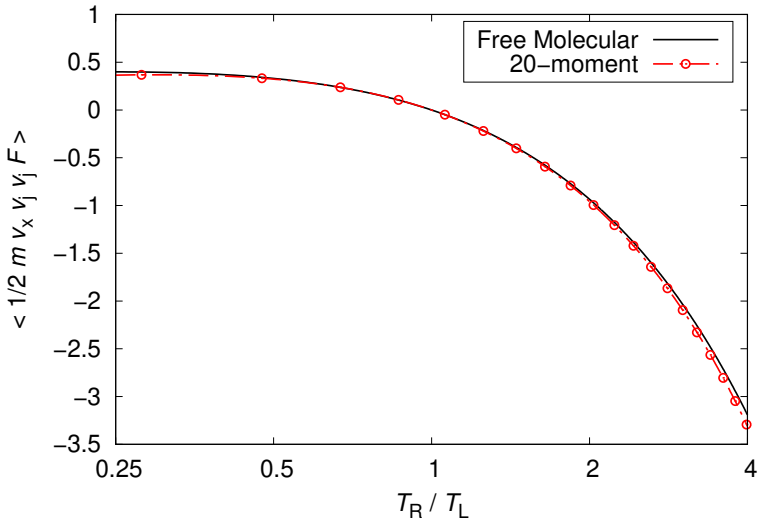

Figure 5.9: Contracted heat flux prediction for varying temperature ratios

traditional Fourier's law predictions by taking the half trace $q_i = \frac{1}{2}Q_{ijj}$. A comparison of this for the free molecular and 20-moment predictions for q_x in to the wall is shown in Figure 5.9. Here, the overpredicted Q_{xxx} balances with the underpredicted Q_{xyy} and Q_{xzz}. This results in a large range of temperatures for which accurate heat flux predictions can be expected.

5.4 Canonical Wall-Bounded Flows Across Regimes

To demonstrate the performance of the new formulation for boundary conditions, flows of a multidimensional gas between two infinitely long flat plates are studied as a canonical boundary-value problem. The domain of study is shown in Figure 5.10. The wall temperatures, T_t and T_b, and velocities, u_t and u_b, are prescribed for the top and bottom plates respectively. By varying the distance between the plates, L, the Knudsen number of the resulting flow can be varied. This can be computed as

$$L = \frac{\tau v_{th}}{\mathrm{Kn}}, \tag{5.13}$$

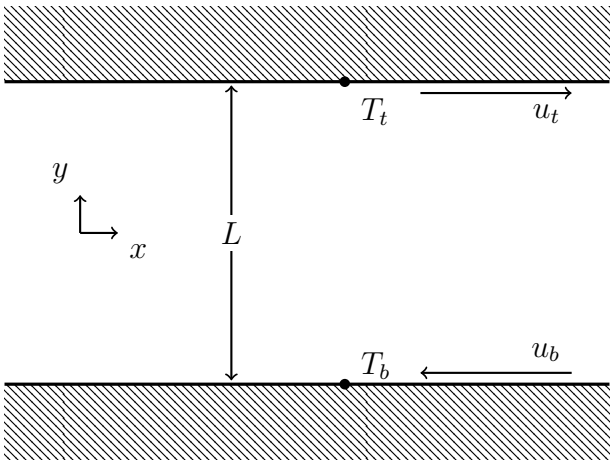

Figure 5.10: Illustration of the domain for the boundary condition test cases

where τ is the collision relaxation time, Kn is the Knudsen number, and v_{th} is the so-called thermal velocity,

$$v_{th} = \sqrt{\frac{8p}{\pi\rho}}\,, \tag{5.14}$$

representing the mean velocity of the particles of a monatomic gas. The study spans $10^{-4} \leq \text{Kn} \leq 10^4$, from the continuum to free molecular limits.

The walls are assumed to be fully accommodating, with $\chi = 1$. In the first study, Couette flow and the resulting prediction for shear stress in the fluid between the plates is studied for both the 10-moment and 20-moment models with the new boundary conditions. Then, heat transfer through the fluid between two plates at different temperatures is studied with just the 20-moment model.

5.4.1 Couette Flow

For this case, both walls are assumed to be at the temperature $T_t = T_b = T = 1$. The bottom wall is stationary with $u_b = 0$, and the top wall is moving with $u_x = 1$. As both models can handle shear stress, the 10-moment and 20-moment models are investigated.

In the continuum limit, the Navier-Stokes equations predict the shear stress to be

$$P_{xy} = -\frac{\mu(u_t - u_b)}{L}\,, \tag{5.15}$$

with the viscosity, μ, coming from BGK approximation as shown in Equation (2.17).

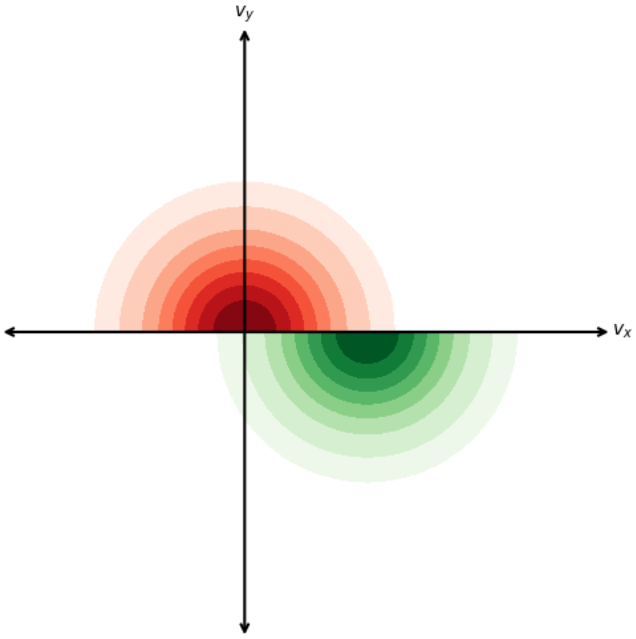

Figure 5.11: Distribution function for steady-state, free-molecular Couette flow

In the free molecular regime, the distribution function is known, as in steady state any particles which have negative y-velocities must have been emitted from the top plate, and conversely those with positive y-velocities from the bottom plate. The resulting distribution is shown in Figure 5.11. This can be directly integrated to find that the shear stress is

$$P_{xy} = -\sqrt{\frac{p}{2\pi\rho}}\rho(u_t - u_b)\,, \tag{5.16}$$

in the free molecular limit. There are also approximations for the shear stress as a function of the Knudsen number, like the Lees approximate solution [49]. For the described state, this predicts the shear stress to be

$$P_{xy} = -\left(\frac{2\mathrm{Kn}}{1+2\mathrm{Kn}}\right)\sqrt{\frac{p}{2\pi\rho}}\rho(u_t - u_b)\,, \tag{5.17}$$

which recovers both the Navier-Stokes and free molecular limits.

The interior of the computational domain is 1000 cells tall, and was solved using the third-order accurate scheme described in Section 4.1. The initial state of the gas is

$$\rho_0 = 1\,, \quad \text{and} \quad P_0 = 1\,, \tag{5.18}$$

with the velocity, u_x, and shear stress, P_{xy}, preset to either Navier-Stokes solution for Knudsen numbers Kn $\leq 10^{-1}$, or the free molecular solution for Knudsen numbers 10 and above. A fifty-fifty superposition of the two extremes was used for the Kn $= 1$ case. The final time of $t_{final} = 100L/v_{th}$ was used, to allow sufficient time for the wall to fully influence the domain.

The resulting Couette flow profiles with the approximated boundary conditions are shown in Figure 5.12 for the 10-moment model, and Figure 5.13 for the 20-moment model. These show how the density, velocity, thermodynamic pressure, thermodynamic temperature, shear stress, and in the case of the 20-moment model, heat-flux, vary across the domain. Both the 10-moment and 20-moment have good agreement in the continuum regime and free-molecular regimes, with the only changes from the initial condition being due to numerical noise. However, the 10-moment model has issues in the transition regime. With no mechanism to diffuse heat, the fluid heats up. Since it has to recover $T_b = T_t = 1$, the result is that the gas sticks to the walls, increasing the density. The 20-moment results fair much better. The heat flux allows for the formation of a Knudsen layer, and while the gas heats up, it does not overshoot the free-molecular solution like it does in the 10-moment model.

As the major moment of interest for Couette flows, comparison of the predicted shear stress between the three models is shown in Figure 5.14. In the transition regime, at about Kn $= 1$, the 10-moment model overpredicts the shear stress, while the 20-moment model continues to have good agreement with the Lees solution. Again, this is most likely due to the inaccuracy of the resulting temperature and density profiles in the 10-moment model, influencing the pressure tensor to overpredict shear stress in the transition regime.

Both models then slightly underpredict the shear stress in the free molecular regime. This underprediction is expected, as it is also present when comparing BGK solutions [49], as well as the 10-moment equations [33]. In the case of the latter, this can be explained by the fact that the distribution which satisfies at either wall is not equivalent to the distribution which replicates the half-Maxwellian distribution shown in Figure 5.11. This mismatch is further shown in Figure 5.15, showing the top and bottom boundary condi-

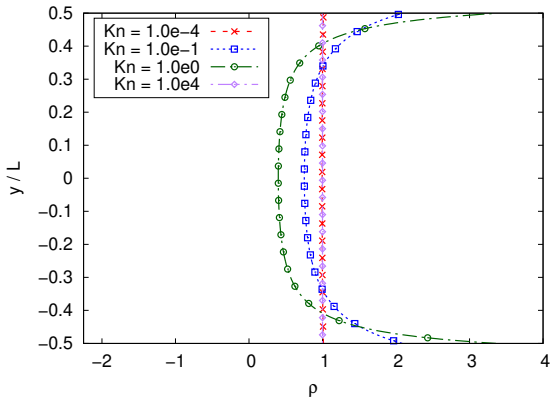

(a) Density

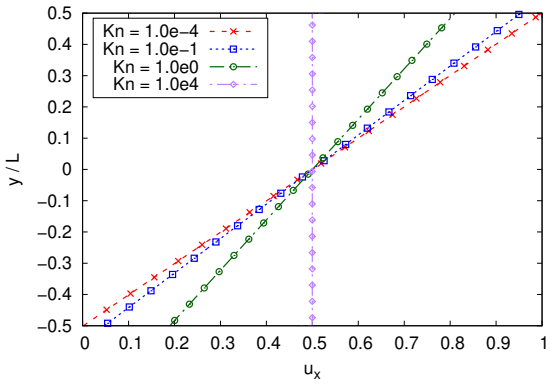

(b) Velocity

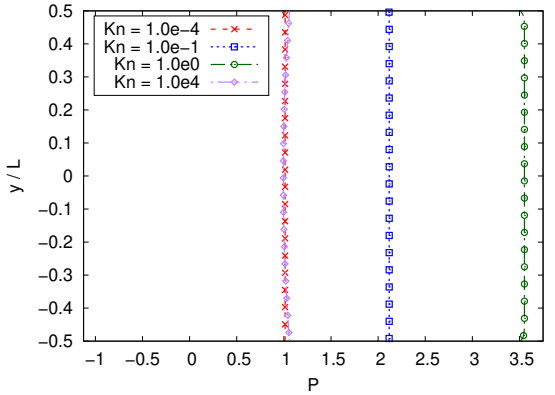

(c) Pressure

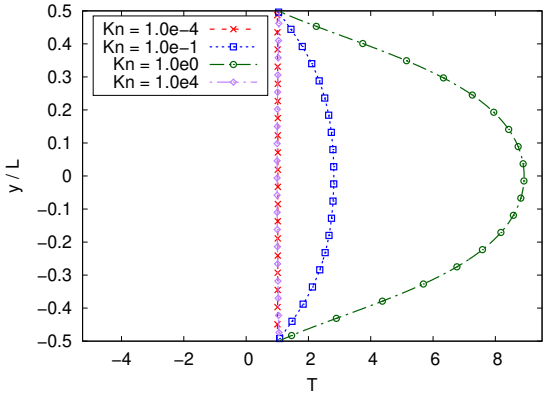

(d) Temperature

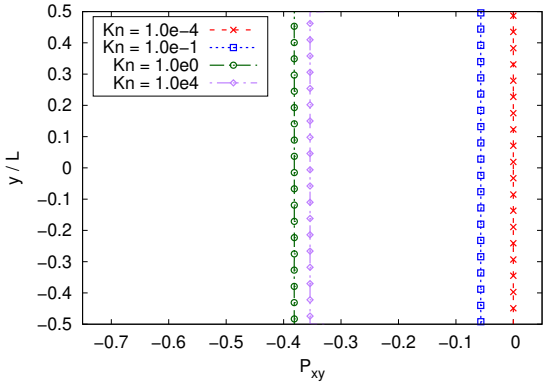

(e) Shear Stress

Figure 5.12: Couette flow profiles across the regimes of interest for the 10-moment model

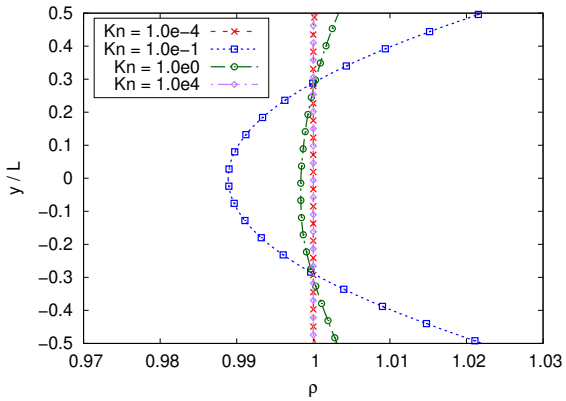

(a) Density

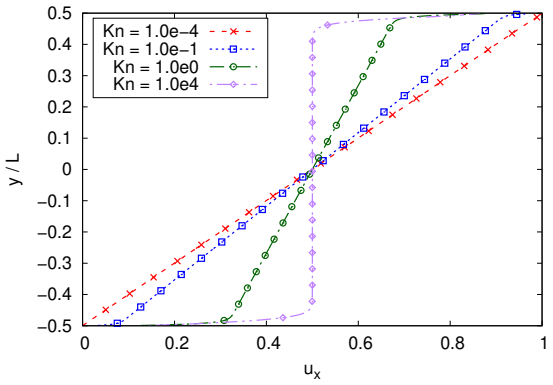

(b) Velocity

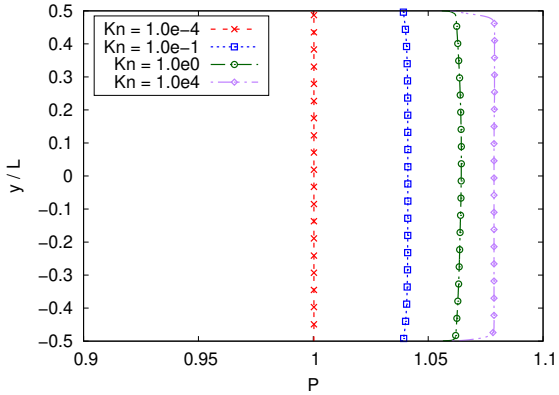

(c) Pressure

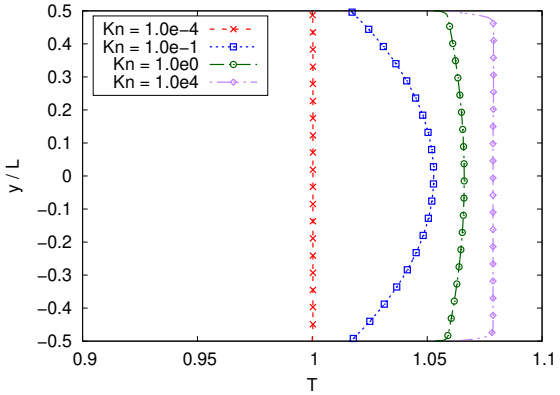

(d) Temperature

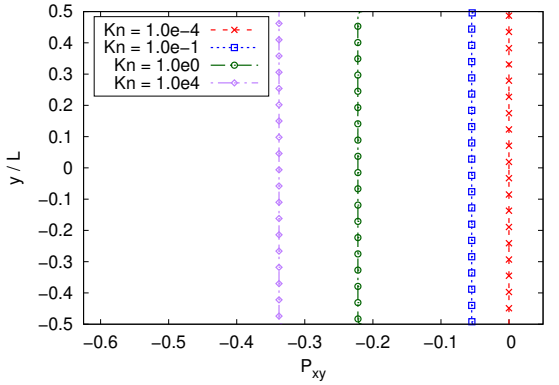

(e) Shear Stress

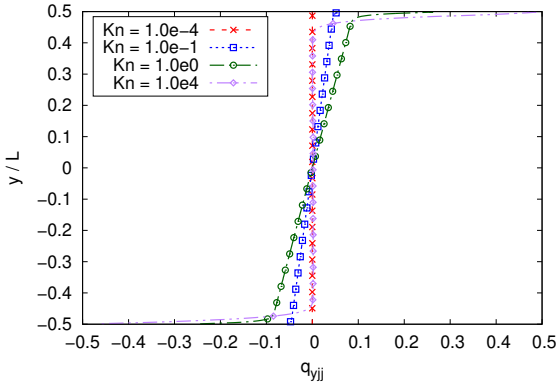

(f) Heat Flux

Figure 5.13: Couette flow profiles across the regimes of interest for the 20-moment model

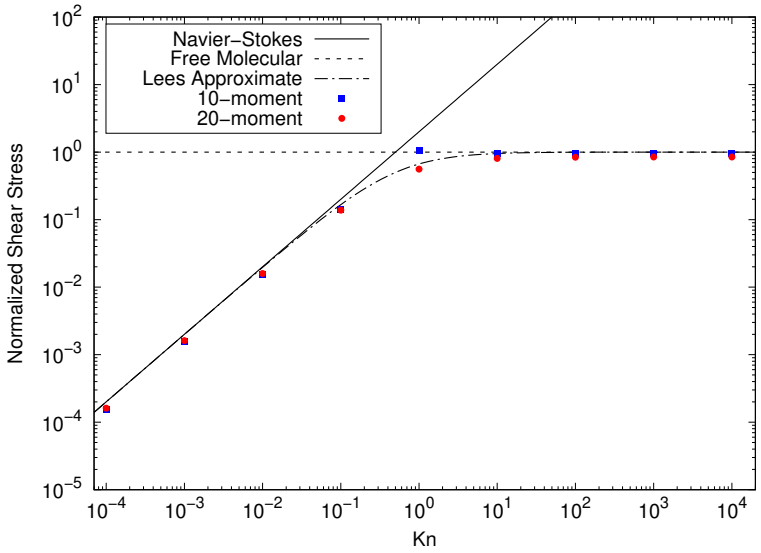

Figure 5.14: Results of the shear stress study

tions, and a comparison between resulting distribution and the exact solution. While the 20-moment model does not have a known distribution function, it does replicate many of the structures of the 10-moment model, and thus the replication of this deficiency is not necessarily unexpected.

A last important feature of the boundary conditions is the slip velocity, which in Figures 5.12b for the 10-moment model and 5.13b for the 20-moment model. In the free-molecular regime, the distribution function has a clear mean at $(u_t - u_b)/2$, as seen in Figure 5.11. This is captured by both models, with the 10-moment model having a complete discontinuity at the wall, while the 20-moment model has a layer in which the gas attenuates to the wall. Again, this is due to the ability of the 20-moment model to conduct heat to the other energy modes, and is more realistic than the pure discontinuity predicted by the 10-moment [15, 49].

5.4.2 Heat Transfer Between Plates

To demonstrate the accuracy of the 20-moment models predictions for heat flux, the plates shown in Figure 5.10 are used again, with stationary walls such that $u_t = u_b = 0$. The bottom wall is again set to $T_b = 1$, and the top wall's temperature $T_t = 2$, around the range in which differences in between the free-molecular solution and the 20-moment

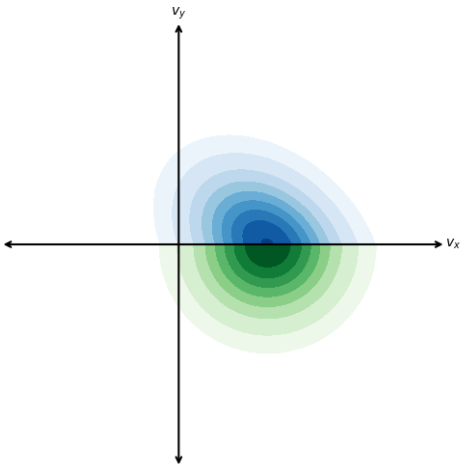

(a) Gaussian top wall boundary condition

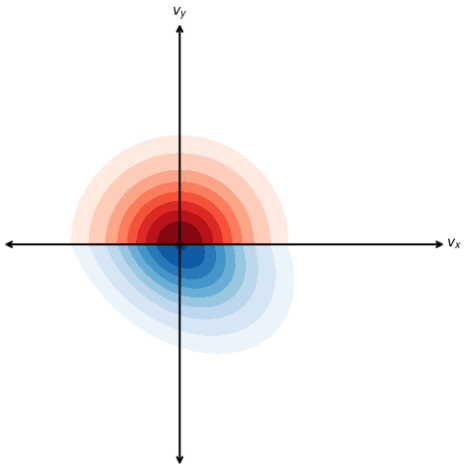

(b) Gaussian bottom wall boundary condition

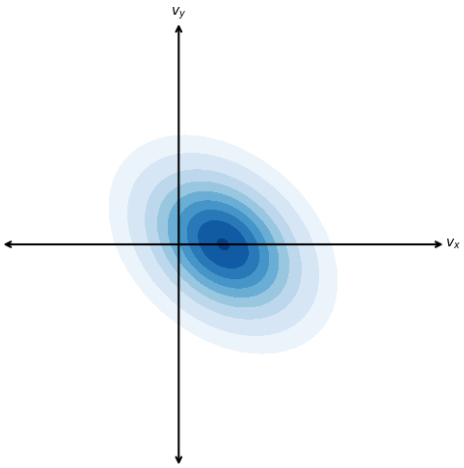

(c) Resulting Gaussian distribution

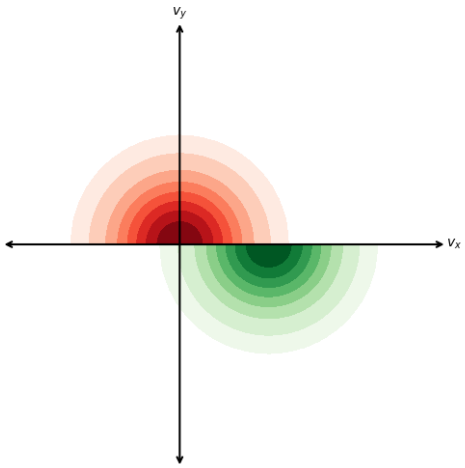

(d) Exact distribution

Figure 5.15: Comparison of the distribution function of the 10-moment equations for free molecular Couette flow

model can become apparent as shown in Section 5.3.2.

As mentioned in Chapter 2, the traditional heat flux vector can be related to the moments through the half trace of the generalized heat flux tensor $q_i = \frac{1}{2}Q_{ijj}$. In the continuum limit, the Navier-Stokes equations predict the heat transfer to be

$$q_y = k\frac{T_b - T_t}{L}\,, \tag{5.19}$$

where L is computed the same as in the previous Couette flow study, described in Equation 5.13, and k is the conductivity of the gas. When considering BGK collisions, the Prandtl number is inaccurately captured, and predicted to be unity. While physically inaccurate, it is predictable for the context of this study. Thus, the conductivity for a monatomic gas is

$$k = c_p\mu = \frac{5}{2}R_s p\tau\,, \tag{5.20}$$

where R_s is the specific gas constant. The free molecular solution once again has a known distribution function, shown in Figure 5.16, and is the same distribution as shown in Figure 5.7 but with it axes rotated 90°. This can once again be directly integrated to find

$$q_y = \rho\sqrt{\frac{2}{\pi}}(T_b^{3/2} - T_t^{3/2})\,, \tag{5.21}$$

as the expression for heat transfer.

The results for the planar heat transfer study are shown in Figure 5.17, showing the density and temperature gradients, as well as the normal and transverse heat fluxes. The 20-moment model performs very well here, accurately capturing Fourier's law in the continuum regime, before smoothly varying across the transition regime to the free molecular solution. As the primary physical phenomenon that the 20-moment model has added, this gives a great indication that heat transfer is being accurately captured with both this model and boundary conditions.

The results of the heat transfer study across all the regimes of interest are shown in Figure 5.18, showing the normal heat flux more in depth. These again have great agreement in the continuum regime, and transition follows the same behaviour as the

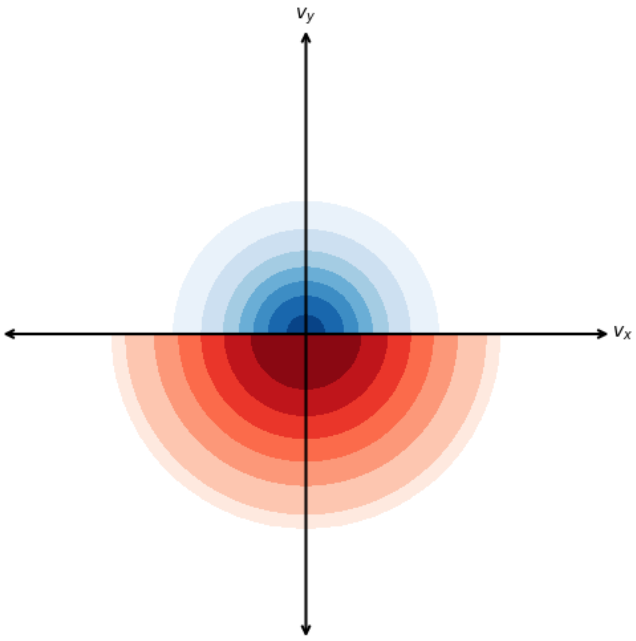

Figure 5.16: Distribution function for steady-state, free-molecular planar heat transfer

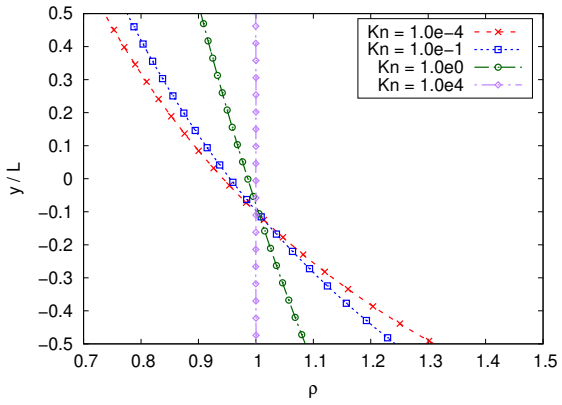

(a) Density

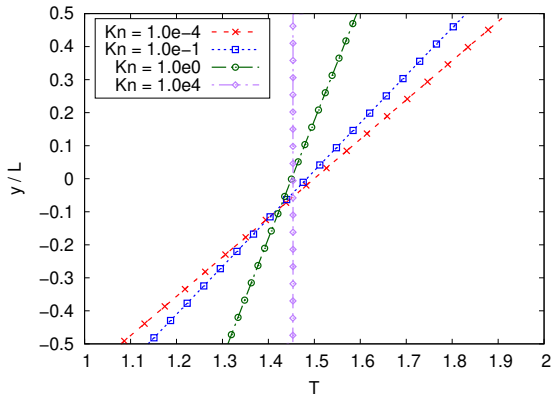

(b) Temperature

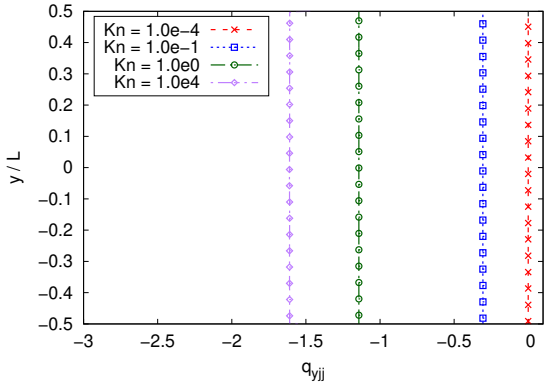

(c) Normal Heat Flux

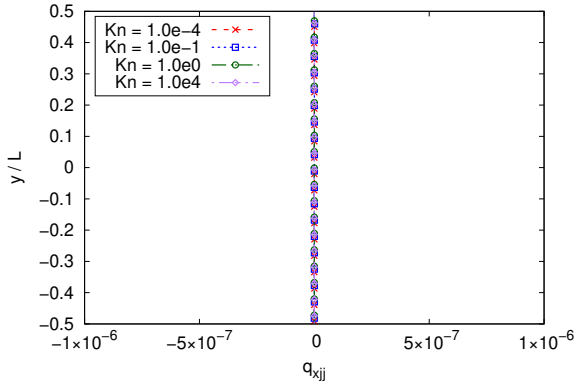

(d) Transverse Heat Flux

Figure 5.17: Planar heat transfer flow profiles across the regimes of interest for the 20-moment model

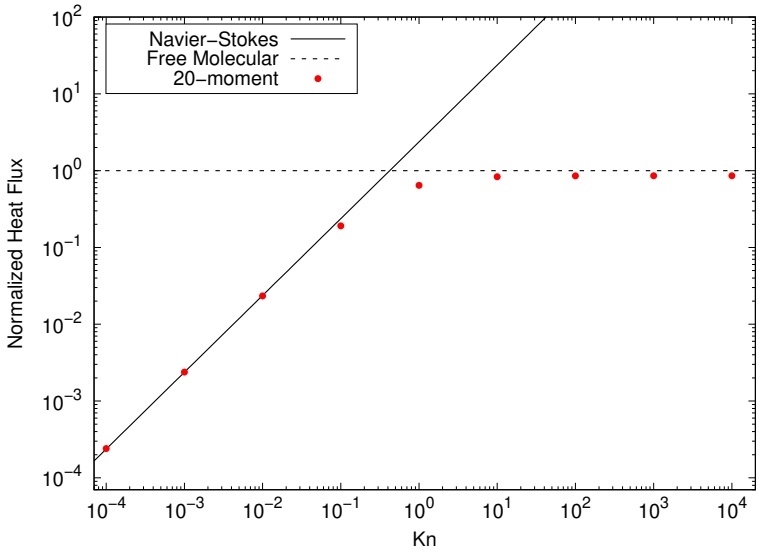

Figure 5.18: Results of the heat transfer study

results in Section 5.4.1, smoothly varying from the continuum prediction line to the free molecular line. The slight underprediction seen in Figure 5.9 is seen here again, with the 20-moment free molecular solution underpredicting the heat transfer by about 14%.

5.5 Walls with a Known Heat Transfer

The current implementation of the solid-wall boundary conditions described in this chapter assumes that the temperature of the wall is known, and unchanging over the timescale of the problems. However, it would also be useful to be able to model heat-transfer from the wall itself as well. Much like the non-penetration condition in Equation (5.3), this would result in needing to also ensure

$$q_w = \int_{-\infty}^{\infty}\int_{-\infty}^{\infty}\int_{0}^{\infty} mv_x v_j v_j \mathcal{F}(x_i, v_i, t)\partial v_x \partial v_y \partial v_z + \int_{-\infty}^{\infty}\int_{-\infty}^{\infty}\int_{-\infty}^{0} mv_x v_j v_j \mathcal{M}_w(x_i, v_i, t)\partial v_x \partial v_y \partial v_z \,, \tag{5.22}$$

along with no-penetration when solving for the boundary conditions. In this formulation, q_w is the heat flux from the wall. In the simplest case, an adiabatic wall, $q_w = 0$, and conceptually any other wall heat flux could just as easily be modelled in this framework. While theoretically simple, for the demonstrative cases that are shown here and in Chapter 6, heat transfer to the boundary surfaces for these simple cases can be neglected.

Chapter 6

Investigation of Non-Equilibrium Flows

The primary purpose of this work is for the consideration of higher-order moment effects in non-equilibrium settings. With both the models in Chapter 3, and the boundary conditions in Chapter 5, this practical framework has been developed. This chapter demonstrates the applications of these new developments in to practical settings.

Much of this study will use the condition number of a matrix, $\kappa(A_{ij})$, to get a sense of the amount of anisotropy found in the solutions. For a diagonal matrix, $\kappa = 1$, which for the temperature and pressure tensors implies that the gas is in local thermodynamic equilibrium. Values $\kappa \geq 1$ imply that the principal axis of the matrix is that multiple of the minor axes. For example, a temperature anisotropy of $\kappa(T_{ij}) = 2$ would imply that the primary axis temperature is twice that of the temperatures in the transverse directions.

First, subsonic and transonic rarefied flows past cylinders are presented in Section 6.1, and compared against equivalent DSMC data. The DSMC and Navier-Stokes results were provided by Dr. Stefano Boccelli at NASA Goddard Space Flight Center, using modified versions of the SPARTA and Hyper2D solvers [50] respectively. These modifications ensure replication of the simplified effects of BGK collisions, and enforces a unity Prandtl number. A continuum, transonic flow is also presented in this section, to

demonstrate flows which are far too expensive for DSMC but for which the 20-moment equations are perfectly suitable. Next, strong shock structure is discussed beginning with a one-dimensional investigation of the shock structure for a three-dimensional gas in Section 6.2. Then, the influence of the correct implementation of boundary conditions, and the resulting non-equilibrium shock structure, are studied through Mach reflection cases in Section 6.3. Finally, Section 6.4 studies supersonic plate crossflow, and the resulting breakdown of the 20-moment model in extreme cases.

6.1 Rarefied Flows Past Cylinders

To confirm the validity of the new model and boundary conditions in the transition regime, three flows past cylinders with fully accommodating walls are studied in comparison with equivalent DSMC data. Both transonic and subsonic flows are studied, to the limit at which DSMC produces coherent results. The domain is shown in Figure 6.1, with the outer blue circle representing the far-field boundary that is fixed to the free-stream state, and the red inner circle has the fully accommodated boundary condition. The far-field boundary was chosen to be at a distance 15 times larger than the diameter of the cylinder to allow the flow to fully return to the free-stream state inside the domain. The free-stream temperature is $T_\infty = 300$ K, and the free-stream velocity is chosen as a function of the Mach number,

$$u_\infty = \mathrm{Ma}\sqrt{\gamma \mathrm{R_s T_\infty}} \ \mathrm{m/s}\,, \tag{6.1}$$

where R_s is the specific gas constant for Argon, and $\gamma = 5/3$ for monatomic gases. The free stream density is then chosen as a function of the Knudsen number,

$$\rho_\infty = \frac{8.591 \times 10^{-8}}{\mathrm{Kn}} \ \mathrm{kg/m^3}\,, \tag{6.2}$$

for a cylinder with $D = 1$ m.

A 512×512 mesh was used with the third-order scheme for the 20-moment calcu-

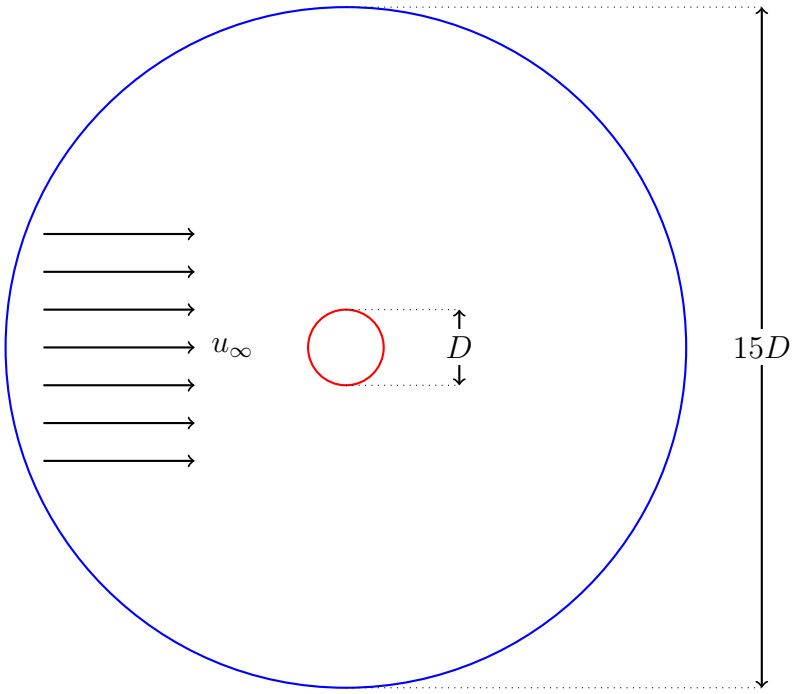

Figure 6.1: Illustration of cylinder flow domain, not to scale

lations, shown in Figure 6.2. Figure 6.2a shows the full domain, where each block is a 16×16 grid. The mesh was also scaled so that the grid becomes denser nearer to the surface of the cylinder. Figure 6.2b shows the full mesh near the surface of the cylinder in comparison with the DSMC mesh. It is particularly noteworthy that behind the cylinder, there is a region that is much less dense in the DSMC mesh, due to the lack of particles in that region. Other regions further from the cylinder are conversely quite dense, despite relatively little changes of the moments across these regions. This greatly increases the computational cost of the equivalent DSMC calculations, whereas field-based moment methods can reduce the computational difficulty in these regions without sacrificing accuracy. Due to this, the far-field for the DSMC results are much smaller, being reduced to 5 times the diameter of the cylinder. It should be noted that particle methods are less sensitive to the far-field boundaries, but this will still produce minor difference in the field at locations near the boundary.

Much like the Couette flow and planar heat transfer studies shown in Chapter 5, a final time was chosen based of the thermal velocity, although at a reduced value of $t_{final} = 20D/v_{th}$, as at this point the solution's residuals had converged. The results of the predicted densities are shown in Figures 6.3, 6.5, and 6.7 with the top field showing

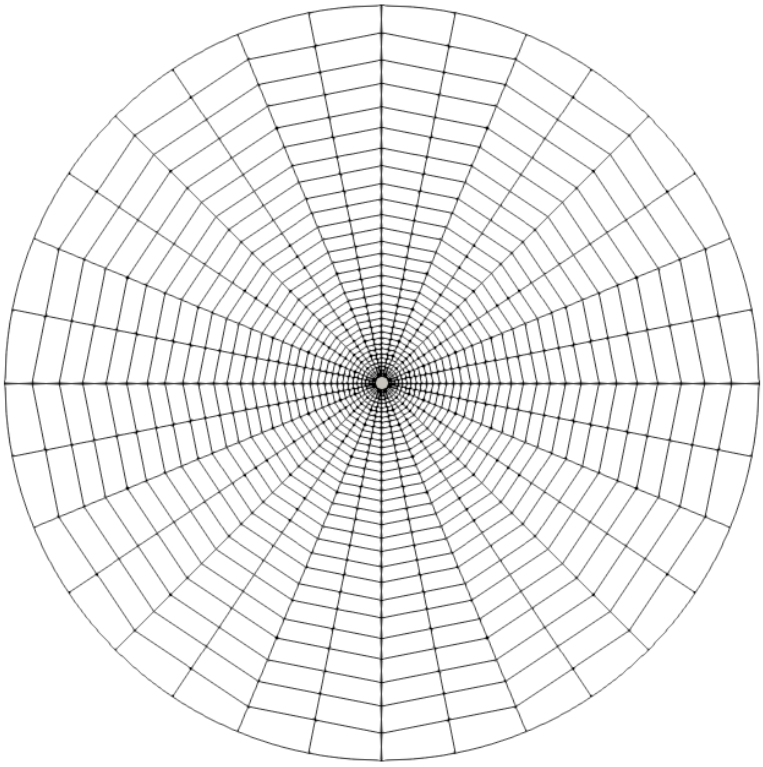

(a) Blocks of 20-Moment calculation domain

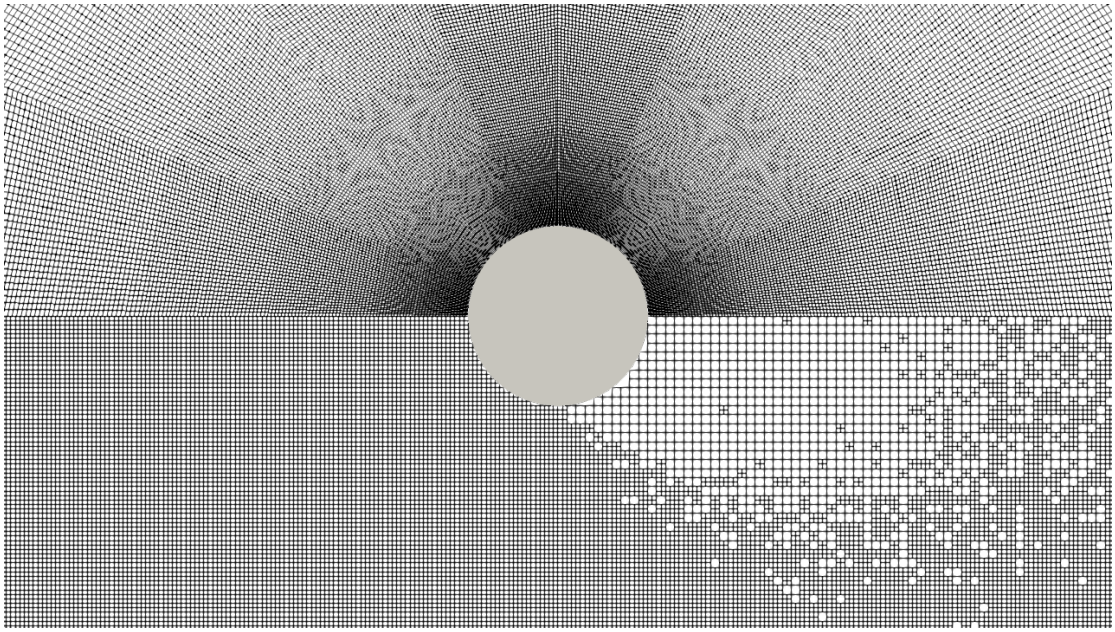

(b) Mesh comparison between DSMC and 20-moment calculations

Figure 6.2: Mesh for Knudsen 0.1 flows past cylinders

the 20-moment results, and the bottom field showing the DSMC result. The results of the predicted temperatures are shown in Figures 6.4, 6.6, and 6.8 with the top field showing the 20-moment temperature tensor condition number, and the bottom field showing the DSMC temperature tensor condition number.

The transonic results have very good agreement, especially in front of the cylinder, as can be seen in Figures 6.3 and Figures 6.4. While the density agrees behind the cylinder in this case, the temperature diverges quite a bit. The DSMC results predict a much higher degree of anisotropy behind the cylinder, however as shown in Figure 6.2b, there are also fewer particles in this region, which gives more statistical uncertainty. The DSMC temperature results are also much less spatially coherent overall, and have a large amount of statistical noise. In the compressible subsonic regime, Figures 6.5 and 6.6 show that the spatial coherence of the DSMC results decreases even more. The noise in both the density and temperature fields increases compared to the transonic results. This trend continues in to the low-speed, Mach 0.2 flows, shown in Figures 6.7 and 6.8. The DSMC results are consumed with noise, while the 20-moment model continues to perform with the same physical coherence. To achieve a similar level of physical validity, DSMC would require much more computational time, whereas the 20-moment model remains relatively computational cheap across all these regimes.

The other direction for which DSMC can become prohibitively expensive is the continuum limit. Lower than Knudsen numbers of about 10^{-2}, DSMC can simply be too costly to compute solutions. This final case of this investigates the transonic, Mach 0.95 flow past a cylinder in the continuum regime, with a Knudsen number of 10^{-3}. Instead of using a fixed mesh, adaptive mesh refinement was used to resolve the eddies that result from vortex shedding after the cylinder. The final mesh is shown in Figure 6.9.

Figure 6.10 shows the resulting density profile. The 20-moment model manages to capture many of the interesting physics in this regime, including the resulting shocks from the acceleration of the flow on the top and bottom of the cylinder. It also manages to capture vortex shedding in the wake region of the cylinder. In the continuum limit, vortex shedding is a Navier-Stokes feature driven by viscosity-controlled boundary-layer

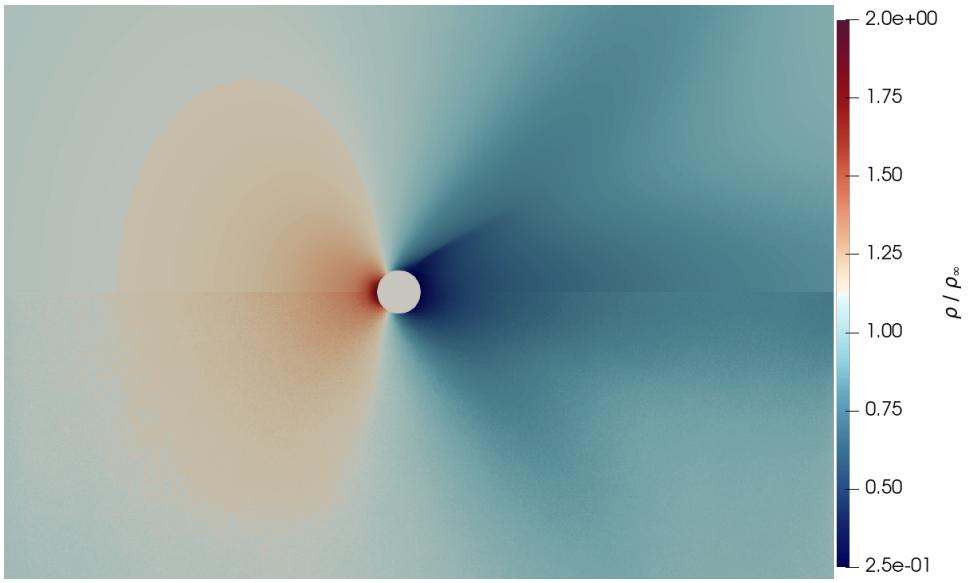

(a) Density field

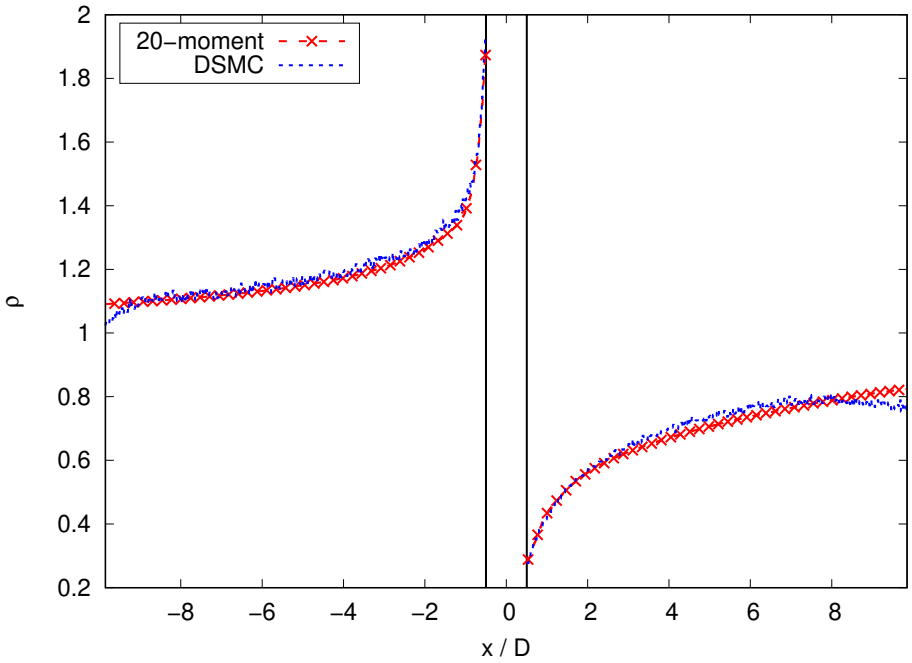

(b) Stagnation line density

Figure 6.3: Density profiles for Knudsen 0.1, Mach 0.95 flow past a cylinder

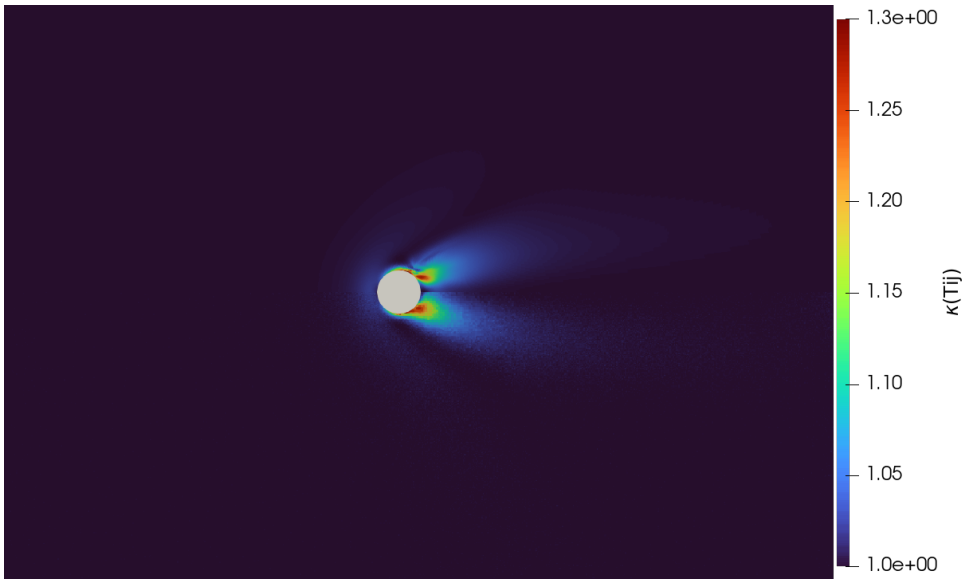

(a) Temperature anisotropy field

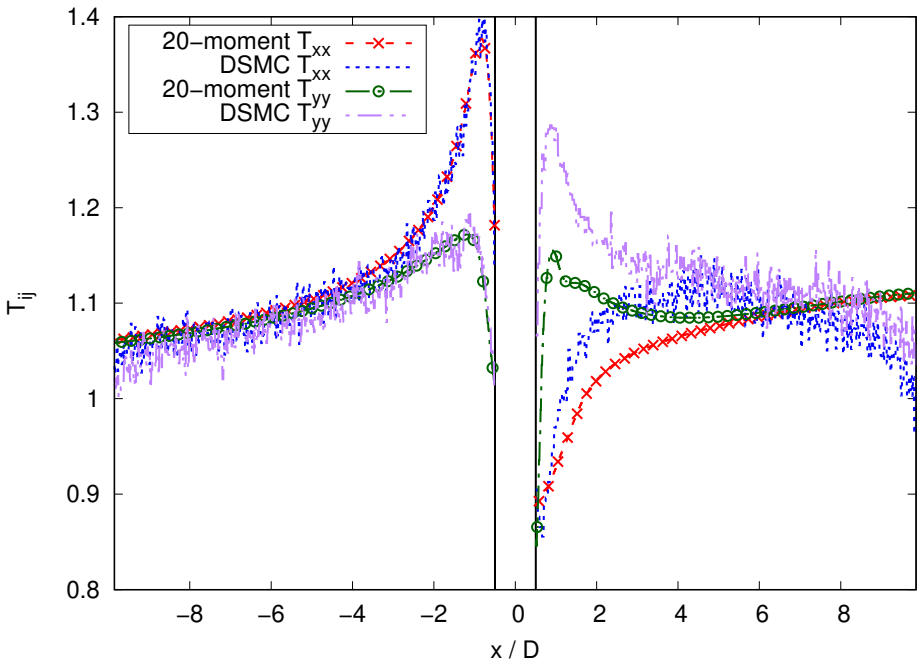

(b) Stagnation line temperatures

Figure 6.4: Temperature profiles for Knudsen 0.1, Mach 0.95 Flow Past Cylinder

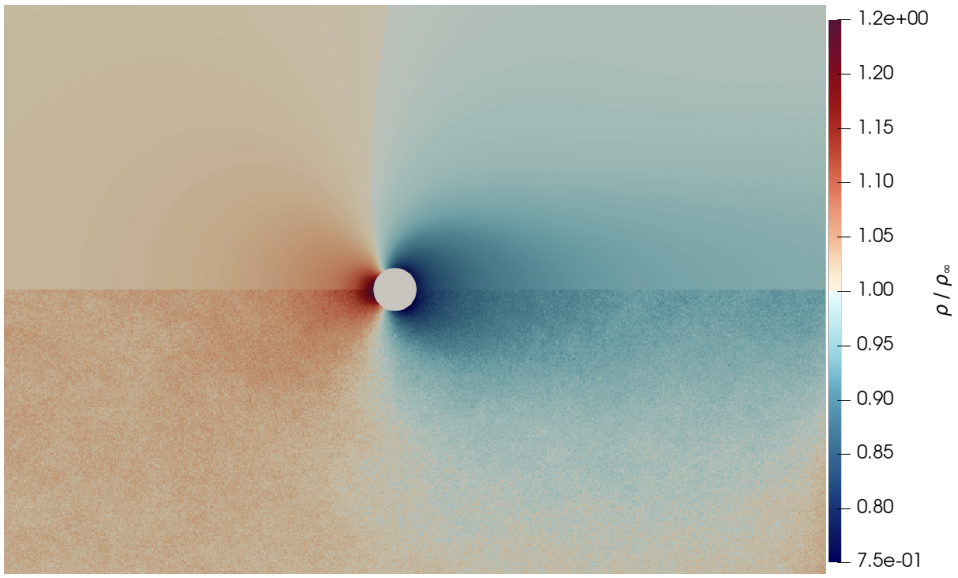

(a) Density field

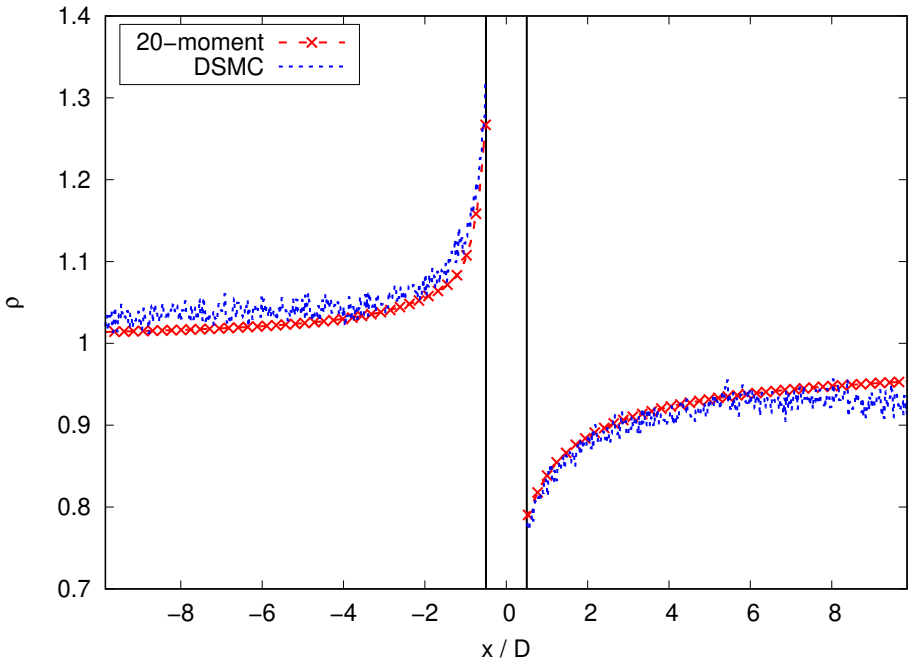

(b) Stagnation line density

Figure 6.5: Density profiles for Knudsen 0.1, Mach 0.5 flow past a cylinder

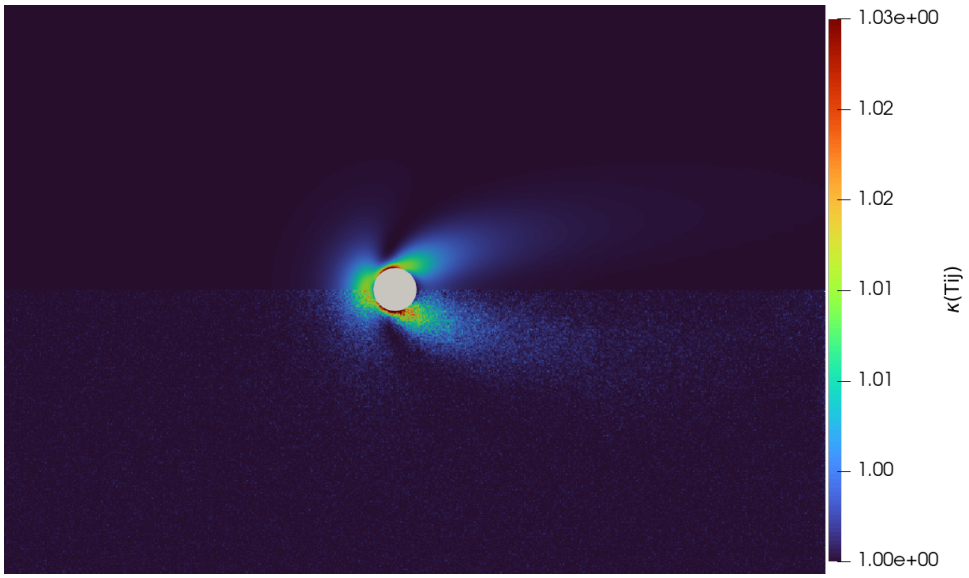

(a) Temperature anisotropy field

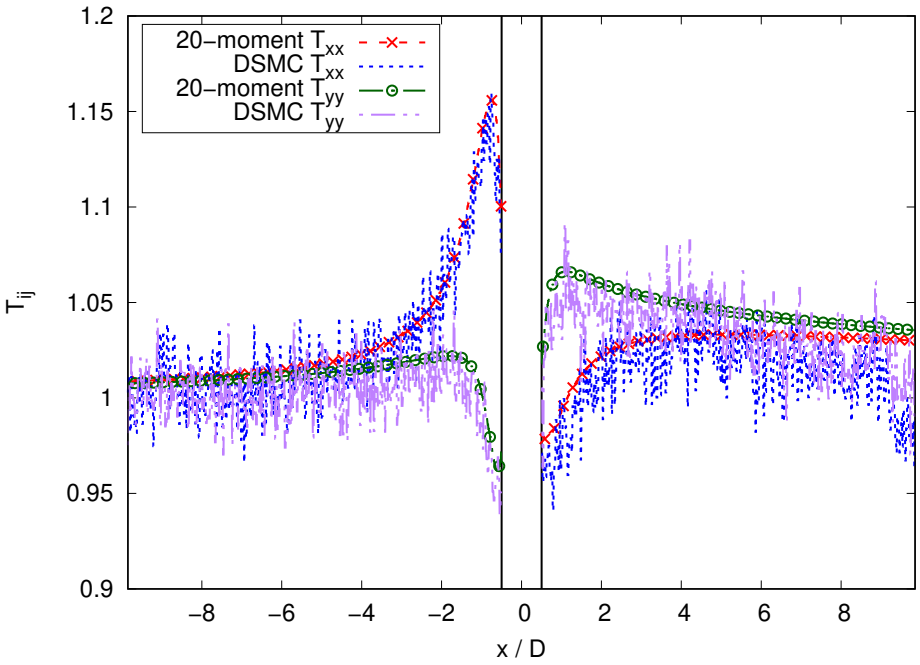

(b) Stagnation line temperatures

Figure 6.6: Temperature profiles for Knudsen 0.1, Mach 0.5 Flow Past Cylinder

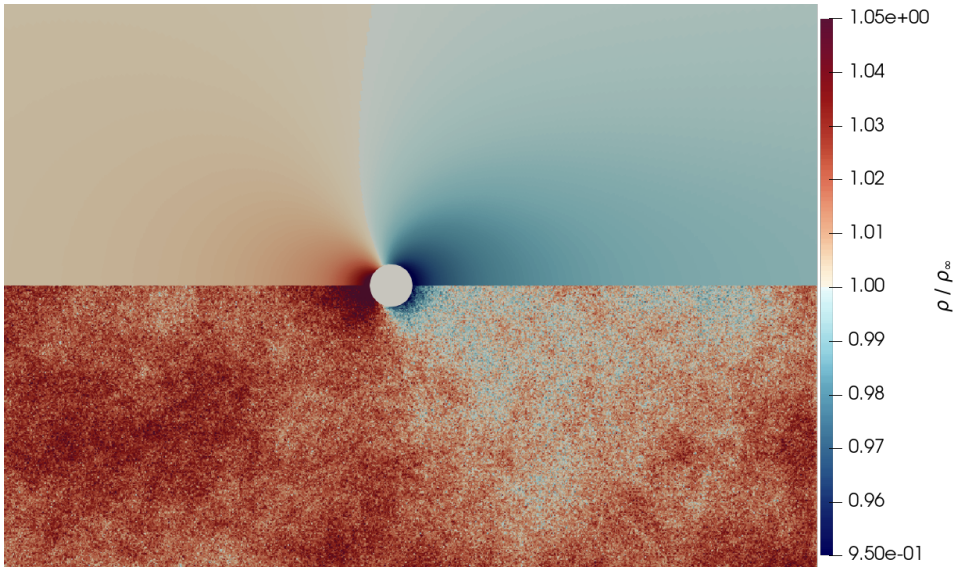

(a) Density field

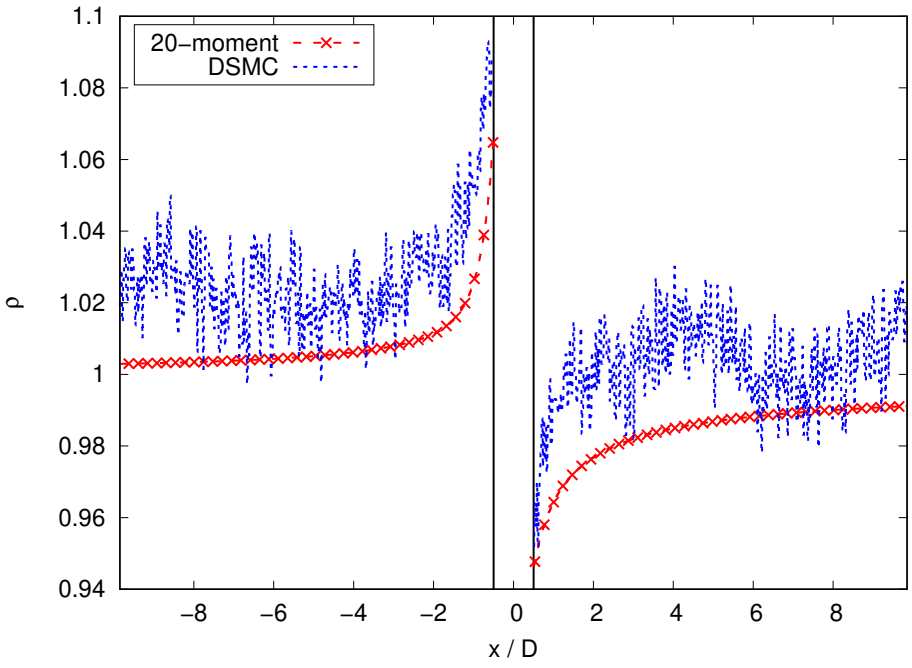

(b) Stagnation line density

Figure 6.7: Density profiles for Knudsen 0.1, Mach 0.2 flow past a cylinder

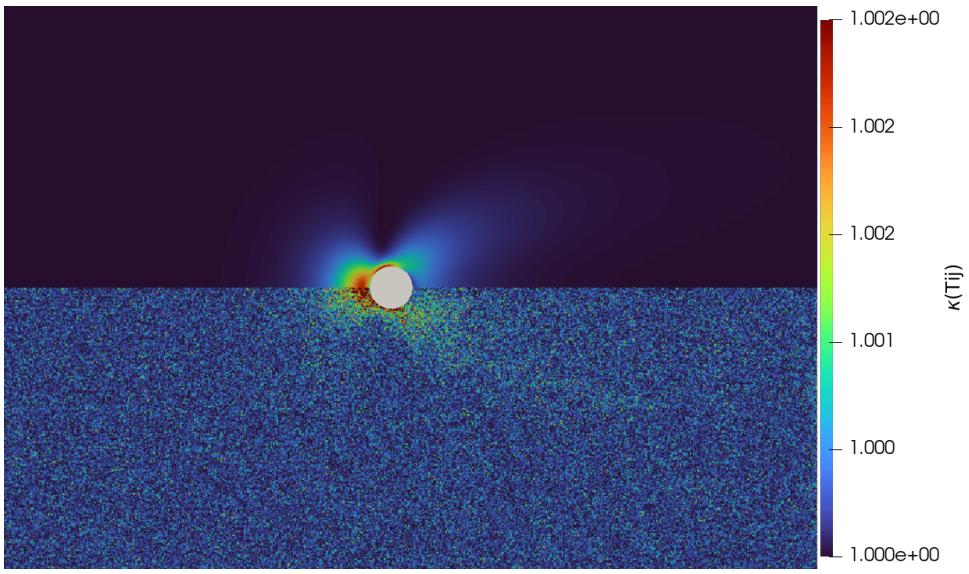

(a) Temperature anisotropy field

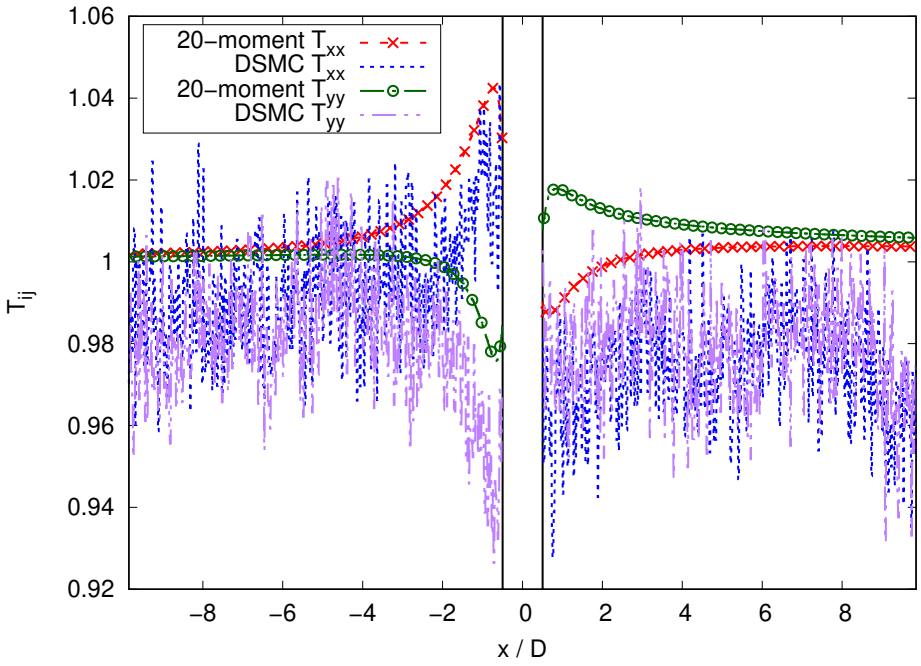

(b) Stagnation line temperatures

Figure 6.8: Temperature profiles for Knudsen 0.1, Mach 0.2 Flow Past Cylinder

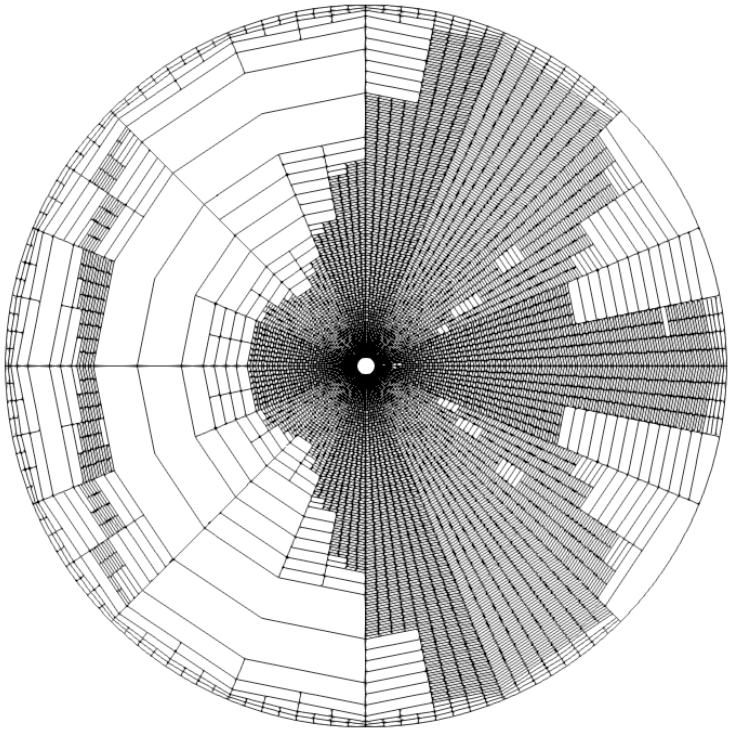

Figure 6.9: Mesh for transonic continuum flow past the cylinder

separation and shear-layer instability. Capturing it with a 20-moment closure supports the statement that the model's non-equilibrium stresses and heat flux relax in a way that reproduces the correct continuum instability mechanism, rather than suppressing it.

A final noteworthy feature is the AMR's response to the non-physical effects of the 20-moment closure. On the left of Figure 6.9, there is a region upstream of the cylinder which the AMR has resolved. While the physical phenomena, like the shocks on the top and bottom of the cylinder, as well as the vortex shedding in the wake behind it, are further resolved as regions with large gradients, it turns out the subshocks predicted by the 20-moment model are resolved as well. This gives some confidence that, while these mathematical artifacts are not physically real, they are sufficiently resolved and do not negatively impact the predicted solution.

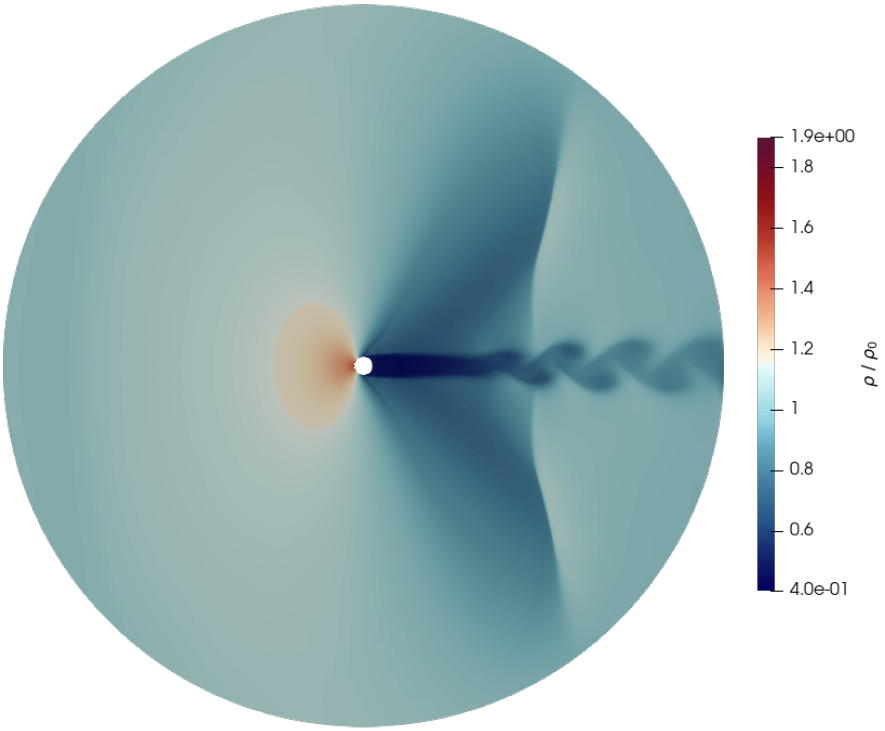

Figure 6.10: Density field for transonic continuum flow past the cylinder

6.2 Stationary One-Dimensional Shock Waves

One area in which moment methods are particularly promising is the prediction of strong shock profiles, as they contain regions of significant thermodynamic non-equilibrium. Figure 6.11 shows the BGK results of a Mach 8 shockwave, with Θ_t representing the thermodynamic temperature, while Θ_{xx}, Q_{xxx}, Θ_{yy}, and Q_{xyy}, represent the anisotropic temperatures and heat fluxes in the directions normal and transverse to the shock. This phenomenon occurs as when particles encounter a shock wave, their velocity which is normal to the shock is excited more than velocities which are transverse to it. It is only after sufficient collisions that the energy dissipates in to the other modes, and that the distribution relaxes back to equilibrium with a distribution at a higher variance, corresponding to the higher temperature gas after the shock. This effect is what results in the overshoot seen in the Θ_{xx} profile. While this overshoot can be captured by the 10-moment model, there is also heat fluxes through the shock. Due to the 10-moment model being adiabatic, this cannot be captured. This study aims to see how the model

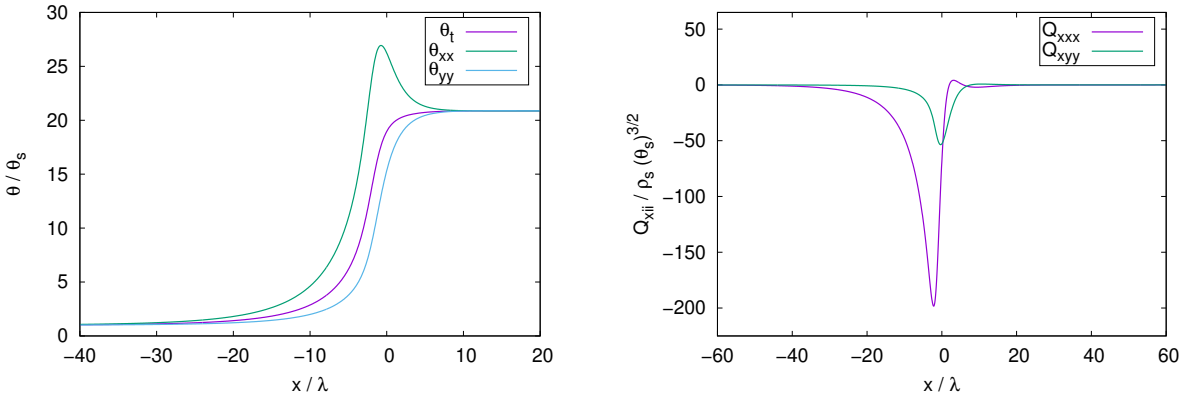

(a) Temperature profiles

(b) Heat-flux profiles

Figure 6.11: BGK results for a Mach 8 Shockwave

developed in Section 3.3.2 performs in these strong shock scenarios.

In order to see how the new models can resolve anisotropic effects in strong shocks, two steady-state shock profiles are studied, Mach 4 and Mach 8. A resolution of 2048 cells are used for the x-direction for both the BGK and 20-Moment results. A discontinuous initial condition of the Rankine-Hugoniot shock jump relations were used, with Dirichlet boundary conditions at the ends of the domain, fixed to the pre-shock and post-shock states. The shock structure was allowed to develop until convergence was reached.

The BGK velocity domain was set to be $-11\sqrt{p_s/\rho_s} \leq v_x \leq 17\sqrt{p_s/\rho_s}$ for the Mach 4 shock, and $-11\sqrt{p_s/\rho_s} \leq v_x \leq 24\sqrt{p_s/\rho_s}$ for the Mach 8 shock, in the x-direction. Both had a transverse velocity space domain of $0 \leq v_r \leq 11\sqrt{p_s/\rho_s}$, using the same axisymmetry discussed in Section 4.2. A resolution of 1000 velocity space cells was used for both directions. DSMC data was obtained using the modified SPARTA DSMC solver [51], and the Navier-Stokes solutions are obtained with the modified Hyper2D solver [50].

Figures 6.12a to 6.12f show comparisons between the models for the density, velocity, temperature, and heat-flux profile solutions for the Mach 4 shock, while Figures 6.13a to 6.13f show the same comparisons for the Mach 8 shock. Both 20-moment models have very good agreement with the BGK and DSMC data, with the rotationally improved closure having a slightly better profile than the translationally invariant only 20-moment closure.

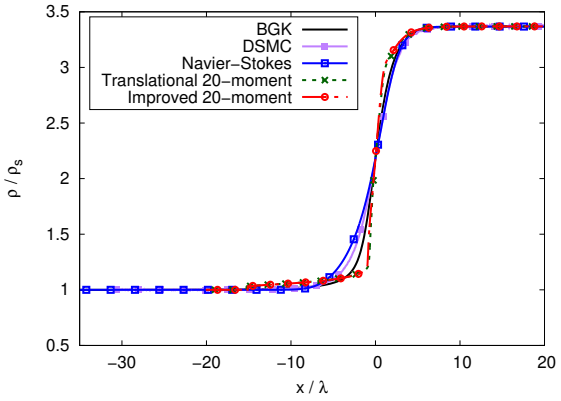

(a) Density profile

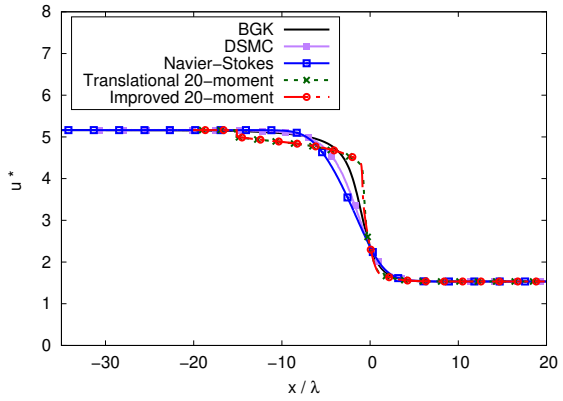

(b) x-direction velocity profile

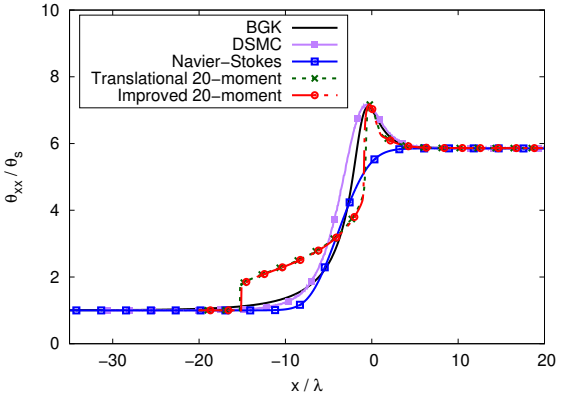

(c) x-direction temperature profile

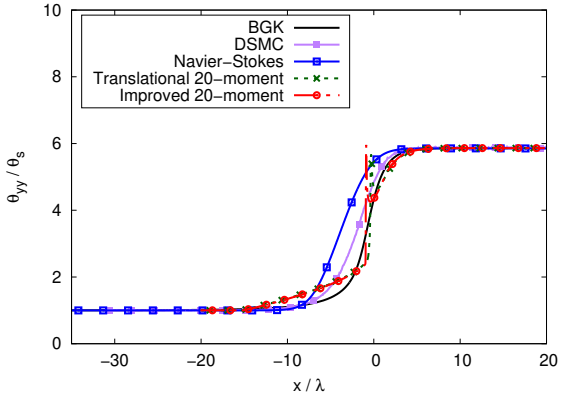

(d) Transverse temperature profile

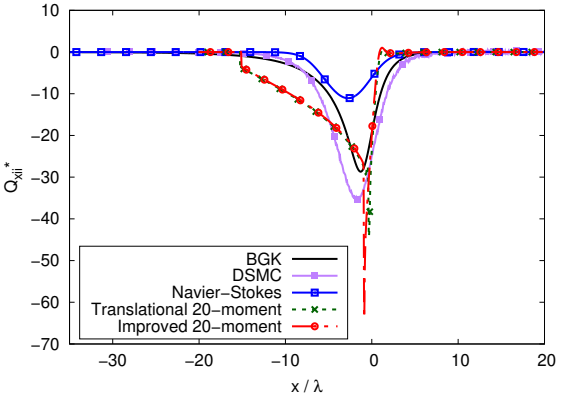

(e) x-direction heat-flux profile

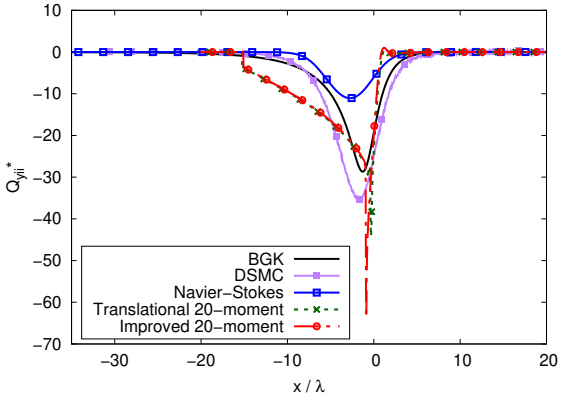

(f) Transverse heat-flux profile

Figure 6.12: Stationary Mach 4 shock profile solutions

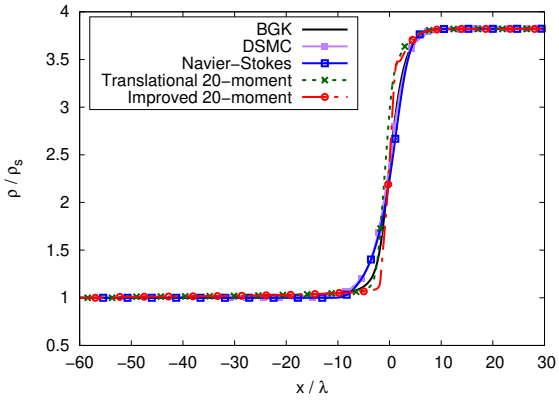

(a) Density profile

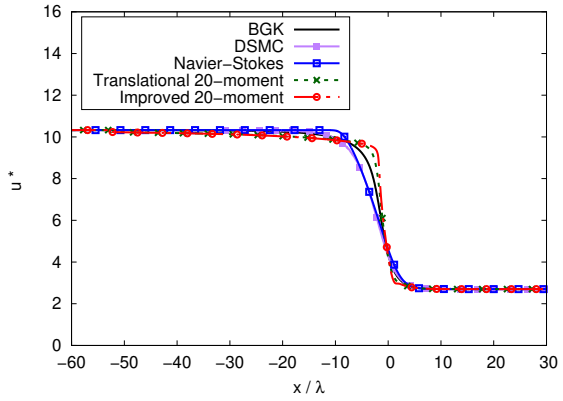

(b) x-direction velocity profile

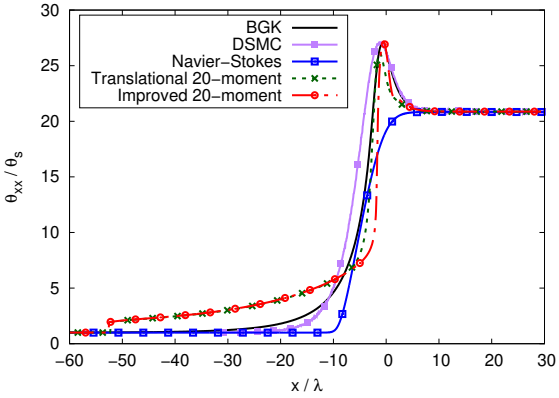

(c) x-direction temperature profile

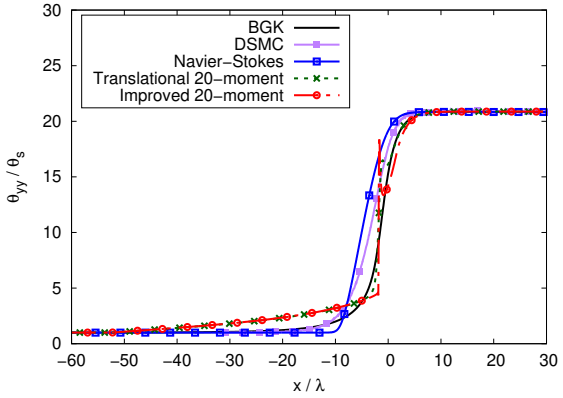

(d) Transverse temperature profile

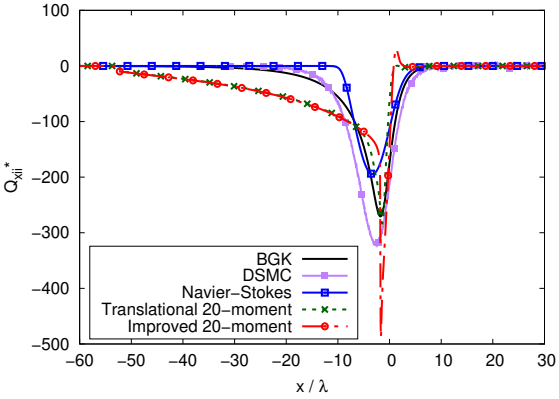

(e) x-direction heat-flux profile

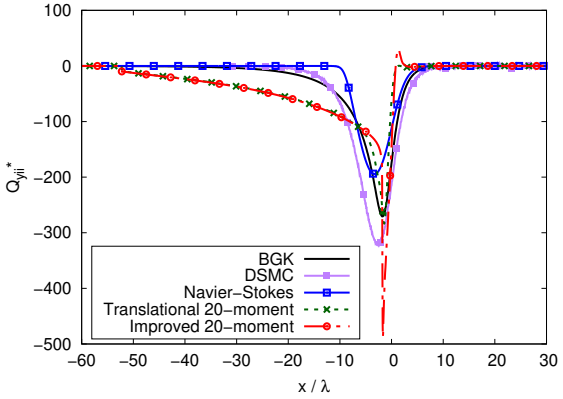

(f) Transverse heat-flux profile

Figure 6.13: Stationary Mach 8 shock profile solutions

There are many physically real and desirable structures that appear in the solutions which continuum models like Euler fail to capture. Both the temperature profiles in Figures 6.12c, 6.12d, 6.13c and 6.13d show anisotropic temperature profiles between θ_{xx} and θ_{yy}, capturing the overshoot that occurs for particles with velocities normal to the shock, before the energy is dissipated to particles with velocities transverse to the shock through collisions. The heat-flux profiles in Figures 6.13e and 6.13f are also anisotropic, and while there is some overprediction of the peak heat flux, they are still on the order of the BGK and DSMC solutions.

One minor inconvenience is that the front upstream of the shock does appear to have a small subshock. The subshocks become most apparent in the higher moments. While these are mathematical artifacts and not physically real structures, most hyperbolic systems in practical use have these artifacts as well [11]. The other notable-but-inconvenient feature is the delta shock structures seen in T_{yy}, Q_{xxx}, and Q_{xyy}. However, these spikes are confined to a few grid cells around the maximum gradient region, and does not alter the upstream/downstream states or the overall shock thickness.

6.3 Mach Reflections for Multidimensional Strong Shock Waves

To further investigate the use of these new models in non-equilibrium settings, shock reflections are studied. Sufficiently strong shocks which encounter a surface can generate structures known as Mach reflections, comprised of an incident shock, a Mach shock, and a reflected shock. The three shocks meet at the so-called triple point. An example of these structures is shown in Figure 6.14, where the initial shock wave is moving to the left with shock strength M_s. After encountering the wedge, the incident shock is denoted with I, the Mach shock with M, and the reflected shock with R.

Cases of Mach reflections are well studied in non-equilibrium gas dynamics [1, 52–54], as they can result in regions with significant translational non-equilibrium. Mach reflections are also an important part of cellular detonation structures. When chemi-

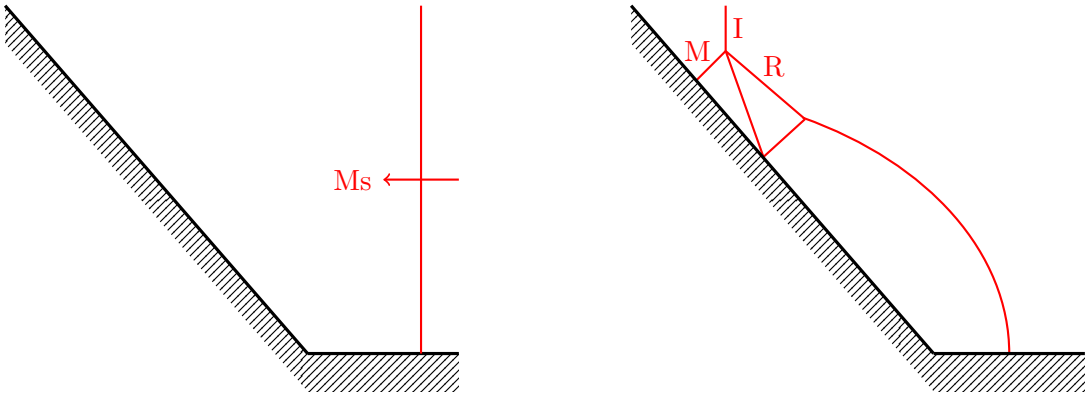

(a) Shock prior to encountering wedge (b) Double Mach reflection after wedge

Figure 6.14: Illustration of the double Mach reflection shock structure

cal reactions are coupled with the shock wave, non-equilibrium effects like temperature anisotropy and heat-fluxes, particularly at the triple point, have been theorized to be relevant to the chemical kinetics [55–57]. Recent developments have been made with the 10-moment model and including these non-equilibrium effects in reaction rates [58]. While the present work does not consider chemical effects, the importance of resolving these regions of non-equilibrium can still be investigated, as they are invisible to traditional models.

Experiments with Argon gas done by Deschambault and Glass [1] are used as a reference for the numerical cases solved using the 20-moment model. Both a single Mach reflection and a double Mach reflection from their study are replicated, the former being used to investigate the role of appropriate boundary conditions, and the latter being used to investigate non-equilibrium effects in the setting of a stronger shock.

To probe the effects of proper boundary conditions, a single Mach reflection case was studied. For this case, a Mach 3.05 shock encounters a 20° wedge, and the resulting interaction will be studied with two different accommodation coefficients, $\chi = 0$ and $\chi = 1$. The wall is assumed to retain the temperature of the pre-shocked state in order to see the effect on the structure's development. A 4096×4096 computational domain was used, shown in Figure 6.15, with 16×16 blocks. The mesh was refined so that the layer closer to the wall was denser, to allow more accurate boundary layer and shock-structure development.

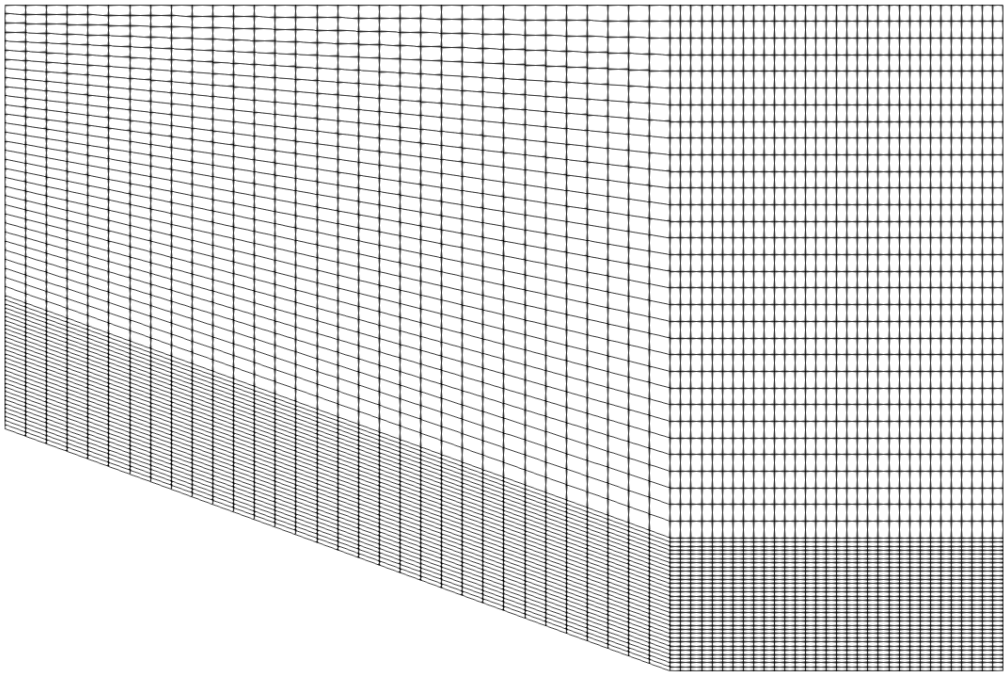

Figure 6.15: Single Mach reflection mesh

The experiments of Deschambault and Glass are presented in Figure 6.16. Figure 6.17 shows the resulting density profiles, Figure 6.18 the resulting pressure profiles, and Figure 6.19 the resulting thermodynamic temperature profiles. The density fields match relatively well with the interferogram images, and there is only a very small difference between the locations of the triple point. While the jetting at the bottom of the slip line is marginally different, as can be seen in the density and temperature fields, this difference has little impact on the resulting shock structure. The pressure field has little difference between the two accommodation coefficients. For both cases, probing the results shown in Figures 6.18 and 6.19 for the condition number of the respective tensors, the anisotropy at the triple point was found to be

$$\kappa\left(T_{ij}\right) = \kappa\left(P_{ij}\right) \approx 1.2\,, \tag{6.3}$$

as the peak value across a region of about 30×30 cells, for both accommodation coefficients. This indicates that the principal axis of the tensors is about 20% larger than the minor axes. As mentioned, both result in very similar cell structure, with the only difference being that the Mach shock is weakened slightly. Previous numerical studies of

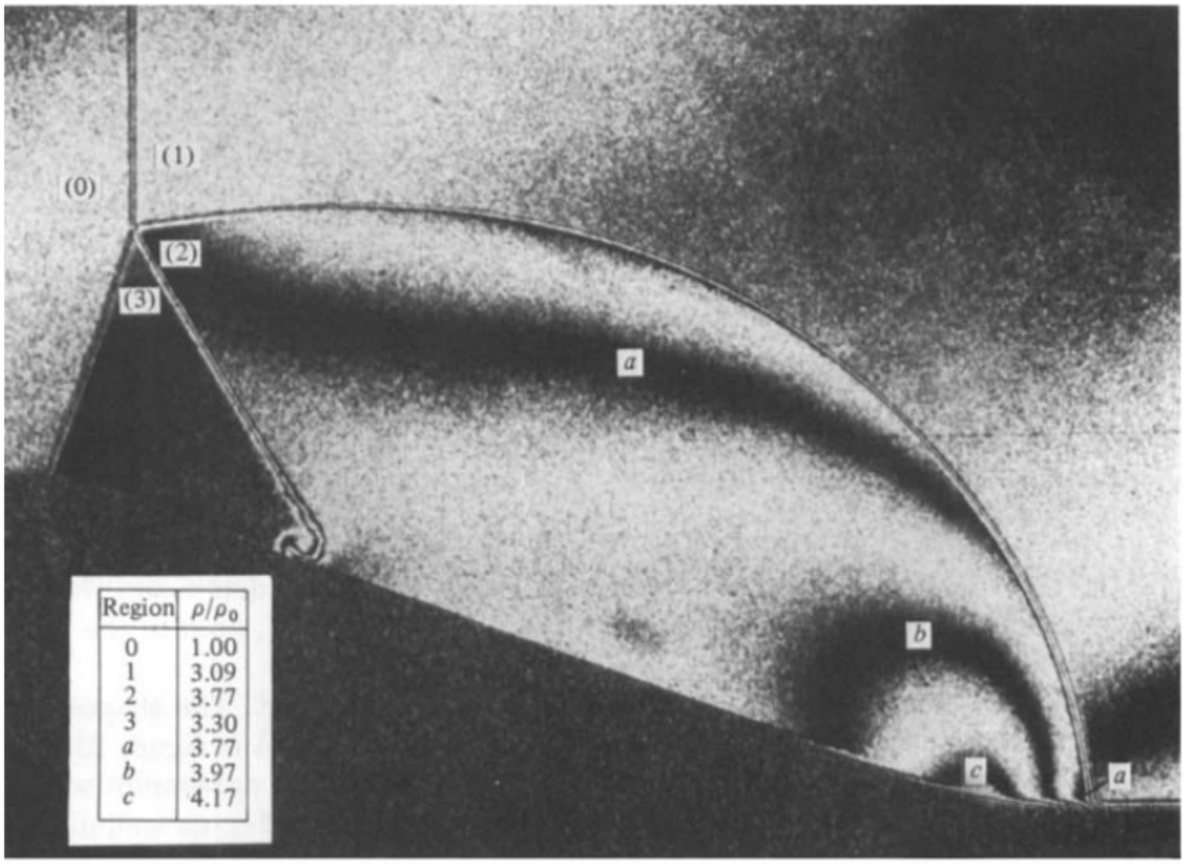

Figure 6.16: Experimental density field [1]

these phenomena have assumed fully specular walls [58], and these results indicate that, while there are differences when assuming a fully accommodating wall, they are marginal for the development of the shock structure.

As a second case with a larger region of non-equilibrium, a double Mach reflection is studied. A Mach 7.1 shock encounters a 49° wedge, generating two triple points that can be investigated for their anisotropies. This was performed using the third-order scheme, fully specularly reflecting walls, at a resolution of 5120×4096. The mesh is shown in Figure 6.20, with each block representing a 64×64 grid. The results of the double Mach reflection study are shown in Figures 6.21, comparing the density to the experimental result, and in Figure 6.22, showing the thermodynamic pressure and temperatures.

While the density profiles shown in Figure 6.21 have the same range of density values between the experimental and numerical results, it is clear that the structure formed by the double Mach reflection are much larger than those seen in the experiment. To see if the reporting of the original case might have a mistake, the exact same calculation for

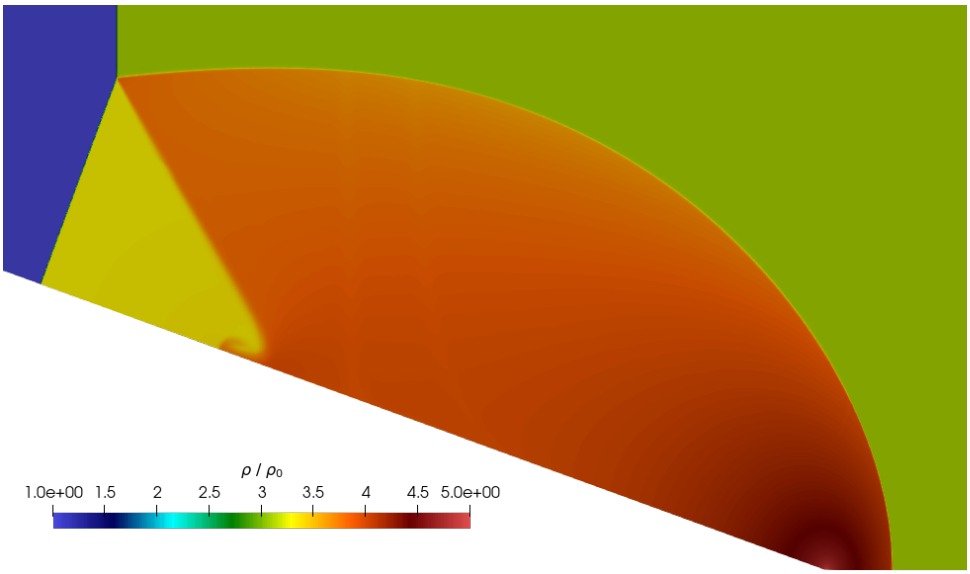

(a) Specular wall

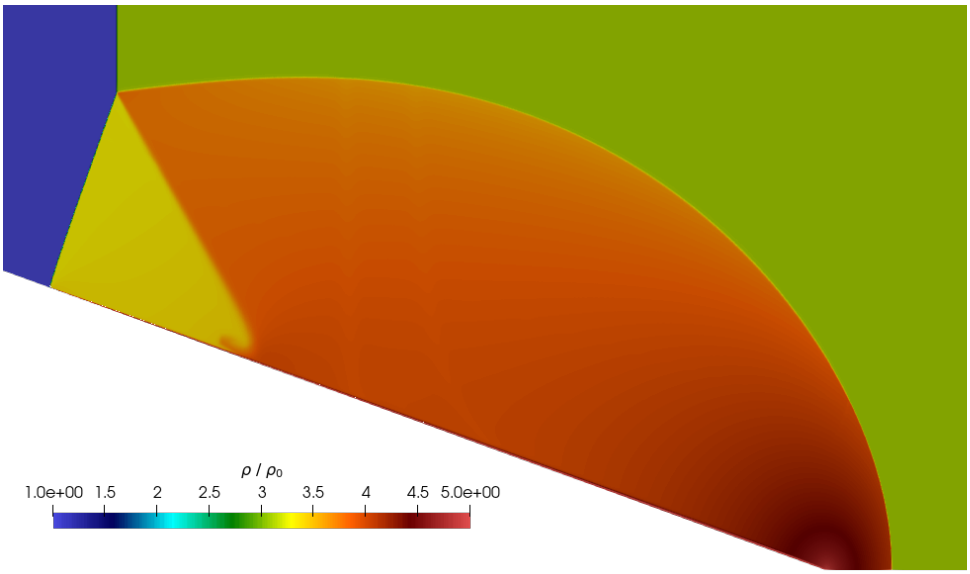

(b) Accommodating wall

Figure 6.17: Comparison of density profiles for double Mach reflection

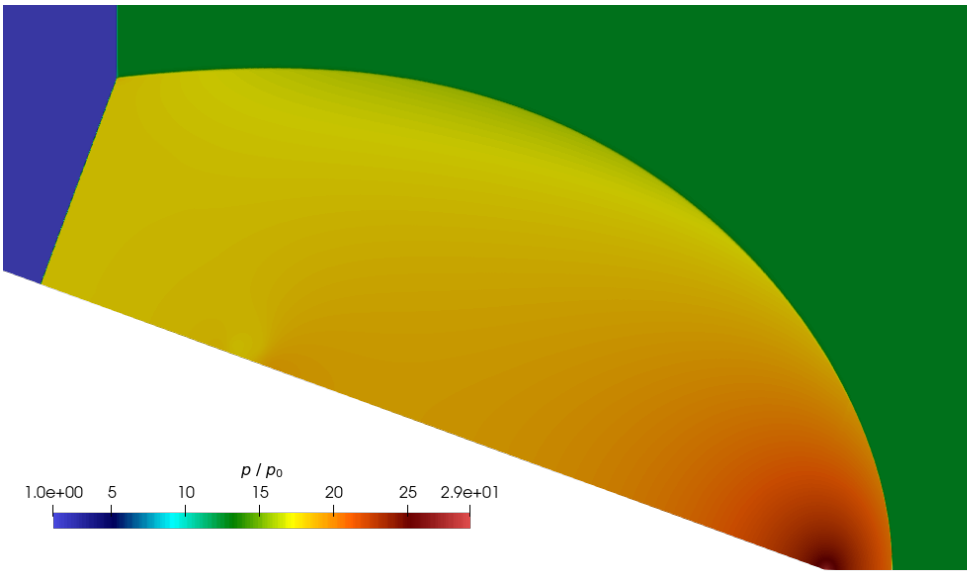

(a) Specular wall

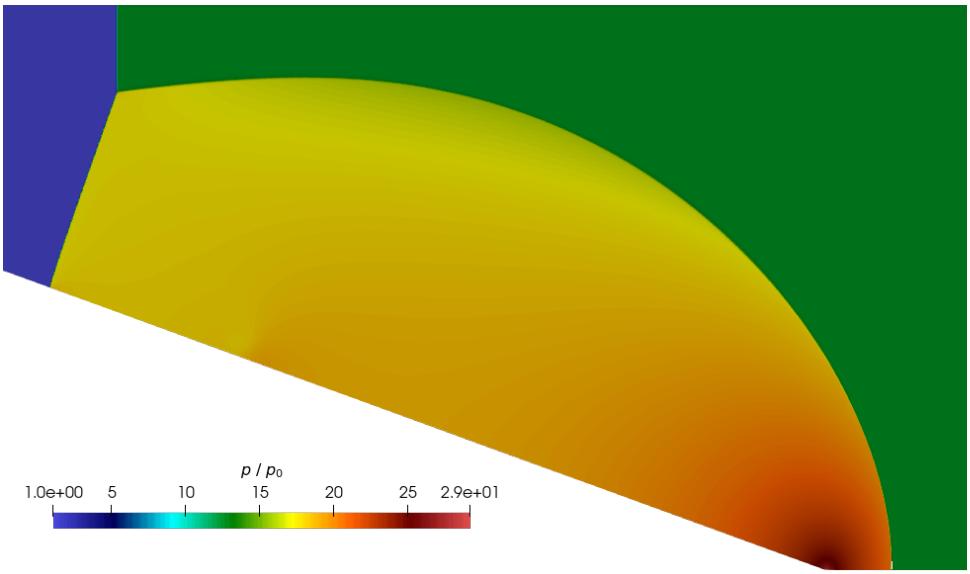

(b) Accommodating wall

Figure 6.18: Comparison of pressure profiles for double Mach reflection

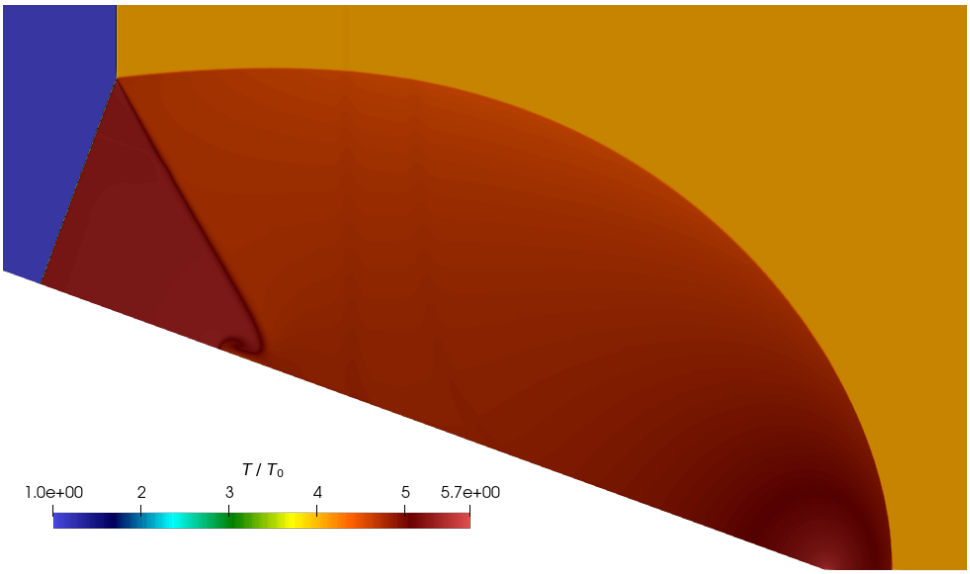

(a) Specular wall

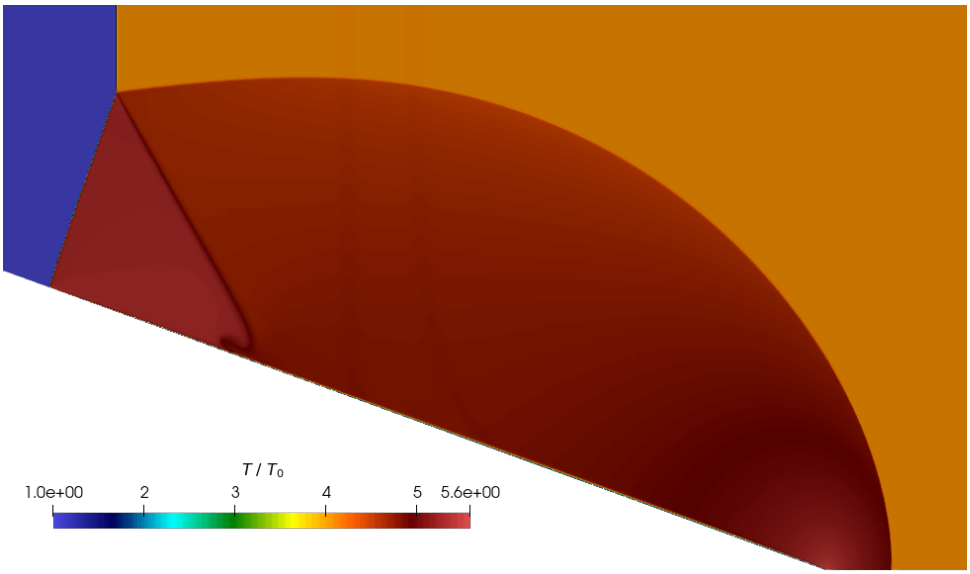

(b) Accommodating wall

Figure 6.19: Comparison of temperature profiles for double Mach reflection

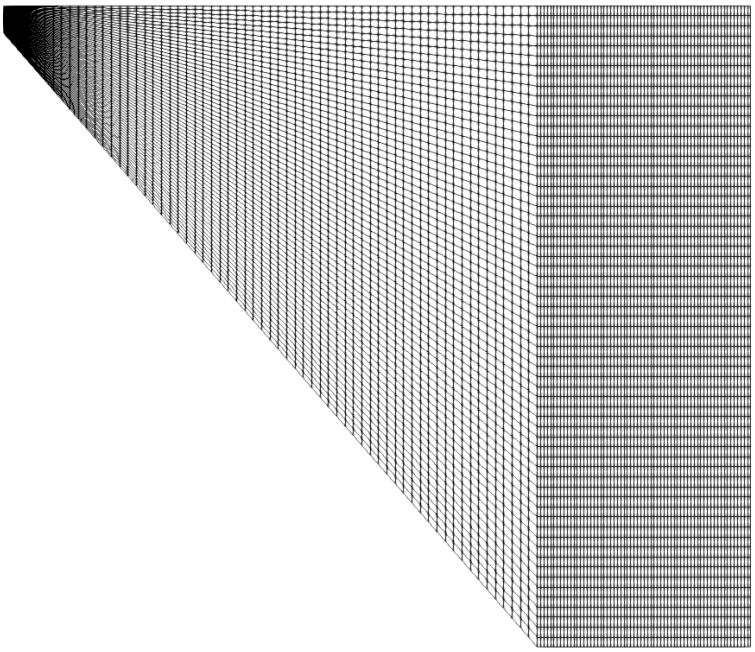

Figure 6.20: Double Mach reflection mesh

the double Mach reflection was done with the Euler equations. The results of the density field are shown in Figure 6.23. These again do not match the experiment, and instead match the 20-moment result. This gives an indication that the shock might have been of a different strength than the Mach 7.1 shock reported by Deschambault and Glass, or that imperfections at the corner in the physical model of the experiment can have a greater impact on the resulting shock structure, which are not reflected in the numerical solutions.

While the shock structure is not accurately reflected in the double Mach reflection results, the resulting triple point can still be investigated. Probing the temperature and pressure fields shown in Figure 6.22, the condition number of the pressure and temperature tensors was found to be

$$\kappa\left(T_{ij}\right)_1 = \kappa\left(P_{ij}\right)_1 \approx 2.92\,, \tag{6.4}$$

as the peak value for the first triple point, across a region of about 30×30 cells, and

$$\kappa\left(T_{ij}\right)_2 = \kappa\left(P_{ij}\right)_2 \approx 1.04\,, \tag{6.5}$$

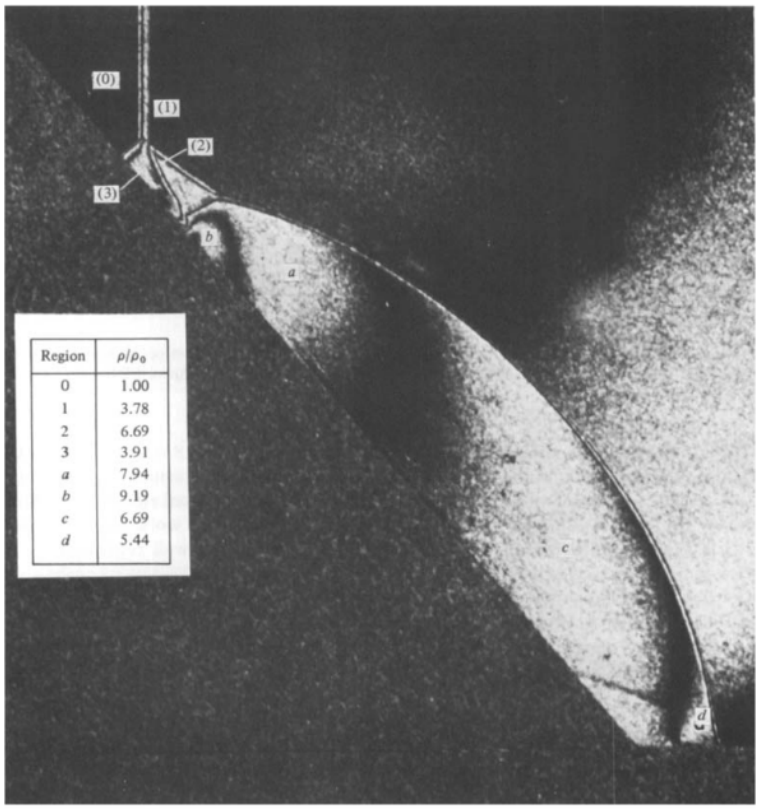

(a) Experimental density interferogram image [1]

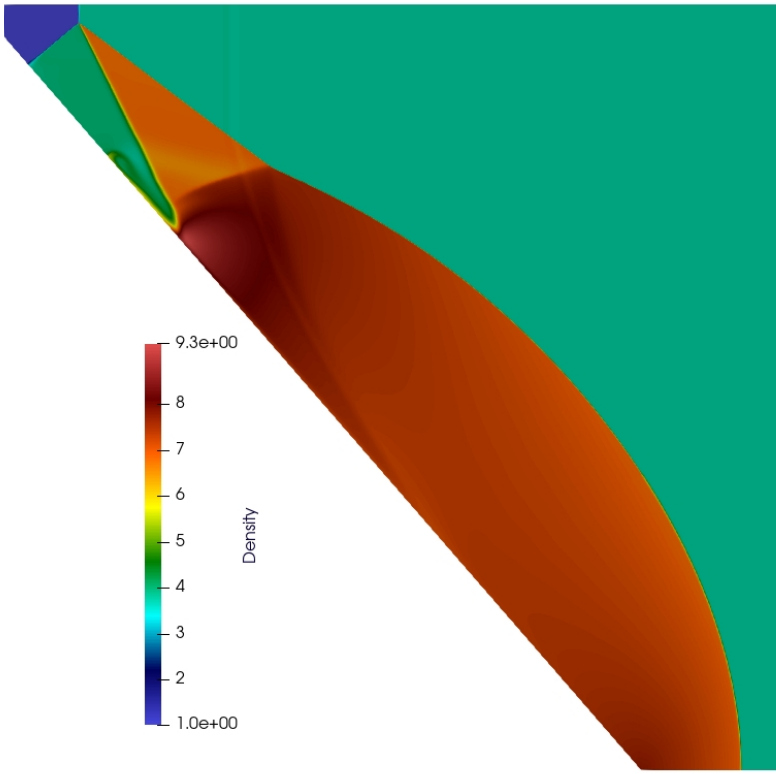

(b) 20-moment density field

Figure 6.21: Comparison of density profiles for double Mach reflection

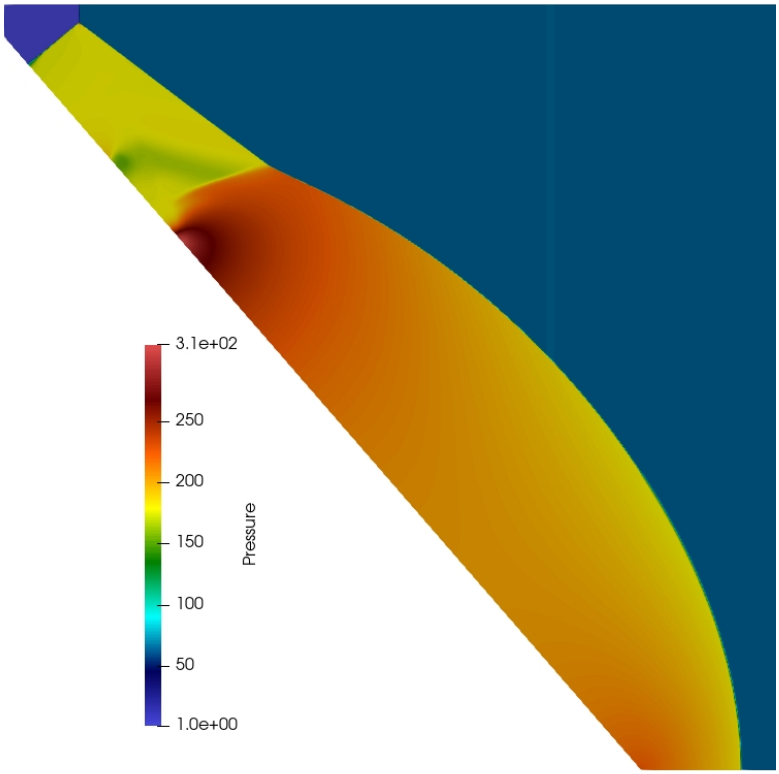

(a) Pressure field

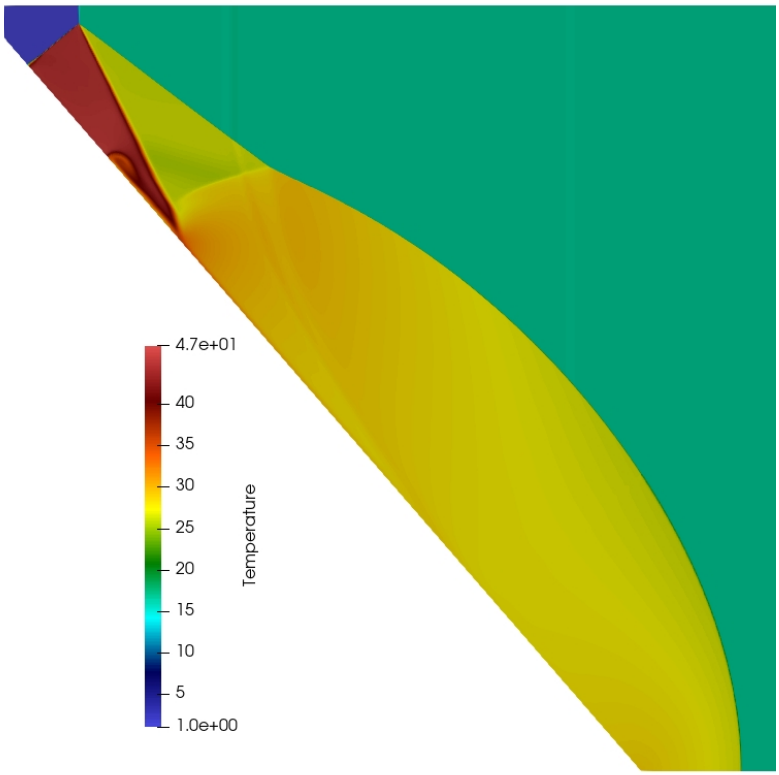

(b) Temperature field

Figure 6.22: Thermodynamic pressure and temperature for double Mach reflection

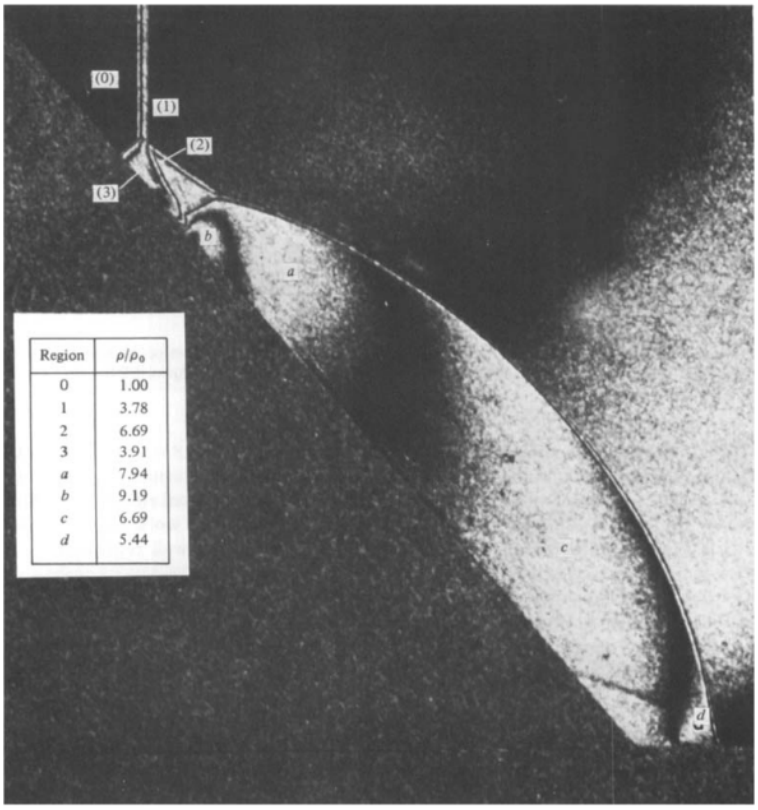

(a) Experimental density interferogram image [1]

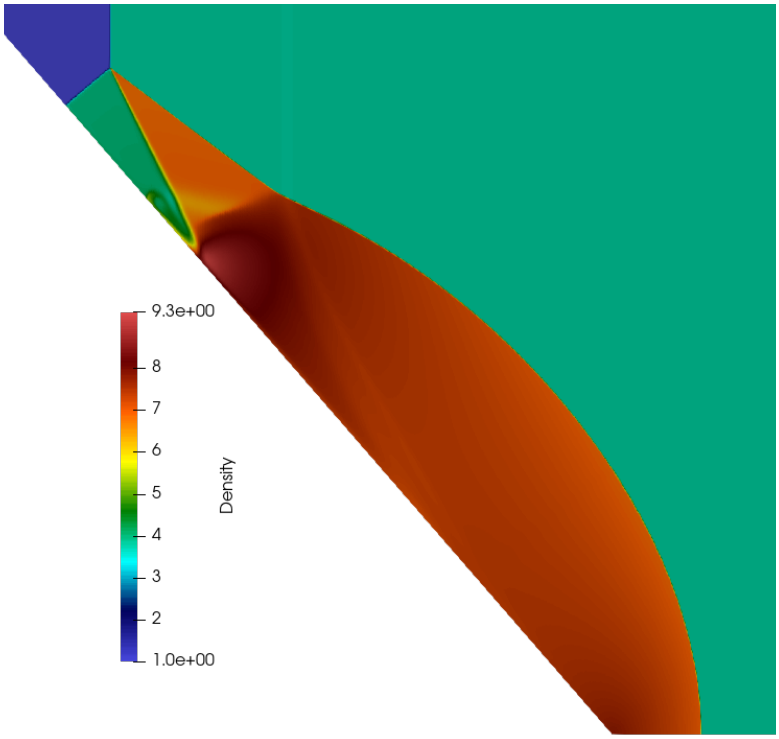

(b) Euler density field

Figure 6.23: Comparison of density profiles for double Mach reflection, using the Euler equations

as the peak value for the second triple point, across a region of about 10×10 cells. This implies that at least the first triple point is highly anisotropic, with the principal axis of the tensor being nearly three times larger than the minor axes. The second, being generated from the second Mach shock and the reflected shocks, is much weaker, however it does still have some anisotropy, with the principal axis of the temperature tensor being about 4% larger than the transverse axes.

6.4 Plate Crossflow for Rarefied Multidimensional Strong Shock Waves

As an extension of the one-dimensional shock and cylinder flow studies, the final problem of interest is supersonic flows past objects in a rarefied setting, replicating previous studies on moment methods for similar cases [59]. As BGK is prohibitively expensive for this extreme of a case, the 20-moment model is compared against DSMC data. Again, the same two shock strengths were studied, Mach 4 and Mach 8, at a Knudsen of 0.1 to allow large regions of thermodynamic non-equilibrium to develop. An illustration of the domain is shown in Figure 6.24, and is initially filled with a gas moving at the appropriate speed. The red boundaries were set to be specularly reflective walls with $\chi = 0$, the blue boundaries to be fixed to the initial state, the green to extrapolate from the previous cells state, and the purple boundary is the axisymmetry line. A computational domain of 1152×384 was used, with a final time of $t_{final} = 100L\sqrt{P_0/\rho_0}$, where P_0 and ρ_0 are the initial upstream pressure and density. The first-order scheme was used, due to the difficulty of resolving the infinitely thin corner of the plate with the 20-moment model and the third-order scheme. For both flows, the resulting field and a plot of the moments along the axisymmetry line are presented.

Figures 6.25, 6.26, 6.27, and 6.28, show the density, thermodynamic temperature, temperature anisotropy, and heat-flux results for the Mach 4 shock. These results are quite impressive, accurately capturing the density and thermodynamic temperature profiles when compared against the DSMC data. The subshock, which is seen in the one-

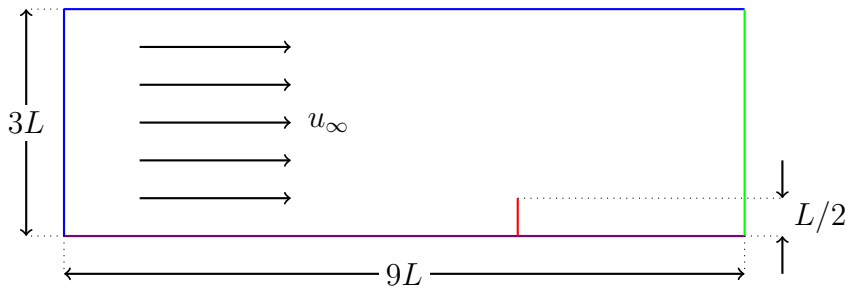

Figure 6.24: Illustration of supersonic plate crossflow domain

dimensional results, can again be seen in the temperature and temperature anisotropy fields, where the 20-moment model overpredicts the upstream propagation of T_{xx}. This is a minor inconvenience, as the more important features, such as the temperature overshoot inside the shock, as well as the stagnation temperatures for both modes are accurately captured. Behind the plate, both DSMC and the 20-moment model have difficulties, as the density nearly becomes a vacuum. While the 20-moment model underpredicts the drop in T_{xx} due to particles not moving in the x-direction, and the increase in T_{yy} as collisions carry the energy down from the corner, there is a lot of noise in the DSMC results for the heat flux, while the 20-moment model is much more spatially coherent. There is also a noticeably larger temperature anisotropy at the corner of the plate for the 20-moment model than in the DSMC result. This mostly pertains to the lack of rotational invariance in the 20-moment model.

Figures 6.29, 6.30, 6.31, and 6.32, show the density, thermodynamic temperature, temperature anisotropy, and heat-flux results for the Mach 8 shock. These results are unfortunately substantially worse than those of the Mach 4 shock. While the symmetry line plots match quite well, the fields show how the 20-moment model can begin to break down. Due to the subshock, information in the post-shock state can propagate upstream past the shock-structure and all the way to the subshock front. In the weaker Mach 4 case, this effect is contained and does not have a notable effect on the solution. But in the stronger Mach 8 case, the excessive anisotropies that the 20-moment model predicts at the corner of the plate can propagate past the shock. This results in unsteadiness ahead of the shock, polluting the solution. While this is unfortunate, it is not completely devastating for simulating strong shocks with models of this style. The DSMC results also show

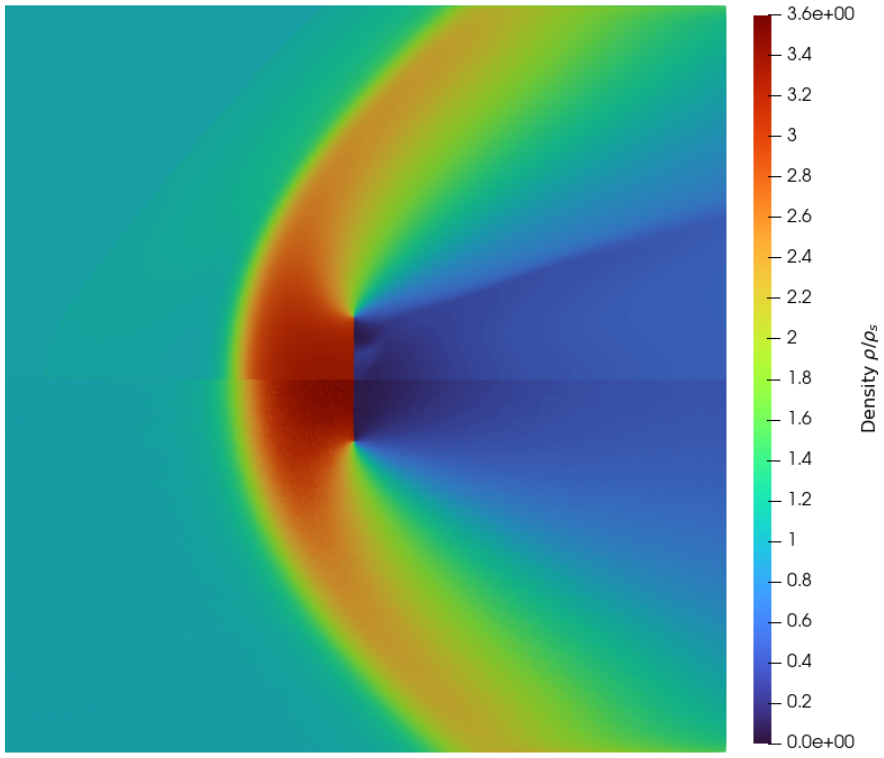

(a) Density field

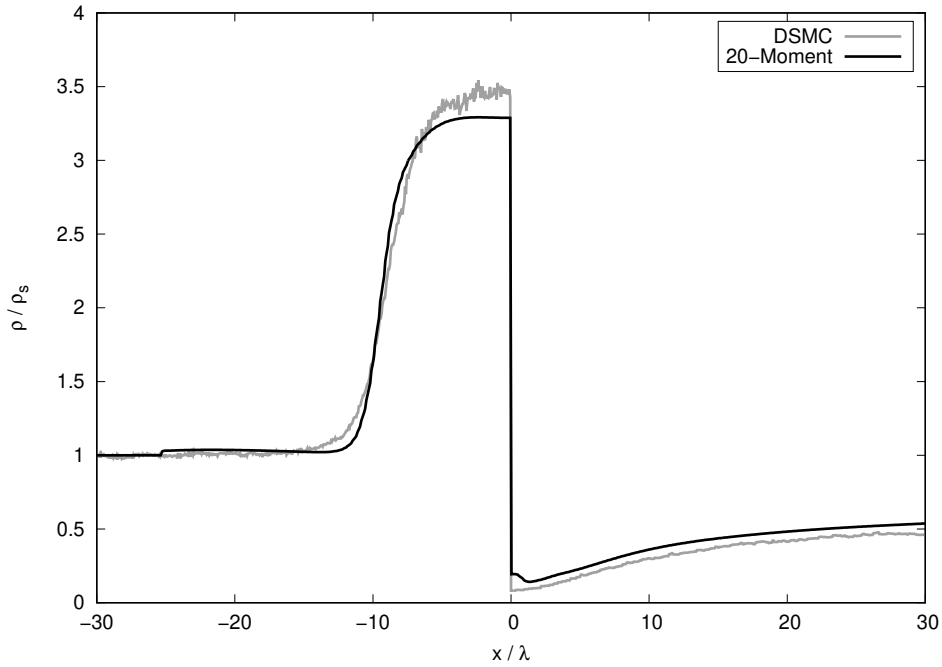

(b) Symmetry line profile

Figure 6.25: Mach 4, Knudsen number 0.1, plate crossflow density

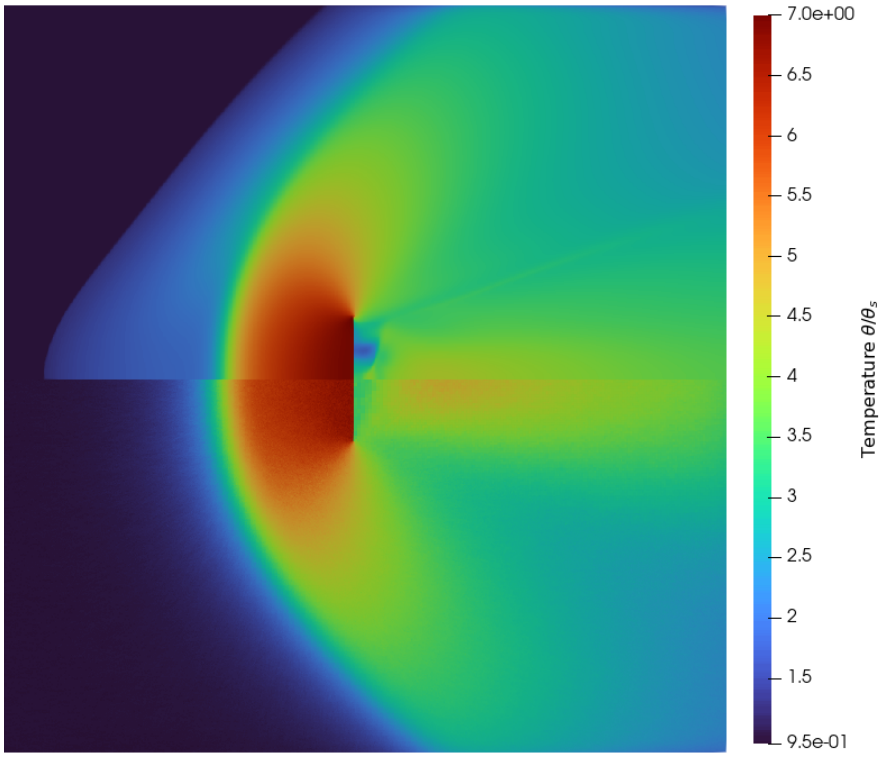

(a) Thermodynamic temperature field

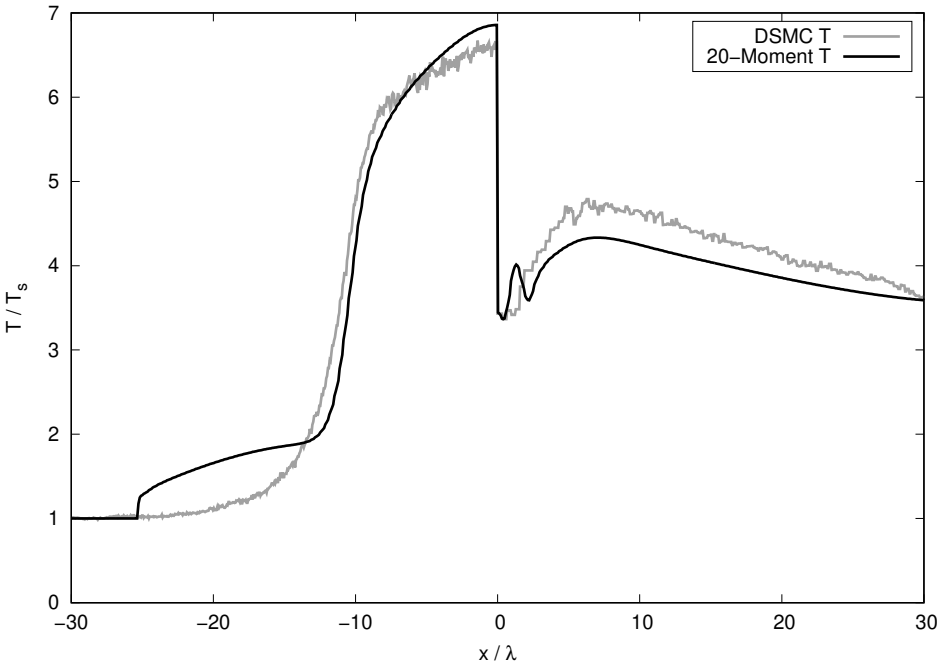

(b) Symmetry line profile

Figure 6.26: Mach 4, Knudsen number 0.1, plate crossflow thermodynamic temperature

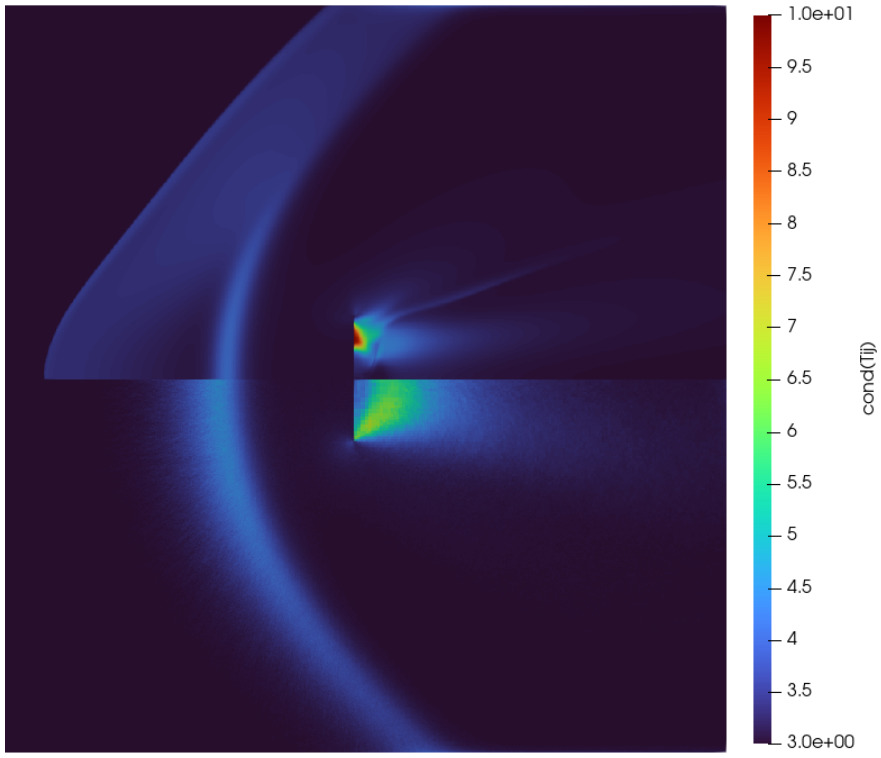

(a) Temperature anisotropy field

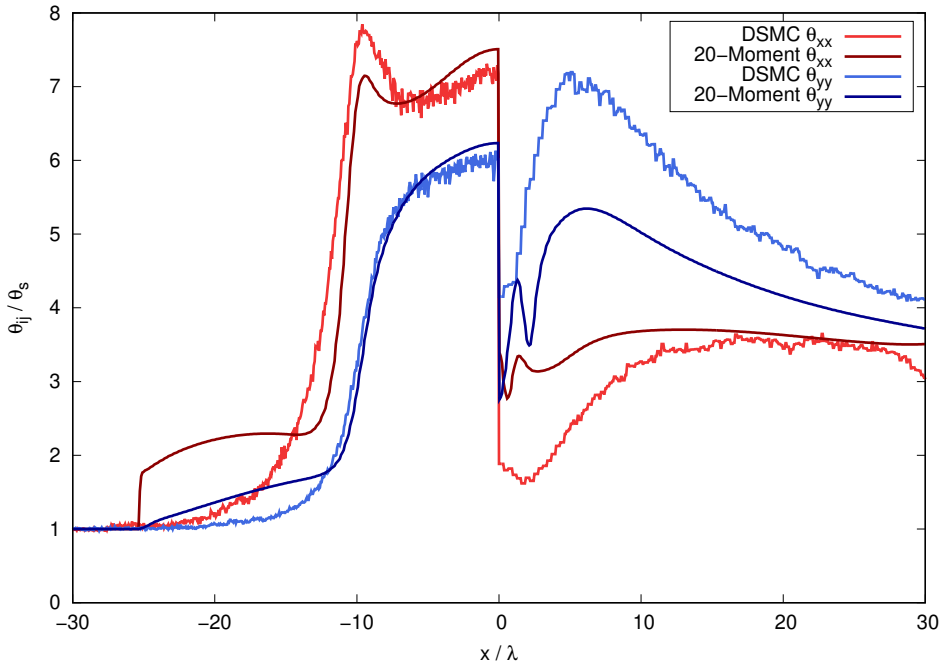

(b) Symmetry line profile

Figure 6.27: Mach 4, Knudsen number 0.1, plate crossflow anisotropic temperatures

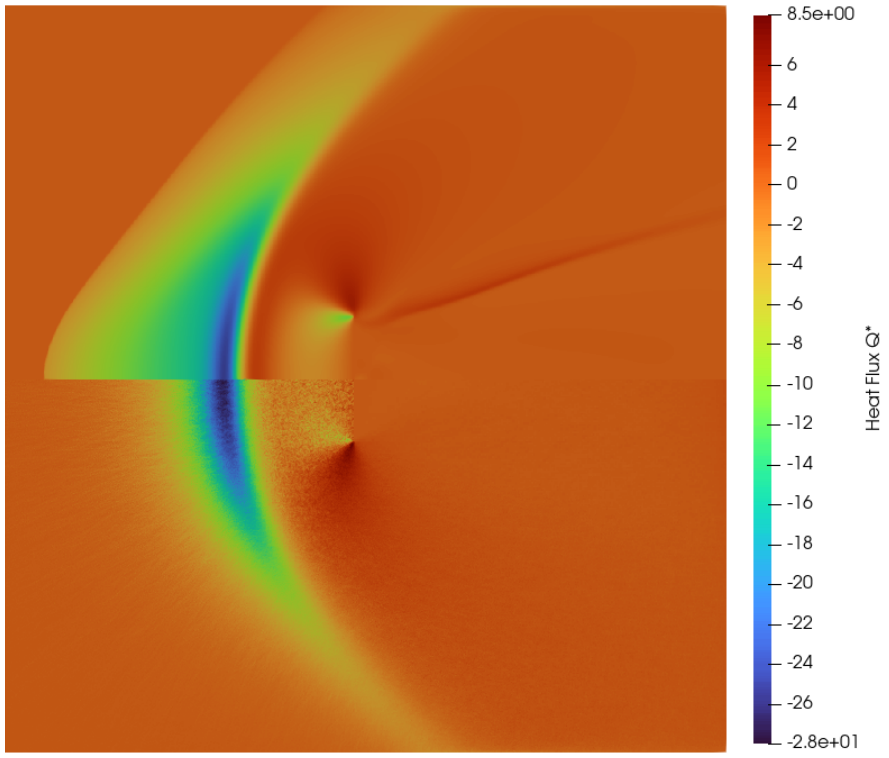

(a) Heat-flux field

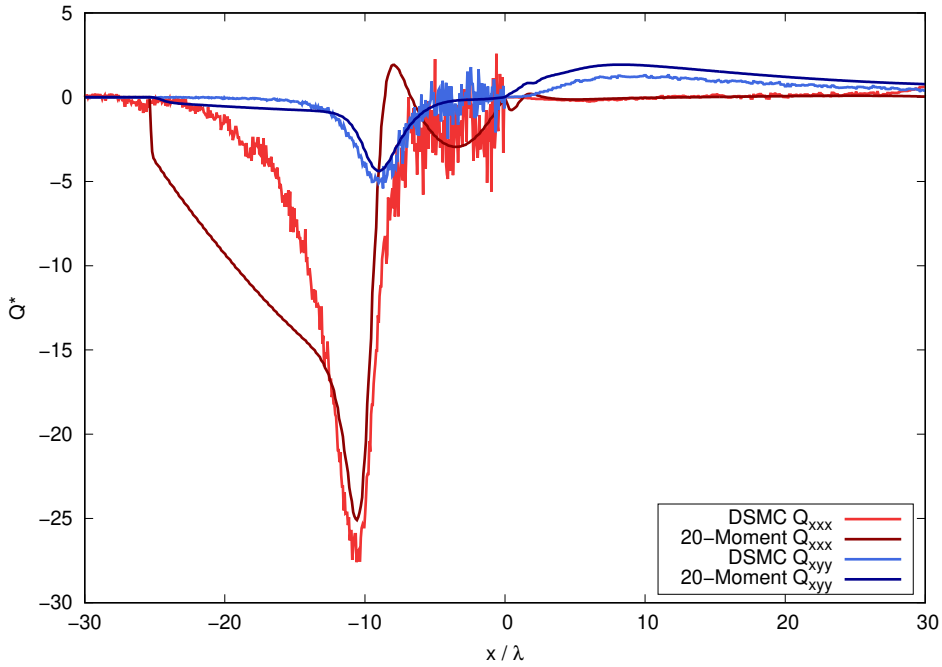

(b) Symmetry line profile

Figure 6.28: Mach 4, Knudsen number 0.1, plate crossflow thermodynamic temperature

excessive upstream propagation of anisotropies, with streaking upstream of the shock in the $\kappa(T_{ij})$ field. With more tuning of the closing fluxes, and a better understanding of the rotational invariance issue, this effect could be mitigated and the region of physical validity of the 20-moment model extended further.

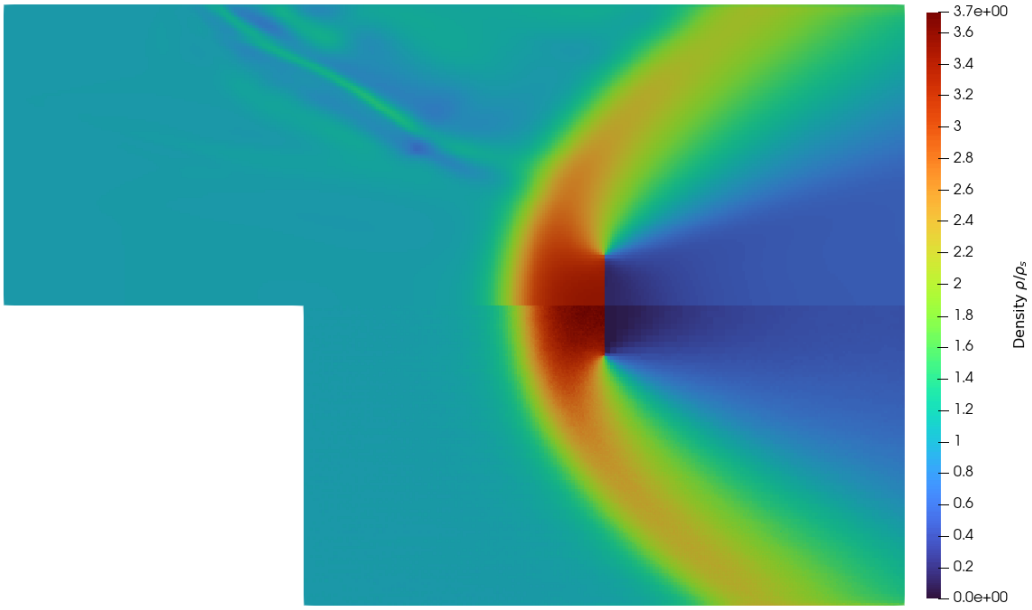

(a) Density field

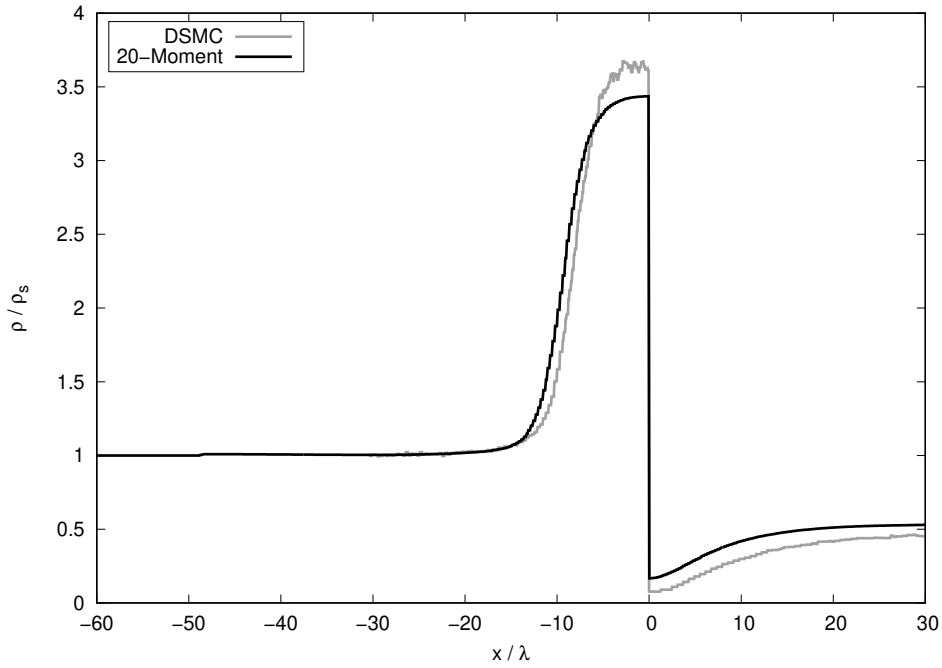

(b) Symmetry line profile

Figure 6.29: Mach 8, Knudsen number 0.1, plate crossflow density

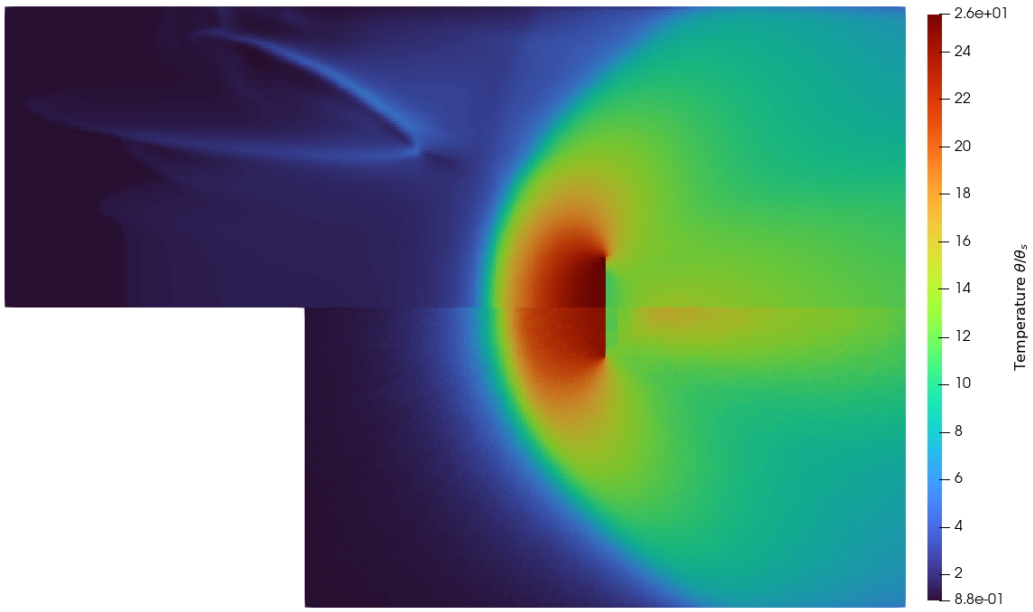

(a) Thermodynamic temperature field

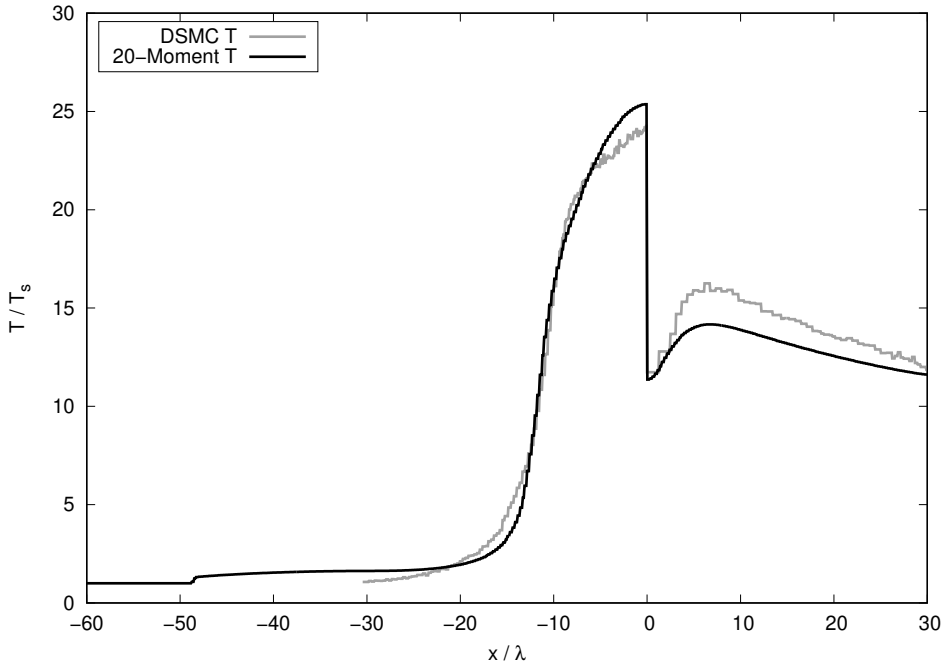

(b) Symmetry line profile

Figure 6.30: Mach 8, Knudsen number 0.1, plate crossflow thermodynamic temperature

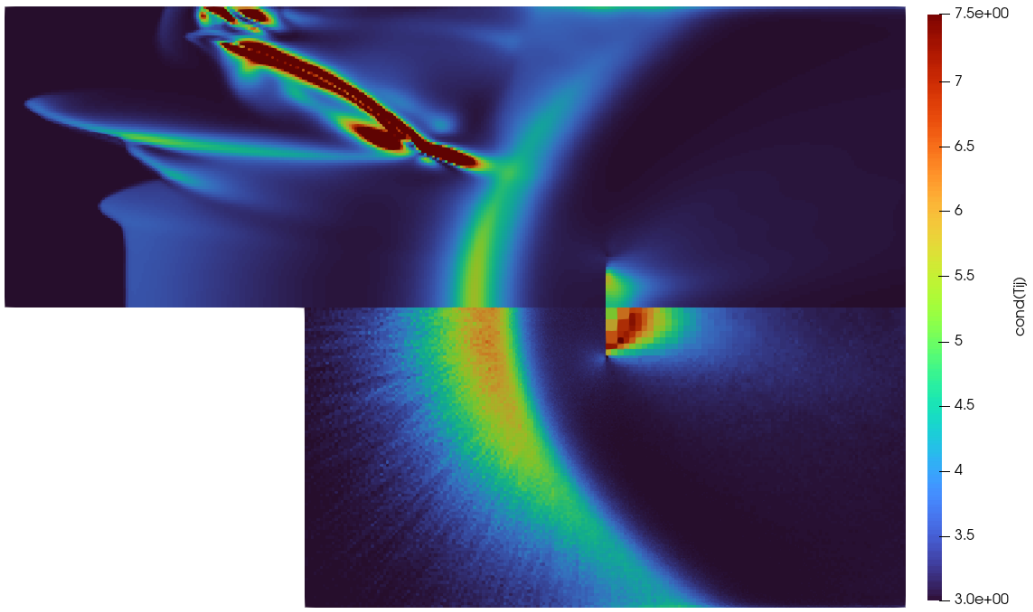

(a) Temperature anisotropy field

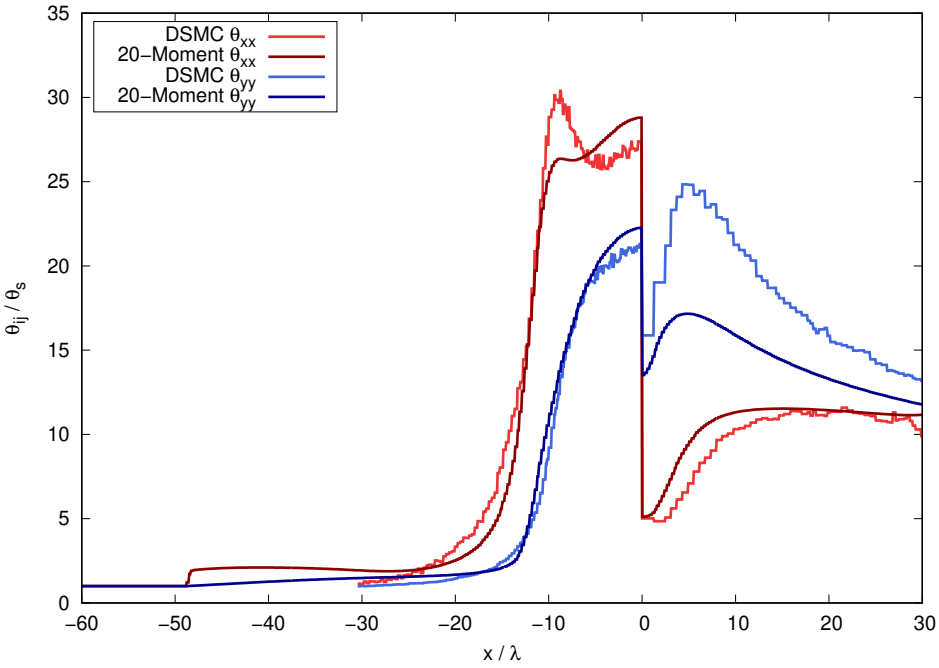

(b) Symmetry line profile

Figure 6.31: Mach 8, Knudsen number 0.1, plate crossflow anisotropic temperatures

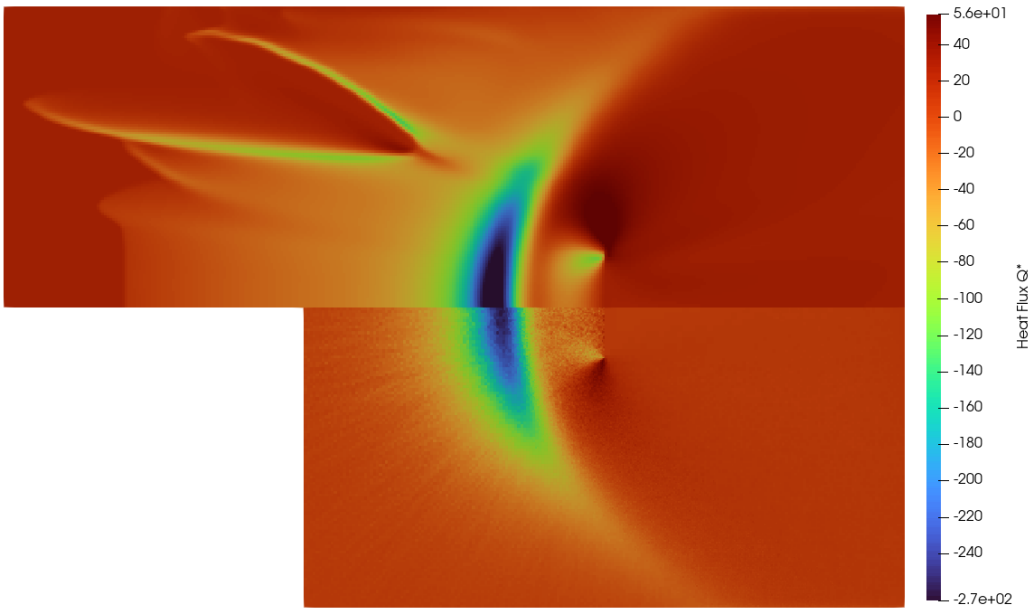

(a) Heat-flux field

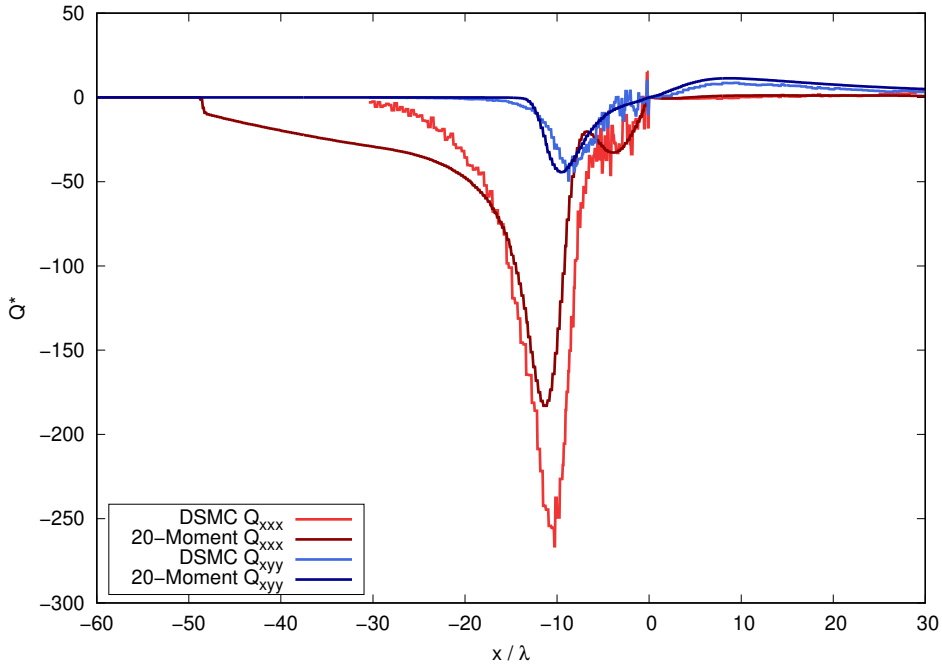

(b) Symmetry line profile

Figure 6.32: Mach 8, Knudsen number 0.1, plate crossflow thermodynamic temperature

Chapter 7

Conclusion

In this work, a technique for the construction of robustly hyperbolic, multidimensional moment closures is proposed. These models are well posed, and in balance law form, for any physically realizable state of the gas. They demonstrate linear stability, and can accurately capture a variety of non-equilibrium effects such as temperature anisotropies and heat fluxes for the simple demonstrative cases across a breadth of regimes. Despite some minor deficiencies in the model pertaining to its rotational properties, these models have great promise for non-equilibrium gas flow predictions.

This work has also resulted in a new formulation of the Knudsen-layer boundary condition approximation. This new variant of Steger-Warming flux splitting can be used to accurately capture the effect of half-velocity-space integrals without requiring a distribution function. This formulation is applicable not only to the new models developed in this work, but any moment closure model which is robustly hyperbolic and has real valued wave speeds. It has been demonstrated that they accurately capture the fluxes of the 10-moment equations, and continue to agree for higher-order models through all the regimes of interest. When coupled with the new models developed in this work, they demonstrate higher physical fidelity when applied to simple flows.

Finally, it has been explored how the models can be applied to non-equilibrium flow predictions. They accurately capture many of the physical effects which have previously only been seen in these regimes through the use of the more computationally expensive

counterparts to the models. There is great promise for the utilization of these new higher-order moment methods for the prediction of gas flows outside of local thermodynamic equilibrium, allowing for the use of traditional and efficient CFD techniques in these exotic regimes.

7.1 Future Work

While the models presented in this work achieve many of the desirable properties which were the goals of this work, they have been developed in a simplified setting. There are still many regimes in which these new models can provide important insights for non-equilibrium physics in realistic three-dimensional settings. This work has also been completed entirely for a monatomic gas, which allows for easy modelling of the hyperbolic part of the Boltzmann equation, but there are many practical settings in which it would be desirable to extend the model further for the greatest impact. This can include polyatomic gases or plasma flows. However, due to the structure of the models, pathways for these extensions are relatively straightforward.

7.1.1 Extensions for Polyatomic Gases

Polyatomic gases are a much more widely present in typical engineering applications than the monatomic gases discussed in this work. Extension of 20-moment models would require the consideration of additional internal energy modes of the gas molecules. Extensions to the 10-moment equations for a polyatomic gas have already been done [37, 60], and similar pathways could be used for the new models.

To extend the framework to a diatomic gas, the internal energy modes need to be considered. From kinetic theory, gases with these energy modes have the distribution function,

$$\mathcal{F}\left(x_i, v_i, \omega_r, t\right) , \tag{7.1}$$

only differing from the one presented in Chapter 2 by the variable ω_r, representing the internal degrees of freedom of the molecules, and the index r representing the axis of

rotation, vibration, or other modes. This gives additional moments to consider,

$$\rho e_{rr} \,, \quad \text{and} \quad q_{irr} \,, \tag{7.2}$$

being the internal energy density and internal heat fluxes of the molecules, respectively. Conveniently, for the extension of the 20-moment closure, the internal energy is fully decoupled. The heat flux is not, but at least for 20-moment closures like those studied in depth in this work, coupling is no more difficult than it was between the other heat fluxes. Conceptually, diatomic extensions to the model involve no more than additional rows in the flux Jacobian, below those seen in Figures 3.3 and 3.4.

7.1.2 Extensions for Magnetohydrodynamics

The 10-moment equations and other maximum entropy inspired closures have been used to great effect in plasma applications [8, 61–63]. Extensions of the model into this setting would require the addition of the external acceleration fields shown in Equation (2.7) that were neglected in Chapter 2. For monatomic plasmas, like the models developed in this work, the acceleration field for plasma's takes the form,

$$a_i = \frac{e_s}{m_s} \left(\boldsymbol{E}_i + \epsilon_{ijk} v_j \boldsymbol{B}_k \right) \,, \tag{7.3}$$

where $\boldsymbol{E}_i$ represents the electric field, $\boldsymbol{B}_k$ represents the magnetic flux density, e_s and m_s are the charge and mass of a species, s. The final symbol, ϵ_{ijk}, is the Levi-Civita epsilon, very similar to the Kronecker delta from Equation (2.22), and defined as

$$\epsilon_{ijk} = \begin{cases} +1 & \text{if } (i,j,k) = (x,y,z),\ (y,z,x), \text{ or } (z,x,y), \\ -1 & \text{if } (i,j,k) = (z,y,x),\ (x,z,y), \text{ or } (y,x,z), \\ 0 & \text{if } i = j,\ i = k, \text{ or } j = k. \end{cases} \tag{7.4}$$

The electric field can then be defined from Maxwell's equations of electromagnetism,

$$\varepsilon_{ijk}\frac{\partial \mathbf{E}_k}{\partial x_j} = -\frac{\partial \mathbf{B}_i}{\partial t}\,, \tag{7.5}$$

$$\varepsilon_{ijk}\frac{\partial \mathbf{B}_k}{\partial x_j} = \mu_0 \mathbf{J}_i + \mu_0\varepsilon_0\frac{\partial \mathbf{E}_i}{\partial t}\,, \tag{7.6}$$

$$\frac{\partial \mathbf{E}_i}{\partial x_i} = \frac{\rho_c}{\varepsilon_0}\,, \tag{7.7}$$

$$\frac{\partial \mathbf{B}_i}{\partial x_i} = 0\,. \tag{7.8}$$

Here, μ_0 and ε_0 are the permeability and permittivity of free space, while ρ_c and $\mathbf{J}_i$ are the charge and the current densities. They are defined as sums over all the present species,

$$\rho_c = \Sigma n_s e_s\,, \quad \text{and} \quad \mathbf{J}_i = \Sigma n_s e_s u_i\,, \tag{7.9}$$

with n being the number density of that species.

Unlike the diatomic gases discussed in Section 7.1.1, the terms that are added here through the consideration of the electromagnetic field are coupled to the known moments. However, it turns out that these can be moved to the right-hand side of the equations, effectively acting as another interparticle effect source term. After some massaging, the 20-moment equations have the form

$$\frac{\partial}{\partial t}\left(\rho_s\right) + \frac{\partial}{\partial x_i}\left(\rho_s u_i\right) = 0\,, \tag{7.10}$$

$$\frac{\partial}{\partial t}\left(\rho_s u_i\right) + \frac{\partial}{\partial x_j}\left(\rho_s u_i u_j + P_{ij}\right) = \rho_s e_s\left(\boldsymbol{E}_i + \epsilon_{ijk} v_j \boldsymbol{B}_k\right) + \boldsymbol{S}_i\,, \tag{7.11}$$

$$\begin{aligned}&\frac{\partial}{\partial t}\left(\rho_s u_i u_j + P_{ij}\right) + \frac{\partial}{\partial x_k}\left(\rho_s u_i u_j u_k + P_{ij}u_k + P_{ik}u_j + P_{jk}u_i + Q_{ijk}\right)\\ &= \rho_s e_s u_i \boldsymbol{E}_j + e_s \epsilon_{jkl} P_{jk} \boldsymbol{B}_l + \boldsymbol{S}_{ij}\left(\boldsymbol{U}\right)\,,\end{aligned} \tag{7.12}$$

$$\begin{aligned}&\frac{\partial}{\partial t}\left(\rho_s u_i u_j u_k + P_{ij}u_k + P_{ik}u_j + P_{jk}u_i + Q_{ijk}\right) + \frac{\partial}{\partial x_l}(\rho_s u_i u_j u_k u_l + P_{ij}u_k u_l + P_{ik}u_j u_l\\ &+ P_{jk}u_i u_l + P_{il}u_j u_k + P_{jl}u_i u_k + P_{kl}u_i u_j + Q_{ijk}u_l + Q_{ijl}u_k + Q_{ikl}u_j + Q_{jkl}u_i + R_{ijkl})\\ &= e_s\left(\boldsymbol{E}_i P_{jk} + \epsilon_{ilm} Q_{jkl}\boldsymbol{B}_m\right) + \boldsymbol{S}_{ijk}\left(\boldsymbol{U}\right)\,,\end{aligned} \tag{7.13}$$

for every species. This gives a very natural pathway of extension of these generalizable extended moment closures for magnetohydrodynamic predictions.

Bibliography

[1] R. L. Deschambault and I. I. Glass. An update on non-stationary oblique shock-wave reflections: actual isopycnics and numerical experiments. *Journal of Fluid Mechanics*, 131:27–57, 1983.

[2] G. A. Bird. *Molecular gas dynamics and the direct simulation of gas flows*. Oxford university press, 1994.

[3] L. Mieussens. Discrete velocity model and implicit scheme for the BGK equation of rarefied gas dynamics. *Mathematical Models and Methods in Applied Sciences*, 10 (08):1121–1149, 2000.

[4] H. T. Huynh. An upwind moment scheme for conservation laws. In *Computational Fluid Dynamics 2004: Proceedings of the Third International Conference on Computational Fluid Dynamics, ICCFD3, Toronto, 12–16 July 2004*, pages 761–766. Springer, 2006.

[5] A. Harten. High resolution schemes for hyperbolic conservation laws. *Journal of computational physics*, 135(2):260–278, 1997.

[6] A. Harten, P. D. Lax, and B. Van Leer. On upstream differencing and Godunov-type schemes for hyperbolic conservation laws. *SIAM review*, 25(1):35–61, 1983.

[7] Y. Suzuki. *Discontinuous-Galerkin Methods for Extended Hydrodynamics*. PhD thesis, University of Michigan, 2008.

[8] J. Juno, A. Hakim, J. TenBarge, E. Shi, and W. Dorland. Discontinuous Galerkin

algorithms for fully kinetic plasmas. *Journal of Computational Physics*, 353:110–147, 2018. ISSN 0021-9991. doi: https://doi.org/10.1016/j.jcp.2017.10.009.

[9] H. Grad. On the kinetic theory of rarefied gases. *Communications on Pure and Applied Mathematics*, 2:331–407, 1949.

[10] W. Dreyer. Maximisation of the entropy in non-equilibrium. *Journal of Physics A: Mathematical and General*, 20(18):6505, 1987.

[11] I. Müller and T. Ruggeri. *Rational extended thermodynamics*, volume 37. Springer Science & Business Media, 1993.

[12] C. D. Levermore. Moment closure hierarchies for kinetic theories. *Journal of Statistical Physics*, 83:1021–1065, 1996.

[13] Sydney Chapman and Thomas George Cowling. *The mathematical theory of non-uniform gases: an account of the kinetic theory of viscosity, thermal conduction and diffusion in gases*. Cambridge university press, 1990.

[14] M. R. A. Abdelmalik and E. H. Van Brummelen. Moment closure approximations of the Boltzmann equation based on φ-divergences. *Journal of Statistical Physics*, 164(1):77–104, 2016.

[15] H. Struchtrup. *Macroscopic Transport Equations for Rarefied Gas Flows*. Springer New York, 2005. ISBN 1860-6245.

[16] H. Struchtrup and M. Torrilhon. Regularization of Grad's 13 moment equations: Derivation and linear analysis. *Physics of Fluids*, 15(9):2668–2680, 09 2003. ISSN 1070-6631. doi: 10.1063/1.1597472.

[17] J. G. McDonald and M. Torrilhon. Affordable robust moment closures for CFD based on the maximum-entropy hierarchy. *Journal of Computational Physics*, 251: 500–523, 2013.

[18] R. O. Fox, F. Laurent, and A. Vié. Conditional hyperbolic quadrature method of moments for kinetic equations. *Journal of Computational Physics*, 365:269–283, 2018.

[19] R. O. Fox and F. Laurent. Hyperbolic quadrature method of moments for the one-dimensional kinetic equation. *SIAM Journal on Applied Mathematics*, 82:750–771, 2022.

[20] R. O. Fox. Higher-order quadrature-based moment methods for kinetic equations. *Journal of Computational Physics*, 228(20):7771–7791, 2009.

[21] C. Yuan and R. O. Fox. Conditional quadrature method of moments for kinetic equations. *Journal of Computational Physics*, 230(22):8216–8246, 2011.

[22] W. Morin and J. G. McDonald. Development of globally hyperbolic one-dimensional moment closures based on orthogonal polynomials. *Journal of Computational Physics*, 2024.

[23] H. Struchtrup and H. C. Öttinger. Thermodynamically admissible 13-moment equations. *Physics of Fluids*, 34(1), 2022.

[24] L. Bell and H. Struchtrup. 13-moment-equations from nonequilibrium thermodynamics and kinetic theory: Comparison for non-linear one-dimensional flows. *Physics of Fluids*, 37(6):067122, 2025.

[25] T. I. Gombosi. *Gaskinetic theory*. Number 9. Cambridge University Press, 1994.

[26] P. L. Bhatnagar, E. P. Gross, and M. Krook. A model for collision processes in gases. i. small amplitude processes in charged and neutral one-component systems. *Physical review*, 94(3):511, 1954.

[27] I. D. Boyd and T. E. Schwartzentruber. *Nonequilibrium gas dynamics and molecular simulation*, volume 42. Cambridge University Press, 2017.

[28] Z. Cai, Y. Fan, and R. Li. On hyperbolicity of 13-moment system. *Kinetic and Related Models*, 7(3):415–432, 2014. ISSN 1937-5093. doi: 10.3934/krm.2014.7.415.

[29] Z. Cai, Y. Fan, and R. Li. Globally hyperbolic regularization of Grad's moment system. *Communications on pure and applied mathematics*, 67(3):464–518, 2014.

[30] M. Junk. Domain of definition of Levermore's five-moment system. *Continuum Mechanics and Thermodynamics*, 14:563–576, 2001.

[31] S. K. Godunov. An interesting class of quasilinear systems. *Soviet Mathematics Doklady*, 2:947–949, 1961.

[32] K. O. Friedrichs and P. D. Lax. Systems of conservation laws with a convex extension. *Proceedings of the National Academy of Sciences*, 68(8):1686–1688, 1971. doi: 10.1073/pnas.68.8.1686.

[33] F. Giroux and J. G. McDonald. An approximation for the twenty-one-moment maximum-entropy model of rarefied gas dynamics. *International Journal of Computational Fluid Dynamics*, 35(8):632–652, 2021.

[34] R. G. Patel, O. Desjardins, and R. O. Fox. Three-dimensional conditional hyperbolic quadrature method of moments. *Journal of Computational Physics*, 1:100006, 2019.

[35] C. P. T. Groth and J. G. McDonald. Towards physically realizable and hyperbolic moment closures for kinetic theory. *Continuum Mechanics and Thermodynamics*, 21:467–493, 2009.

[36] M. Arora and P. L. Roe. Issues and strategies for hyperbolic problems with stiff source terms. In *Barriers and Challenges in Computational Fluid Dynamics*, pages 139–154. Springer, 1998.

[37] J. A. Hittinger. *Foundations for the Generalization of the Godunov Method of Hyperbolic Systems with Stiff Relaxtion Source Terms*. PhD thesis, University of Michigan, 2000.

[38] C. Yan. *First-Order Hyperbolic Relaxation Turbulence Modelling for Moment-Closures*. PhD thesis, University of Ottawa, 2022.

[39] W. Kaufmann and J. G. McDonald. Large-scale investigation of 3D discontinuous-Galerkin-Hancock method for hyperbolic balance laws with stiff local source. In *Proceedings of ICCFD11*, 2022.

[40] B. Cockburn. Discontinuous Galerkin methods. *ZAMM-Journal of Applied Mathematics and Mechanics/Zeitschrift für Angewandte Mathematik und Mechanik: Applied Mathematics and Mechanics*, 83(11):731–754, 2003.

[41] G. Wanner and E. Hairer. *Solving ordinary differential equations II*, volume 375. Springer Berlin Heidelberg New York, 1996.

[42] V. Venkatakrishnan. Convergence to steady-state solutions of the Euler equations on unstructured grids with limiters. *Journal of Computational Physics*, 118(1):120–130, 1995.

[43] L. H. Khieu. *Solid-boundary treatment for moment systems*. PhD thesis, University of Michigan, 2012.

[44] J. L. Steger and R. F. Warming. Flux vector splitting of the inviscid gasdynamic equations with application to finite-difference methods. *Journal of computational physics*, 40(2):263–293, 1981.

[45] B. Van Leer, J. L. Thomas, P. L. Roe, and R. W. Newsome. A comparison of numerical flux formulas for the Euler and Navier-Stokes equations. 1987.

[46] J. Zhao, P. He, and H. Tang. Steger-Warming flux vector splitting method for special relativistic hydrodynamics. *Mathematical Methods in the Applied Sciences*, 37(7): 1003–1018, 2014.

[47] F. D. Witherden and A. Jameson. On the spectrum of the Steger-Warming flux-vector splitting scheme. *International Journal for Numerical Methods in Fluids*, 87 (12):601–606, 2018.

[48] M. Wolff, H. H. Abada, and H. A. K. Saad. Numerical investigation of supersonic

flow over a wedge by solving 2d Euler equations utilizing the Steger-Warming flux vector splitting (FVS) scheme. *Mathematics*, 12(9):1282, 2024.

[49] W. G. Vincenti and C. H. Kruger. *Introduction to Physical Gas Dynamics*. Krieger Publishing Company, 1986.

[50] S. Boccelli. Hyper2D: A finite-volume solver for hyperbolic equations and non-equilibrium flows. *Software Impacts*, 17:100557, 2023.

[51] S. J. Plimpton, S. G. Moore, A. Borner, A. K. Stagg, T.P. Koehler, J. R. Torczynski, and M. A. Gallis. Direct simulation Monte Carlo on petaflop supercomputers and beyond. *Physics of Fluids*, 31(8), 2019.

[52] H. G. Hornung. Regular and Mach reflection of shock waves. *Annual Review of Fluid Mechanics*, 18:33–58, 1986. doi: 10.1146/annurev.fl.18.010186.000341.

[53] G. Ben-Dor. *Shock Wave Reflection Phenomena*. Springer, New York, 2 edition, 2007.

[54] S.S.-M. Lau-Chapdelaine and M. I. Radulescu. Viscous solution of the triple-shock reflection problem. *Shock Waves*, 26(5):551–560, 2016.

[55] Y. B. Zeldovich, A. P. Genich, and G. B. Manelis. Distinctive features of translational relaxation at a shock-wave front in gas mixtures. In *Soviet Physics Doklady*, volume 24, page 756, 1979.

[56] A. S. Jayaraman, E. S. Genter, W. Dong, and H. Wang. Collision enhancement in shocks and its implication on gas-phase detonations: A molecular dynamics and gas-kinetic theory study. *Proceedings of the Combustion Institute*, 40(1):105741, 2024. ISSN 1540-7489. doi: https://doi.org/10.1016/j.proci.2024.105741.

[57] R. Murugesan and M. I. Radulescu. The influence of non-equilibrium translational effects on reactive dynamics during shock to detonation transition using molecular dynamics. In *29th International Colloquium on the Dynamics of Explosions and Reactive Systems*, 2023.

[58] W. Morin, J. G. McDonald, and M. I. Radulescu. A temperature non-equilibrium reactive model for detonation hydrodynamics. In *30th International Colloquium on the Dynamics of Explosions and Reactive Systems*, 2025.

[59] S. Boccelli, P. Parodi, T. E. Magin, and J. G. McDonald. Modeling high-Mach-number rarefied crossflows past a flat plate using the maximum-entropy moment method. *Physics of Fluids*, 35(8), 2023.

[60] J. G. McDonald. Numerical modeling of micron-scale flows using the Gaussian moment closure. Master's thesis, University of Toronto, 2005.

[61] A. Hakim. Extended MHD modelling with the ten-moment equations. *Journal of Fusion Energy*.

[62] S. Boccelli, J. G. McDonald, and T. E. Magin. 14-moment maximum-entropy modeling of collisionless ions for Hall thruster discharges. *Physics of Plasmas*, 29(8): 083903, 2022.

[63] S. Boccelli, F. Giroux, C. P. T. Groth, T. E. Magin, and J. G. McDonald. A 14-moment maximum-entropy description of electrons in crossed electric and magnetic fields. *Physics of Plasmas*, 27(12), 2020.

[64] D. C. Gilliland. Integral of the bivariate normal distribution over an offset circle. *Journal of the American Statistical Association*, 57(300):758–768, 1962.

[65] D. C. Gilliland and E. R. Hansen. A note on some series representations of the integral of a bivariate normal distribution over an offset circle. *Naval Research Logistics Quarterly*, 21(1):207–211, 1974.

Appendix A

Translationally Invariant 35-Moment Closure

In order to demonstrate that the technique can be extended to an arbitrarily high order of moments, a 35-moment closure was also constructed. This closure has the primitive variables

$$\begin{aligned}\boldsymbol{V} = \Big[& \rho\, u_x\, P_{xx}\, Q_{xxx}\, R_{xxxx}\, u_y\, P_{xy}\, Q_{xxy}\, R_{xxxy}\, u_z\, P_{xz}\, Q_{xxz}\, R_{xxxz}\, P_{yy} \\ & Q_{xyy}\, R_{xxyy}\, P_{yz}\, Q_{xyz}\, R_{xxyz}\, P_{zz}\, Q_{xzz}\, R_{xxzz}\, Q_{yyy}\, R_{xyyy}\, Q_{yyz}\, R_{xyyz} \\ & Q_{yzz}\, R_{xyzz}\, Q_{zzz}\, R_{xzzz}\, R_{yyyy}\, R_{yyyz}\, R_{yyzz}\, R_{yzzz}\, R_{zzzz} \Big]^T \end{aligned} \tag{A.1}$$

in their diagonalized order, including all 20 of the moments used in the 20-moment closure. The closing fluxes are then the entries of the 5^{th}-order tensor S_{ijklm}.

While the orthogonal-polynomial closure could again be used, another hierarchy which extends well with this technique, other than the extension of the orthogonal-polynomial hierarchy shown in Section 3.3, are the QMOM hierarchies of Fox and Laurent [18, 19]. This hierarchy was used for the construction of a 35-moment closure which only fulfills Properties 1 and 2. Once again starting in the top right corner with the largest subsystem,

the HyQMOM closing flux is

$$S_{xxxxx} = -\frac{Q_{xxx}P_{xx}}{2\rho} + \frac{5Q_{xxx}R_{xxxx}}{2P_{xx}} - \frac{3Q_{xxx}^3}{2P_{xx}^2}\,, \tag{A.2}$$

and can once again be directly substituted into the 5×5 system. This results in the subsystem

$$\widehat{\frac{\partial \boldsymbol{F}_x}{\partial \boldsymbol{U}}}_{5\times5} = \begin{bmatrix} 0 & 1 & 0 & 0 & 0 \\ 0 & 0 & 1 & 0 & 0 \\ 0 & 0 & 0 & 1 & 0 \\ 0 & 0 & 0 & 0 & 1 \\ \frac{\partial U_{xxxxx}}{\partial U_0} & \frac{\partial U_{xxxxx}}{\partial U_x} & \frac{\partial U_{xxxxx}}{\partial U_{xx}} & \frac{\partial U_{xxxxx}}{\partial U_{xxx}} & \frac{\partial U_{xxxxx}}{\partial U_{xxxx}} \end{bmatrix}, \tag{A.3}$$

as the top right corner of the Jacobian where the relevant closing flux derivatives are

$$\begin{aligned}
\frac{\partial U_{xxxxx}}{\partial U_0} =& u_x^5 + \frac{Q_{xxx}P_{xx}}{2\rho^2} + \frac{u_x^3P_{xx}}{2\rho} - \frac{u_x^2Q_{xxx}}{2\rho} + \frac{5u_xR_{xxxx}}{2\rho} - \frac{5u_x^2Q_{xxx}R_{xxxx}}{2P_{xx}^2} + \frac{3u_x^2Q_{xxx}^3}{P_{xx}^3} \\
&- \frac{3u_xP_{xx}^2}{2\rho^2} - \frac{5u_x^3R_{xxxx}}{2P_{xx}} + \frac{9u_x^3Q_{xxx}^2}{2P_{xx}^2} - \frac{7u_xQ_{xxx}^2}{2\rho P_{xx}} + \frac{5u_x^4Q_{xxx}}{2P_{xx}}\,, \\
\frac{\partial U_{xxxxx}}{\partial U_x} =& -5u_x^4 - \frac{3P_{xx}u_x^2}{2\rho} + \frac{Q_{xxx}u_x}{\rho} - \frac{5R_{xxxx}}{2\rho} + \frac{5u_xQ_{xxx}R_{xxxx}}{P_{xx}^2} - \frac{6u_xQ_{xxx}^3}{P_{xx}^3} + \frac{3P_{xx}^2}{2\rho^2} \\
&+ \frac{15R_{xxxx}u_x^2}{2P_{xx}} - \frac{27Q_{xxx}^2u_x^2}{2P_{xx}^2} + \frac{7Q_{xxx}^2}{2\rho P_{xx}} - \frac{10Q_{xxx}u_x^3}{P_{xx}}\,, \\
\frac{\partial U_{xxxxx}}{\partial U_{xx}} =& 10u_x^3 - \frac{Q_{xxx}}{2\rho} - \frac{5Q_{xxx}R_{xxxx}}{2P_{xx}^2} + \frac{3Q_{xxx}^3}{P_{xx}^3} + \frac{3u_xP_{xx}}{2\rho} - \frac{15u_xR_{xxxx}}{2P_{xx}} + \frac{27u_xQ_{xxx}^2}{2P_{xx}^2} \\
&+ \frac{15u_x^2Q_{xxx}}{P_{xx}}\,, \\
\frac{\partial U_{xxxxx}}{\partial U_{xxx}} =& -10u_x^2 - \frac{P_{xx}}{2\rho} + \frac{5R_{xxxx}}{2P_{xx}} - \frac{9Q_{xxx}^2}{2P_{xx}^2} - \frac{10u_xQ_{xxx}}{P_{xx}}\,, \\
\frac{\partial U_{xxxxx}}{\partial U_{xxxx}} =& 5u_x + \frac{5Q_{xxx}}{2P_{xx}}.
\end{aligned}$$

The 4×4 systems are slightly more complicated, as HyQMOM can only be constructed for odd-order moment systems. However, another earlier closure, the conditional hyperbolic QMOM (CHyQMOM) [18], was developed that has some convenient properties. This closure was designed to solve odd numbered systems, but forced one of the eigenvalues to be at the mean velocity of the gas, and was shown to be equivalent to building a closure

with the solution vector

$$\boldsymbol{U} = \begin{bmatrix} \rho u \\ \rho u^2 + P \\ \rho u^3 + 3Pu + Q \\ \rho u^4 + 6Pu^2 + 4Qu + R \end{bmatrix}, \tag{A.4}$$

for a one-dimensional gas. This is convenient, as this extension technique is also imposing eigenvalues to be at the mean velocity through the other subsystems in the Jacobian. It also gives rise to subsystems that begin with the first-order momentum moment, instead of the zeroth-order density moment. Both of these properties make it a natural choice to extension of HyQMOM for multidimensional gas.

This gives the random part of the closing flux for the 4×4 subsystems to be

$$S_{xxxxy} = \frac{\left(2Q_{xxx}R_{xxxy} + 2Q_{xxy}R_{xxxx}\right)P_{xx}^2 + \left(-2P_{xy}Q_{xxx}R_{xxxx} - 3Q_{xxx}^2R_{xxy}\right)P_{xx} + 2P_{xy}Q_{xxx}^3}{P_{xx}^3}, \tag{A.5}$$

for the y-direction, and is of the same form for the z-direction. This leads to

$$\widehat{\frac{\partial \boldsymbol{F}_x}{\partial \boldsymbol{U}}}_{4\times4} = \begin{bmatrix} 0 & 1 & 0 & 0 \\ 0 & 0 & 1 & 0 \\ 0 & 0 & 0 & 1 \\ \frac{\partial U_{xxxxy}}{\partial U_y} & \frac{\partial U_{xxxxy}}{\partial U_{xy}} & \frac{\partial U_{xxxxy}}{\partial U_{xxy}} & \frac{\partial U_{xxxxy}}{\partial U_{xxxy}} \end{bmatrix}, \tag{A.6}$$

as the 4×4 subsystem Jacobian, with the relevant derivatives as

$$\begin{aligned}
\frac{\partial U_{xxxxy}}{\partial U_y} =& -u_x^4 - \frac{R_{xxxx}}{\rho} + \frac{2u_xQ_{xxx}R_{xxxx}}{P_{xx}^2} - \frac{2u_xQ_{xxx}^3}{P_{xx}^3} + \frac{2R_{xxxx}u_x^2}{P_{xx}} - \frac{3Q_{xxx}^2u_x^2}{P_{xx}^2} \\
&+ \frac{Q_{xxx}^2}{\rho P_{xx}} - \frac{2Q_{xxx}u_x^3}{P_{xx}}, \\
\frac{\partial U_{xxxxy}}{\partial U_{xy}} =& 4u_x^3 - \frac{2Q_{xxx}R_{xxxx}}{P_{xx}^2} + \frac{2Q_{xxx}^3}{P_{xx}^3} - \frac{4u_xR_{xxxx}}{P_{xx}} + \frac{6u_xQ_{xxx}^2}{P_{xx}^2} + \frac{6u_x^2Q_{xxx}}{P_{xx}}, \\
\frac{\partial U_{xxxxy}}{\partial U_{xxy}} =& -6u_x^2 + \frac{2R_{xxxx}}{P_{xx}} - \frac{3Q_{xxx}^2}{P_{xx}^2} - \frac{6u_xQ_{xxx}}{P_{xx}}, \\
\frac{\partial U_{xxxxy}}{\partial U_{xxxy}} =& 4u_x + \frac{2Q_{xxx}}{P_{xx}}
\end{aligned}$$

and the derivatives for $\frac{\partial U_{xxxxz}}{\partial U_z}$ to $\frac{\partial U_{xxxxz}}{\partial U_{xxxz}}$ having the same form. Each term of these subsystem Jacobians are also simply polynomials of moments from the previous subsystem,

Finishing the bottom right corner with the Euler, isothermal Euler, and convection systems from Equations (3.6), (3.7), and (3.8) respectively, results in the random components for the closing fluxes moments

$$
\begin{aligned}
S_{xxxxx} &= -\frac{Q_{xxx}P_{xx}}{2\rho} + \frac{5Q_{xxx}R_{xxxx}}{2P_{xx}} - \frac{3Q_{xxx}^3}{2P_{xx}^2}\,, \\
S_{xxxxy} &= \frac{2Q_{xxx}R_{xxxy} + 2Q_{xxy}R_{xxxx}}{P_{xx}} - \frac{2P_{xy}Q_{xxx}R_{xxxx} + 3Q_{xxx}^2R_{xxxy}}{P_{xx}^2} + \frac{2P_{xy}Q_{xxx}^3}{P_{xx}^3}\,, \\
S_{xxxxz} &= \frac{2Q_{xxx}R_{xxxz} + 2Q_{xxz}R_{xxxx}}{P_{xx}} - \frac{2P_{xz}Q_{xxx}R_{xxxx} + 3Q_{xxx}^2R_{xxxz}}{P_{xx}^2} + \frac{2P_{xz}Q_{xxx}^3}{P_{xx}^3}\,, \\
S_{xxxyy} &= \frac{3P_{xx}Q_{xyy}}{\rho}\,, \quad S_{xxxyz} = \frac{3P_{xx}Q_{xyz}}{\rho}\,, \quad S_{xxxzz} = \frac{3P_{xx}Q_{xzz}}{\rho}\,, \\
S_{xxyyy} &= \frac{Q_{yyy}P_{xx}}{\rho}\,, \quad S_{xxyyz} = \frac{Q_{yyz}P_{xx}}{\rho}\,, \quad S_{xxyzz} = \frac{Q_{yzz}P_{xx}}{\rho}\,, \quad S_{xxzzz} = \frac{Q_{zzz}P_{xx}}{\rho}\,, \\
S_{xyyyy} &= S_{xyyyz} = S_{xyyzz} = S_{xyzzz} = S_{xzzzz} = 0\,,
\end{aligned}
$$

and the resulting flux Jacobian structure shown in Figure A.1. Once again, the result is a robustly hyperbolic set of equations with flux Jacobian eigenvalues that are guaranteed to be real.

The dispersion analysis for the 35-moment model is shown in Figure A.2, and was performed as described in Section 3.4. While the 20-moment models wave speeds are fairly simple, the 35-moment model results in some interesting complexities. The first is that the 3×3 subsystems have two different behaviours. For the U_{yy} to U_{xxyy} and U_{zz} to U_{xxzz} systems, the waves stay constant as the wave number varies, remaining at the mean velocity u_x, and speeds $u_x \pm \sqrt{\frac{3P_{xx}}{\rho}}$. However, while the U_{yz} to U_{xxyz} system does have one wave that stays at the mean velocity, the other two decay to $u_x \pm \sqrt{\frac{P_{xx}}{\rho}}$. This change is due to the source term dominating, and the wave speeds of the system being forced back to the isothermal Euler waves it had in the 10-moment closure.

The second complexity is the waves denoted as re-coupled waves, shown in orange. These waves arise from the U_{yyyy} and U_{zzzz} subsystems, which are closed by simply convecting the moments such that $S_{xyyyy} = S_{xzzzz} = 0$. For both large and small wave

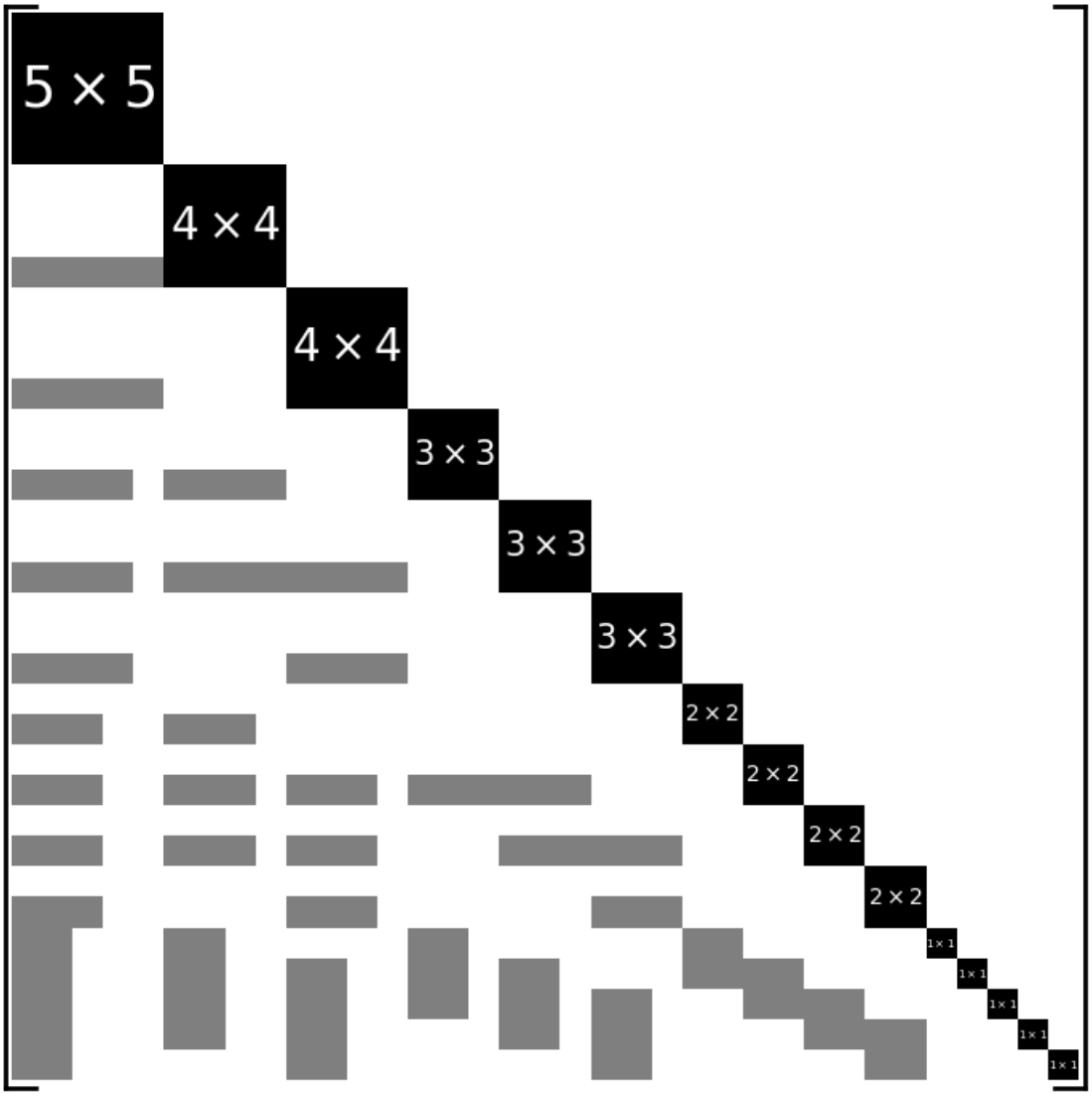

Figure A.1: 35-moment closure flux Jacobian structure.

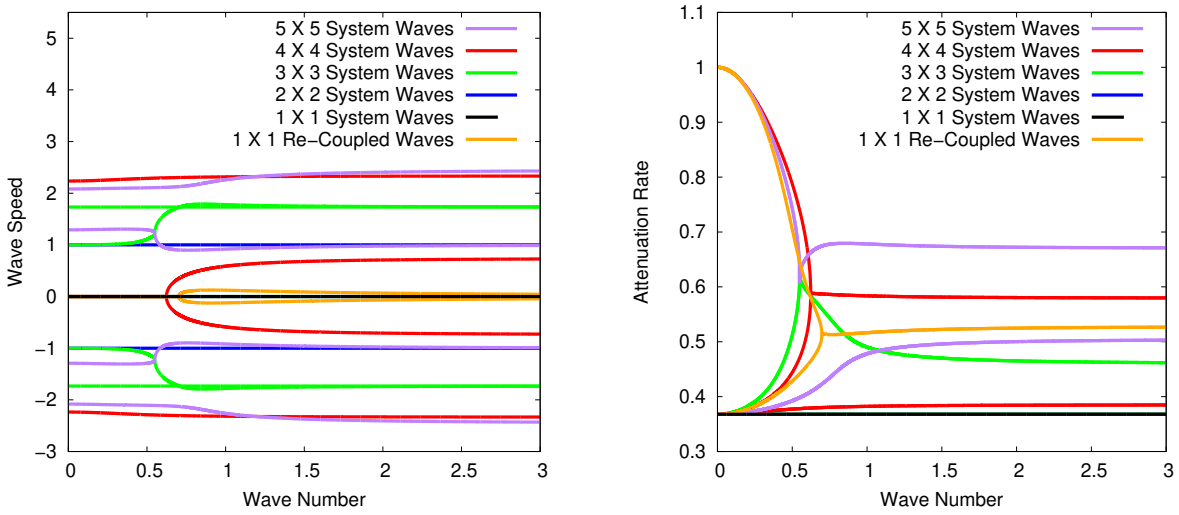

(a) (b)

Figure A.2: Dispersion analysis for the translationally invariant 35-moment closure

numbers, these moments have the prescribed wave speed u_x, however near $k = 1$ when both the flux and source Jacobian effects are of the same magnitude, there is some interaction between these two subsystems and the 5×5 subsystem. This stems from this model decoupling R_{yyyy} and R_{zzzz} from the full x-direction moments, but in equilibrium this is not true. The fourth order random moment for the y-direction and z-directions of the Maxwellian is

$$\left\langle mc_y^4 \mathcal{M} \right\rangle = \left\langle mc_z^4 \mathcal{M} \right\rangle = \frac{3p^2}{\rho} = \frac{\left(P_{xx} + P_{yy} + P_{zz}\right)^2}{3\rho}, \tag{A.7}$$

which through the thermodynamic pressure p re-couples these moments to earlier subsystems. When both Jacobians have roughly equal influence on the wave dispersion, the result is that these two waves diverge from the mean velocity briefly, before coming back together.

Results for the model presented in Section 4.2. Due to the difficulty in extension of the improved 20-moment closure to being rotationally invariant, improving the rotational properties of the 35-moment was not attempted, and this model is currently limited to the translationally invariant only family of closures. However, it does demonstrate that the technique can continue to extend so long as the structure of the Jacobian is maintained in order to ensure robust hyperbolicity.

Appendix B

Exact Solution for the Discontinuous Bubble Problem in the Free-Molecular Regime

Multidimensional solutions by direct integration of the kinetic equations are very computationally expensive. While the continuum-regime limit which agrees with the Euler equations is easily verifiable, the free-molecular and transition regimes are more difficult to know if an accurate solution has been obtained. By finding an exact solution to the free-molecular bubble problem, and comparing the BGK solution, there can be more confidence for the accuracy of the solver in these regimes.

In the absence of collisions, the bubble problems outlined in Section 4.3 can be simplified in order to find nearly exact solutions that are only a function of the initial condition and the time that has passed. Beginning with the Boltzmann equation shown in Equation (2.7), but in polar coordinates, gives

$$\frac{\partial \mathcal{F}}{\partial t} + \frac{1}{r}\frac{\partial \left(r v_r \mathcal{F}\right)}{\partial r} + \frac{1}{r}\frac{\partial \left(v_\theta \mathcal{F}\right)}{\partial \theta} + \frac{\partial \left(v_z \mathcal{F}\right)}{\partial z} = 0\,, \tag{B.1}$$

which further simplifies to

$$\frac{\partial \mathcal{F}}{\partial t} + \frac{\partial \left(v_r \mathcal{F}\right)}{\partial r} = -\frac{v_r}{r}\mathcal{F}\,, \tag{B.2}$$

due to symmetry. Introducing the change of variables

$$r = r_0 + v_r s\,, \quad t = s\,, \tag{B.3}$$

gives the equations in the form

$$\frac{\mathrm{d}\mathcal{F}}{\mathrm{ds}} = -\frac{v_r}{r + v_r s}\mathcal{F}\,, \tag{B.4}$$

which can be directly integrated from the initial distribution, $\mathcal{F}\left(r, t = 0\right)$, to the distribution at any time in the future $\mathcal{F}\left(r, t\right)$

$$\int_{\mathcal{F}(r,t=0)}^{\mathcal{F}(r,t)} \frac{\mathrm{d}\mathcal{F}}{\mathcal{F}} = \int_0^t -\frac{v_r}{r_0 + v_r s}\mathrm{ds}\,. \tag{B.5}$$

This results in the distribution in the future being

$$\mathcal{F}(r, t) = \mathcal{F}(r - v_r t, 0)\frac{r - v_r t}{r}\,, \tag{B.6}$$

or the distribution of the initial condition shifted and scaled radially.

Because the initial distribution is in equilibrium and discontinuous such that the bubble is at the same temperature as its surroundings, the only variables needed to describe the initial distribution are the densities inside and outside the bubble, ρ_{in} and ρ_{out}, and the temperature, T. Particles outside the bubble have a Maxwellian distribution

$$\mathcal{F}_{out} = \frac{\rho}{m}\left(\frac{1}{2\pi T}\right)^{\frac{3}{2}} \exp\left[-\frac{1}{2T}\left(v_x^2 + v_y^2 + v_z^2\right)\right], \tag{B.7}$$

and for an arbitrary point outside the bubble, (x_p, y_p), this can be directly integrated to find their effect. However, the effect of particles which came from inside the bubble, the distribution is not centred on the origin of velocity space. One then only needs to ask in which regions of velocity space did the particles come from inside the bubble.

The boundary between particles which came from inside or outside the bubble for an arbitrary point in space is shown in Figure B.1, showing velocities of particles that come

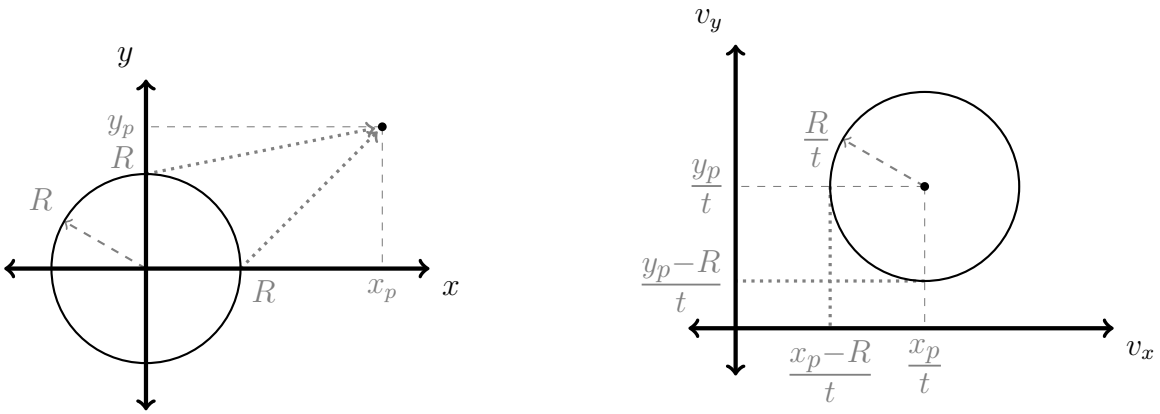

(a) Physical space (b) Velocity space

Figure B.1: Illustration of the physical and velocity spaces of the free molecular bubble problem

from the boundary of the bubble and reach an arbitrary point in space outside the bubble after some time. The boundary is given by

$$\left(\frac{R}{t}\right)^2 = \left(v_x - \frac{x_p}{t}\right)^2 + \left(v_y - \frac{y_p}{t}\right)^2, \tag{B.8}$$

as particles on the boundary of the bubble with radius, R, could only have reached the point by traveling in a straight line. The velocity is then simply how far in a straight line the particle needs to travel, divided by the time, t. This gives the distribution of particles which arrived from inside the bubble as

$$\mathcal{F}_{in} = \frac{\rho}{m}\left(\frac{1}{2\pi T}\right)^{\frac{3}{2}} \exp\left[-\frac{1}{2T}\left(\left(v_x - \frac{x_p}{t}\right)^2 + \left(v_y - \frac{y_p}{t}\right)^2 + v_z^2\right)\right], \tag{B.9}$$

however due to the circular boundary, it is more convenient to integrate this in cylindrical coordinates. By defining $r = \sqrt{x_p^2 + y_p^2}$, $v_r = \sqrt{v_x^2 + v_y^2}$, and $\theta = \arctan\left(\frac{y_p}{x_p}\right)$, the distribution can be rewritten as

$$\mathcal{F}_{in} = \frac{\rho}{m}\left(\frac{1}{2\pi T}\right)^{\frac{3}{2}} \exp\left[-\frac{1}{2T}\left(v_r^2 - 2v_r\frac{r}{t}\cos^2\theta - 2v_r\frac{r}{t}\sin\theta\cos\theta + \frac{r^2}{t^2} + v_z^2\right)\right], \tag{B.10}$$

which can be integrated over the circle in velocity space in order to find the contribution of effects of particles which came from inside the bubble.

Both distributions can then be integrated

$$U_{ijk\ldots l} = \left\langle m\rho_{out} v_x^{n_x} v_y^{n_y} v_z^{n_z} \mathcal{F}_{out} \right\rangle + (\rho_{in} - \rho_{out}) \int_{-\infty}^{\infty} \int_0^{\frac{R}{t}} \int_0^{2\pi} m \left(v_r \cos\theta - \frac{x_p}{t} \right)^{n_x} \left(v_r \sin\theta - \frac{y_p}{t} \right)^{n_y} v_z^{n_z} \mathcal{F}_{in} v_r \, \mathrm{d}\theta \, \mathrm{dv_r} \, \mathrm{dv_z} \,, \tag{B.11}$$

to find the moments. While straightforward in description, integration over an offset circle of a Maxwellian distribution isn't known in closed form in the literature [64, 65]. To illustrate this, consider the density moment

$$U_0 = \left\langle m\rho_{out} \mathcal{F}_{out} \right\rangle + (\rho_{in} - \rho_{out}) \int_{-\infty}^{\infty} \int_0^{\frac{R}{t}} \int_0^{2\pi} v_r \mathcal{F}_{in} \, \mathrm{d}\theta \, \mathrm{dv_r} \, \mathrm{dv_z} \,, \tag{B.12}$$

which can almost be completely integrated in closed form up to

$$\begin{aligned} U_0 = \rho_{out} - (\rho_{in} - \rho_{out}) \int_0^{2\pi} & \frac{A}{2\sqrt{\pi}} \frac{r}{R} \cos\theta \left[\mathrm{erf}\left(\mathrm{A} \frac{\mathrm{r}}{\mathrm{R}} \cos\theta \right) \right. \\ & \left. + \mathrm{erf}\left(\mathrm{A} - \mathrm{A} \frac{\mathrm{r}}{\mathrm{R}} \cos\theta \right) \right] \exp\left(-A^2 \frac{r^2}{R^2} \left(1 - \cos^2\theta \right) \right) \\ & - \frac{1}{2\pi} \exp\left(-A^2 \left(1 + \frac{r^2}{R^2} - 2\frac{r}{R} \cos\theta \right) \right) \\ & + \frac{1}{2\pi} \exp\left(-A^2 \frac{r^2}{R^2} \right) \mathrm{d}\theta \,, \end{aligned} \tag{B.13}$$

with the coefficient, $A = \frac{R}{\sqrt{2Tt}}$, being a constant with respect to θ. While the terms which are solely exponentials have closed form solutions, there is no solution in the literature for the part of the integral of the form

$$\int_0^{2\pi} \frac{A}{2\sqrt{\pi}} \frac{r}{R} \cos\theta \left[\mathrm{erf}\left(\mathrm{A} \left(1 - \frac{\mathrm{r}}{\mathrm{R}} \cos\theta \right) \right) \right] \exp\left(-A^2 \frac{r^2}{R^2} \left(1 - \cos^2\theta \right) \right) \mathrm{d}\theta \,, \tag{B.14}$$

which makes finding closed form solutions to the moments impossible. In absence of a closed form solution, there are arbitrarily accurate series solutions, or numerical integration, which can approximate the moments to arbitrarily high accuracy. For this work, we consider numerical integration of Equation (B.13) using a five point Gaussian quadrature rule, which is sufficiently accurate for comparison with the BGK solution.

A comparison between the numerical solutions for density of Equation (B.13), and

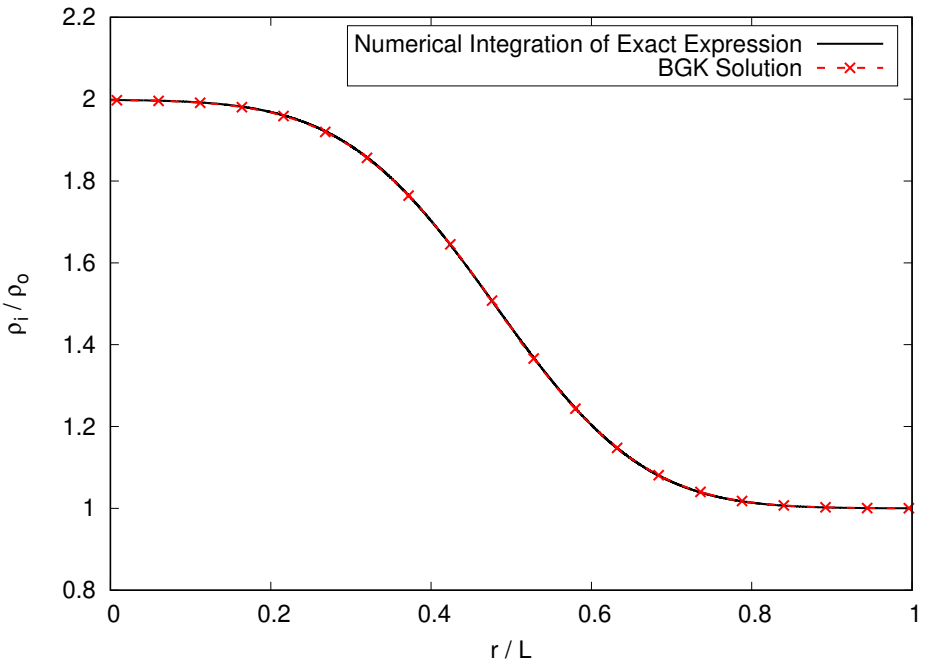

Figure B.2: Comparison of Exact and BGK density profile solutions for the discontinuous bubble problem

the BGK solutions, are shown in Figure B.2. There is good agreement between both approaches, indicating that the BGK solution is correct in the free molecular limit. With both the continuum and free molecular limits being nearly identical to their theoretical solutions, the transition-regime solutions (for which there is not a theoretical solution) can be trusted for comparison against the high-order moment models.